

DESIGN OF HIGH-PERFORMANCE AND EFFICIENT ALGORITHM FOR CARDIAC ABNORMALITY DETECTION FROM ECG SIGNALS

Thesis submitted in Fulfilment of the requirements for the Degree of

DOCTOR OF PHILOSOPHY

By

PRASHANT MANI TRIPATHI

Enrolment No: E19SOE805

Under the supervision of

Dr. Rama S. Komaragiri

Dr. Manjeet Kumar



BENNETT
UNIVERSITY
THE TIMES GROUP

Department of Electronics and Communication Engineering

BENNETT UNIVERSITY

(Established under UP Act No 24, 2016)

Plot Nos 8-11, Tech Zone II,

Greater Noida-201310, Uttar Pradesh, India.

Month.....year.....

©PRASHANT MANI TRIPATHI, (2023)

Bennett University has the royalty-free permission to reproduce and distribute copies of this

Thesis for teaching and research as well as for dissemination of Knowledge.

Thesis Evaluation

This is to certify that **Prashant Mani Tripathi** (Enrolment Number E19SOE805) has successfully defended the Thesis titled **Design of High Performance and Efficient Algorithm for Cardiac Abnormality Detection from ECG Signals** on .../.../20...

The committee recommends the candidate for the award of the Degree of Doctor of Philosophy.

Signature of External Examiner

Signature of Internal Examiner

DECLARATION

I hereby declare that the work reported in the Ph.D. thesis entitled "**Design of High Performance and Efficient Algorithm for Cardiac Abnormality Detection from ECG Signals**" submitted at **Bennett University, Greater Noida, India**, is an authentic record of my work carried out under the supervision of **Dr. Rama S. Komaragiri and Dr. Manjeet Kumar**. I have not submitted this work elsewhere for any other degree or diploma. I am fully responsible for the contents of my Ph.D. Thesis.



Signature

Prashant Mani Tripathi

Department of Electronics and Communication Engineering

Bennett University, Greater Noida, India

18/03/2024

CERTIFICATE

This is to certify that the thesis entitled **Design of High Performance and Efficient Algorithm for Cardiac Abnormality Detection from ECG Signals** submitted by **Prashant Mani Tripathi** at **Bennett University, Greater Noida, India**, is a bonafide record of his original work carried out under our supervision. This work has not been submitted elsewhere for any other degree or diploma.



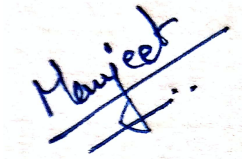
Dr. Rama S. Komaragiri

Professor

Department of ECE

SEAS, Bennett University

Greater Noida, Uttar Pradesh



Dr. Manjeet Kumar

Assistant Professor

Department of ECE

Delhi Technological University

Delhi

Place: Bennett University

(Signature of the Head of the Department)

Date:

(Office Seal)

Dedicated to my *Parents*
Dr. D.N.M. Tripathi
And
Neelam Tripathi

ACKNOWLEDGMENT

First, I would like to thank the almighty God for His blessing, strength, faithfulness, and love from the beginning of my academic life up to this doctoral level. There are no proper words to convey my deep gratitude and respect for my thesis and research supervisors, Dr. Rama S. Komaragiri and Dr. Manjeet Kumar. They always inspired me to become an independent researcher and helped me realize the power of critical reasoning. Their knowledge and expertise always helped me at every step of this work. From, Both, I learned, not only the knowledge of biomedical signal processing but also the rigorous scientific approach and the dedicated spirit for work. Without their supervision, I would not have completed this challenging work.

I would like to thank Dr. Ashish Kumar for his invaluable guidance, encouragement, academic stimulus, and generous help.

I'm extremely grateful to Dr. Neelanchali Asija Bhalla, Dr. Rahul Mukherjee, and Dr. Tanveer Ahmad for their time and valuable suggestions for improving my work.

I also thank all the staff members of the Department of ECE, Bennett University for their prompt support whenever needed.

My special thanks to Mrs. Neha Sharma for providing valuable suggestions and support whenever required.

I would like to express my gratitude to my parents Dr. D. N. M. Tripathi and Smt. Neelam Tripathi for their unfailing emotional support, trust, and patience.

I deeply thank my sisters, Khushboo and Dr. Namrata for their unconditional trust, timely encouragement, and endless patience. It was their love that raised me up again when I got weary. The family of my sisters, Er. A.N. Shukla, Er. Abhinav Mishra, my nephews Amiya, Priyam, Hemang, and my niece Ahana, have also been generous with their love and encouragement despite the long distance between us.

As to my sweet little girl, Arayana, my love and longing for her are beyond words. She is the softest point of my heart. I am sorry for not being able to give enough time to her during the period of my Ph.D. work.

Finally, but not least, I thank with love Shristy, my wife. Understanding me best as a Ph.D. herself, Shristy has been my best friend and great companion, loved, supported, encouraged, entertained, and helped me get through the period of my Ph.D. work in the most positive way.

ABSTRACT

Cardiovascular disease (CVD) affecting millions of people worldwide, poses a significant and growing health problem. CVD refers to a range of diseases affecting the heart and blood vessels. The serious and rapid nature of CVD demands an early, prompt diagnosis and treatment to reduce its high mortality and morbidity rate. Electrocardiogram (ECG), reflecting the hearts' electrical activity is a popular clinical tool to detect CVD and other heart abnormalities. In ECG signal analysis, noises and artifacts are the most problematic. Denoising ECG signals are vital for efficiently detecting morphological features such as R peak and QRS complex. In the literature, various denoising techniques based on time, frequency, and time-frequency domain have been proposed. The time-frequency domain-based techniques are advantageous as they have information about time as well as frequency both. In this report, an algorithm based on the Fourier decomposition method (FDM) (time-frequency domain technique) is found suitable for denoising ECG signals. The proposed algorithm performs well with various noises and artifacts present in ECG signals. Simulation results show that the proposed denoising method is also effective with real-time ECG signal. After denoising, the detection of ECG morphological features entails cardiac health. A QRS complex detection algorithm is proposed in this work. The proposed algorithm utilizes a fractional Fourier transform to detect QRS complexes present in the ECG signal. The proposed algorithm provides an overall sensitivity, positive predictivity, and error of 99.83%, 99.48%, and 0.008 respectively.

Automatic detection of CVD with a computer-aided cardiac system, involving less human effort has the potential to lower the burden of medical professionals. An algorithm utilizing superlet transform (SLT) and deep convolutional neural networks is proposed to detect atrial fibrillation and ventricular fibrillation from ECG signals. The SLT provides a two-dimensional high-resolution time-frequency spectrogram of ECG signals further utilized for the classification of ECG signals. In the proposed method SLT has successfully detected the QRS complexes in the ECG signal also. The combination of SLT and DenseNet-201 provides an accuracy of 96.2% on the test database. The superior denoising capability of SLT avoids the requirement of extra denoising steps and minimizes the circuit complexity. Nowadays, In the medical field, security, efficient transmission, and storage of biomedical signals are often required. The medical fraternity demands such a kind of security that does not alter the characteristics of biomedical signals along with lossless data compression for efficient transmission and storage. In this thesis, a watermarking approach and FDM-based compression

method are proposed to secure and efficient transmission of ECG signals. The proposed watermarking scheme secures ECG signals without altering the morphological features which is essential. The proposed method improves the quality of the reconstructed ECG signal by removing the noisy components. The proposed method effectively reduces the noises such as muscle contraction, motion artifact, eelectromyographic noise and name a few. The obtained results show that the proposed method provides high output signal-to-noise ratio, low percentage root mean square difference, and high compression ratio compared to existing techniques. The proposed watermarking and compression technique using FDM provides an efficient, reliable, and secure way to transfer the ECG signals by minimizing the losses in the original ECG signal.

Keywords: *Cardiovascular diseases, Electrocardiogram, ECG denoising, QRS complex detection, Fourier decomposition method, Superlet transform, Deep convolutional neural network, watermarking*

Table of Contents

| | |
|--|-----------|
| DECLARATION..... | iv |
| CERTIFICATE..... | v |
| ACKNOWLEDGMENT..... | vii |
| ABSTRACT..... | viii |
| List of Figures..... | xiii |
| List of Tables..... | xv |
| List of Abbreviations..... | xvii |
| List of Symbols..... | xx |
| CHAPTER 1 | 1 |
| INTRODUCTION | 1 |
| 1.1. CARDIOVASCULAR DISEASE | 1 |
| 1.2. NEED AND MOTIVATION | 5 |
| 1.3. IDENTIFYING THE RESEARCH PROBLEM | 5 |
| 1.4. OBJECTIVE OF THE WORK | 7 |
| 1.5. OUTLINE OF THE THESIS | 7 |
| CHAPTER 2 | 11 |
| BASICS OF ELECTRICAL ACTIVITY OF A HUMAN HEART-AN ELECTROCARDIOGRAM | 11 |
| 2.1. ANATOMY OF THE HUMAN HEART | 11 |
| 2.2. THE HUMAN HEART CONDUCTION SYSTEM | 12 |
| 2.3. WORKING OF THE HUMAN HEART | 13 |
| 2.4. THE ELECTROCARDIOGRAM AND ITS CHARACTERISTICS | 14 |
| 2.5. OVERVIEW OF DETECTION OF CVD | 19 |
| 2.6. NOISES AND ARTEFACTS IN ELECTROCARDIOGRAM SIGNALS | 20 |
| 2.7. SUMMARY | 23 |
| CHAPTER 3 | 25 |
| LITERATURE SURVEY | 25 |
| 3.1. ECG SIGNAL PROCESSING ALGORITHM | 25 |
| 3.2. PREPROCESSING OF AN ECG SIGNAL | 26 |
| 3.3. ECG SIGNAL CHARACTERISTIC DETECTION TECHNIQUES | 46 |

| | |
|--|-----|
| 3.4. DATABASES TO EVALUATE THE PERFORMANCES OF ECG ANALYSIS ALGORITHMS | 59 |
| 3.5. PARAMETERS TO EVALUATE THE PERFORMANCE OF AN ECG SIGNAL ANALYSIS ALGORITHM | 63 |
| 3.6. DISCUSSION, CHALLENGES, GAPS | 65 |
| 3.7. SUMMARY | 67 |
| CHAPTER 4 | 69 |
| DENOISING OF ECG SIGNAL FOR DETECTION OF CARDIOVASCULAR DISEASE | 69 |
| 4.1. ECG SIGNAL DENOISING METHODS | 69 |
| 4.2. MATHEMATICAL DESCRIPTION OF FOURIER DECOMPOSITION METHOD | 72 |
| 4.2.1 Continuous Time Fourier Decomposition Method | 72 |
| 4.2.2 Discrete Fourier Decomposition Method | 74 |
| 4.3. ECG SIGNAL DENOISING USING THE FOURIER DECOMPOSITION METHOD | 75 |
| 4.4. SIMULATIONS AND PERFORMANCE EVALUATION OF THE FDM-BASED DENOISING METHOD | 78 |
| 4.4.1 Simulation Results with Power Line Interference | 79 |
| 4.4.2 Simulation Results with White Gaussian Noise | 84 |
| 4.4.3 Simulation Results with Baseline Wander | 86 |
| 4.4.4 Simulation Results with Muscle Contraction, Motion Artifacts, And Electromyographic Noise | 91 |
| 4.5. SUMMARY | 94 |
| CHAPTER 5 | 95 |
| ECG SIGNAL ANALYSIS USING QRS COMPLEX DETECTION | 95 |
| 5.1. DETECTION OF QRS COMPLEX | 95 |
| 5.2. MATHEMATICAL DESCRIPTION OF FRACTIONAL FOURIER TRANSFORM | 96 |
| 5.2.1 Continuous Fractional Fourier Transform | 96 |
| 5.2.2 Discrete Fractional Fourier Transform | 98 |
| 5.3. FRACTIONAL FOURIER TRANSFORM-BASED ALGORITHM TO DETECT QRS COMPLEX | 99 |
| 5.4. PERFORMANCE EVALUATION AND RESULTS | 101 |
| 5.4.1 Qualitative Analysis of the FrFT-based QRS Complex Detection Method ... | 102 |

| | |
|---|-----|
| 5.4.2 Quantitative Analysis of the FrFT-Based QRS Complex Detection Method. | 102 |
| 5.5. SUMMARY..... | 107 |
| CHAPTER 6..... | 108 |
| CLASSIFICATION OF CARDIAC ARRHYTHMIA | 108 |
| 6.1. CLASSIFICATION OF ECG SIGNALS..... | 108 |
| 6.2. MATHEMATICAL DESCRIPTION OF SUPERLET TRANSFORM | 109 |
| 6.3. CLASSIFICATION OF ARRHYTHMIAS USING SUPERLET TRANSFORM AND DEEP CONVOLUTIONAL NETWORKS..... | 111 |
| 6.4. SIMULATIONS AND PERFORMANCE EVALUATION OF THE SLT-BASED CLASSIFICATION TECHNIQUE..... | 116 |
| 6.4.1 Time-Frequency Representation of ECG signals Using SLT | 116 |
| 6.4.2 Classification of Images With Deep Convolutional Neural Networks..... | 120 |
| 6.4.2.1 Simulation results with AlexNet | 121 |
| 6.4.2.2 Simulation results with GoogLeNet | 122 |
| 6.4.2.3 Simulation results with DenseNet-201 | 123 |
| 6.5. SUMMARY..... | 127 |
| CHAPTER 7..... | 128 |
| SECURITY AND COMPRESSION OF ECG SIGNAL | 128 |
| 7.1. WATERMARKING OF ECG SIGNAL..... | 128 |
| 7.2. SIMULATIONS AND PERFORMANCE EVALUATION OF THE FDM-BASED WATERMARKING METHOD | 133 |
| 7.3. COMPRESSION OF ECG SIGNALS USING THE FOURIER DECOMPOSITION METHOD..... | 136 |
| 7.4. SIMULATIONS AND PERFORMANCE EVALUATION OF THE FDM-BASED COMPRESSION METHOD..... | 137 |
| 7.5. COMPARISON WITH EXISTING WORKS..... | 139 |
| 7.6. SUMMARY..... | 140 |
| CHAPTER 8..... | 141 |
| CONCLUSIONS AND FUTURE WORK | 141 |
| Publications From The Thesis..... | 143 |
| REFERENCES..... | 144 |

List of Figures

| | |
|---|----|
| Fig. 1.1: CVD mortality rate (per <i>lac</i> population) in Asian countries..... | 3 |
| Fig. 1.2: The age-standardized rates per <i>100,000</i> people for the incidence and prevalence of CVDs in countries that are members of the ESC..... | 4 |
| Fig. 1.3: Proportion of various CVDs in mortality..... | 5 |
| Fig. 1.4: Flow chart of the thesis | 8 |
| Fig. 2.1: The structure of the human heart | 11 |
| Fig. 2.2: The electrical activity of various cardiac tissues | 13 |
| Fig. 2.3: A schematic representation of an ECG waveform and its components..... | 15 |
| Fig. 2.4: R wave in different leads in normal ECG signal | 16 |
| Fig. 2.5: Effect of various noises on ECG signal (a) powerline interference (b) electrode contact noise (c) baseline drift (d) motion artifacts (e) muscle contraction (f) instrumentation noise | 23 |
| Fig. 3.1: Representation of various steps involved in an ECG signal processing algorithm .. | 25 |
| Fig. 3.2: Input ECG signal (Record-203) from (a) MIT-BIH arrhythmia database and (b) when subjected to a low-pass filter with a cut-off frequency of 11 Hz | 29 |
| Fig. 3.3: Input ECG signal (Record-203) from MIT-BIH arrhythmia database when subjected to a band-pass filter with a pass band frequency of 5-15 Hz | 29 |
| Fig. 3.4: ECG signal (Record-203) from MIT-BIH arrhythmia database and when subjected to a high-pass filter with a cut-off frequency of 5 Hz..... | 29 |
| Fig. 3.5: Input ECG signal (Record-203) from MIT-BIH arrhythmia database when subjected to a notch filter with a notch frequency 50 Hz..... | 30 |
| Fig. 3.6: Block diagram of a typical ECG signal filtering method based on low-pass and high-pass filters in ECG signal analysis | 30 |
| Fig. 3.7: Representation of an ECG signal analysis using filter banks | 34 |
| Fig. 3.8: Representation of an ECG signal analysis using wavelet transform | 42 |
| Fig. 3.9: (a) Input ECG signal (b) denoised ECG signal using WT | 43 |
| Fig. 3.10: ECG signal analysis with the help of the EMD method | 44 |
| Fig. 3.11: Input ECG signal and the resultant eight IMFs after EMD decomposition..... | 45 |
| Fig. 4.1: Simplified representation of an ECG signal | 69 |
| Fig. 4.2: Block diagram of an automatic ECG signal analysis system..... | 70 |
| Fig. 4.3: Flow chart of the FDM-based denoising method..... | 76 |
| Fig. 4.4: Block diagram of (a) FDM based on DFT (b) FDM based on DCT | 78 |
| Fig. 4.5: A pictorial representation of body movements during daily activities, used for recording the realtime ECG signal..... | 78 |
| Fig. 4.6: (a) Realtime ECG signal (b) FIBFs obtained by the proposed FDM-based denoising method (c) TFE plot of realtime ECG signal (d) denoised realtime ECG signal | 80 |
| Fig. 4.7: Comparison of PRD_{out} with other existing methods in the case of white Gaussian noise corrupted ECG signals..... | 85 |
| Fig. 4.8: SNR_{out} and PRD_{out} for ECG signal-100 in the presence of (a) PLI, (b) white Gaussian noise, (c) BW..... | 92 |
| Fig. 4.9: Average SNR_{out} by the proposed FDM-based denoising method at different values of SNR_{in} in the presence of various noise..... | 93 |

| | |
|--|-----|
| Fig. 4.10: Average PRD_{out} by the proposed FDM-based denoising method at different values of SNR_{in} in the presence of various noises | 93 |
| Fig. 5.1: Rotation of axis in FrFT | 97 |
| Fig. 5.2: Flow chart of the proposed FrFT-based peak detection method | 100 |
| Fig. 5.3: (a) The raw ECG signal (MIT-BIH record-207) (b) noisy ECG signal (c) fractional Fourier transformed ECG signal (d) detected QRS complexes (represented by an arrow) on the record-207 (e) detected QRS complexes on the record-118 (f) detected QRS complexes | 104 |
| Fig. 5.4: Variation of TP and FP with α for record-222, record-222 contains 13 TP peaks. | 104 |
| Fig. 6.1: Block diagram of the proposed SLT-based method..... | 112 |
| Fig. 6.2: The architecture of AlexNet..... | 113 |
| Fig. 6.3: GoogLeNet architecture | 114 |
| Fig. 6.4: Architecture of DenseNet-201 | 115 |
| Fig. 6.5: (a) The ECG signal-100 from MIT-BIH arrhythmia database (b) Time-frequency power spectrum of ECG signal-100 (c) detected QRS complex peaks in ECG signal-100 .. | 117 |
| Fig. 6.6: (a) The ECG signal-209 from MIT-BIH arrhythmia database (b) Time-frequency power spectrum of ECG signal -209 (c) detected QRS complex peaks in ECG signal -209 | 117 |
| Fig. 6.7: (a) ECG signal-cu13 from CU ventricular tachyarrhythmia database (b) Time-frequency power spectrum of ECG signal -cu13 (c) detected QRS complex peaks in ECG signal-cu13..... | 118 |
| Fig. 6.8: Variation of detection parameter with base cycle and central frequency for ECG signal-100 from MIT-BIH arrhythmia database (a) $p=3$, $f=1$ Hz (b) $p=6$, $f=2$ Hz (c) $p=9$, $f=3$ Hz (d) $p=12$, $f=4$ Hz | 119 |
| Fig. 6.9: (a) Noisy ECG record and its time-frequency representation provided by (b) STFT (c) CWT (d) SLT | 120 |
| Fig. 6.10: (a) Confusion matrix of validation database (b) Confusion matrix of test database by AlexNet..... | 121 |
| Fig. 6.11: (a) Confusion matrix of validation database (b) Confusion matrix of test database by transferred GoogLeNet | 122 |
| Fig. 6.12: (a) Confusion matrix of validation database (b) Confusion matrix of test database by transferred DenseNet-201 | 123 |
| Fig. 7.1: Block diagram of the ECG watermarking system | 129 |
| Fig. 7.2: Process flow diagram of the FDM based method..... | 131 |
| Fig. 7.3: A schematic representation of DFT based FDM | 132 |
| Fig. 7.4: (a) Input ECG signal (MIT-BIH-109) (b) ECG signal with watermark (c) compressed ECG signal (d) reconstructed output ECG signal..... | 138 |

List of Tables

| | |
|--|-----|
| Table 3.1: Overview of studies conducted on ECG signal denoising..... | 36 |
| Table 3.2: Summary of some studies conducted on ECG signal detection | 48 |
| Table 3.3: Overview of various databases used in ECG signal processing | 61 |
| Table 4.1: SNR_{out} after removing 60 Hz PLI from MIT-BIH arrhythmia database ECG signals at different SNR_{in} | 81 |
| Table 4.2: PRD_{out} from the proposed FDM-based denoising method with 60 HZ PLI corrupted ECG signals from MIT-BIH arrhythmia database | 82 |
| Table 4.3: Comparison of the proposed FDM-based denoising method to EVD and EMD-WT-based denoising methods using SNR_{out} for ECG signals corrupted with PLI..... | 83 |
| Table 4.4: Comparison of the proposed FDM-based denoising method to EVD and EMD-WT-based denoising methods using PRD_{out} for ECG signals corrupted with PLI | 84 |
| Table 4.5: Computed SNR_{out} , after removal of white Gaussian noise, at different SNR_{in} | 85 |
| Table 4.6: Computed PRD_{out} after removing white Gaussian noise at different SNR_{in} | 86 |
| Table 4.7: Computed SNR_{out} after removing BW by the proposed FDM-based denoising method at different SNR_{in} | 87 |
| Table 4.8: Comparison SNR_{out} of the proposed FDM-based denoising method with EVD and EKF methods to remove BW | 88 |
| Table 4.9: Computed PRD_{out} by the proposed FDM-based denoising method when the ECG signals are corrupted with BW noise | 90 |
| Table 4.10: Comparison of the proposed FDM-based denoising method with EVD and EMD-WT methods in terms of PRD_{out} for ECG signals corrupted with BW | 91 |
| Table 4.11: Computed SNR_{out} , after removing muscle contraction, motion artifacts, and electromyographic noise from an ECG signal acquired in realtime with different SNR_{in} | 92 |
| Table 4.12: Computed PRD_{out} , after removing muscle contraction, motion artifacts, and Electromyographic noise from an ECG signal acquired in realtime with different SNR_{in} | 92 |
| Table 5.1: Effect of α on the detection of QRS complexes in ECG signal-222 from MIT-BIH arrhythmia database | 105 |
| Table 5.2: The performance evaluation parameters for the FrFT-based QRS detection algorithm evaluated on the MIT-BIH database | 105 |
| Table 5.3: Performance comparison of the proposed FrFT-based QRS complex detection method with other existing methods using the MIT-BIH arrhythmia database..... | 107 |
| Table 6.1: Variation of locations of QRS complex peaks with standard deviation (D) for ECG signal-100 from MIT-BIH arrhythmia database | 118 |
| Table 6.2: Variation of locations of QRS complex peaks with base cycle and central frequency for ECG signal-100 from MIT-BIH arrhythmia database | 119 |
| Table 6.3: Detection summary (on test dataset) for each class using SLT and transferred AlexNet..... | 121 |
| Table 6.4: Detection summary (on test dataset) for each class using SLT and transferred GoogLeNet..... | 122 |
| Table 6.5: Detection summary of the test dataset for each class using SLT and transferred DenseNet-201 | 124 |
| Table 6.6: Summary of computed true positive (TP), true negative (TN), false positive (FP), and false negative (FN) for the SLT-based classification method..... | 124 |

| | |
|--|-----|
| Table 6.7: Performance comparison of different models on the combination of SLT and transferred network | 124 |
| Table 6.8: Performance comparison of various methods for atrial fibrillation detection | 125 |
| Table 6.9: Performance comparison of various methods for ventricular fibrillation detection | 125 |
| Table 6.10: Performance comparison of the proposed method with other existing methods | 126 |
| Table 7.1: PRD_{out} of various MIT-BIH ECG signals as a function of SNR values | 134 |
| Table 7.2: Output SNR obtained at different values of SNR_{in} | 135 |
| Table 7.3: Output SNR obtained at different values of SNR_{in} in the presence of various noises | 136 |
| Table 7.4: Compression ratio and computation time for ECG records | 139 |
| Table 7.5: Comparing the results of the proposed FDM-based method and some existing methods | 140 |

List of Abbreviations

AES: Advanced Encryption Standard

A/D: Analog to Digital

AI: Artificial Intelligence

AHA: American Heart Association

AV Node: Atrioventricular Node

BPF: Band Pass Filter

BW: Baseline Wander

CNN: Convolutional Neural Network

CVD: Cardiovascular Disease

CWT: Continuous Wavelet Transform

DCT: Discrete Cosine Transform

DFT: Discrete Fourier Transform

DNN: Dense Neural Network

DPCM: Differential Pulse Code Modulation,

DWT: Discrete Wavelet Transform

ECG: Electrocardiogram

ESC: European Society of Cardiology

EEG: Electroencephalogram

EEMD: Ensemble Empirical Mode Decomposition

EKF: Extended Kalman Filter

EKS: Extended Kalman Smoother

EM: Electrode Motion Artifact

EMD: Empirical Mode Decomposition

EMG: Electromyographic

FDM: Fourier Decomposition Method

FFT: Fast Fourier Transform

FIBF: Fourier Intrinsic Band Function

FIR Filter: Finite Impulse Response Filter

FrFT: Fractional Fourier Transform

HPF: High Pass Filter

IIR: Infinite Impulse Response

IMF: Intrinsic Mode Functions

KF: Kalman Filter

KNN: k-Nearest Neighbor

LPF: Low Pass Filter

LMS: Least Mean Square

MA Filter: Moving Average Filter

MM: Mathematical Morphology

NLM filtering: Non-Local Mean filtering

NLMS: Normalized Least Mean Square

OHCA: out-of-hospital cardiac arrests

PLI: Power Line Interference

RLS: Recursive Least Square

RNN: Recurrent Neural Network

SA Node: Sinoatrial Node

SE: Structuring Element

S-G Filter: Savitsky-Golay filter

SLT: Superlet Transform

STFT: Short Time Fourier Transform

SVM: Support Vector Machine

TFE: Time-Frequency-Energy

UKF: Unscented Kalman Filter

UT: Unscented Transform

VMD: Variational Mode Decomposition

WHO: World Health Organization

WGN: White Gaussian Noise

WT: Wavelet Transform

ZCD: Zero-crossing Detection

List of Symbols

α : Fractional order

Θ : Rotation angle

Ac : Accuracy

Da : Detection accuracy

Er : Error rate

Fs : F1 score

MSE : Mean square error

PRD : Percentage root mean square difference

$+P$: Positive predictivity

QDR : QRS detection rate

Se : Sensitivity

SNR_{in} : Input signal-to-noise ratio

SNR_{out} : Output signal-to-noise ratio

SNR_{imp} : Improvement in signal-to-noise ratio

Sp : Specificity

Y_w : Youden index

CHAPTER 1

INTRODUCTION

Cardiovascular disease (CVD) has firmly established itself as the primary cause of mortality in contemporary societies. While previously regarded as a disease primarily affecting the Western world, recent evidence indicates that CVD also afflicts populations in emerging and even low-income countries. CVD is characterized by an impairment in the normal functioning of the cardiovascular system, resulting in diverse complications and posing a substantial risk to overall health. Besides high mortality, longer hospitalization, increased cost of care, and physical disabilities are the other consequences of CVD. The higher prevalence rate of CVD significantly burdens medical infrastructure as it demands skilled medical practitioners, various diagnostic equipment, and high-quality treatment facilities. Economically, CVD imposes putting an enormous burden on our society.

1.1. CARDIOVASCULAR DISEASE

The heart is a vital organ in human anatomy, and proper care is essential. Any abnormality or minute dysfunction in the heart severely affects human health. With the aging population and lifestyle changes, heart diseases are proliferating worldwide. Addressing Cardiovascular diseases (CVDs) is essential due to its severity among cardiac abnormalities. CVD is a disorder related to the heart and blood vessels. CVD is a major health concern to humanity. The mortality rate due to CVD is still the highest across the world. According to the World Health Organization (WHO) report, CVD alone accounts for approximately 20.5 million (33% of global death) mortality yearly. The number of mortality due to CVD is expected to increase from 22.2 million (in 2030) to 32.3 million (in 2050) in 20 years [1]. In low and middle-income countries, the number of deaths caused by CVD is enormous [2]. Approximately 75% of CVD mortality occurs in low and middle-income countries.

In high-income countries, CVD mortalities are expected to increase by 4%, while in low-income countries, 44% is expected between 2020-2030 [2]. The number of disability-adjusted life years and years lost due to CVD is increasing significantly. The years lived with a disability doubled from 17.7 million to 34.4 million during 1990-2019 [3]. Economically, CVDs are leaving an enormous burden on societal resources. Globally, the burden of CVD in terms of mortality and disability-adjusted life years is rising continuously. CVD includes congenital heart defects (defects occurred at the time of birth), coronary artery disease (reduction or blockage of the flow of blood to the heart muscle), cardiomyopathy (disease of heart muscles), myocarditis (inflammation of heart muscles), myocardial infarction (reduction or blockage of

the flow of blood to the coronary artery of the heart), and peripheral artery disease (narrowing or blockage of arteries that supply blood to the arms or legs). Heart attacks and strokes are the two events most accountable for CVD mortality. According to WHO, out of five, four CVD mortalities are due to heart attacks and strokes, and one-third of this mortality occurs prematurely at an age below 70 years [2].

The mortality rate in Asian countries due to CVD is depicted in Fig. 1.1 [4]. The Central Europe, Central Asia region, and Eastern Europe, along with the North Africa and Middle East region, exhibit the highest age-standardized death rates from CVD. Across most regions, age-standardized death rates from CVD are more pronounced in males compared to females. Nonetheless, in a significant portion of West African countries, females face a heightened risk of succumbing to CVD in comparison to males. The statistical data on CVD outlined in the CVD Realities 2022 report [5] underscores the formidable challenges encountered in mitigating the prevalence and disparities associated with CVD. Across member countries of the European Society of Cardiology (ESC), approximately 113 million individuals grapple with CVD, solidifying its status as the predominant cause of mortality in the region [5]. Annually, 2.2 million women succumb to CVD in countries that are members of the ESC.

The ESC Atlas highlights seven ESC member countries categorized as middle-income, wherein Europe, Central Asia region, and Eastern Europe, along with the North Africa and Middle East region, exhibit the highest age-standardized death rates from CVD. Across most regions, age-standardized death rates from CVD are more pronounced in males compared to females. Nonetheless, in a significant portion of West African countries, females face a heightened risk of succumbing to CVD in comparison to males. The statistical data on CVD outlined in the CVD Realities 2022 report [5] underscores the formidable challenges encountered in mitigating the prevalence and disparities associated with CVD. Across member countries of the European Society of Cardiology (ESC), approximately 113 million individuals grapple with CVD, solidifying its status as the predominant cause of mortality in the region [5]. Annually, 2.2 million women succumb to CVD in countries that are members of the ESC.

The ESC Atlas highlights seven ESC member countries categorized as middle-income, wherein the incidence of CVD is on a persistent upward trajectory. The incidence and prevalence rate of CVD across ESC countries is shown in Fig. 1.2 [5]. Within the United Kingdom, annually, there are more than 30,000 instances of out-of-hospital cardiac arrests (OHCA) requiring emergency medical services intervention for resuscitation efforts. Regrettably, the survival rate stands at a mere 10%, signifying that only 1 in 10 individuals experiencing OHCA in the UK survives. Fig. 1.3 shows various CVDs and their proportion in mortality [3]. Increasing stress

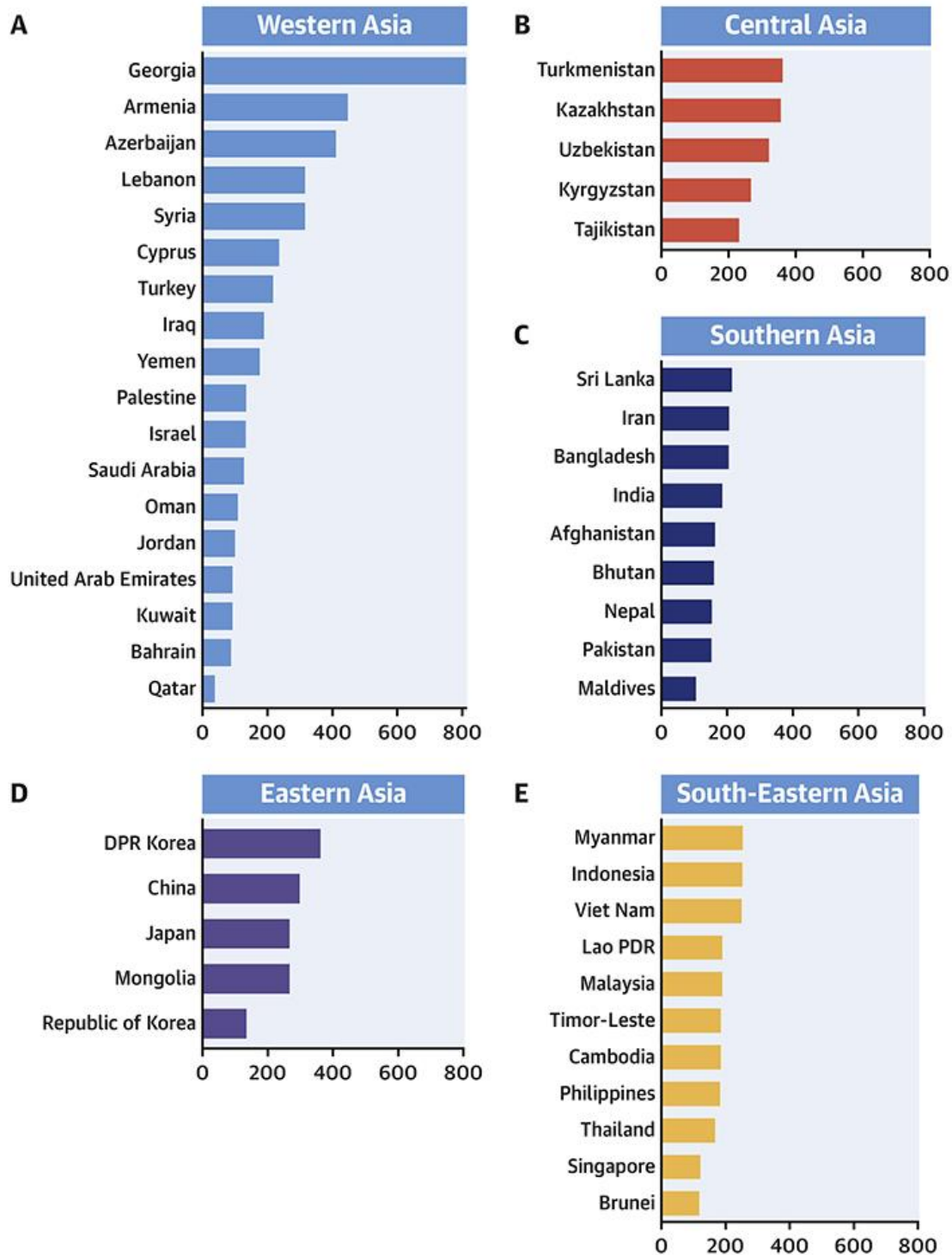


Fig. 1.1: CVD mortality rate (per *lac* population) in Asian countries

due to lifestyle changes, hypertension, unhealthy diet, obesity, physical inactivity, diabetes, hyperlipidemia, and consumption of harmful substances like tobacco and alcohol can cause CVDs. Early detection and diagnosis are vital to prevent and treat CVDs. Electrocardiogram (ECG), a popular and noninvasive tool plays a vital role in the detection and diagnosis of CVDs. An ECG represents the electrical activity within the heart. The electrical signal within the heart

originates from the sinoatrial node and travels through the atrioventricular node and Purkinje fibers to ultimately reach the ventricle. While ECG recording is highly standardized and

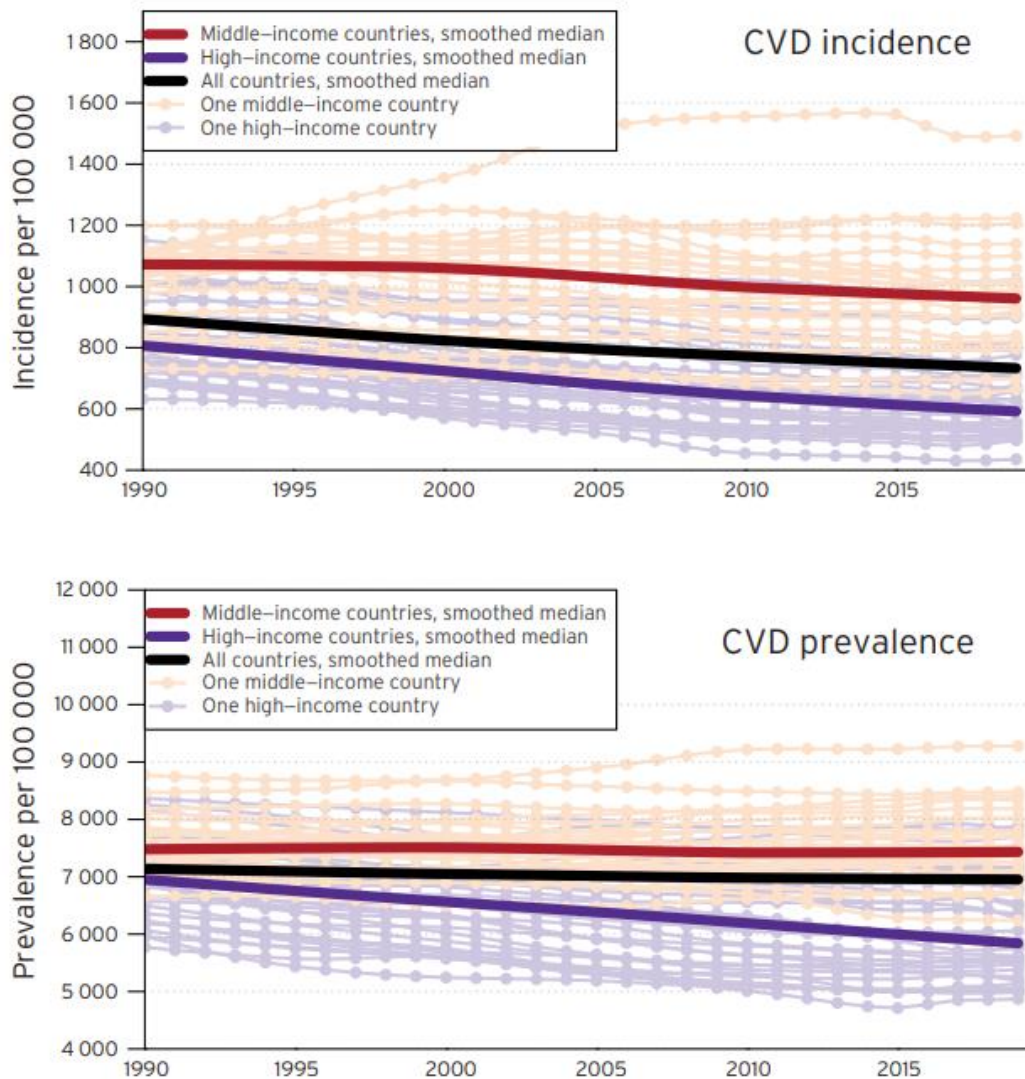


Fig. 1.2. The age-standardized rates per 100,000 people for the incidence and prevalence of CVDs in countries that are members of the ESC

reliable, achieving consistent interpretations requires addressing the issue of human subjectivity. Implementing artificial intelligence (AI)-assisted tools or standardized interpretation frameworks could improve accuracy and reduce variability across different skill levels. Advanced AI methodologies, such as convolutional neural networks in deep learning, have facilitated swift, human-like interpretation of ECG. Multilayer AI networks demonstrate the capability to identify signals and patterns that may elude human interpreters, showcasing precision in ECG analysis. This positions the ECG as a potent, non-invasive biomarker. Utilizing extensive datasets of digital ECGs paired with comprehensive clinical information, AI models have been developed for the discernment of left ventricular dysfunction, detection

of silent atrial fibrillation (previously undocumented and asymptomatic), identification of hypertrophic cardiomyopathy, and the estimation of individual characteristics such as age, sex, and race, among other phenotypes [6].

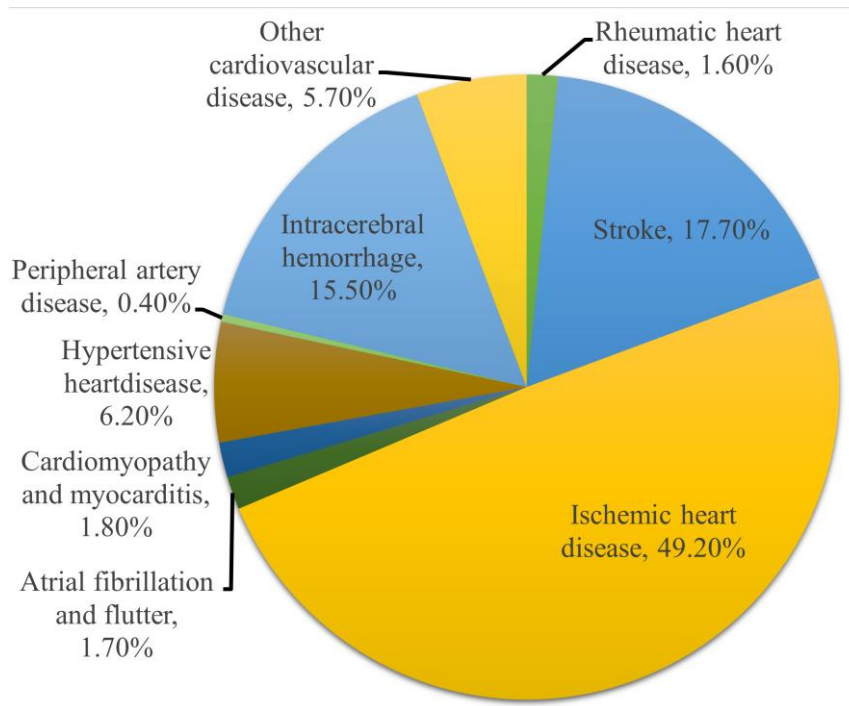


Fig. 1.3: Proportion of various CVDs in mortality

1.2. NEED AND MOTIVATION

The heart, the central part of the cardiovascular system, is responsible for pumping blood and supplying oxygen and nutrients throughout the body. A healthy heart is an essential requirement for a healthy body. Any cardiac abnormality affects the circulatory system and has serious consequences, including untimely death. CVD, the prominent cardiac abnormality, is a severe threat due to its considerable mortality and morbidity worldwide. Early and accurate detection of CVD can save millions of lives and minimize the number of disability-adjusted life years. An efficient and high-performance algorithm is required to detect CVD. Efficacy, self-learning capability, minimum human intervention, reliability, and universal acceptance are the major challenges in algorithm development. Another requirement is minimum computation complexity to provide fast and accurate decisions to identify a maximum number of heart diseases using ECG signals.

1.3. IDENTIFYING THE RESEARCH PROBLEM

CVD is a severe threat worldwide due to its mortality and morbidity rate. In low- and middle-income countries, the number of deaths caused by CVDs is vast [2]. Economically, CVDs are putting an enormous burden on our society. In developing countries, casualties due to CVDs

are more than 75% [2]. India has the highest loss in possible productive years of life among various countries due to CVD-related mortality in people aged 35-64 years [7]. Compared to the Western population, CVDs affect the Indian population at least a decade earlier and in the most productive years of life.

In India, CVDs are estimated to increase from 25.7 million in 1990 to 78.541 million in 2030 [8]. By 2016, deaths and disability-adjusted life years in India due to CVD increased by approximately 200 % from 1990 [9]. In India, rapid progression, high mortality rate, and early age of onset of CVDs are becoming a huge concern. ECG has excellent medical acceptance in detecting CVD and other cardiac abnormalities. However, accurate and rapid interpretation of an extended duration ECG signal monitoring of a subject creates a considerable burden on medical professionals. The availability of an intelligent, self-learning and prognostic ECG analysis system can assist medical professionals in quickly interpreting an ECG signal. Such a system facilitates early and accurate detection of CVD and other cardiac abnormalities.

Nowadays, the wide availability of computing technology offers a significant improvement in ECG signal analysis. The increasing low-cost, high-performance computing technology has provided a reliable and appropriate automatic ECG signal diagnosis solution. Various machine learning algorithms are proposed in the literature to denoise and classify ECG signals. The number of training datasets limits the performance of these machine-learning algorithms. Many training datasets are required for a more accurate system, which increases the system's complexity. A technique must be developed for early and accurate detection of CVDs, which can effectively perform denoising and detection. The technique must provide the characteristic information of the ECG signal. The technique should be practically implementable, cost-effective, and non-invasive with low latency or delay.

In a modern health care system, sometimes it is necessary to continuously monitor the ECG signal of a subject for more than 24 hours, which generates large volumes of data. This data must be transmitted remotely to a medical facility or practitioner. This demands a large storage capacity and channel bandwidth to store and transmit generated ECG data. ECG signal compression is a key technology for efficiently transmitting and storing large amounts of ECG data. So, the system must possess lossless compression capabilities to be easily used in portable and smart ECG detector devices.

The data security of ECG signals during transmission is vital as it contains cardiac and personal information [10]. So, some security measures must be added to the system to secure ECG signals from intruders. This security measure should neither alter the morphological features of an ECG signal nor corrupt any detail.

1.4. OBJECTIVE OF THE WORK

Based on the above analysis, the following points are identified as the objectives of this work:

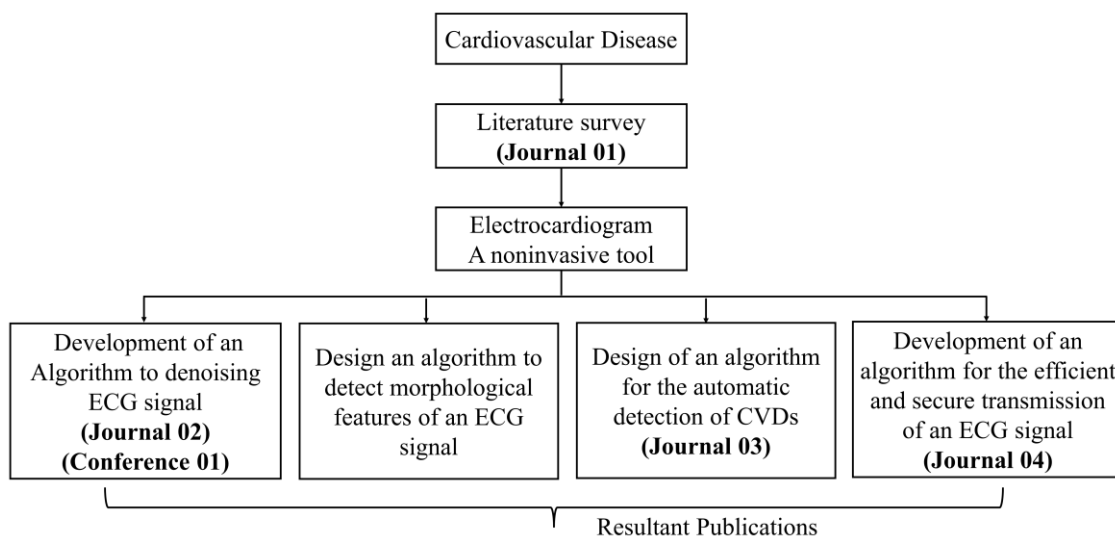
- Design an efficient denoising technique to remove or suppress all the noises in an ECG signal.
- Design an algorithm that can detect morphological features of an ECG signal.
- Design an efficient algorithm for the automatic detection of CVDs.
- Design a denoising technique that can provide denoising and lossless compression.
- Develop an algorithm that can be used to watermark an ECG signal.

The flow chart of this thesis is shown in Fig. 1.4.

1.5. OUTLINE OF THE THESIS

The proposed thesis contains eight chapters. Chapter 1 comprises an introduction to CVD, need and motivation, and identification of the research problem. The objective of the proposed work and thesis organization is mentioned in the last two sections of the chapter.

Chapter 2 discusses the anatomy of the human heart and its electrical activity. A description of



JOURNAL PAPER

[1] Tripathi, Prashant Mani, Ashish Kumar, Rama Komaragiri, and Manjeet Kumar. “A Review on Computational Methods for Denoising and Detecting ECG Signals to Detect Cardiovascular Diseases.” *Archives of Computational Methods in Engineering* (2021): 1-40. DOI: 10.1007/s11831-021-09642-2. Impact Factor: **8.171**.

[2] Tripathi, Prashant Mani, Ashish Kumar, Rama Komaragiri, and Manjeet Kumar. “A novel approach for real-time ECG signal denoising using Fourier decomposition method.” *Research on Biomedical Engineering*, DOI: 10.1007/s42600-022-00237-9. Impact Factor: **1.80**.

[3] Tripathi, Prashant Mani, A. Kumar, M. Kumar, and R. Komaragiri, “Multilevel

Classification and Detection of Cardiac Arrhythmias With High-Resolution Superlet Transform and Deep Convolution Neural Network,” *IEEE Transactions on Instrumentation and Measurement*, vol. 71, pp. 1-13, 2022, Art no. 4006113, **DOI:** 10.1109/TIM.2022.3186355. Impact Factor: **5.332**.

- [4] Tripathi, Prashant Mani, Ashish Kumar, Rama Komaragiri, and Manjeet Kumar. “Watermarking of ECG signals compressed using Fourier decomposition method.” *Multimedia Tools and Applications* (2022): 1-15. **DOI:**10.1007/s11042-021-11492-w. Impact Factor: **2.577**.
- [5] Tripathi, Prashant Mani, Ashish Kumar, Rama Komaragiri, and Manjeet Kumar. “QRS complex detection using a fast Fourier transform.” communicated in *Biomedical Engineering Letters*.
- [6] Tripathi, Prashant Mani, Ashish Kumar, Rama Komaragiri, and Manjeet Kumar. “Multi-label Arrhythmia Classification of ECG Signal Using Deep Learning Techniques: Performance Evaluation of Deep Convolution Neural Network,” communicated in *Journal of Biomedical Informatics*.

CONFERENCE PAPER

- [1] Tripathi, Prashant Mani, Ashish Kumar, Manjeet Kumar, and Rama S. Komaragiri. "Hardware Requirements of Different Wavelet Filter Bank Architectures for ECG Signal Denoising." In 2022 IEEE Conference on Interdisciplinary Approaches in Technology and Management for Social Innovation (IATMSI), pp. 1-5. IEEE, 2022.

Fig. 1.4: Flow chart of the thesis

ECG signal characteristics and various types of noises that corrupt an ECG signal is given in this chapter. A brief description of the techniques to diagnose CVDs is also discussed.

A literature survey on ECG signal denoising and detection techniques is provided in Chapter 3. A detailed description of various standard databases and various performance parameters used to measure the effectiveness of ECG denoising, ECG detection, ECG compression, and ECG classification techniques are also included in this chapter.

In Chapter 4, ECG signal-denoising techniques to detect CVD are discussed. The details of the proposed algorithm and required mathematical analysis are described. The efficacy of the proposed method is also compared with other methods existing in the literature.

Detection of QRS complexes in ECG signal using fractional Fourier transform (FrFT) is discussed in Chapter 5. Chapter 5 includes the description of FrFT and the proposed method to detect QRS complexes. The proposed method is also compared with existing methods using various performance parameters introduced in Chapter 3.

Chapter 6 is dedicated to detecting various CVDs using a deep convolutional neural network (CNN). A mathematical description of superlet transform to detect the peak of a QRS complex in an ECG signal and deep CNNs is given in the chapter. The proposed algorithm, along with

its performance, is discussed in this chapter.

In Chapter 7, a combined algorithm to watermark the ECG signal, denoise the ECG signal, and compress the ECG signal is discussed. The proposed algorithm, experimental results, and a comparison of the proposed algorithm obtained results with other existing methods are also presented in the chapter.

Chapter 8 concludes the thesis by summarizing the work and discussing future avenues.

CHAPTER 2

BASICS OF ELECTRICAL ACTIVITY OF A HUMAN HEART-AN ELECTROCARDIOGRAM

Lack of a healthy lifestyle is one of the most significant contributors to detrimental cardiac health and high cardiovascular disease (CVD) mortality. The human heart is a muscular organ that circulates blood throughout the body. CVDs lead to disturbances in blood circulation, resulting in severe consequences and even untimely death. Early and accurate detection of CVDs can reduce the high mortality and morbidity rate. Electrocardiogram (ECG) is a non-invasive tool to analyze cardiac health and detect abnormalities. This chapter describes the human heart, its electrical activity, and the resultant electrical activity represented by ECG signals. The various noises associated with ECG signals are also discussed.

2.1. ANATOMY OF THE HUMAN HEART

A human cardiovascular or circulatory system is also known as the blood-vascular system. A cardiovascular system consists of the heart, blood, and a closed system of vessels known as arteries, veins, and capillaries. The heart is a vital organ responsible for sustaining life in the cardiovascular system. Every day, the heart beats approximately *100,000* times, delivering

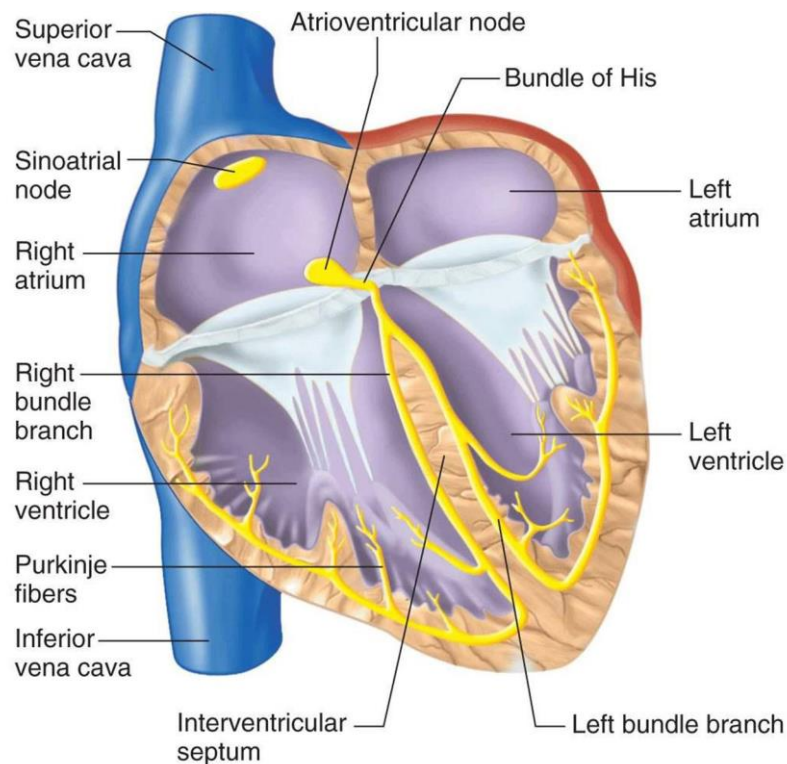


Fig. 2.1: The structure of the human heart

7500 liters of blood to the tissues of the body. The heart, made of muscle tissues, pumps the

blood to deliver oxygen and nutrients to organs and tissues and removes carbon dioxide, waste, and other metabolic substances. The heart pumps blood into two circulatory pathways known as pulmonary and systemic circulation, which act together to make a closed circulatory system. In pulmonary circulation, the deoxygenated blood flows from the heart into the lungs, where it gets oxygenated. The oxygenated blood then comes back to the heart. The oxygenated blood moves from the heart to different body tissues in the systemic circulation. The heart is encapsulated in a double-layered membranous sac, pericardium. The external layer of the pericardium, known as the fibrous pericardium, is made of dense fibrous tissues and attached to the central part of the diaphragm. The inner serous layer of the pericardium that directly surrounds the heart is called the serous pericardium.

The heart is divided into four chambers, and all four chambers function differently. The upper two chambers, the left and right atria, operate together. The lower two chambers, the left and right ventricles, are synchronized. The left atrium and left ventricle make the left heart, while the right atrium and right ventricle identify as the right heart, as shown in Fig. 2.1 [11]. A wall of tissues, the septum, separates the heart into two sides. The right heart pumps the blood for pulmonary circulation, while systemic circulation is forced by the left heart. The heart wall comprises three layers: the epicardium, myocardium, and endocardium. The epicardium, the outermost layer of the heart wall, is composed of a thin-layered membrane to lubricate and protect the outer section. The myocardium is the muscular middle layer with excitable tissue and the conducting system. The innermost layer of the heart wall is the endocardium which lines the inner heart chambers and constitutes the superficial surface of the valves. Valves are flaps to ensure unidirectional blood flow. Valves lie between ventricles and atria and between major arteries and ventricles.

2.2. THE HUMAN HEART CONDUCTION SYSTEM

The pumping of the heart is regulated by an electrical conduction system that includes the sinoatrial node (SA node), atrioventricular node (AV node), atrioventricular bundle (bundle of His), and Purkinje fibers. The SA node, also known as the sinus node, located at the junction of the right atrium and superior vena cava, generates electrical impulses without any neural stimulation. The SA node acts as a natural pacemaker to excite the heart. The electric impulse generated by the SA node propagates in all directions along the surface of both atria and reaches the AV node, located at the center of the heart. Some special fibers act as a delay line at the AV node, slowing the electrical impulses. This delay allows the atria to contract fully before the ventricles are stimulated. Once the electrical impulse has passed through the delay line, the

electrical impulse travels to all parts of both ventricles by the bundle of His. Purkinje fibers, the special fibers in the bundle of His, divide into two branches and transmit the electrical impulse simultaneously to the muscle of the ventricles resulting in the contraction of the ventricles. Thus, the propagation of electrical impulses causes the contraction of the atria and ventricles. The electrical activity of the tissues of the heart is shown in Fig. 2.2 [11].

2.3. WORKING OF THE HUMAN HEART

The heart's primary function is to pump blood throughout the body. This continuous pumping action, known as the heartbeat, is made possible by the coordinated contractions and relaxations of the heart muscle, or myocardium. During a normal heartbeat, the blood from two veins, the superior and inferior vena cava, enters the right atrium. Apart from these two veins, the blood flowing through the heart also arrives at the right atrium through the coronary sinus. The right atrium contracts after filling and forces blood into the right ventricles through the valve. The right ventricle propels the blood through the semilunar pulmonary valve into the pulmonary artery. The blood enters the lungs through the pulmonary artery, where carbon dioxide and oxygen exchange occur. The oxygenated blood from the lungs is returned to the left atrium through the pulmonary vein.

The blood from the left atrium is pumped through the bicuspid or mitral valve into the left ventricle. The contraction of the left ventricle closes the bicuspid valve and opens the aortic valve resulting a blood flow from the ventricle into the aorta. The aorta supplies blood to different parts of the body. For the proper functioning of the cardiovascular system, both the

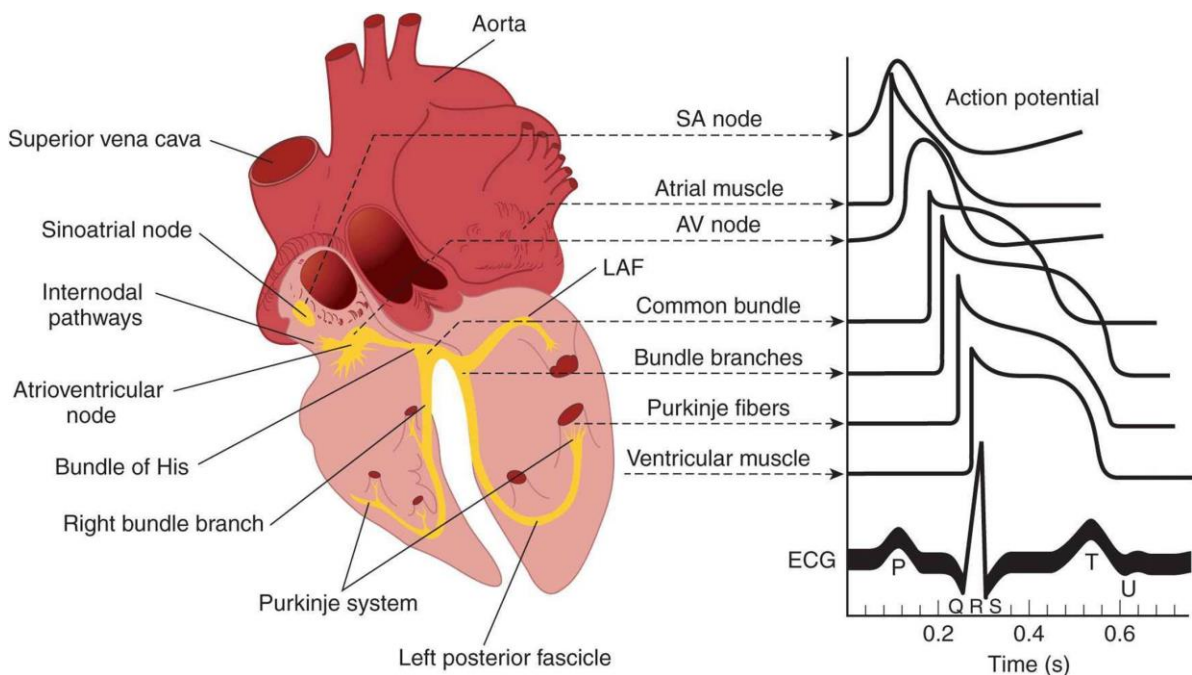


Fig. 2.2: The electrical activity of various cardiac tissues

different parts of the body. For the proper functioning of the cardiovascular system, both the atria and ventricles must operate synchronized.

The heart's pumping cycle comprises two significant events: systole and diastole. The contraction of the heart muscles (ventricular contraction) is known as systole, whereas diastole represents the relaxation (ventricular filling) of heart muscles. Systole starts with the closing of the mitral valve and ends with the closure of the aortic valve. At this point, ventricles contract and force blood into the arteries. Diastole starts when the aortic valve closes and ends with the closing of the mitral valve. In diastole, the blood vessels return blood to the heart. Systole and diastole occur in both parts of the heart with different pressure.

2.4. THE ELECTROCARDIOGRAM AND ITS CHARACTERISTICS

The electrical signals generated by a heart play a vital role in the contraction of heart muscles that cause blood circulation. The electrical activity of a heart depends on the pacemaker that generates the electrical impulse. The cardiac cells in the resting state have negative ions inside and positive ions outside. Cells in this resting state are called polarized. The potential across the cell is known as resting potential. When the electrical impulse propagates across the heart, it forces the cardiac cells for an ionic shift called depolarization. Depolarization reverses the polarity of the cell is reversed, keeping positive ions inside the cell and negative ions outside the cell. A potential is developed across the cell, known as the action potential in this condition. Soon after, the cell returns to its resting state and becomes polarized; this process is called repolarization. The action potential in a cardiac cell generates an electric current that can be recorded using electrodes placed at specific locations on the body. This recording of electrical signals is known as an ECG. ECG represents the complete electrical activity of the heart as a function of time. An ECG is a graphical representation of the electrical activity of a heart.

The ECG records starting of electrical impulses and how they propagate within the heart. A schematic of the ECG waveform with its constituent waves, segments, and intervals is shown in Fig. 2.3 [12]. The *five* waves, namely, P wave, Q wave, R wave, S wave, and T wave, represent various events of cardiac tissues and constitute the ECG waveform. Sometimes a wave named U wave also appears in the ECG waveform. The time duration between these waves is called a segment. For example, the time duration between the S and T waves is called the ST segment. An interval represents the time duration that includes waves and segments. ECG machines provide the ECG signals by drawing a trace on a moving paper or a display. ECG machines record an ECG signal at a standard rate of 25 mm/s. The paper used in ECG machines has a standard-sized square. Each large square on the x -axis has a side length of *five*

mm; thus represents an ECG signal for a duration of 200 ms. A large square comprises five small squares. A small signal represents an ECG signal for a duration of forty ms.

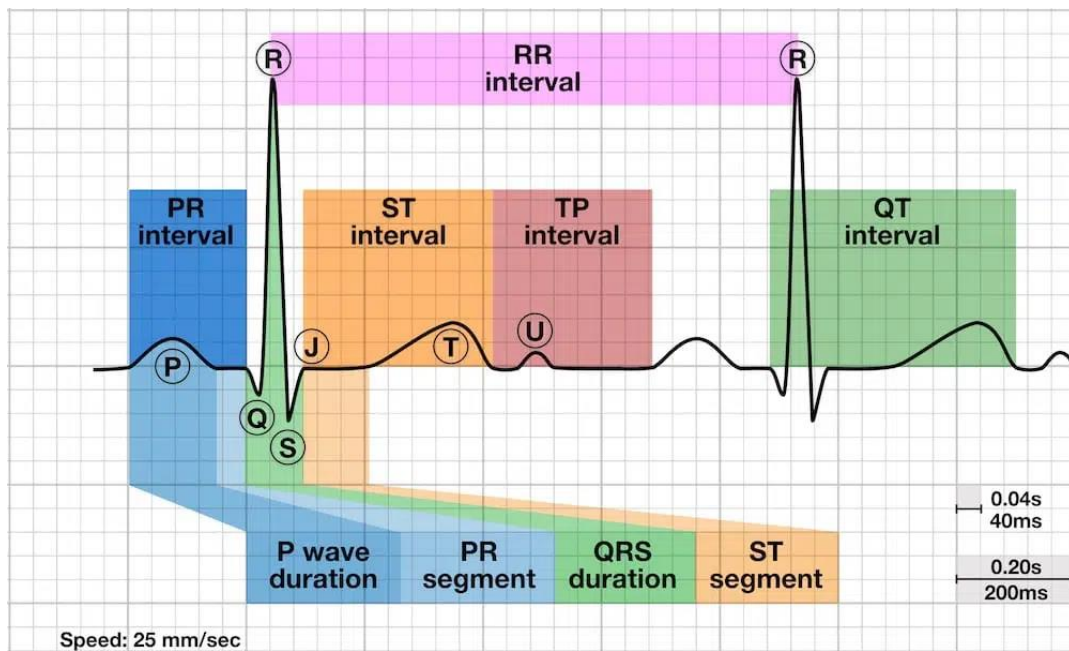


Fig. 2.3: A schematic representation of an ECG waveform and its components

The horizontal segment preceding the P wave is the isopotential line or baseline in an ECG waveform. The P wave represents the depolarisation of the atrial myocardium that results in atrial contraction to pump blood to the ventricles. The P wave has an amplitude of 0.25 mV with a duration ranging from 0.06 to 0.10 seconds. The Q wave is the first negative deflection following a P wave and corresponds to the depolarization of the interventricular septum. Q waves with a duration of less than forty ms and an amplitude of 25% of the corresponding R wave are recorded from the *I*, *aVL*, *V5*, and *V6* (left-sided leads) for a healthy heart. The Q wave is not visualized in leads *V1-V4* (right-side leads). The first positive deflection after the P wave is the R wave, representing early ventricular depolarization. Under normal circumstances, the R wave amplitude is less than two millivolts for leads *I*, *II*, and *III*. In a normal ECG signal R wave in different electrodes is shown in Fig. 2.4. The R wave duration ranges from 0.08 to 0.12 seconds. The S wave, the downward deflection following the R wave, indicates ventricle depolarization at the base. For a healthy heart, a large amplitude of the S wave is observed in lead *V1* and progressively decreases to the point where no S wave is present in lead *V6*. The Q, R, and S waves are called a QRS complex.

The QRS complex reflects the electrical impulse propagation through the ventricles and represents ventricular depolarization. Under normal circumstances, the duration of the QRS complex in an adult lies between 0.06 to 0.10 seconds. A QRS complex can be positive or

negative based on the area enclosed above and below the baseline. If the area above the baseline exceeds the area below the baseline, the QRS complex is said to be positive and vice-versa. In leads *I, II, III, V5, V6, aVL, and aVF*, the QRS complex is positive, while in leads *aVR, V1, and V2*, the QRS complex is negative. After the QRS complex, the next wave is the T wave which represents the repolarization of the ventricular myocardium. Under normal conditions, the duration of a T wave ranges from *0.13 to 0.30* seconds, and the amplitude is less than one-third of the corresponding QRS complex. The T wave is positive in leads *I, II, V2, V3, V4, V5, and V6* and negative in lead *aVR*. Sometimes, a small wave appears between a T wave and a P wave, known as a U wave. The U wave has the same direction as the T wave. The amplitude of the U wave is less than *10%* of the QRS complex (less than *0.25* times the corresponding T wave amplitude). U wave represents late repolarization of Purkinje fibers and left ventricular myocytes. The U wave best appears in leads *V2* and *V3*. A prominent U wave reflects abnormal conditions like drug toxicity and electrolyte imbalance.

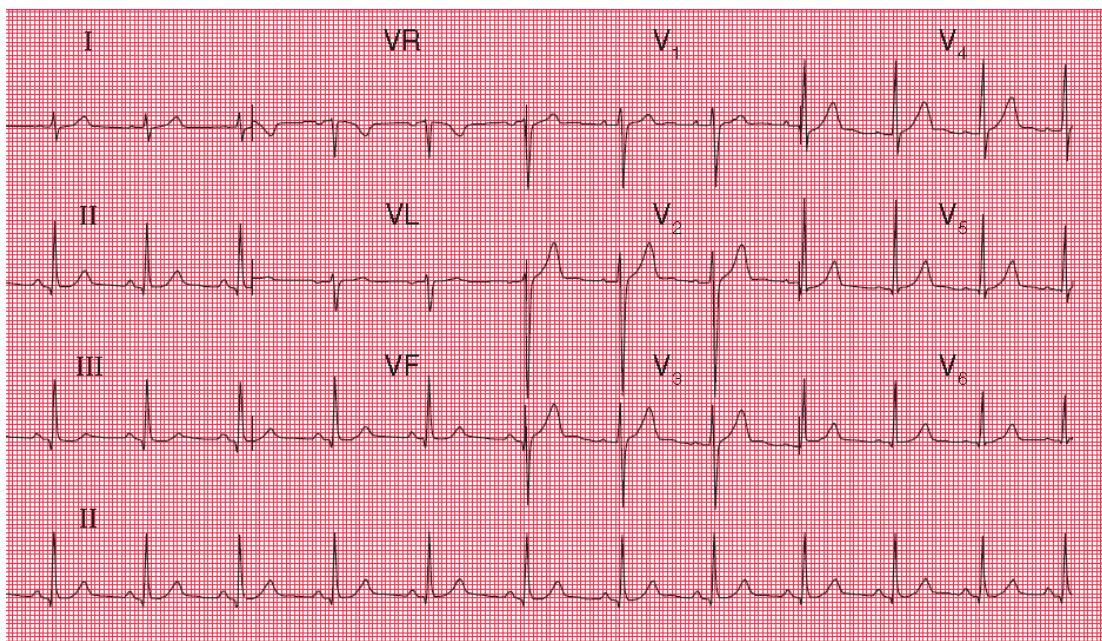


Fig. 2.4: R wave in different leads in normal ECG signal

An ECG signal includes four intervals: P-R, Q-T, S-T, and R-R. The P-R interval, measured from the commencement of the P wave to the commencement of the QRS complex, represents the time the electrical excitation propagates from the SA node to ventricular muscles (atrioventricular conduction). Under normal circumstances, the P-R interval is *0.12-0.20* seconds. A short P-R interval signifies Lown-Ganong-Levine syndrome or Wolff-Parkinson-White syndrome, while an extended P-R interval shows the presence of first-degree atrioventricular block. The Q-T interval represents the period of ventricular systole that starts

at the beginning of the QRS complex and terminates at the end of the T wave. An inverse relationship exhibits between Q-T interval and heart rate. An enlarged Q-T interval corresponds to an increased risk of ventricular arrhythmias. The S-T interval commences from the beginning of the ST wave and ends at the offset of the T wave. The R-R interval is the time between two successive R peaks in an ECG signal. R-R interval is used to determine the heart rate. The R-R interval is a function of the intrinsic properties of the sinus node.

Immediately after the QRS complex, a positive deflection occurs at the junction (J point) between the QRS complex and the ST segment, known as the J wave or Osborn wave. The J wave appears as a J point elevation of at least *one* mm above the isoelectric line in the form of QRS slurring or notching in the lateral lead (*I*, *aVL*, and *V4 – V6*) or inferior lead (*II*, *III*, and *aVF*), or both. The J wave is associated with hypothermia and Brugada syndrome.

An ECG signal also observes two segments, P-R and S-T. The P-R segment is a flat section of the ECG signal between the offset of the P wave and the beginning of the QRS complex. The P-R segment also acts as a baseline or isoelectric line. The P-R segment indicates the time delay between atrial and ventricular activation. Abnormalities in segments appear in the form of elevation or depression (change in amplitude from the isoelectric line). A depression in P-R segment indicates atrial infarction or pericarditis. The S-T segment reflects ventricular repolarization. The ST segment is the interval between the end of the S wave and the onset of the T wave. An elevation or depression in the S-T segment represents myocardial ischemia or infarction.

Apart from ECG, other cardiac tests such as echocardiogram, cardiac magnetic resonance imaging (MRI), coronary angiography, and cardiac computed tomography angiography (CCTA) scan are also popular methods to analyze cardiac health. In echocardiograms, high-frequency sound waves are utilized to provide a real-time visualization of heart and blood vessels. During an echocardiogram, a transducer is positioned on the chest, emitting sound waves that bounce off the heart and are subsequently received. The computer processes these echoes and transforms them into a visual image. Compared to an ECG, an echocardiogram takes a longer time (about 45 minutes) [13]. An echocardiogram is used in diagnosing structural heart diseases, assessing cardiac function, and valvular disorders. Cardiac MRI is a noninvasive, widely used tool that provides highly detailed images of heart anatomy and function, enabling the identification of structural abnormalities and the assessment of blood flow and tissue damage. Cardiac MRI is a precise and reliable modality for evaluating both cardiac anatomy and ventricular function [14]. Compared to echocardiography, cardiac MRI has better reproducibility and quality control at a high cost [14]. A coronary angiogram is a

specialized X-ray examination used to determine the presence of narrowed or blocked coronary arteries. Compared to ECG, echocardiogram, and cardiac MRI, a coronary angiogram is an invasive tool in which a small tube is inserted into an artery to determine the location and degree of blockage. The duration of a coronary angiogram test lies between 30-50 minutes [13]. A CCTA is a noninvasive procedure utilizing X-rays to capture images of the heart and blood vessels. Subsequently, these images are compiled by a computer to generate a three-dimensional (3D) image of the heart [14]. This test assesses the structure and function of the heart, examines cardiac muscle damage resulting from a heart attack, identifies fluid accumulation in the pericardial sac, gauges the extent of plaque buildup, and detects abnormalities in the large blood vessels.

ECG has numerous applications in clinical settings due to its ability to assess cardiac functionality and diagnose diseases. In clinical practice, ECG is utilized for the identification, detection, and classification of various arrhythmias (such as atrial fibrillation, ventricular fibrillation, and bradycardia), the assessment of ischemic heart disease, preoperative screening, monitoring the effect of medication on cardiac function, assessing cardiac function in intensive care units, conducting exercise stress tests, risk stratification after myocardial infarction, and more. ECG is employed for prolonged monitoring using Holter devices, capturing extended durations of cardiac activity to evaluate intermittent arrhythmias or other abnormalities. Also, the ECG plays a pivotal role in advancing the identification, management, and treatment of acute myocardial infarction (MI) [15]. The extensive and crucial reliance on ECG for the detection of life-threatening arrhythmias and acute MIs has become so ubiquitous that it is now an integral component of the core curriculum for the majority of medical trainees. The ECG also proves valuable in diagnosing, assessing recurrence, and monitoring resolution in inflammatory conditions, specifically pericarditis. Timely and precise diagnosis, coupled with the prompt initiation of pericarditis treatment, is crucial in reducing recurrence rates and mitigating resource demands stemming from complications [16]. After diagnosis and treatment commencement, the dynamic changes observed in the ECG can assist in monitoring the resolution process [16].

While the ECG plays a vital and vast role in clinical practice the interpretation of ECG is quite difficult and demands expertise. Stewart Hart and Calvin Smith have cautioned about the intricate nature and precision demanded for the analysis and interpretation of ECGs. They emphasize that this invaluable skill necessitates regular, systematic, and faithful practice to be maintained [15]. Only a skilled and trained medical trainee can analyze and interpret ECG signals accurately. A less experienced medical trainee may establish an inadequate setup for

ECG measurements, potentially leading to the generation of ECG signals with noise that could mislead the diagnostic process. In clinical practice, certain medications can influence ECG behavior, making it challenging to arrive at the right decision regarding cardiac health through ECG analysis in this condition [17]. With aging, ECG patterns change significantly, complicating the interpretation. Accurate differentiation between these age-related variations and potential cardiac abnormalities becomes crucial for ensuring appropriate diagnosis and treatment. Despite advancements in interpretation, the sensitivity of ECG in detecting cardiac tamponade remains relatively low. Consequently, it cannot be relied upon as a definitive clinical tool to rule out the presence of cardiac tamponade. ECG does not always provide a clear indication of cardiac abnormalities. For example, for a long time, ECG has been used to identify incomplete and complete right bundle-branch blocks; however, Suarez de Lezo et al. [18] emphasize that an ECG showing a right bundle-branch block does not necessarily confirm complete blockage in the main right bundle branch itself.

2.5. OVERVIEW OF DETECTION OF CVD

Electrocardiography [19], echocardiogram [20], cardiac catheterization [21], cardiac computerized tomography scan [22], and cardiac magnetic resonance imaging [23] are some popular methods to detect CVDs. ECG is ubiquitous as it is a reliable and popular method to trace and study the electrical activity of a heart. Being a non-invasive method, ECG avoids the perils of invasive methods. A careful analysis of each heartbeat is required to detect CVDs [24, 25, 26]. The ECG signal characteristics such as P wave, QRS complex, T wave, intervals, and segments provide information on heart functioning and help find cardiac diseases. ECG signal is also used to calculate heart rate, which is crucial in detecting CVDs. For a normal heart rhythm, the heart rate from ECG is calculated by counting the large squares (*0.20* seconds) between the two consecutive R waves and dividing *300* by this number. The heart rate in a healthy adult ranges between *60-100* beats/minute. Healthcare professionals use an ECG signal to compute heart rate and detect the cause of variation (if any) in heart rate. CVD also affects the heart rate, causing the heart to beat too slowly or fast.

Earlier, the detection of CVD involves two steps: denoising or preprocessing and detecting the morphological features (R-peak or QRS complex) of the ECG signal. In the denoising step, the noises from an ECG signal are removed or minimized. In literature, various algorithms based on filtering, frequency domain filtering, short-time Fourier transform (STFT), wavelet transform (WT), and decomposition methods are proposed to denoise the ECG signal. Decomposition methods such as empirical mode decomposition (EMD), ensemble empirical

mode decomposition (EEMD), and variational mode decomposition (VMD) are widely used for ECG signal denoising. The denoising of ECG signals reduces the risk of faulty interpretation of cardiac health. Further, a denoised ECG signal detects events such as the P wave, QRS complex, and T wave. After detecting the events, amplitude, width, location, frequency content, and the interval between the events are analyzed to diagnose CVD. Various researchers have concentrated on the QRS complex and R peak detection in literature, as detecting the P and T waves is challenging. Various researchers proposed different methods to detect QRS complexes and achieved good results. Nowadays, the rapid growth in computing speed and machine learning techniques enabled a new horizon in the detection of CVDs.

Machine learning can be supervised or unsupervised. An algorithm is trained with the available inputs and outputs in supervised machine learning. The trained algorithm is then used to classify outputs from a given set of inputs. In unsupervised machine learning, the algorithm learns itself from the input data. Various machine learning-based algorithms are proposed to detect CVD and other heart abnormalities. Deep learning, a branch of machine learning inspired by the human brain structure, is gaining popularity in biomedical signal analysis due to its finding complex structures in a large amount of data [27]. In deep learning, the convolutional neural network (CNN) has shown its efficacy while analyzing medical images [28]. The pre-trained CNN, 2D-CNN, and 3D-CNN are some CNN models used to detect CVD. These models have achieved very good results in CVD detection and may be used as an efficient system to detect CVDs in realtime from an ECG signal.

2.6. NOISES AND ARTEFACTS IN ELECTROCARDIOGRAM SIGNALS

Noise, the most critical object in the ECG signal analysis, must be addressed continuously to accurately and precisely detect QRS complexes. Various noises in an input ECG signal must be filtered or suppressed before further processing. Various noises and artifacts that contaminate an ECG signal are discussed below.

(i) Power line Interference (PLI) is the most common noise in an ECG signal due to the inductive interference between the power line and the electronics of ECG recording equipment. PLI has an amplitude of up to 50% of peak-to-peak ECG amplitude. The frequency of PLI is 60 Hz, and its harmonics (or 50 ± 0.2 Hz in some data sets). PLI affects both amplitude and frequency components in an ECG signal. The bandwidth of PLI noise is below *one* Hz [29]. Fig. 2.5 (a) depicts an ECG signal corrupted with PLI.

(ii) Electrode contact noise is a noise that occurs randomly with an amplitude equal to the maximum recorder output. The loss of contact between skin and electrodes results in a transient

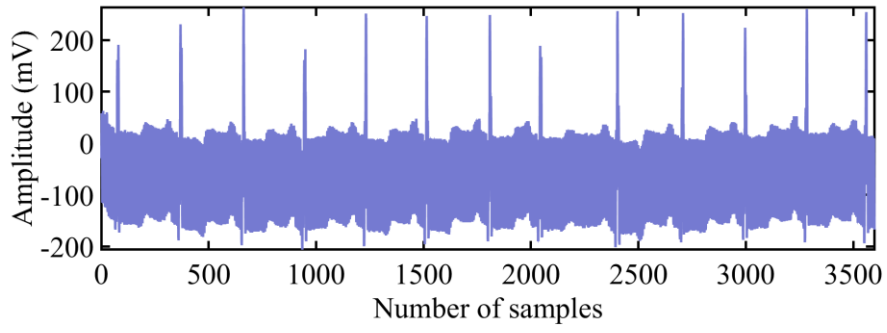
interference of *one*-second duration. The contact break can be permanent; it can be spasmodic when a loose electrode comes into contact or out of contact with the skin due to vibration and movement. The consequence of this noise affects the amplitude of the baseline. An ECG signal corrupted with electrode contact noise has amplitude variation from peak to baseline, which decreases exponentially [29]. The effect of electrode contact noise on the ECG signal is shown in Fig. 2.5 (b).

(iii) Baseline Wander (BW) or baseline shift is a low-frequency noise in the frequency range of $0.15\text{-}0.3$ Hz with an amplitude of 15% of peak-to-peak ECG amplitude. The respiration of a subject causes a baseline shift in the ECG signal, which causes BW noise. Baseline wandering increases with an increase in breathing rate. Various aspects, like the impedance of the skin, the subject movement electrode features, and electrolyte properties, influence the amplitude and duration of a baseline shift [30, 31]. Fig. 2.5 (c) represents the effect of baseline wander on an ECG signal.

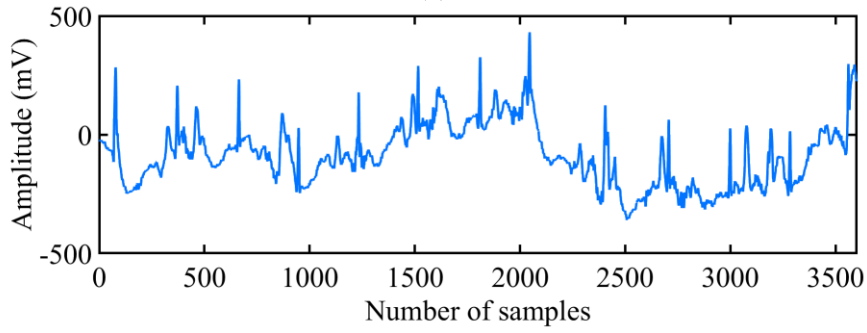
(iv) Motion artifacts result from the electrode movement over the skin due to movements by the subject. The movement of electrodes causes a change in the skin-electrode impedance, resulting in a variation in the ECG signal baseline. The amplitude of motion artifact is about 500% of peak-to-peak ECG signal amplitude for a duration ranging from $100\text{-}500$ milliseconds. The motion artifact thus results in a transient baseline change. Motion artifacts and baseline wander corrupt low-frequency components and the S-T segment in an ECG signal. Distorted S-T segments may falsely predict various diseases like myocarditis, ischemia, infarction, Brugada syndrome, and infiltrative or myopathic processes [30, 31]. An ECG signal corrupted by motion artifacts is represented in Fig. 2.5 (d).

(v) Electromyographic (EMG) noise is due to muscle contraction, generating potentials in the range of millivolts. The duration of EMG noise is about 50 milliseconds and contains frequency components in the $0\text{-}10$ kHz range. The average amplitude of EMG noise is about 10% of the peak-to-peak ECG signal amplitude. The EMG noise overlaps with the ECG signal in the $0.01\text{-}0.1$ kHz frequency range [30, 31]. Removing EMG without disturbing the features in an ECG signal is quite challenging. The effect of EMG noise on an ECG signal is represented in Fig. 2.5 (e).

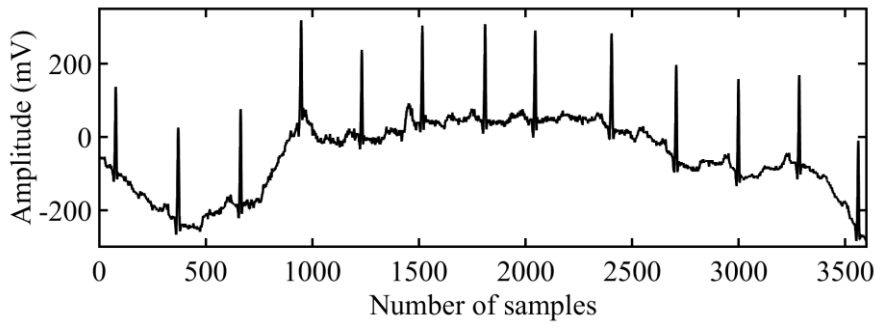
(vi) Instrumentation noise is produced when electronic components are improperly used to record ECG signals. An example of instrumentation noise is due to the saturation in the amplitude of an ECG signal due to improper biasing of an input amplifier, thus causing an improper recording of an ECG signal [30, 31]. Instrumentation noise is shown in Fig. 2.5 (f). A proper system design and handling reduces the risk of instrumentation noise.



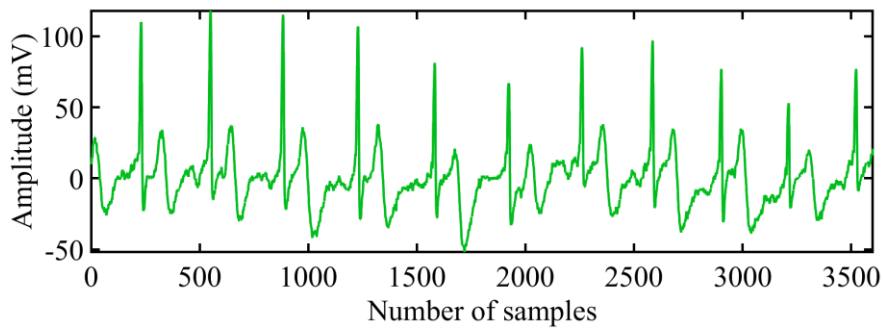
(a)



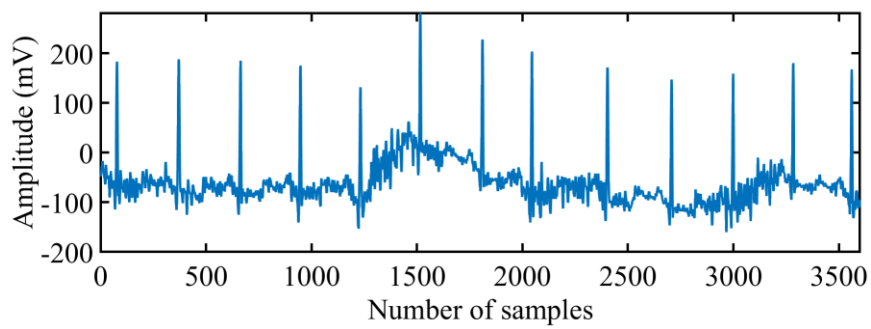
(b)



(c)



(d)



(e)

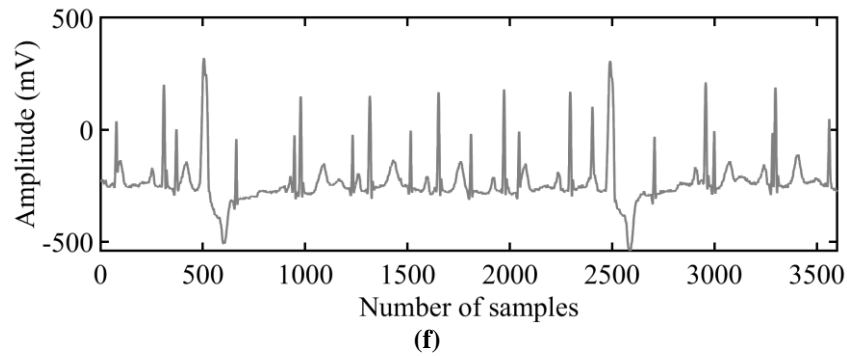


Fig. 2.5: Effect of various noises on ECG signal (a) powerline interference (b) electrode contact noise (c) baseline drift (d) motion artifacts (e) muscle contraction (f) instrumentation noise

(vii) Electrosurgical noise is produced by other medical pieces of equipment present in the subject monitoring environment. This type of noise significantly corrupts the ECG signals. This noise is modeled as a sinusoidal signal of large amplitude with frequencies ranging between $0.1-1$ MHz for $1-10$ seconds. The amplitude of this noise is approximately 200% of the peak-to-peak ECG amplitude.

2.7. SUMMARY

In this chapter, the anatomy of the human heart and its electrical activity is discussed. The human heart conduction system and ECG signal characteristics are summarized in this chapter. Various types of noises like PLI, electrode contact noise, BW, motion artifacts, name to few, that corrupt an ECG signal are discussed in detail. A brief introduction to CVDs and the techniques to diagnose CVDs is also discussed.

CHAPTER 3

LITERATURE SURVEY

Cardiac health of the human heart has been an intriguing issue for many decades as cardiovascular disease (CVD) is the leading cause of death worldwide. An electrocardiogram (ECG) signal is the primary choice of various health practitioners to determine vital information about the human heart. ECG signals are studied to diagnose and detect heart abnormalities such as enlargement of a heart chamber, detect CVDs, detect ischemia, measure heart rate, and biometric identification. Early and accurate detection of CVD involves two main steps: denoising and detecting a morphological feature. The increasing mortality rate due to CVD compelled researchers to invent techniques that automatically detect abnormalities in the functionality of a heart. Researchers have proposed many computational methods to denoise and detect ECG signals in recent decades. This chapter presents a study of various existing techniques used to analyze an ECG signal. The advantages and drawbacks of each ECG signal denoising and detection method are discussed briefly.

3.1. ECG SIGNAL PROCESSING ALGORITHM

Early detection and diagnosis are vital to prevent and treat CVD. Realtime monitoring of heart activity is required to detect CVDs accurately. ECG, echocardiogram, cardiac catheterization, cardiac computerized tomography scan, and cardiac magnetic resonance imaging are popular methods to detect CVDs. Nowadays, ECG is not only used to detect CVD but also for various other purposes like biometric identification [10], identification of various other diseases like pneumonia [32], and estimation of respiratory frequency [33]. As the researchers use ECG for cardiac monitoring and various applications, it is essential to analyze and classify the ECG signals sensibly and precisely. During continuous monitoring, manual analysis of an ECG signal is a tedious and erroneous task. Hence, an automatic system to analyze and classify the ECG signal is in great demand.

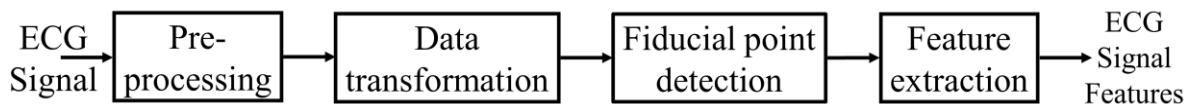


Fig. 3.1: Representation of various steps involved in an ECG signal processing algorithm

A fully automatic system to analyze and categorize an ECG signal includes preprocessing, data transformation, fiducial point detection, and feature extraction. The block diagram representing various steps involved in ECG signal analysis is shown in Fig. 3.1. Preprocessing or noise filtering is vital because it directly influences system performance. Hence removing various

kinds of noises present in the ECG signal is vital and challenging. The preprocessed signal is applied to data transformation, including differentiation and squaring. This data transformation aims to compute the slope and width information of a QRS complex. The derivative stage provides the slope information of a QRS complex, while the squaring operation converts the bipolar signal into a unipolar signal and provides non-linear amplification to the output of the derivative stage. The squaring operation helps minimize the false positives caused by the T waves, whose energies are higher than usual spectral energies [34]. The moving window integration provides a signal that contains the slope and width information of the QRS complex [34]. This vital information (slope and width of the QRS complex) is used to detect the R peak (peak of the QRS complex). The feature extraction unit extracts various statistical and morphological features of an ECG signal, including the P wave, QRS complex, and T wave. The abovementioned features analyze an ECG signal to obtain various heart conditions.

3.2. PREPROCESSING OF AN ECG SIGNAL

Until the 1970s, the direct-writing electrocardiograph was prominent, and the recorded signals were analog. Before further processing, nearly all ECG machines digitize the analog ECG signal at a particular sampling rate [35] using analog-to-digital (A/D) conversion techniques. At the front end, the initial A/D conversion sampling rate is significantly higher than the targeted sampling rate of the ECG signal processing. This higher initial sampling rate is known as oversampling. Oversampling is required to detect the output stimulus of a pacemaker with a duration smaller than 0.5 milliseconds. Oversampling can improve quantization error, aids the implementation of an efficient precision of the least significant bit, and lower-order analog anti-aliasing filters [35, 36]. In the sampling process, aliasing is a common problem that must be removed. A low pass filter (LPF), an anti-aliasing filter, removes aliasing. In ECG signal processing, two LPFs are used to avoid aliasing: an analog LPF and a digital decimation LPF. The analog anti-aliasing LPF is used before A/D conversion to prevent aliasing. Digital decimation LPF is located after digitization for the down-sampling process to remove any high-frequency components that may produce aliasing when the sampling rate is reduced. If both the filters have a weak attenuation at their stopbands, aliasing could appear [35].

The analog LPF at the front of an A/D converter avoids aliasing by limiting the spectrum of the input ECG signal at the limit set by the Nyquist criterion. The analog LPF performs three more functions: offers a flat frequency response in the passband, minimizes non-linear phase response, and oversampling cut-off much higher than 150 Hz. Similarly, the decimation filter provides a flat frequency response in the passband and sets the upper cut-off frequency at 150

Hz with 3-dB attenuation [35]. However, implementing an analog filter involves low-tolerance value resistors and capacitors. When realized using VLSI implementation, these circuits require a large chip area, which increases process and circuit complexity. The resistors implemented in VLSI circuits have a vast process variation. The quality factor and 3-dB frequency of a filter depend on component values. The process variations can result in substantial parametric variations. Parasitic capacitances can also affect the performance of these integrated circuits. Parasitic capacitances significantly affect high-impedance nodes due to their small values [37]. Various techniques are proposed to suppress noises and artifacts in an ECG signal. A detailed description of some noise removal techniques is provided in Table 3.1. The existing techniques are compared for signal-to-noise ratio (SNR), improvement in signal-to-noise ratio (SNR_{imp}), mean square error (MSE), and percentage root mean square difference (PRD). Filters are attractive tools for ECG signal preprocessing and denoising. Digital filters are preferred over analog filters to remove noises and artifacts [38, 39] as digital filter offers design flexibility. A digital filter can be implemented in a software environment before realizing it as hardware. Any change in filter characteristics can be realized in a digital filter by merely changing the filter coefficients, achieved by tweaking the program code. Once the performance is satisfactory, the digital filter can be realized in hardware. The physical construction of a circuit is required to design an analog filter which demands more resources. Unlike analog filters, digital filters are immune to environmental conditions and aging, as their operation depends on numerical computations rather than the electrical characteristics of components [40]. The cut-off frequency of a digital filter can be realized to excellent precision, while in analog filtering, a 5% deviation in cut-off frequency is more of a norm [40, 41]. These virtues of the digital filter make them suitable for analyzing very low-frequency signals. Various researchers use various types of filters like an LPF, high pass filter (HPF), band pass filter (BPF), median filter, notch filter, adaptive filter, Savitsky-Golay (S-G) filter, and moving average (MA) filter for noise removal.

LPF is universally used to denoise an ECG signal [42]. An LPF attenuates high-frequency components from an ECG waveform and leaves a significant portion of the ECG waveform for further processing. The popular cut-off frequencies of LPFs used in ECG signal analysis are 11 Hz, 30 Hz, 35 Hz, 50 Hz, and 90 Hz. An LPF removes high-frequency noises like PLI and EMG but, more importantly, affects high-frequency components of ECG signals such as QRS complex, pacemaker spike, and J-wave. To preserve these useful high-frequency components, the American Heart Association (AHA) has changed its recommendation for cut-off frequencies of an LPF from 35 Hz to 150 Hz and 250 Hz for adults and children, respectively

[35, 43]. At frequencies lower than the cutoff frequency of 150 Hz, the low-frequency and high-frequency components of an ECG signal are significantly distorted [35]. Filtering with a cut-off frequency greater than 150 Hz produces high residual noise [43]. The effect of LPF on an ECG signal is shown in Fig. 3.2. An ECG signal (Record-203) from MIT-BIH arrhythmia database and when subjected to a low-pass filter are shown in Fig. 3.2 (a) and Fig. 3.2 (b), respectively. The amplitude is normalized in Fig. 3.2. The cut-off frequency of LPF is 11 Hz. Although the LPF removes high-frequency noises like PLI and many more, it also attenuates the amplitude of an ECG signal and distorts some significant ECG characteristics.

The LPF significantly affects the ECG signal, so various researchers proposed an HPF as an alternative for noise elimination. HPF, simple and easily implementable, removes BW, DC offset, and drift suppression [44]. HPF with cut-off frequencies of 0.05 Hz, 0.5 Hz, 1 Hz, and 2.2 Hz are frequently used to remove baseline wander and drift. The effect of an HPF on the ECG signal is demonstrated in Fig. 3.3. The cut-off frequency for this high-pass filter is 5 Hz. shows that the HPF removes the DC offset and minimizes the BW. Since all the heart information lies in a frequency range that varies from 0.05 to 100 Hz., researchers are interested in using a BPF for preprocessing. BPF eliminates noise like BW, EMG, PLI, and other low-frequency and high-frequency noise components. In literature, BPF with different frequency ranges: 0.5-40 Hz, 1-30 Hz, 0.05-40 Hz, and 1-100 Hz are used. The response of a typical BPF with a cut-off frequency of 5-15 Hz for an ECG signal is shown in Fig. 3.4. Fig. 3.4 shows that the BPF enhances the QRS complex characteristics by eliminating undesired low and high-frequency noises.

Along with many advantageous features, a BPF suffers from some disadvantages. The disadvantages of a BPF are as follows. First, the BPF output may contain artifacts and ripples due to low-frequency components. Second, selecting cut-off frequencies that do not overlap with the desired ECG signal is challenging. Above mentioned filters can remove a range of frequencies, but sometimes removing a single frequency is necessary. A notch filter is popularly used to remove a single frequency component like PLI (50 or 60 Hz). A notch filter is a band-stop filter with a very narrow passband.

A good quality notch filter should attenuate the targeted frequency and preserve the rest. Various research groups use a notch filter with a 50 or 60 Hz center frequency to remove the PLI. Although a notch filter preserves other frequency components for rapidly changing waveforms, it produces unusual ringing. Notch filters are suitable for removing a single-frequency noise, but other noises cannot be removed simultaneously. The effect of the notch filter on the ECG signal is shown in Fig. 3.5. The block diagram of a typical filtering method,

based on low-pass and high-pass filters in ECG signal analysis, is shown in Fig. 3.6.

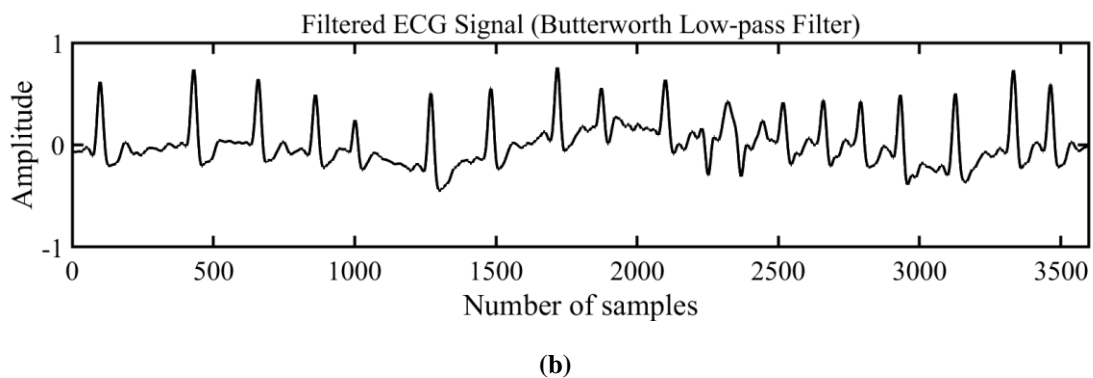
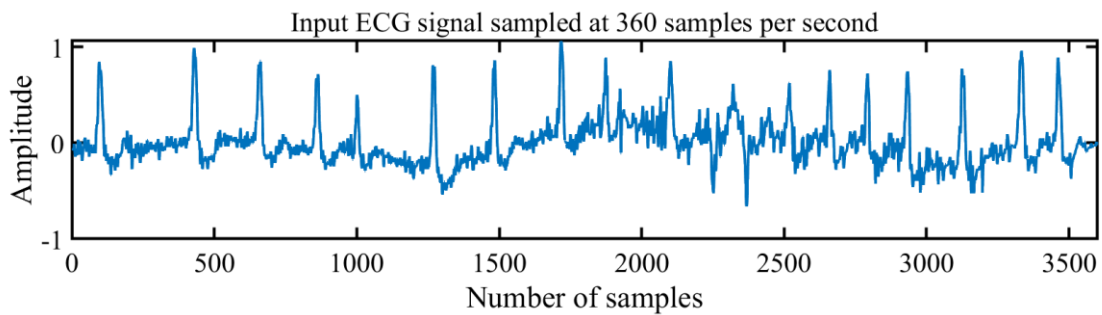


Fig. 3.2: Input ECG signal (Record-203) from (a) MIT-BIH arrhythmia database and (b) when subjected to a low-pass filter with a cut-off frequency of 11 Hz

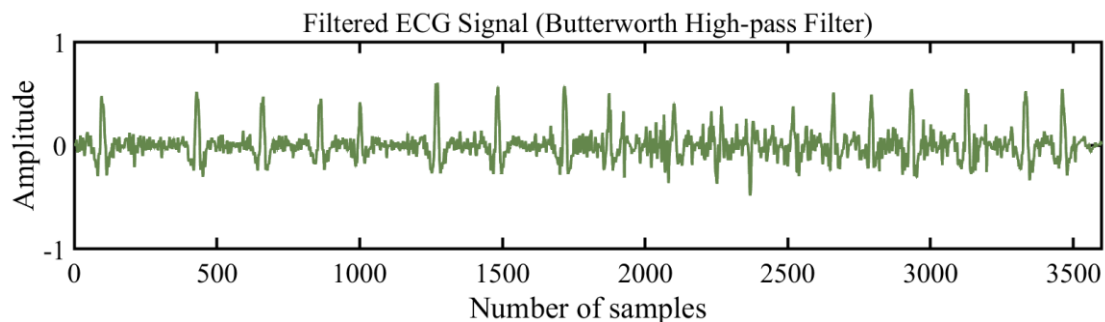


Fig. 3.3: Input ECG signal (Record-203) from MIT-BIH arrhythmia database when subjected to a band-pass filter with a pass band frequency of 5-15 Hz

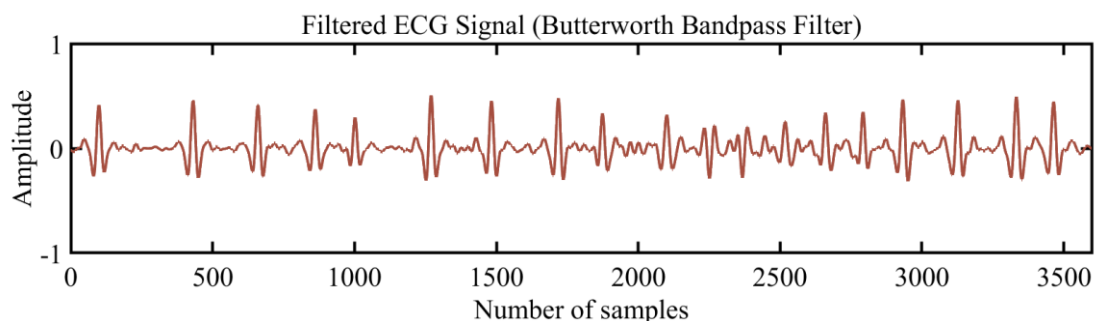


Fig. 3.4: ECG signal (Record-203) from MIT-BIH arrhythmia database and when subjected to a high-pass filter with a cut-off frequency of 5 Hz

As the ECG signal contains some impulsive noises, their presence may lead to false detection

of the QRS complex or R peak. Conventional filters like LPF and HPF cannot remove impulsive noises. Hence many researchers propose a median filter as an attractive tool to remove impulsive noise while preserving signal edges. A median filter is a non-linear digital filter that removes noises from the images and signals. Median filtering has unique advantages over linear filtering techniques.

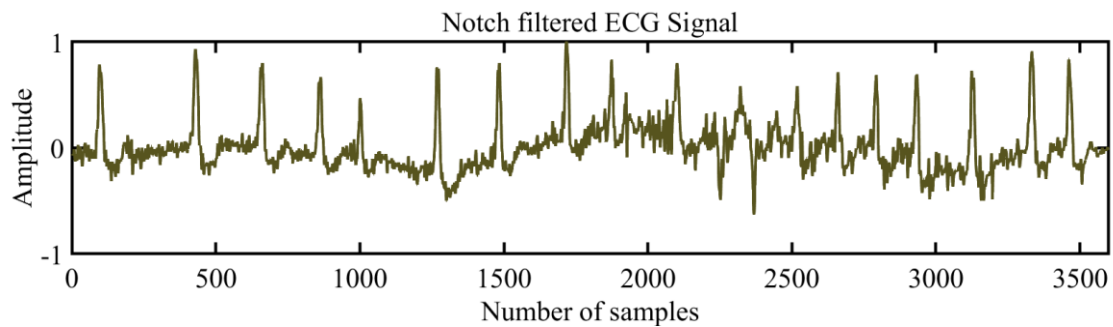


Fig. 3.5: Input ECG signal (Record-203) from MIT-BIH arrhythmia database when subjected to a notch filter with a notch frequency 50 Hz

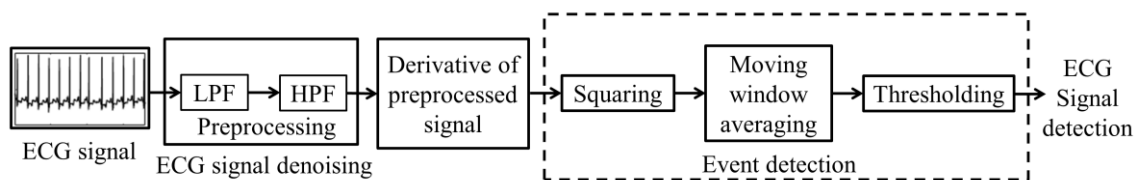


Fig. 3.6: Block diagram of a typical ECG signal filtering method based on low-pass and high-pass filters in ECG signal analysis

A linear filter cannot handle impulsive noise (sharp discontinuities of a small duration) without altering the signal characteristics. The median filter operates on the signal, entry by entry, and replaces every entry with the median of neighboring entries. The neighboring pattern is called a window, which slides over the entire signal. Generally, median filters with a window size of 200 to 600 milliseconds are used to restore the baseline of an ECG signal.

In the median filter, the predicted value of the current point depends on the past and future values. A median filter removes the baseline wander by assuming that the ECG signal and baseline wander have different amplitude distributions within the window. The main drawback of a median filter is that it requires longer computational time for a larger window and complex behavior. During filtering, preserving the shape of the ECG waveform is essential as the shape contains crucial information on cardiac health. Savitzky-Golay (S-G) filtering scheme removes noise and preserves the shape of the waveform. This filtering scheme based on the least square polynomial approximation method draws the attention of many researchers. Preserving the peak height and width of the signal waveform in a noisy environment makes S-G filtering an attractive choice for ECG signal analysis. S-G filters are LPFs obtained by fitting a polynomial

to the input sample sequence and calculating the polynomial at a point within the selected interval. An extremely flat passband and moderate attenuation in the stopband of an S-G filter help achieve excellent results. In S-G filtering, the computational time is proportional to window width, so window width must be appropriately selected. S-G filters are helpful in those applications where the signal spectrum overlaps with the noise spectrum. This fact of the S-G filter is used to remove the baseline drift in the ECG signal. The denoising accuracy of an S-G filter depends on the frame length and order of the polynomial. In an S-G filter, the frame length and order of the polynomial are determined by experimentation, which is a disadvantage of the S-G filter.

All the filters mentioned above require some prior knowledge about signal or noise. Based on this knowledge, the filters are designed for a particular task and thus categorized as fixed filters. A fixed filter requires a new design whenever there is a change in the input or any other condition. An adaptive filter resolves the problem of a fixed filter. Adaptive filters can automatically adjust the filter coefficients according to the specific requirement. Unlike a fixed filter, the design of an adaptive filter requires little or no prior knowledge of input or noise. The adaptive filter minimizes the mean squared error between the primary input and a reference signal. Generally, the primary input is a noisy ECG signal, and the reference signal is either noise or a signal correlated with the noise or ECG signal in the primary input, respectively. Easy implementation of advanced hardware or microcontrollers with digital numerical capabilities makes adaptive filters suitable for the digital environment [39]. Based on requirements, various algorithms like the least mean square (LMS), normalized least mean square (NLMS), recursive least square (RLS), sign-LMS, and sign-sign LMS are used to design adaptive filters. LMS algorithm is simple in implementation and can track the statistical changes of non-stationary signals. The RMS algorithm offers a faster convergence rate at the cost of increased computational complexity.

Based on the computational unit used to implement an adaptive filter, the filters are categorized as linear and non-linear adaptive filters. In a linear adaptive filter, the output is a linear combination of the observations applied to the filter input. The linear adaptive filter has a single computational unit for each output. Linear adaptive filtering cannot explore the higher-order statistics of input data. On the other hand, non-linear adaptive filtering uses non-linear computational units to explore the complete information contained in the input signal. Non-linear components in non-linear adaptive filtering make mathematical analysis much more complicated than linear filtering methods. Adaptive filtering helps remove motion artifacts, PLI, BW, and EMG [45]. Although adaptive filtering has numerous advantages, the main

drawback is the reference signal requirement, as the choice of the reference signal may significantly affect the efficiency.

Many researchers used a moving average filter in ECG signal processing due to its simplicity and ease of use. A moving average filter is a finite impulse response filter that minimizes the random noise while maintaining a sharp step response. The idea behind the moving average filter is to take samples from the input dataset at predefined intervals and take the average of that input to produce an output. This process is repeated over the entire dataset, and a line, known as the moving average, is constructed by connecting all these averages. The moving average filter loses the interbeat information due to averaging. The moving average filter is more suitable for time-domain encoded signals. A moving average filter is not suitable for frequency-domain encoded signals as it cannot separate one frequency band from the other. While denoising, the edge-preservation of the ECG signal is essential. Hence non-local mean filtering (NLM) is suitable for denoising an ECG signal. The NLM filtering is a patch-based method that calculates the weighted sum of a patch. NLM filter uses neighboring and non-neighboring patches to compute weight. Based on the weighted sum, the noise is filtered out. NLM filtering provides good denoising results and preserves the edges of an ECG signal at the expense of computational complexity and cost [67].

The above filtering techniques are offline methods where the ECG signals are recorded first and then denoised to improve the signal quality. However, these methods are inefficient in realtime applications, where the ECG data are provided by wearable sensors and transmitted to mobile devices. Realtime ECG signal processing requires computationally efficient filtering schemes. A recursive filter is an infinite impulse response (IIR) filter whose output is a linear combination of present input, previous inputs, and outputs. A recursive filter is computationally efficient with low computational time and memory requirements. Recursive filtering provides low computational cost, fast operation, steeper selectivity, and large gain with fewer filter sections. Recursive filters are based on nonconvex optimization problems [83]; hence challenging to implement.

Another edge-preserving denoising method is the Kalman filter (KF). It is a powerful tool to estimate the hidden state of a system by using a dynamic model of the system and measured data. KF effectively deals with noisy data with random external factors. KF assumes a linear relationship between the system dynamics and measured data. As most systems are non-linear, variants of KF are used to analyze non-linear systems. The popular variants of extended Kalman filter (EKF) are unscented Kalman filter (UKF) and extended Kalman smoother (EKS). EKF is an extension of KF for non-linear systems that assume a non-linear relationship

between measured data and the system. The purpose of EKF is to linearize the non-linear system model close to the previously estimated points. EKF is not an optimal filter like KF. UKF method uses an unscented transform (UT) to denoise an ECG signal. The estimated covariance and sensitive matrices using UT are semidefinite. Hence it is difficult to realize a numerically stable UKF system to cancel noise in an ECG signal.

The EKS denoising method is a non-causal approach, utilizing future observations to estimate the present state. EKS consists of the forward EKF stage and the backward recursive smoothing stage. The non-causal nature of EKS provides better performance as compared to EKF. Denoising techniques based on EKF, UKF, and EKS provide relatively better results. However, sometimes these methods require operator interaction to initialize parameters such as amplitude, phase, and width to estimate an ECG signal. Butterworth filters are generally preferred in biomedical signal processing applications due to their maximally flat magnitude response, less computational cost, and accuracy. IIR Butterworth filter has a better frequency response than a finite impulse response (FIR) filter. The filtering techniques suffer from many drawbacks, such as the ringing effect and lack of information on the frequency content of the signal. The filtering technique also affects the morphology of an ECG signal. Frequency-domain techniques remove some of these drawbacks. Popular frequency-domain techniques are discrete Fourier transform (DFT), fast Fourier transform (FFT), and discrete cosine transform (DCT). These techniques provide the frequency content of the signal. DFT converts the time-domain samples into the frequency domain. DFT is not a function of any variable but a sequence. DFT decomposes the signal to orthogonal sine and cosine functions of different frequencies. These individual signal components can be easily analyzed and processed compared to the original signal. For N samples, namely $x(0), x(1), \dots, x(k), \dots, x(N-1)$ of a signal $x(n)$, the N -point DFT of the signal is given by (3.1).

$$X(k) = \sum_{n=0}^{N-1} x(n)W_N^{kn}, 0 \leq k \leq N-1 \quad (3.1)$$

Here $W_N = e^{\frac{-j2\pi}{N}}$ is known as the twiddle factor.

DFT is a powerful tool and provides spectral information of a signal. DFT deals with finite data points; it is easy to implement DFT in computers with numerical algorithms. DFT involves many calculations, so a fast-computational FFT algorithm is developed. FFT is a tool to perform DFT efficiently. DFT requires N^2 multiplications and $N(N-1)$ additions for a data sequence of N -points, whereas FFT requires $\frac{N}{2}(\log_2 N)$ multiplications and $N \log_2(N)$ additions.

Fig. 3.7 shows a frequency-domain-based method to analyze ECG signals, where an analysis filter bank is used to preprocess a signal. When operated on nonstationary signals, DFT/FFT fails to provide information about instantaneous frequency. Further, one cannot apply DFT/FFT to a multichannel signal. Other frequency-domain techniques like discrete cosine transform (DCT) can express a discrete-time-domain signal into a sum of cosine functions having different frequencies. Due to the energy compaction property, DCT is used for ECG compression. The major disadvantage of DCT is that it requires a quantization step to get an integer-valued output [84].

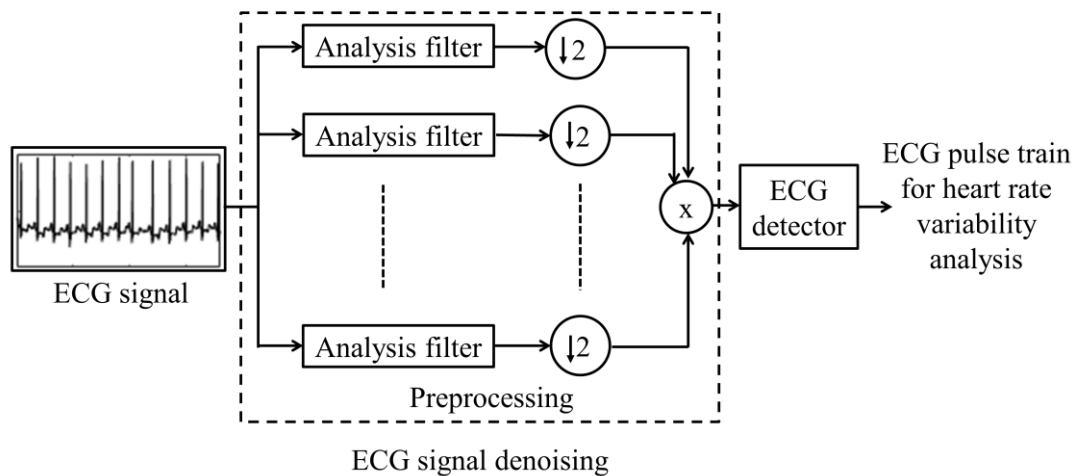


Fig. 3.7: Representation of an ECG signal analysis using filter banks

Although these frequency-domain techniques provide spectral information of an ECG signal, they do not provide temporal information. ECG signal, being nonstationary, possesses highly complex time-frequency characteristics. ECG signals cannot be analyzed only using time or frequency-domain techniques. STFT, introduced by Gabor in 1946, is a technique that combines both the time and frequency component analysis, which enables a comprehensive analysis of an ECG signal [85]. STFT provides time-localized frequency information for a situation in which the frequency component of a signal varies with time. In STFT, multiple signal frames are extracted with the help of a moving and fixed-width time window. The multiple frames of a signal are subjected to an FT to get the frequency information of these multiple frames. The window size is narrow so that the frame would appear stationary. Thus, STFT eliminates the limitation of FT by providing both time and frequency information. The main limitation of STFT is a trade-off between time and frequency resolution. Selecting a narrow time window provides a good time resolution but degrades the frequency resolution. Similarly, a broader time window degrades the time resolution but improves the frequency resolution. Further, a fixed window length limits non-stationary information extracted from the

signal. A wavelet transform (WT) reduces the limitations imposed by STFT. WT improves the time-frequency resolution by varying the window length. The flexible window length of wavelet transform helps to obtain long-duration, low-frequency, and small-duration, high-frequency components of a signal simultaneously. In WT, a set of basis functions known as wavelets represent the signal. A wavelet is a waveform with a limited duration and zero average value. A function with the following criteria can be used as a wavelet [86].

- (i) It must have finite energy.
- (ii) It must have zero mean value.
- (iii) The Fourier transform of a complex function must be real and zero for negative frequencies.

Various researchers used Daubechies wavelet, Symlet wavelet, Haar wavelet, biorthogonal wavelets, Coiflet wavelet, and Meyer wavelet to decompose an ECG signal. The application determines the type of wavelet. WT can be classified into discrete wavelet transform (DWT) and continuous wavelet transform (CWT). DWT decomposes the signal into a set of orthogonal functions to its translation and scaling coefficient. On the other hand, CWT provides an output vector larger by one dimension than the input signal. CWT uses non-orthogonal wavelets, which provide highly correlated output vector values. Using non-orthogonal wavelets in CWT improves the visualization of signals in higher dimensions but is not very useful in classification. Sabherwal et al. [87], Sahoo et al. [88], and Banerjee et al. [89] used Daubechies-6 (dB6), Rakshit and Das [90] used dB10 wavelet, Park et al. [91] used Symlets wavelet (sym5). Li et al. [92] used a quadratic spline wavelet as a mother wavelet for ECG signal denoising. Sabherwal et al. [87], Sahoo et al. [88], Banerjee et al. [89], and Li et al. [93] achieved a sensitivity greater than 99.5% using wavelet transform. Rakshit and Das [90], Park et al. [91], Yochum et al. [94], and Sabherwal et al. [95] have gained a sensitivity of 99.93%, 99.93%, 99.87%, and 99.99%, respectively. Yu et al. [96] propose an accurate wavelet thresholding method based on signal estimation to denoise ECG signals.

The principle of the wavelet transform to analyze an ECG signal is represented in Fig. 3.8. The wavelet decomposer decomposes the ECG signal into wavelet coefficients. With the help of these wavelet coefficients, the denoised ECG signal is generated to be further analyzed for heart rate variability. The effect of the wavelet transform on the ECG signal is shown in Fig. 3.9. Fig. 3.9 demonstrates that the WT has successfully removed BW, EMG, and other noises. Although WT has many advantages over other techniques like filtering and FT, there are still some drawbacks. First, it is not able to capture the edges adequately. Second, a trade-off exists between accuracy and computational time. A significant drawback of WT is low directional

Table 3.1: Overview of studies conducted on ECG signal denoising

| Reference | Method | Database | Record | Evaluation Parameters |
|--------------------------|--|---------------------|---|---|
| Lee and Hwang, 2018 [42] | High-pass filter + low-pass filter + periodic non-local means filter | MIT-BIH | 100, 103 to 106, 115, and 215 | $SNR_{IMP}=7.678$ dB (avg.), $MSE\approx 0.0010$, $PRD>10\%$ (for 10 dB I/P SNR for white noise) |
| | | Realtime ECG signal | | $SNR_{IMP}=3.987$ dB (avg.), $MSE>0.0010$, $PRD>12\%$ (for 10 dB I/P SNR for pink noise) |
| | | | | $SNR_{IMP}=4.757$ dB (avg.), $MSE=0.0020$, $PRD>5\%$ (for 10 dB I/P SNR EMG) |
| Wang et al., 2019 [46] | Linear time-invariant filtering + sparse optimization | MIT-BIH | 103, 105, and 213 | $SNR_{out}=15.94$ dB, $MSE=0.003$ dB (5 dB I/P SNR for record 103) |
| | | NSTDB | | |
| Wang et al., 2015 [47] | Parallel-type fractional zero-phase filtering | MIT-BIH | 115 | $SNR=14.2565$ dB, $MSE=0.0128$ (50 Hz PLI) |
| | | | | $SNR=13.6817$ dB, $MSE=0.0146$ (EMG interference) |
| | | | | $SNR=13.4716$ dB, $MSE=0.0153$ (WGN) |
| Cuomo et al., 2016 [48] | Recursive filtering | Long-term ST | s20011, s20021, s20031, s20041, s20051, s20061, s20071, s20081, s20091, and 20101 | $SNR=21.28$ dB (s20031) |
| Mourad, 2019 [49] | Band-pass filter + group sparsity and singular spectrum analysis | Simulated ECG data | | $SNR_{IMP}>10.00$ dB (5 dB I/P SNR for record) |
| | | MIT-BIH | 100, 103, 113, 115, 122, 124, and 231 | $SNR_{IMP}\geq 10.00$ dB (5 dB I/P SNR for record 103) |
| Cuomo et al., 2015 [50] | Recursive filter | Long-term ST | s20011, s20051, s20061, s20071, s20081, and s20121 | $SNR=15.88$ dB (s-20061) |

| Reference | Method | Database | Record | Evaluation Parameters |
|-------------------------------|--|----------------------|--|---|
| Panigrahy and Sahu, 2016 [51] | Phase assignment + template extraction + optimized parameters estimation using differential evolution + extended Kalman smoother | MIT-BIH | 100, 103, 104, 105, 106, 115, and 215 | $SNR_{IMP}=1.566742$ dB (avg.), $MSE=0.017396$ (avg.), $PRD=46.96928$ (avg.) (at 5 dB I/P SNR for real muscle artifact) |
| Jenkal et al., 2016 [52] | Discrete wavelet transform + adaptive dual threshold filter | MIT-BIH | 100, 101, 103, 113, 115, 117, 119, and 122 | $SNR_{IMP}=9.70$ dB, $PRD=18.26\%$, $MSE=0.0044$, $RMSE=0.066$ (for record 100 at 5 dB WGN) |
| Singh et al., 2017 [53] | Discrete wavelet transform + denoising + reconstruction | MIT-BIH | 100, 103, 104, 105, 106, 115, and 215 | $SNR_{IMP}\geq 8.00$ dB, $MSE=0.000893$, $PRD=7.75$ (10 dB I/P SNR for record 103) |
| Lin et al., 2014 [54] | Discrete wavelet transform + soft thresholding | MIT-BIH | All 48 records | $SNR_{IMP}=11.53$ dB at (0 dB I/P SNR) |
| Wang and Ji, 2014 [55] | Dual-tree complex wavelet transform | MIT-BIH | 100 to 109, and 111 | $SNR=55.4198$ dB, $MSE=0.00063647$ (for record 103) |
| B'Charri et al., 2017 [56] | Dual-tree complex wavelet transform + hyperbolic thresholding | Synthetic ECG | | $SNR_{IMP}=10.85304$ dB, $MSE=0.00120$ (at 5 dB I/P SNR for CN) |
| | | MIT-BIH | 100 to 109, and 111 | $SNR=113.8190$ dB (for record 109) |
| Zhang et al., 2013 [57] | Wavelet transform + composite threshold | MIT-BIH | 124 | $SNR=150.0776$ dB, $MSE=0.0049$ (for PLI+EMG+BW noise at I/P SNR =121.7965 dB and $MSE=0.0222$) |
| Peng and Wang, 2017 [58] | Discrete wavelet transform (optimal wavelet) | ECG ID | Record of Person_01 to Person_10 | $MSE=0.076$ (avg.), $NSR=0.0668$ |
| Han and Xu, 2016 [59] | Improved wavelet thresholding (sigmoid function thresholding) | MIT-BIH | 100 | $SNR_{out}=17.35$ dB, $MSE=0.00025$, $PRD=13.75\%$ (at 10 dB I/P SNR) |
| Hong and Yonghong, 2018 [60] | Adaptive wavelet thresholding method | Practical ECG signal | 150 (Practical ECG signal) | $SNR_e=3.2225$, $RMSE_e=0.0593$, $r_e=0.1383$ (avg.) |

| Reference | Method | Database | Record | Evaluation Parameters |
|--------------------------|--|-----------|------------------|--|
| Kumar et al., 2018 [61] | Wavelet transform | MIT-BIH | 16 records | $SNR = 30.0051$ dB, $MSE = 0.0008$ (Random Noise) |
| | | PTB | (80+365) records | $SNR = 32.6583$ dB, $MSE = 0.0003$ (WGN) |
| | | BIDMC | 15 records | $SNR = 28.3821$ dB, $MSE = 0.0029$ (BWN) |
| | | ST | 17 records | $SNR = 30.0051$ dB, $MSE = 0.0008$ (PLI) |
| Kumar et al., 2018 [62] | Modified bio-orthogonal 3.1 wavelet transform | MIT-BIH | 48 records | Avg. $SNR = -45.7617$ dB, Avg. $RMSE = 0.008$, Avg. $PRD = 12.141\%$ (10 seconds) |
| | | | | Avg. $SNR = -45.9406$ dB, Avg. $RMSE = 0.003$, Avg. $PRD = 11.943\%$ (1 min.) |
| | | | | Avg. $SNR = -46.0681$ dB, Avg. $RMSE = 0.002$, Avg. $PRD = 12.008\%$ (full length) |
| | | Fantasia | NA | Avg. $SNR = -45.3998$ dB, Avg. $RMSE = 0.008$, Avg. $PRD = 11.853\%$ (full length) |
| | | QT | 105 records | Avg. $SNR = -45.5263$ dB, Avg. $RMSE = 0.002$, Avg. $PRD = 11.871\%$ (full length) |
| | | ADB | NA | Avg. $SNR = -45.9285$ dB, Avg. $RMSE = 0.003$, Avg. $PRD = 11.943\%$ (full length) |
| | | Apnea ECG | NA | Avg. $SNR = -45.1232$ dB, Avg. $RMSE = 0.006$, Avg. $PRD = 12.210\%$ (full length) |
| Smital et al., 2013 [63] | Adaptive wavelet Wiener filtering | CSE | All records | Avg. $SNR_{IMP} = 10.6$ dB, $STD_{IMP} = 2.2$ dB |
| Hao et al., 2017 [64] | Subspace projection + multivariate wavelet denoising- | PTB | NA | $SNR > 13.5$ dB (for 8 dB I/P SNR) |
| Kumar et al., 2019 [65] | Three-band biorthogonal wavelet filter bank + adaptive threshold | MIT-BIH | NA | Avg. $SNR > 40$ dB, Avg. $PRD < 5\%$, Avg. $E_{MA} = 0.0013$, Avg. $C_R = 22.61$, Avg. $Q_S = 27.81$, Avg. $C_T = 327.29$ ms, Avg. $RMSE = 0.0016$ |

| Reference | Method | Database | Record | Evaluation Parameters | |
|------------------------------------|--|--------------|---|--|---|
| Yadav et al., 2015 [66] | Non-local wavelet transform (similarity data matrix extraction + shrinkage of Transform coefficient and Aggregation) | MIT-BIH | 100, 103, 104, 105, 106, 115, and 215 | $SNR_{IMP} > 5$ dB, $PRD > 10\%$, $MSE \geq 0.002$ (for record 100) | |
| | | PTB | s0032_rem, s0207_rem, s0508_rem, s0510_rem, s0430_rem, s0035_rem, s0354_lrem, s0370_lrem, s0003_rem, s0012_rem, s0432_rem, and s0390_lrem | $SNR_{IMP} = 18.92$ dB, $PRD = 18.82\%$, $MSE = 0.0006$ (for record id-s0508_rem) | |
| Tracey and Miller, 2012 [67] | Non-local mean | MIT-BIH | 100, 103, 104, 105, 106, 115, and 215 | $SNR_{IMP} = 6 \sim 7$ dB, $MSE = 0 \sim 0.01$, $PRD < 20\%$ (at 15 dB I/P SNR) | |
| Qian et al., 2019 [68] | Noise estimation and local mean denoising | MIT-BIH | 100, 103, 104, 105, 106, 115, and 215 | $SNR_{IMP} > 10$ dB, $MSE < 0.004$, $PRD > 12\%$ (at 6 dB I/P SNR) | |
| | | Long term ST | s20011, s20021, s20031, s20041, s20051, s20061, s20071, s20081, s20091, and s20101. | $SNR_{IMP} > 8$ dB, $MSE < 0.005$, $PRD > 12\%$ (at 6 dB I/P SNR) | |
| Anapagamini and Rajavel, 2016 [69] | Empirical mode decomposition + power line interference removal + detector | MIT-BIH | 106 | $RMSE = 11.9$, $CC = 0.9884$ | $RMSE = 12.01$, $CC = 0.9872$ (DSP implementation) |
| | | | 111 | $RMSE = 6.87$, $CC = 0.9883$ | $RMSE = 06.92$, $CC = 0.9840$ (DSP implementation) |
| | | | 121 | $RMSE = 5.58$, $CC = 0.9902$ | $RMSE = 5.83$, $CC = 0.9900$ (DSP implementation) |

| Reference | Method | Database | Record | Evaluation Parameters |
|------------------------------|---|----------|--|---|
| Jain et al., 2018 [70] | Empirical mode decomposition + Savitzky-Golay filtering + Riemann Liouville fractional integral + median filtering | MIT-BIH | 115 | $SNR_{IMP} = 7.5288$ dB, $MSE = 0.0027$ (AWGN) |
| | | | | $SNR_{IMP} = 10.6116$ dB, $MSE = 0.0013$ (MA) |
| | | | | $SNR_{IMP} = 12.0526$ dB, $MSE = 0.00096$ (PLI) |
| | | | | $SNR_{IMP} = 7.6487$ dB, $MSE = 0.0026$ (BWN) |
| Kumar et al., 2018 [71] | Empirical mode decomposition + non-local mean | MIT-BIH | 100, 103, 105, 106, 115, and 215 | $SNR_{IMP} \geq 10$ dB, $PRD > 50\%$, $MSE < 0.01$ (for record 100 at -5 dB SNR with AWGN) |
| Rakshit and Das, 2018 [72] | Empirical mode decomposition + adaptive switching mean filter | MIT-BIH | 100, 101, 103, 105, 115, 200, 215, and 230 | $SNR_{IMP} = 9.2980$ dB, $PRD = 34.3190\%$, $MSE = 0.02022$. (at 0 dB I/P SNR) |
| Kabir and Shahnaz, 2012 [73] | Empirical mode decomposition + windowing + wavelet with soft thresholding | MIT-BIH | 07 | $SNR_{IMP} > 6$ dB (at 15 dB I/P SNR), $PRD > 10$, $MSE = 0.0019$ (at record 100) |
| Singh et al., 2018 [74] | Non-local mean + modified empirical mode decomposition | MIT-BIH | 100, 103, 104, 105, 106, 115, and 215 | $SNR_{IMP} \approx 8$ dB, $PRD > 8\%$, $MSE = 0.000464$ (at 10 dB I/P SNR for record 100) |
| Jain et al., 2018 [75] | Ensemble empirical mode decomposition-particle swarm optimization algorithm (PSO) + cuckoo-search (CS) optimization algorithm | MIT-BIH | 115 | $SNR_{IMP} = 10.0809$ dB, $MSE = 0.0015$ (Random Noise) |
| Wang et al., 2019 [76] | Improved complete ensemble empirical mode decomposition-zero-crossing scale thresholding | MIT-BIH | 100 | $SNR_{out} = 22.2600$ dB, $RMSE = 0.0315$ (at 15 dB I/P SNR) |
| Das and Ari, 2013 [77] | S transform and thresholding | MIT-BIH | 100-103, 113, 201, 207, 214, 217, and 231 | $SNR = 9.44$ dB, $RMSE = 0.1024$ and $PRD \approx 30\%$ (for record number 113 at 5 dB input SNR) |

| Reference | Method | Database | Record | Evaluation Parameters |
|-------------------------------|--|----------|--|--|
| Singhal et al., 2020 [78] | Fourier decomposition method | MIT-BIH | 100, 101, 103, 105, 109, 111, 112, 113, 115, 116, 117, 118, 122, 123, 210, and 212 | $SNR_{out} = 28.5$ dB, $PRD > 0$ (for 5 dB I/P SNR and record 100) (60Hz PLI) |
| | | | | $SNR_{out} = 23.0$ dB, $PRD > 5\%$ (for 5 dB I/P SNR and record 100) (BW) |
| | | | | $SNR_{out} = 23.3$ dB, $PRD > 5$ (for 5 dB I/P SNR and record 100) (60Hz PLI+BW) |
| Tan et al., 2019 [79] | Blaschke unwinding adaptive Fourier decomposition | MIT-BIH | All 48 records | $SNR = 31.05$ dB, $PRD = 1.47\%$, $CR = 35.53$, $QS = 32.58$ |
| Sharma and Pachori, 2018 [80] | Eigenvalue decomposition of Hankel matrix | MIT-BIH | 100, 101, 103, 105, 108, 109, 111, 112, 113, 115, 116, 117, 118, 121, 122, 123, 210, and 212 | $SNR_{out} = 11.52$ dB, $PRD \geq 20\%$ (for record 100) |
| Kumar et al., 2021 [81] | Stationary wavelet transform | MIT-BIH | 100, 101, 102, 103, 104, 105, 109, 112, 117, 118, 123, 200, 205, 213, 221, 231, and 234 | $SNR_{out} = 49.35$ dB, $RMSE = 0.0006$, $PRD = 0.254$ (for record 100 at 14.32 dB I/P SNR) |
| Prashar et al., 2021 [82] | High-pass filter + dual-tree complex wavelet transform | MIT-BIH | All 48 records | $SNR = 58.23$ dB, $MSE = 0.0000000963$, $PRD = 0.001$ (for record 100) |

***AWGN**: Additive white Gaussian noise, **C_T** : compression time, **QS** : Compression efficiency, **CC** : correlation coefficient, **MSE** : mean squared error, **NSR** : noise suppression ratio, **PRD** : percentage root mean square difference, **$RMSE$** : root mean squared error, **SNR** : signal to noise ratio, **I/P SNR**: input signal to noise ratio, **SNR_{IMP}** : improvement in signal to noise ratio, **SNR_{out}** : output signal to noise ratio, **STD_{IMP}** : improvement in standard deviation.

selectivity. Selecting the basis function in the WT is also a rigorous task.

Some drawbacks of wavelet transform are addressed by EMD, which decomposes the signal into intrinsic mode functions (IMF). The basic idea of EMD is to identify proper time scales to reveal the physical characteristic of a signal and then decompose the signal into modes intrinsic to the function, referred to as IMF. IMFs are signals that satisfy the following criteria:

- (i) In the whole data set, the difference between the number of extrema and zero-crossing count must be either equal to zero or differ by one.
- (ii) At any point, the mean value of the envelope defined by local maxima and envelope defined by local minima is zero.

The number of IMF depends on the length of the ECG segment [97]. A long-duration ECG segment produces many IMF. EMD is an iterative process. The iterations can be converged by imposing conditions like standard deviation, the amplitude of the remaining signal, the mean value of the envelope, and the cross-correlation coefficient between the original signal and the remaining signal. EMD is a model-free, data-driven method that naturally copes with non-stationarities and non-linearities. EMD-based algorithms are helpful for the removal of baseline wander and high-frequency noise. A typical EMD algorithm is a multi-step process and is simple to implement. EMD uses several equations to extract various features of an ECG signal. EMD is one of the most relevant techniques to remove respiratory signals from a single-channel ECG recording [98, 99]. The main drawbacks of the EMD technique are a deficiency of theoretical background and mode mixing.

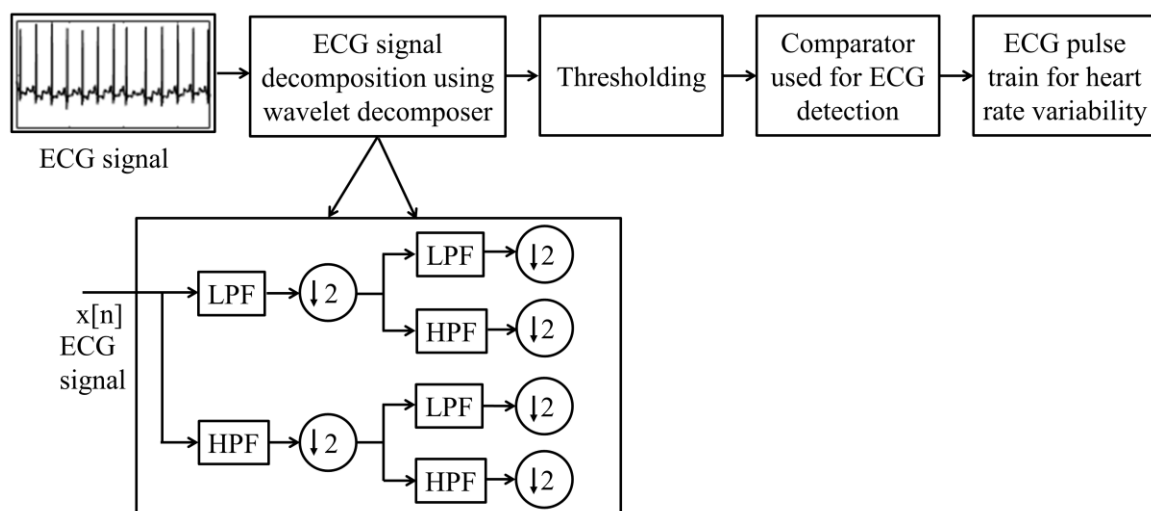


Fig. 3.8: Representation of an ECG signal analysis using wavelet transform

The block diagram of the EMD-based ECG signal denoising system is shown in Fig. 3.10. The EMD method decomposes the ECG signal into many IMFs. The IMFs corresponding to various

noises are discarded to obtain a clean ECG signal. Denoised ECG signal is then used to detect events like P wave, QRS complex, R peak, and T wave. A typical ECG signal and its IMFs obtained from an EMD operation are shown in Fig. 3.11. The ECG signal is decomposed into eight IMFs and a residue signal.

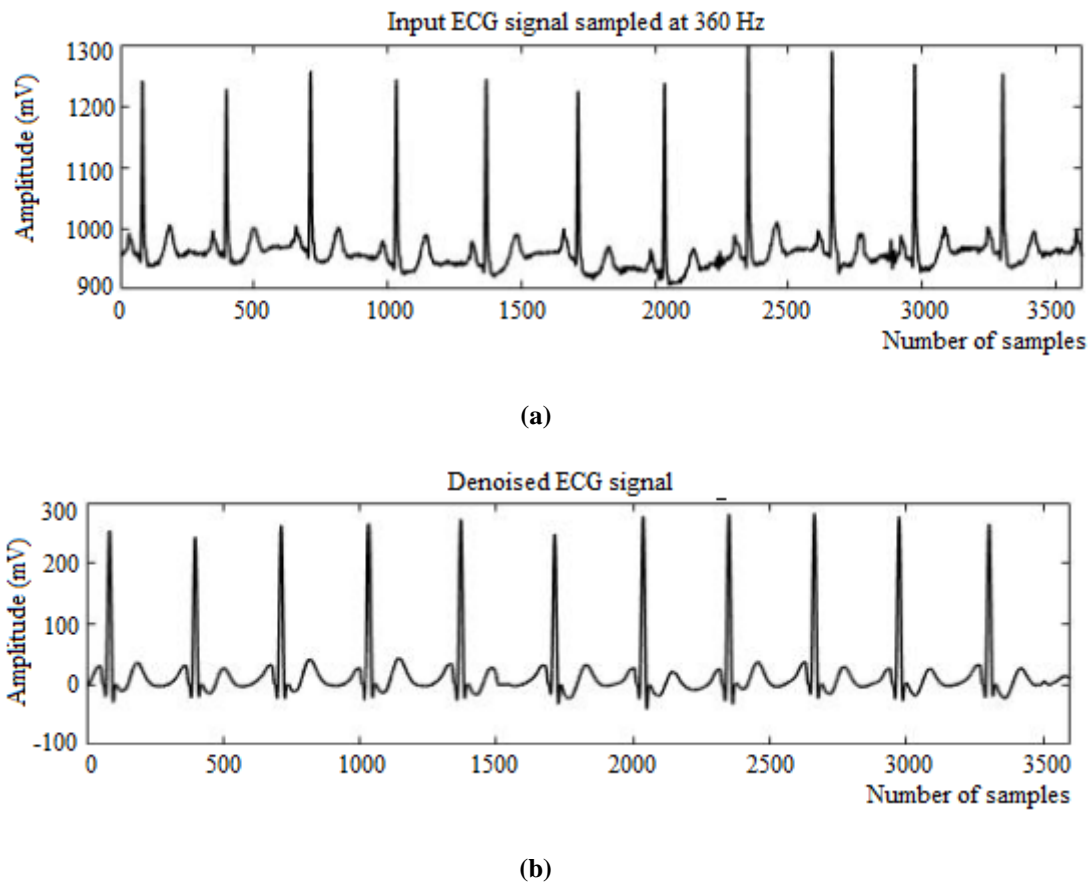


Fig. 3.9: (a) Input ECG signal (b) denoised ECG signal using WT

The oscillatory behavior of the signal decreases continuously from IMF1 to the residue signal, as shown in Fig. 3.11. The lower-order IMFs represent the high-frequency components of a signal, and noise is spread over these IMFs. EMD suffers from a significant drawback known as mode mixing. In mode mixing, oscillations from different time scales appear in each IMF, or oscillations from the same scale appear in different IMFs [100]. Like a wavelet transform, EMD cannot preserve the edges. Also, the lack of a theoretical framework is another major problem of EMD. Wu and Huang [101] introduced a new technique known as ensemble empirical mode decomposition (EEMD) to eliminate the mode mixing problem of EMD. EEMD is a noise-assisted EMD algorithm. In EEMD, different series of white noise is added to the original signal in many trials. Since the noise is different in each trial, the resulting IMFs differ from each trial, which does not correlate. If the number of trials is adequate, the added noise can be eliminated from the ensembles by averaging the IMFs from different trials. The

number of ensembles and the noise amplitude are required to define an EEMD. Chang [100], Rajesh and Dhuli [102], Jebaraj and Arumugam [103] demonstrated EEMD as a powerful tool

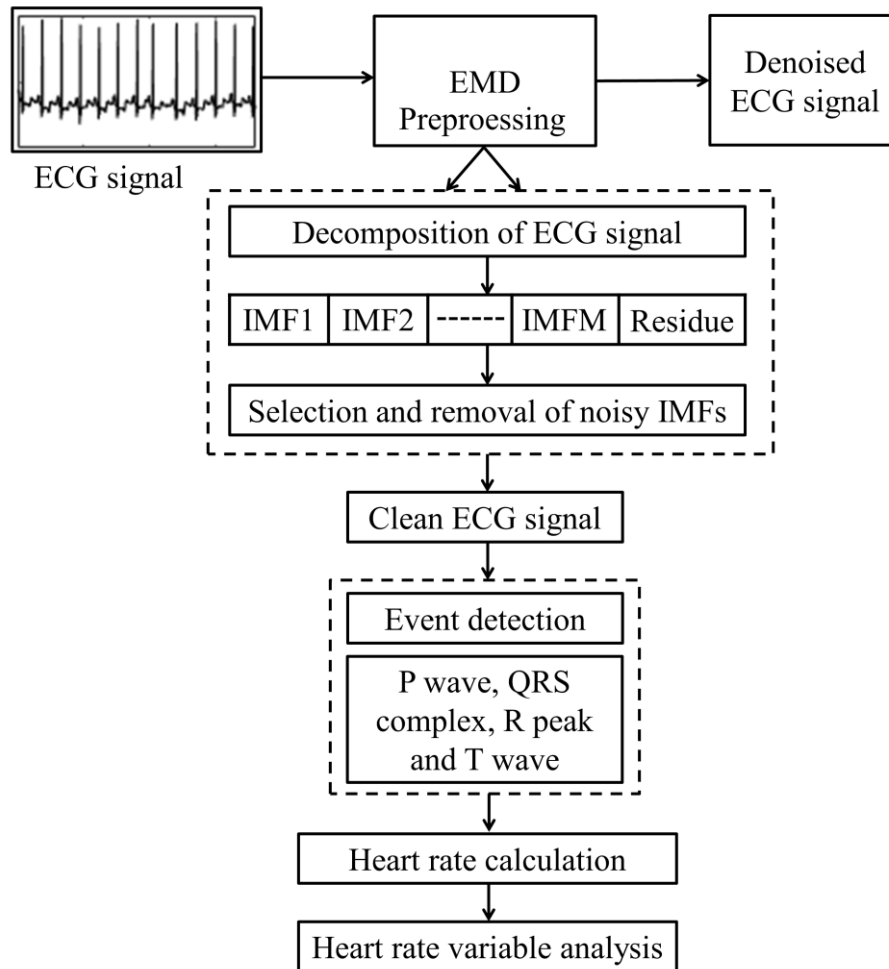


Fig. 3.10: ECG signal analysis with the help of the EMD method

to denoise an ECG signal. Although EEMD significantly performs better than EMD, it still suffers from some problems.

- (i) In EEMD, each trial produces a set of IMFs. The addition of these IMFs may not result in a true IMF
- (ii) IMF provides no information on handling the multi-mode distribution and
- (iii) higher computational complexity.

VMD is an enhanced version of EMD used to analyze non-stationary and non-linear signals. Like EMD, VMD also decomposes the signal into a set of bandlimited amplitude and frequency-modulated oscillations known as modes. All these modes have a specific sparsity property to reproduce the signal. The bandwidth of all the modes in the spectral domain is called sparsity. The high operational efficiency of VMD is based on its robust mathematical theory. VMD avoids information loss because it reconstructs a good signal from decomposed

signals. VMD has some superiority over EMD because the EMD algorithm includes extrema finding, interpolation, and stopping criterion. Detecting any false maxima detection may generate a wrong decomposition, but in VMD, the signal is decomposed around the center

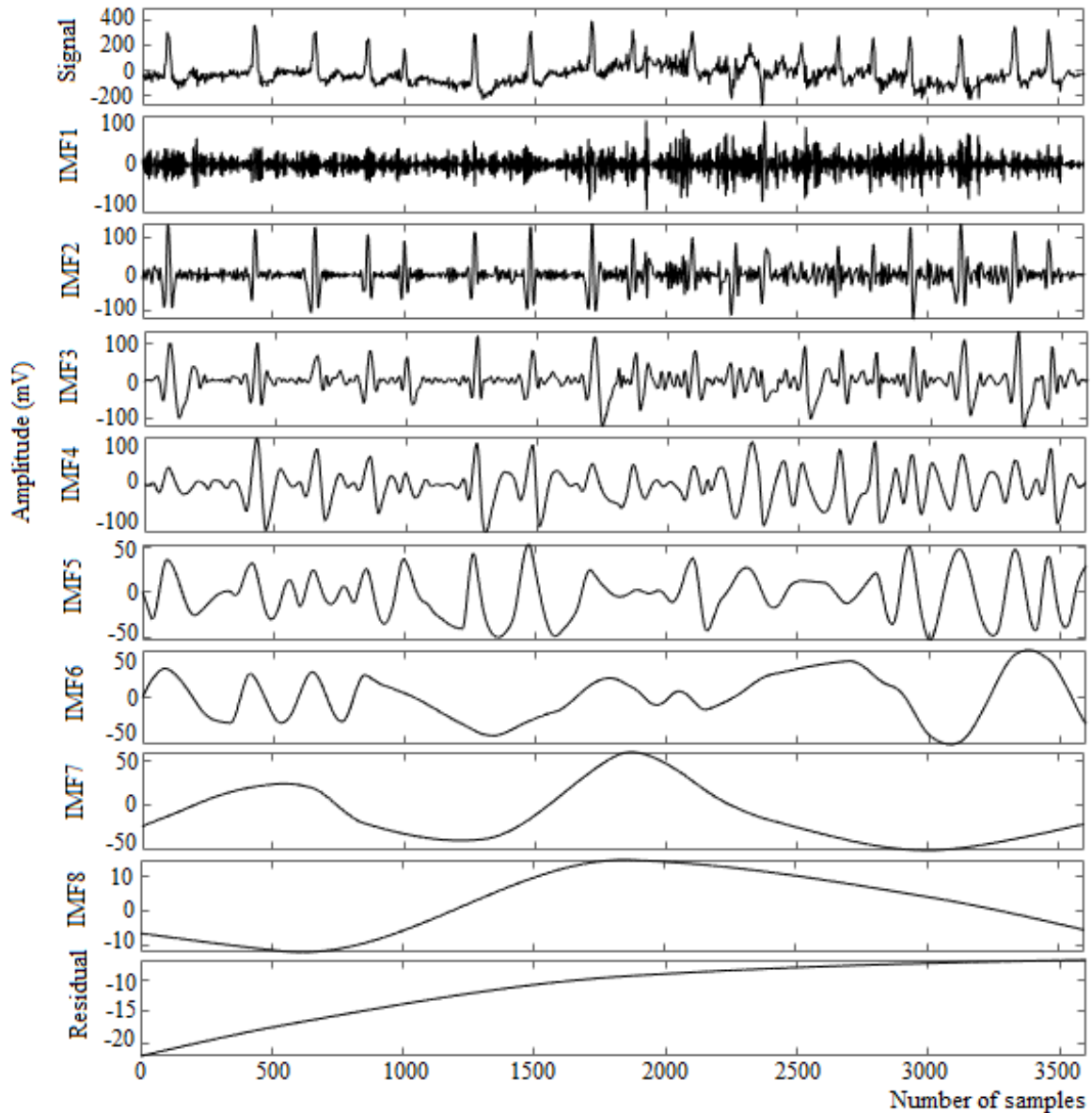


Fig. 3.11: Input ECG signal and the resultant eight IMFs after EMD decomposition

frequency of modes. EMD may decompose the ECG signal into unnecessary modes because the decomposition level is independent of the user, but VMD has a controlled decomposition. The most advantageous feature of VMD is the central frequency of the mode, which helps to characterize the modes. VMD also provides features like phase angle, which helps categorize the heart rhythm with abnormalities [104, 105]. Researchers use statistical techniques like principal component analysis (PCA) and independent component analysis (ICA) to denoise the ECG signal. PCA and ICA remove the in-band noise of the ECG signal by removing the

dimensions corresponding to the noise. PCA and ICA do not show good results with single-lead ECG recordings because these techniques are based on correlation and uncorrelation [106]. Hu et al. [107] propose a lightweight U-Net model to denoise the ECG signals of varying lengths. The method provides an *RMSE* value of 0.0116 ± 0.0016 , 0.0122 ± 0.0015 , 0.0149 ± 0.0033 , and 0.0098 ± 0.0012 for BW, electrode motion artifacts, MA, and AWGN, respectively.

Although the techniques mentioned above provide excellent results, the reliability of these techniques for realtime applications requires extensive validation.

3.3. ECG SIGNAL CHARACTERISTIC DETECTION TECHNIQUES

In ECG, a complete heart cycle comprises three main events: P wave, QRS complex, and T wave. Each event has its characteristic peak amplitude, duration, and frequency. It is necessary to detect the events to diagnose CVD and arrhythmias properly and accurately. After detecting any event, the corresponding signal can be analyzed for its peak amplitude, QRS complex width, frequency content, energy, and the interval between events. Accurate detection of a P wave, QRS complex, and T wave enables accurate analysis of an ECG signal. Over several years, various researchers have focused their investigations on QRS complex detection, as detecting the P and T waves is quite tricky compared to QRS complex detection. Accurately detecting P and T waves is difficult because of their low amplitude, morphology and amplitude variability, and low *SNR*. Also, from the clinical point of view, detecting the QRS complex is crucial because multiple premature QRS complexes indicate cardiac dysfunction. Various researchers proposed different methods to detect QRS complex [108, 118, 121, 126, 129, 137, 139, 144, 151, 153, 154, 155, 156, 157]. However, none of the algorithms can detect all possible variations in a QRS complex due to its complex morphology and noisy ECG signal.

QRS complex detection is a two-step process that includes preprocessing and decision stages. As mentioned in section 3.2, the preprocessing stage removes noise. After noise removal, the denoised signal is subjected to the decision stage. As shown in Table 3.2, many detection techniques are proposed in the literature to detect QRS complex and R peak. These techniques include thresholding, zero-crossing detection (ZCD), syntactic methods, matched filter, mathematical morphology, hidden Markov process, and singularity techniques. Also, almost all algorithms use additional decision rules to reduce false-positive detection. Two essential criteria, complexity and performance, are used in selecting a detection technique. Relatively simple algorithms are used in practice. The performance criterion rejected those detection techniques, which gave many false-positive at low noise levels.

The simple and widely used detection method is the thresholding technique, in which a feature of the preprocessed signal is compared with a fixed or adaptive threshold to detect a QRS complex. The thresholding technique can be applied in time and the time-frequency domain. Fixed thresholding is simple and provides good results for stationary ECG signals, where beat-to-beat morphology does not change. However, noise and baseline wander significantly alter the beat-to-beat morphology of an ECG signal, and the probability of accurate detection of the QRS complex decreases with fixed thresholding. The adaptive threshold [85, 110, 111, 112, 124, 129] increases the probability of accurately detecting QRS complexes.

Researchers [28, 105, 110, 111, 112] filtered the signal before thresholding to attenuate noises like PLI, BW, MA, and other signal components like P and T waves. Usually, a band-pass filter is used in the preprocessing stage, but other filters like low-pass [85, 123], high-pass, median, and moving average [125, 126] are also used. In [129], a high-pass filter called MaMeMi removes noise from an ECG signal. Using the MaMeMi filter and adaptive threshold, Rufas and Carrabina [129] obtained a sensitivity of 99.43%. Christov [126] employed a moving average filter and combined threshold (adaptive steep-slope threshold + adaptive integrating threshold + adaptive beat expectation thresholds) for QRS complex detection. Bajaj and Kumar [146] proposed a QRS detection algorithm that uses the concept of Stockwell transform and fractional Fourier transform (FrFT) along with thresholding. Even though the thresholding technique is simple, setting multiple empirical thresholds is the main drawback of this technique. When a beat does not appear long in a threshold-based detection method, the search back mechanism is activated, producing many false beats. In the wavelet-based detection method used by various researchers [92, 94, 135], an ECG signal is decomposed into many coefficients. Only those coefficients that coincide with the QRS complex are selected. The wavelet-based detection method has two limitations: (a) the unavailability of a universal rule to select a mother wavelet (b) the effectiveness of the method depends on the level of decomposition. A wavelet-based algorithm is realized using an integrated circuit with a detection accuracy of 99% [93]. In [158], Coast et al. proposed a hidden Markov model for QRS complex detection. In hidden Markov modeling, the observed data sequence is characterized by a probability density function that varies with the state of the underlying Markov chain. The Markov chain in hidden Markov modeling models the observed sequence, waveform duration, and intervals within each beat. The Markov chain preserves the structural properties of the underlying process, and state parameters represent the probabilistic nature of the observed data. Hidden Markov modeling offers excellent flexibility in the selection of observation sequences. The problems associated with hidden Markov modeling are

Table 3.2: Summary of some studies conducted on ECG signal detection

| Reference | Brief Description of the Algorithm | Feature Detected | Database | No. of Record Used | Total Peaks | Assessment Parameters |
|-------------------------------|--|------------------|-------------------------|--------------------|-------------|---|
| Sharma and Sharma, 2017 [108] | Band-pass filter + differentiation + weighted total variation denoising + low-pass filter | R peak | MIT-BIH | 48 | 109494 | $Se=99.90\%$, $+P=99.88\%$, $Er=0.23\%$ |
| | | | European ST-T | 20 | 92403 | $Se=99.82\%$, $+P=99.63\%$, $Er=0.56\%$ |
| | | | Fantasia | 20 | 82835 | $Se=99.95\%$, $+P=99.73\%$, $Er=0.32\%$ |
| | | | Realtime implementation | 1 | NR | $Se=99.86\%$, $+P=99.85\%$, $Er=0.29\%$ |
| Saadi et al., 2015 [109] | Band-pass filter + absolute value + smoothening + dual adaptive thresholds | QRS complex | MIT-BIH | 48 | 91285 | $Se=99.90\%$, $+P=99.87\%$ |
| | | | EDB | 90 | 759878 | $Se=99.84\%$, $+P=99.71\%$ |
| | | | eTDB | 120 | 45248 | $Se=99.88\%$, $+P=99.37\%$ |
| | | | eVDB | 61 | 38429 | $Se=99.91\%$, $+P=99.79\%$ |
| Kim and Shin, 2016 [110] | Band-pass filter + squaring + differentiation + moving average filter + adaptive threshold | QRS complex | MIT-BIH | 48 | 435700 | $Se=99.90\%$, $+P=99.91\%$ |
| | | | AHA | 135 | | $Se=99.84\%$, $+P=99.84\%$ |
| Yakut and Bolat, 2018 [111] | Band-pass filter + squaring + moving average + normalization + adaptive thresholding | R peak | MIT-BIH | 48 | 109494 | $Se=99.83\%$, $+P=99.83\%$ |
| | | | Fantasia | 40 | 283747 | $Se=99.94\%$, $+P=99.98\%$ |
| | | | NSTDB | 12 | 25590 | $Se=93.62\%$, $+P=94.52\%$ |
| | | | QT | 82 | 86741 | $Se=99.89\%$, $+P=99.96\%$ |
| | | | European ST-T | 90 | 790565 | $Se=99.61\%$, $+P=99.83\%$ |
| Pan and Tompkins, 1985 [34] | Band-pass filter + differentiation + squaring + integration + dual thresholding | QRS complex | MIT-BIH | 48 | 116137 | $Dr=99.3\%$, $Er=0.675\%$ |
| Ferdi et al., 2003 [112] | Band-pass filter + non-linear transform and smoothing + adaptive threshold detection | R peak | MIT-BIH | 48 | 109492 | $Er=0.37\%$ |

| Reference | Brief Description of the Algorithm | Feature Detected | Database | No. of Record Used | Total Peaks | Assessment Parameters |
|---------------------------------|---|------------------------------------|------------------------|--------------------|-------------|--|
| Benmalek and Charef, 2009 [113] | Fractional order band-pass filter + differentiation + squaring + smoothing + differentiation | R peak | MIT-BIH | 47 | 107632 | $Se=99.86\%$, $+P=99.86\%$, $Er=0.28\%$, $QDR=99.86\%$ |
| Nayak et al., 2018 [114] | Band-pass filter + digital first-order differentiator + Hilbert transform + zero crossing detector | R peak | MIT-BIH | 48 | 109494 | $Se=99.93\%$, $+P=99.92\%$, $Er=0.15\%$, $QDR=99.92\%$ |
| Nayak et al., 2019 [115] | Band-pass filter + gases Brownian motion optimization based digital differentiator + Hilbert Transform + zero crossing detector | R peak | MIT-BIH | 48 | 109494 | $Se=99.92\%$, $+P=99.92\%$, $Da=99.84\%$, $Er=0.15\%$, $QDR=99.92\%$, $Fs=0.9992\%$ |
| Bashar et al., 2019 [116] | Band-pass filter + variable frequency complex decomposition method (VFCDM) for ECG reconstruction and beat detection + dynamic amplitude thresholding | R peak | MIT-BIH | 48 | 109457 | $Se=99.94\%$, $+P=99.95\%$, $Er=0.11\%$ |
| | | | UMass DB | 22(subject) | 10216 | $Se=99.95\%$, $+P=99.89\%$, $Er=0.16\%$ |
| | | | MIMIC III | 20(subject) | 17809 | $Se=100\%$, $+P=99.96\%$, $Er=0.04\%$ |
| | | | Saltwater ECG data set | NR | 1258 | $Se=99.75\%$, $+P=99.75\%$, $Er=0.50\%$ |
| Chin et al., 2019 [117] | Band-pass filter + variance-based detection + maximum-likelihood estimation | Onset, period, and duration of QRS | MIT-BIH | 48 | 109357 | $Se=99.86\%$, $+P=99.85\%$, $Er=0.29\%$ |
| | | | QTDB | NR | NR | $Se=99.96\%$, $+P=99.94\%$, $Er=0.10\%$ |
| Rivas et al., 2015 [118] | Derivative + integral + squaring + thresholding | R peak | MIT-BIH | 48 | 109949 | $Se=99.54\%$, $+P=99.737\%$ |
| | | | NSRDB | NR | 192389 | $Se=99.96\%$, $+P=99.99\%$ |
| | | | ADB | NR | 197009 | $Se=99.45\%$, $+P=99.32\%$ |
| | | | Apnea ECG | NR | 703750 | $Se=99.90\%$, $+P=99.77\%$ |
| | | | Fantasia | NR | 19445 | $Se=99.98\%$, $+P=99.94\%$ |
| | | | Challenge 2014 | NR | 72309 | $Se=99.93\%$, $+P=99.75\%$ |

| Reference | Brief Description of the Algorithm | Feature Detected | Database | No. of Record Used | Total Peaks | Assessment Parameters |
|--------------------------|---|------------------|----------|--------------------|-------------|--|
| Nayak et al., 2019 [119] | Band-pass filter + digital fractional order differentiator + Shannon energy calculation + Hilbert transform + zero crossing detector. | R peak | MIT-BIH | 48 | 109494 | $Se=99.95\%$, $+P=99.94\%$, $Er=0.11\%$ |
| | | | STDB | 28 | 76175 | $Se=99.94\%$, $+P=99.92\%$, $Er=0.14\%$ |
| | | | SVDB | 78 | 184582 | $Se=99.91\%$, $+P=99.90\%$, $Er=0.18\%$ |
| | | | EDB | 90 | 790560 | $Se=99.87\%$, $+P=99.86\%$, $Er=0.27\%$ |
| | | | QTDB | 82 | 86995 | $Se=99.95\%$, $+P=99.98\%$, $Er=0.06\%$ |
| | | | TWADB | 100 | 18993 | $Se=99.43\%$, $+P=99.25\%$, $Er=1.32\%$ |
| Nayak et al., 2019 [120] | Band-pass filter + gravitational search algorithm based Integer order digital differentiator + smooth envelope extractor + non-amplitude threshold R-peak detection logic | R peak | MIT-BIH | 48 | 109494 | $Se=99.92\%$, $+P=99.92\%$, $Er=0.15\%$, $Da=99.84\%$, $QDR=99.92\%$, $Fs=0.999$ |
| | | | QTDB | 105 | 111134 | $Se=99.98\%$, $+P=99.96\%$, $Er=0.07\%$, $Da=99.93\%$, $QDR=99.96\%$, $Fs=0.999$ |
| | | | NSTDB | 12 | 25590 | $Se=95.23\%$, $+P=94.41\%$, $Er=10.41\%$, $Da=90.15\%$, $QDR=94.41\%$, $Fs=0.948$ |
| | | | AFTDB | 60 | 7592 | $Se=99.03\%$, $+P=99.76\%$, $Er=1.21\%$, $QDR=99.03\%$, $Da=98.79\%$, $Fs=99.39$ |
| | | | STDB | 28 | 76175 | $Se=99.93\%$, $+P=99.90\%$, $Er=0.17\%$, $Da=99.83\%$, $QDR=99.90\%$, $Fs=0.999$ |

| Reference | Brief Description of the Algorithm | Feature Detected | Database | No. of Record Used | Total Peaks | Assessment Parameters |
|-------------------------------|--|---------------------------------------|----------|--------------------|-------------|--|
| Kumar et al., 2019 [121] | Fast Fourier transform-based band-pass filter | R peak | MIT-BIH | 48 | NR | $Se=99.65\%$, $+P=99.65\%$, $Er=0.6\%$ (Short length) |
| | | | | | | $Se=99.98\%$, $+P=99.96\%$, $Er=0.03\%$ (full length) |
| Xie et al., 2019 [122] | Band-pass filter + discrete short-time Fourier transform + convolutional neural network. | N, S, V, F, and Q beat | MIT-BIH | 44 | NR | $Se=75.6\%$, $+P=90.1\%$, $Da=98.4\%$, $Sp=99.5\%$, $Fs=0.82$ (S beat) |
| Shaik et al., 2015 [85] | Low-pass filter + short-time Fourier transform + adaptive thresholding | QRS peak | MIT-BIH | 48 | 109011 | $Se=99.56\%$, $Sp=99.52\%$, $Er=0.93\%$ |
| Yazdani and Vesin, 2016 [123] | Low-pass filter + mathematical morphology filtering with a structuring element | QRS complex and other fiducial points | MIT-BIH | 48 | 109494 | $Se=99.87\%$, $+P=99.9\%$, $Er=0.2238$ |
| Jain et al., 2016 [124] | Detrending + linear decreasing inertia - particle swarm optimization-based adaptive filter + adaptive thresholding | QRS complex | MIT-BIH | 48 | 109494 | $Se=99.75\%$, $+P=99.83\%$, $Er=0.42\%$ |
| Pandit et al., 2017 [125] | Moving average filter + dynamic thresholding + max-min difference generation | R peak | MIT-BIH | 48 | 109809 | $Se=99.62\%$, $+P=99.67\%$ |
| | | | EDB | NR | 790495 | |
| | | | STDB | NR | 70755 | |
| | | | INCARTDB | NR | 174644 | |
| | | | QTDB | NR | 86435 | |
| Christov, 2004 [126] | Moving average filter + combined adaptive thresholds | QRS complex | MIT-BIH | 48 | 110050 | $Se=99.69\%$, $Sp=99.66\%$ (algorithm I) |
| | | | | | | $Se=99.74\%$, $Sp=99.65\%$ (algorithm-II) |

| Reference | Brief Description of the Algorithm | Feature Detected | Database | No. of Record Used | Total Peaks | Assessment Parameters |
|---------------------------------|--|------------------|---|--------------------|-------------|--|
| Lee et al., 2018 [127] | Median filter + signal envelope filtering + Shannon energy + Savitzky-Golay filter | R peak | Normal ECG in physical activity (NPADB) | 23 (sit) | 8385 | $Se=99.99\%$, $+P=99.99\%$, $Er=0.03\%$ |
| | | | | 23 (walk) | 10775 | $Se=99.93\%$, $+P=99.52\%$, $Er=0.55\%$ |
| | | | | 23 (ascend) | 14048 | $Se=99.94\%$, $+P=99.82\%$, $Er=0.24\%$ |
| | | | QTDB | 82 | 86892 | $Se=99.96\%$ (± 0.08), $+P=99.96\%$ (± 0.11), $Er=0.08\%$ ($\pm 0.14\%$) |
| | | | NSTDB | 2 | 4265 | $Se=90.20\%$ (± 0.45), $+P=87.73\%$ (± 2.06), $Er=22.43\%$ (± 2.79) (0 dB SNR) |
| Sharma and Sunkaria, 2016 [128] | Median filter + Savitzky-Golay filter + baseline identification + thresholding | QRS complex | MIT-BIH | 48 | 109488 | $Se=99.50\%$, $+P=99.56\%$, $Er=0.93\%$, $Da=99.08\%$ |
| | | | Fantasia | 22 | 160844 | $Se=99.90\%$, $+P=99.91\%$, $Er=0.19\%$, $Da=99.81\%$ |
| | | | NSTDB | 11 | 113138 | $Se=99.36\%$, $+P=99.43\%$, $Er=1.21\%$, $Da=98.81\%$ |
| | | | BIDMC congestive heart failure | 5 | 61682 | $Se=99.68\%$, $+P=99.78\%$, $Er=0.52\%$, $Da=99.46\%$ |
| | | | Self-recorded dataset | 15 | 15164 | $Se=99.97\%$, $+P=99.99\%$, $Er=0.04\%$, $Da=99.96\%$ |
| Rufas and Carrabina, 2015 [129] | MaMeMi filter + triangular detector + adaptive threshold detection | QRS complex | MIT-BIH | 48 | 109494 | $Se=99.43\%$, $+P=99.67\%$, $DR=99.22\%$, $Er=0.88\%$ |
| Jain et al., 2016 [130] | Mean subtraction + adaptive linear predictor + Savitzky-Golay filter + adaptive thresholding | QRS complex peak | MIT-BIH | 48 | 3706 | $Se=99.68\%$, $+P=99.84\%$ |

| Reference | Brief Description of the Algorithm | Feature Detected | Database | No. of Record Used | Total Peaks | Assessment Parameters |
|-----------------------------|---|---|--------------------------------------|--------------------|-------------|---|
| Elgendi et al. 2017 [131] | Sampling rate conversion + TERMA algorithm (Filtering + enhancing + potential block generation + thresholding) | QRS complex | MIT-BIH | 48 | 109985 | $Se=99.78\%$, $+P=99.92\%$ |
| | | | QTDB | 105 | 111201 | $Se=99.90\%$, $+P=99.84\%$ |
| Zidelmal et al. 2014 [132] | S transform and Shannon energy | R peak | MIT-BIH | 48 | 108494 | $Se=99.84\%$, $+P=99.91\%$, $Er=0.25\%$ |
| Birendra Biswal, 2017 [133] | Median filter + band-pass filter + modified S- transform with an amplitude threshold | R peak | MIT-BIH | 48 | 108494 | $Se=99.91\%$, $+P=99.91\%$, $Da=99.77\%$ |
| Chen and Chuang, 2017 [134] | Refreshment of ECG + signal enhancement + QRS fiducial point detection + recognition of R point on templet matching | R peak | MIT-BIH | 48 | 109443 | $Se=99.82\%$, $+P=99.81\%$, $Er=0.36\%$ |
| Yochum et al., 2016 [94] | Continuous wavelet transform | QRS complex, T and P- wave | Computers in Challenge 2011 database | 50 | NR | $Se=99.87\%$, $+P=91.75\%$, $Ac=98.64\%$, $Sp=98.42\%$, $Y_w=98.29\%$ |
| | | | MIT-BIH | 48 | 109491 | $Se=99.85\%$, $+P=99.48\%$, $Er=0.67\%$ |
| Li et al., 1995 [92] | Wavelet transform | R peak, QRS onset, and offset, T and P-wave | MIT-BIH | 46 | 116137 | $Er=0.15\%$, $DR > 99.8\%$ |
| Merah et al., 2015 [135] | Stationary wavelet transform | R peak | MIT-BIH | 48 | 109494 | $Se=99.84\%$, $+P=99.88\%$, $Er=0.28\%$ |
| | | | QTDB | 105 | 86892 | $Se=99.94\%$, $+P=99.89\%$, $Er=0.18\%$ |
| | | | NSTDB | 12 | 25590 | $Se=95.30\%$, $+P=93.98\%$, $Er=10.81\%$ |

| Reference | Brief Description of the Algorithm | Feature Detected | Database | No. of Record Used | Total Peaks | Assessment Parameters |
|-------------------------------|--|-------------------|--|--------------------|-------------|---|
| Banerjee et al., 2012 [89] | Discrete wavelet transform + QRS complex window finding by thresholding | R peak | MIT-BIH | NR | 19098 | $Se=99.6\%$, $+P=99.5\%$ |
| Berwal et al., 2018 [136] | Biorthogonal spline wavelet transform + threshold | QRS complex peak | MIT-BIH , NSTDB, and MIT-BIH atrial fibrillation | 43 | 3208 | $Se=99.31\%$, $+P=99.19\%$, $Er=1.49\%$ |
| Sabherwal et al., 2018 [95] | Discrete wavelet transform + digital filter + adaptive thresholding + fusion algorithm | S peak and R peak | MIT-BIH | 48 | 109498 | $Se=99.99\%$, $+P=99.99\%$, $Da=99.98\%$, $Er=0.135\%$, $MSE=0.039$ |
| Li et al., 2017 [93] | Wavelet transform + modulus maxima pair identification + R position modification | R peak | MIT-BIH | 48 | 109478 | $Se=99.60\%$, $+P=99.77\%$ |
| Rekik and Ellouze, 2016 [137] | Entropic criterion + wavelet transform modulus maxima | R peak | QTDB | 11 | 86995 | $Se=99.94\%$, $+P=99.99\%$ |
| Sharma et al., 2019 [138] | Tunable Q wavelet transform and correntropy based envelop extraction | R peak | MIT-BIH | 48 | 109494 | $Se=99.89\%$, $+P=99.83\%$, $Er=0.29\%$ |
| Sabherwal et al., 2017 [87] | Wavelet transform + first and second derivative and Hilbert transform | R peak | MIT-BIH | 48 | 109494 | $Se=99.9\%$, $+P=99.9\%$, $Da=99.8\%$, $Er=0.2\%$ (Avg.) |
| | | | QTDB | NR | NR | |
| | | | NSTDB | NR | NR | |
| Sahoo et al., 2016 [88] | Wavelet transform + differentiation + Hilbert transform with adaptive threshold | R peak | MIT-BIH | 19 | 44329 | $Se=99.71\%$, $+P=99.72\%$, $Er=0.52\%$ |
| Rakshit and Das, 2017 [90] | Wavelet transform + Shannon energy calculation and Hilbert transform | R peak | MIT-BIH | 48 | 109410 | $Se=99.93\%$, $+P=99.91\%$, $Da=99.83\%$, $Er=0.17\%$, $Fs=0.9992$ |

| Reference | Brief Description of the Algorithm | Feature Detected | Database | No. of Record Used | Total Peaks | Assessment Parameters |
|------------------------------|--|----------------------------|---------------------|--------------------|---------------|--|
| Park et al., 2017 [91] | Wavelet transform + Shannon energy envelope + peak energy envelope | R peak | MIT-BIH | 48 | 109494 | $Se=99.93\%$, $+P=99.91\%$, $Da=99.838\%$, $Er=0.163\%$ |
| Farashi, 2016 [139] | undecimated wavelet transform + multi-resolution time-dependent entropy + thresholding | QRS complex peak | MIT-BIH | 48 | 109965 | $Se=99.75\%$, $+P=99.85\%$, $Er=0.396$ |
| | | | CSE | NR | NR | $DR=99.82\%$ |
| Ravanshad et al., 2014 [140] | asynchronous level-crossing analog-to-digital converter and nonuniformly spaced data processing | QRS complex | MIT-BIH | 48 | 109428 | $Se=98.89\%$, $+P=99.40\%$, $Er=1.71\%$ |
| Qin et al., 2017 [141] | Wavelet-based multi-resolution analysis + adaptive thresholding | R peak | MIT-BIH | 48 | 109966 | $Se=99.39\%$, $+P=99.49\%$, $Da=98.89\%$ |
| | | | QTDB | 82 | 86995 | $Se=99.83\%$, $+P=99.90\%$, $Da=99.73\%$ |
| Deepu and Lian, 2015 [142] | Adaptive sign-sign least mean square predictor + Savitzky-Golay filter + squaring and sum + adaptive thresholding. | R peak | MIT-BIH | 48 | 109508 | $Se=99.64\%$, $+P=99.81\%$ |
| Tang et al., 2018 [143] | Parallel delta modulator + local maximum point and local minimum point algorithms | QRS complex, P, and T wave | MIT-BIH | 48 | 109966 | $Se=99.17\%$, $+P=99.55\%$, $Er=1.28\%$ |
| | | | QTDB | 103 | 3129 (P peak) | $Se=91.12\%$, $+P=92.44\%$ |
| | | | | | 3475 (T peak) | $Se=98.36\%$, $+P=98.99\%$ |
| Hou et al., 2018 [144] | Phase portraits and box scoring algorithm | QRS complex | MIT-BIH | 48 | 110008 | $Se=99.32\%$, $+P=99.45\%$ |
| | | | Experimental result | 23 | 1890 | $Se=96.55\%$, $+P=97.53\%$ |

| Reference | Brief Description of the Algorithm | Feature Detected | Database | No. of Record Used | Total Peaks | Assessment Parameters |
|-----------------------------|---|------------------------|-----------------------------|--------------------|-------------|---|
| Li et al., 2018 [145] | Phase space reconstruction | R peak | MIT-BIH | 48 | 109494 | $Se=99.87\%$, $+P=99.93\%$, $Da=99.81\%$ |
| | | | NSTDB | 24 | 51180 | $Se=99.56\%$, $+P=93.05\%$, $Da=92.67\%$ |
| | | | Long term ST | 86 | 8897780 | $Se=99.87\%$, $+P=99.96\%$, $Da=99.91\%$ |
| Bajaj and Kumar, 2019 [146] | Fractional Stockwell transform and fractional Stockwell Shannon energy | R peak | MIT-BIH | 48 | 109494 | $Se=99.99\%$, $+P=99.97\%$, $Er=0.03\%$, $Da=99.97\%$ |
| Hossain et al., 2019 [147] | Moving window median filter + complete ensemble empirical mode decomposition with adaptive noise approach | QRS complex and P-wave | MIT-BIH | 48 | 109441 | $Se=99.97\%$, $+P=99.93\%$, $Er=0.11\%$ |
| | | | QTDB | 80 | 86989 | $Se=99.96\%$, $+P=99.89\%$, $Er=0.15\%$ |
| | | | NSTDB | NR | 4268 | $Se=99.25\%$, $+P=90.05\%$ |
| Gupta et al., 2019 [148] | Independent principal component analysis + chaos analysis and principal component analysis | R peak | MIT-BIH | 36 | 101275 | $Se=99.95\%$, $+P=99.96\%$, $Er=0.093\%$ |
| | | | Ventricular tachyarrhythmia | 02 | | |
| | | | AF termination challenge | 04 | | |
| | | | AHA | 02 | | |
| | | | MIT-BIH long-term | 04 | | |
| | | | Realtime dataset | 7 | 16501 | $Se=99.96\%$, $+P=99.97\%$, $Er=0.055\%$ |
| Jia et al., 2020 [149] | High-resolution wavelet packet decomposition + convolutional neural network | QRS complex | Telehealth | NR | NR | $Se=98.99\%$, $+P=95.57\%$, $Er=5.61\%$, $Fs=97.25\%$ |
| | | | NSTDB | NR | NR | $Se=99.25\%$, $+P=96.31\%$, $Er=4.55\%$, $Fs=97.76\%$ |
| | | | MIT-BIH | NR | NR | $Se=99.89\%$, $+P=99.90\%$, $Er=0.21\%$, $Fs=99.89\%$ |

| Reference | Brief Description of the Algorithm | Feature Detected | Database | No. of Record Used | Total Peaks | Assessment Parameters |
|---------------------------------|---|-------------------|--------------------------------|--------------------|-------------|---|
| Chen and Maharatna, 2020 [150] | High-pass filter + low-pass filter + hierarchical clustering + discrete wavelet transform | R peak and T peak | MIT-BIH | 48 | NR | $Se=99.89\%$, $+P=99.94\%$, $Da=99.83\%$ |
| | | | QTDB | 103 | NR | $Se=100\%$, $+P=99.83\%$, $Da=99.83\%$ (for R peak) $Se=99.91\%$, $+P=99.38\%$, $Da=NR$ (for T peak) |
| Modak et al., 2021[151] | Median filter + moving average filter + segmentation and statistical false peak elimination | QRS complex | MIT-BIH | 48 | 109494 | $Se=99.82\%$, $+P=99.88\%$, $Er=0.31\%$ |
| | | | Fantasia | 40 | 285308 | $Se=99.92\%$, $+P=99.90\%$, $Er=0.18\%$ |
| Fotoohinasab et al., 2021 [152] | graph-constrained changepoint detection | QRS complex | MIT-BIH | NR | NR | $Se=99.64\%$, $+P=99.71\%$, $Er=0.19$ (manually defined constraint graph) |
| | | | | | | $Se=99.76\%$, $+P=99.68\%$, $Er=0.55$ (automatic learning constraint graph) |
| Morshedlou et al. 2021 [153] | Differentiation + square + low-pass filter | QRS complex | MIT-BIH | 48 | 109428 | $Se=99.20\%$, $+P=99.40\%$, $Er=1.46\%$ |
| | | | NSTDB | 12 | NR | $Se=99.94\%$, $+P=99.80\%$, (For record-11924 at 24 dB SNR) |
| | | | BIDMC congestive heart failure | 15 | 93092 | $Se=98.70\%$, $+P=99.40\%$, $Er=1.88\%$ |

***NR**: Not reported, **Se**: sensitivity, **+P**: positive predictivity, **Er**: error rate, **Da**: detection accuracy, **DR**: detection rate, **QDR**: QRS detection rate

computational complexity; many parameters must be set and manual segmentation for training before analyzing a record [159].

Artificial neural networks (ANN) are helpful for the detection and classification of QRS complexes. As the name suggests, ANN is a computational algorithm based on the biological neural network. The virtues like learning complex and non-linear surfaces among different classes make ANN suitable for ECG beat detection and classification [160]. Multilayer perceptron, self-organizing feature map (SOFM) learning vector quantization, and radial basis function networks are used to process an ECG signal. Xie et al. [122] proposed a convolution neural network (CNN) for classification and achieved a detection accuracy of 98.4%. Kohler et al. [161] proposed zero-crossing detection of QRS complexes. In zero-crossing detection, a feature is obtained by counting the number of zero crossings per segment. The zero-crossing feature primarily does affect the sudden amplitude changes in the ECG signal, thus providing robustness to noise. The amplitude fluctuations in the problematic sections of an ECG signal do not affect the count of zero-crossing, significantly improving detection performance. The zero-crossing detection method has the advantage of simplicity and low computational costs.

In [123], mathematical morphology (MM) is proposed to extract the QRS fiducial point. MM is used to extract the topological information from the analysis of the geometrical structure. MM operator non-linearly transforms the signal into another signal called the structuring element (SE). SE is used to detect QRS complexes. The R peak detection using zero-crossing concepts is reported in [114, 115, 119]. In [114, 115, 119], the properties of Hilbert transform and zero-crossing locations are used to detect the R peak. The odd symmetry property of HT provides a zero at each maximum, thus providing a zero whenever the input signal crosses the axes. These zero crossing locations are used to locate the true position of an R peak. Li et al. [145] proposed a QRS complex detection method by coordinate mapping based on phase space reconstruction. Tang et al. [143] employed a delta modulator along with a local maximum point (LMaP) and local minimum point (LMiP) algorithm to detect the QRS complex, P-wave, and T-wave. In [152], the graph-constrained changepoint detection method detects the QRS complexes in an ECG signal. The reported sensitivity, positive predictivity, and error in [152] are 99.76%, 99.68%, and 0.55. Different researchers have proposed various QRS and R peak detection techniques, but no technique resulted in perfect accuracy with all the standard datasets with all records. Also, their clinical implementation is doubtful. Another important parameter affecting the performance of the available QRS complex detection algorithms is the sampling rate and resolution of the selected ECG data. Varghees et al. [162] propose a method based on VMD for denoising the ECG signal and efficiently detecting the R peak. In [162], the authors reported an

average positive predictivity of 99.91% and sensitivity of 99.77% with the MIT-BIH arrhythmia database. Peng et al. [163] suggest a deep-learning model named ST-Res U-net which is based on an improved U-net model, for the detection of the QRS complex and R peak. A method named BayeSlope is proposed by Giovanni et al. [164] to detect R peaks on wearable ECG sensors.

Sampling is a process of converting a continuous-time signal into a discrete-time signal. According to the Nyquist criteria, the sampling frequency must be greater than or equal to twice the maximum frequency of the signal to be digitized. If the sampling rate is low, the high-frequency components superimpose low-frequency components, introducing an error into the reconstructed signal. It is required to choose the proper sampling frequency so that the accuracy of the QRS complex detection algorithms is not affected [165]. The maximum heartbeat is at most 220 beats per minute (bpm), corresponding to a frequency of less than *four* Hz. In an ECG signal, the spectrum of the heartbeat signal extends up to 15 Hz, and some features extend beyond 25 Hz. Hence as per the Nyquist criterion, a minimum sampling frequency of 50 Hz is required. However, in real ECG recorders, the sampling frequency ranges from 100-500 Hz, whereas in a lab environment, the sampling frequencies go up to 1000 Hz [165]. In 1975, the AHA recommended a minimum sampling rate of 500 Hz, with uniform sampling, generally two or three times the theoretical minimum sampling rate [166]. According to the AHA task force [167], a low sampling rate may yield a jitter in R peak detection, significantly altering the spectrum. The optimal sampling frequency range for R peak detection is 250-500 Hz. The sampling resolution (or bit depth) is another factor affecting heartbeat detection accuracy. Sampling resolution produces a signal-to-quantization noise ratio, which results in an error in beat detection. Ajdaraga et al. [165] showed that *eight-bit* or lower sampling resolution is unacceptable for QRS complex detection, especially at high sampling frequencies. The frequency resolution of *ten-bit* shows acceptable results, but an accurate analysis requires a *12-bit* resolution.

3.4. DATABASES TO EVALUATE THE PERFORMANCES OF ECG ANALYSIS ALGORITHMS

The ECG databases play a significant role in developing any algorithm related to ECG signal analysis. These databases provide various annotated ECG signals recorded under different conditions. Depending on the application, various researchers use various databases to evaluate the performance of the proposed ECG signal analysis algorithms. Table 3.3 summarizes these databases and their salient features [168].

(i) Massachusetts Institute of Technology-Beth Israel Hospital Arrhythmia Database

(MIT-BIH) is a popular database comprising 48 half-hour ECG recordings from *two* channels. ECG signals from 47 subjects are recorded at Boston's Beth Israel Hospital between 1975 to 1979. Of 47 subjects, 25 were men, aged 32 to 89, and 22 were women, aged 23 to 89. Of these recordings, 60% of records are from insubjects, and 40% are from outsubjects. The sampling frequency is 360 samples per second, facilitating 60 Hz notch filters. An 11-bit resolution is used for digitalization.

(ii) **MIT-BIH Atrial Fibrillation Database** is a collection of 25 long-term ECG recordings from subjects experiencing atrial fibrillation. In this database, each recording contains *two* ECG signals. Each ECG signal lasts *ten* hours and is sampled at 250 Hz over an amplitude range of ± 5 millivolts. A 12-bit resolution is used for digitalization.

(iii) **MIT-BIH Noise Stress Test Database** includes 15 recordings, each half hour. Out of 15, *twelve* recordings are noisy ECG records, and rest *three* recordings correspond to noise. The *three* noisy records, BW, EMG, and electrode motion artifact (EM), are prepared from the recordings by selecting the intervals in which BW, EMG, and EM dominate. The noisy ECG recordings are prepared by adding noise from the EM recording to *two* clean ECG records, 118 and 119, from the MIT-BIH arrhythmia database. In each recording, the noise is added after the initial *five* minutes, alternating between a *two*-minute segment of noise and a *two*-minute segment of clean ECG signal [171]. The sampling frequency is 250 Hz and a 11-bit resolution is used for digitalization.

(iv) **MIT-BIH Normal Sinus Rhythm Database**- In this database, 18 long-duration ECG recordings from 18 subjects referred to Beth Israel Deaconess Medical Center are collected. Out of 18, 5 are men aged between 26 and 45, and the remaining are women aged between 20 and 50. All the subjects have no significant arrhythmias. The sampling frequency is 128 Hz.

(v) **MIT-BIH ST Change Database**- 28 ECG recordings of varying duration, mostly recorded during exercise stress tests, are provided in this database. Most of the recordings have ST depression, but the last five recordings numbered 323 to 327, exhibit ST elevation. The sampling frequency is 360 Hz.

(vi) **MIT-BIH Long-Term ECG Database** includes *seven* ECG recordings of long duration varying from 14 to 22 hours. Each recording is manually annotated. The sampling frequency is 128 Hz and a 12-bits per sample is used for digitalization.

(vii) **The American Heart Association Database (AHA)**- The American heart association, along with the funding agency National Heart, Lung, and Blood Institute (NHLBI), created an ECG database at Washington University, which is known as the AHA database. This database includes 80 two-channel recordings. A sampling frequency of 250 Hz per channel over ± 5 mV

Table 3.3: Overview of various databases used in ECG signal processing

| Sr.No. | Database | Subjects | Number of Records | Length of Record (minutes) | Number of lead | Sampling frequency | Bit Resolution (bits per sample) |
|---------------|---|-----------------|--------------------------|-----------------------------------|-----------------------|---------------------------|---|
| 1 | MIT-BIH Arrhythmia [169] | 47 | 48 | 30 | 2 | 360 Hz | 11 |
| 2 | MIT-BIH Atrial Fibrillation [170] | 25 | 25 | 600 | 2 | 250 Hz | 12 |
| 3 | MIT-BIH Noise Stress Test [171] | NA | 15 | 30 | 2 | 360 Hz | 11 |
| 4 | MIT-BIH Normal Sinus Rhythm | 18 | 18 | 1440 | 2 | 128 Hz | NA |
| 5 | MIT-BIH ST Change [172] | 28 | 28 | 13-67 | 1-2 | 360 Hz | NA |
| 6 | MIT-BIH Long-Term ECG | NA | 7 | 840-1320 | NA | 128 Hz | 12 |
| 7 | The American Heart Association [173] | NA | 80 | 35 | 2 | 250 Hz | 12 |
| 8 | Creighton University (CU) Ventricular Tachyarrhythmia [174] | NA | 35 | 8 | 1 | 250 Hz | 12 |
| 9 | BIDMC Congestive Heart Failure [175] | 15 | 15 | 1200 | 12 | 250 Hz | NA |
| 10 | European ST-T [176] | 79 | 90 | 120 | 2 | 250 Hz | 12 |
| 11 | QT database [177] | NA | 105 | 15 | 2 | 250 Hz | NA |
| 12 | Fantasia [178] | 40 | 40 | 120 | NA | 250 Hz | NA |
| 13 | PTB [179] | 290 | 549 | NA | 15 | 1000 Hz | 16 |
| 14 | Non-Invasive Fetal ECG [180] | 1 | 55 | Variable | multiple | 1000 Hz | 16 |
| 15 | St Petersburg INCART 12-lead Arrhythmia | 32 | 75 | 30 | 12 | 257 Hz | NA |
| 16 | Apnea-ECG [181] | NA | 70 | 401-578 | NA | 100 Hz | 16 |
| 17 | Fetal ECG Synthetic [182] | 10 | 1750 | 5 | 34 | 250 Hz | 16 |

*NA: Not available

includes 80 two-channel recordings. A sampling frequency of 250 Hz per channel over ± 5 mV range with a 12-bit resolution is used for digitalization. This database is available in two versions: a short version and a long version. The short version consists of an unannotated recording of 5 minutes before 30 minutes annotated ECG recording. In the long version, 2.5 hours of unannotated recording is present before each annotated part.

(viii) Creighton University (CU) Ventricular Tachyarrhythmia Database consists of 35 eight-minute ECG recordings of subjects suffering from ventricular tachycardia, ventricular flutter, and ventricular fibrillation. All records are digitized at a sampling rate of 250 Hz with a 12-bit resolution of a ± 5 mV range.

(ix) BIDMC Congestive Heart Failure Database includes long-term ECG recordings from 15 subjects. Out of 15, 11 are men aged between 22 and 71, and the remaining are women aged between 54 and 63. All recordings are digitized at a sampling rate of 250 Hz with a 12-bit resolution over ± 10 mV range.

(x) European ST-T Database – Ninety annotated ECG records from seventy-seven subjects are in the database. Seventy subjects are men aged 30 to 84, and eight are women aged 55 to 71. Each record consists of two signals of 2 hours duration. A sampling frequency of 250 samples per second with a 12-bit resolution over the input range of 20 mV is used to digitize the signals.

(xi) QT Database – a collection of various ECG recordings from existing databases. The QT database consists of thirteen records from the MIT-BIH supraventricular Arrhythmia database, fifteen records from the MIT-BIH Arrhythmia database, thirty-three from the European ST-T database, six records from the MIT-BIH ST change database, ten records from the MIT-BIH normal sinus rhythm arrhythmia database, four from MIT-BIH long term database and twenty-four records were from sudden death subjects at Boston's Beth Israel Deaconess Medical center. The database covers 105 records and two-channel recordings to avoid baseline fluctuations or other artifacts. The sampling rate for digitalization is 250 Hz.

(xii) Fantasia Database consists of forty ECG recordings, twenty from the young population aged 21 to 34 years and twenty from the elderly population aged 68 to 85 years. All the recording has a duration of 120 minutes. The ECG signals are recorded when the subjects are at rest and watching a Fantasia movie. The sampling rate for digitalization is 250 Hz.

(xiii) PTB Diagnostic Database is a collection of 549 ECG recordings from 290 subjects. The database contains ECG recordings of 209 men with a mean age of 55.5 years and 81 women with a mean age of 61.6 years. Signals are sampled at a sampling frequency of 1000 Hz. Resolution is 16 bits over a range of ± 16.384 mV.

(xiv) Long Term ST Database includes 86 long-duration ECG recordings from 80 subjects. The recordings are 21 to 24 hours long, containing *two* to *three* ECG signals. The sampling frequency is 250 samples per second over the ± 10 mV range with a 12-bit resolution.

(xv) Non-Invasive Fetal ECG Arrhythmia Database (NIFEA DB) consists of 55 recordings taken from a single pregnant subject recorded over twenty weeks. The ECG signal sampling frequency is 1000 Hz with a 16-bit resolution.

(xvi) ECG ID Database includes 310 recordings from 90 subjects. *Forty-four* men and 46 women from different fields (students, colleagues, and friends of the author) are taken for the recording. The ECG signal sampling frequency is 500 Hz with a 12-bit resolution over ± 10 mV.

(xvii) St Petersburg Institute of Cardiological Technics (INCART) Database includes 75 annotated recordings. The duration of each record is 30 minutes using 12 standard leads. *Seventeen* men and 15 women aged between 18 to 80 years are selected for recording. The ECG recordings are sampled at 257 Hz.

(xviii) Apnea -ECG Database is a dataset of 70 records. The length of these recordings varies between less than 7 hours to 10 hours. Each recording includes three facts: a continuous digitized ECG signal, apnea annotation, and machine-generated QRS annotation. These *seventy* recordings are divided into a learning set and a test set of 35 recordings each. A sampling frequency of 100 Hz with a 16-bit resolution is used for digitalization.

3.5. PARAMETERS TO EVALUATE THE PERFORMANCE OF AN ECG SIGNAL ANALYSIS ALGORITHM

Various parameters are used in the literature to evaluate the ECG algorithms proposed by various researchers. These parameters are an integral part of ECG signal analysis. Evaluation parameters evaluate the algorithms and provide a medium for comparing various proposed algorithms. Different evaluation parameters are presented in this section. In the following equations, $S(n)$, $X(n)$, $X'(n)$, and $Y(n)$ represent a corrupted signal, original signal, preprocessed signal, and denoised signal, respectively. N is the length of the ECG signal.

the signal-to-noise ratio of the input signal,

$$SNR_{input} = 10 \log_{10} \left(\frac{\sum_{n=1}^N (X'[n])^2}{\sum_{n=1}^N (S[n])^2} \right) \quad (3.2)$$

Output signal-to-noise ratio,

$$SNR_{out} = 10 \log_{10} \left(\frac{\sum_{n=1}^N Y^2[n]}{\sum_{n=1}^N (X[n] - Y[n])^2} \right) \quad (3.3)$$

Improvement in signal-to-noise ratio,

$$SNR_{imp} = SNR_{out} - SNR_{input} = 10 \log_{10} \left(\frac{\sum_{n=1}^N (S[n] - X[n])^2}{\sum_{n=1}^N (Y[n] - X[n])^2} \right) \quad (3.4)$$

Mean square error

$$MSE = \frac{1}{N} \sum_{n=1}^N (X[n] - Y[n])^2 \quad (3.5)$$

Percentage root mean square difference

$$PRD = \sqrt{\frac{\sum_{n=1}^N (X[n] - Y[n])^2}{\sum_{n=1}^N [X[n]]^2}} \times 100 \quad (3.6)$$

$$Sensitivity (Se) = \frac{(True\ Positive)}{(True\ Positive + True\ Negative)} \quad (3.7)$$

$$Specificity (Sp) = \frac{(True\ negative)}{(True\ Positive + False\ Positive)} \quad (3.8)$$

$$Positive\ predictivity (+P) = \frac{(True\ positive)}{(True\ Positive + False\ Positive)} \quad (3.9)$$

$$Accuracy (Ac) = \frac{(True\ Positive + True\ negative)}{(True\ Positive + True\ negative + False\ Positive + False\ Negative)} \quad (3.10)$$

$$Detection\ Accuracy (Da) = \frac{(True\ Positive)}{(True\ Positive + False\ Positive + False\ Negative)} \quad (3.11)$$

$$Error\ Rate (Er) = \frac{(False\ Positive + False\ Negative)}{Total\ beat} \quad (3.12)$$

$$QRS\ Detection\ Rate (QDR) = Min(sensitivity, positive\ predictivity) \quad (3.13)$$

$$F\text{-score} (Fs) = \frac{(2 \times Sensitivity \times positive\ predictivity)}{(Sensitivity + positive\ predictivity)} \quad (3.14)$$

$$\text{Youden index}(Y_w) = Se + Sp - 1 \quad (3.15)$$

True positive represents the number of true QRS complexes that are correctly detected. *False-negative* is the number of QRS complexes not detected as a QRS complex. *False-positive* is the number of non-QRS complexes that are detected as QRS complexes. Sensitivity represents the percentage of true beats that an algorithm can correctly detect. Positive predictivity is the percentage of detected beats that were true beats. *Accuracy* represents the ratio of correctly detected beats to the total number of beats. *QRS detection rate* is the minimum value between sensitivity and positive predictivity.

3.6. DISCUSSION, CHALLENGES, GAPS

Detection of CVD requires accurate and precise detection of QRS complexes. As ECG signals suffer from various noises and artifacts, an ECG signal must be preprocessed. The preprocessing step suppresses the noises and artifacts in an ECG signal and directly influences the analysis outcome. This chapter summarizes some of the existing ECG signal preprocessing techniques and QRS complex detection techniques. Researchers used the most popular preprocessing methods: filtering, transform, and decomposition. The study showed that a single technique could not remove different artifacts and noises.

Moreover, each denoising technique produces some impact on the ECG signal. It is essential to identify the nature of noise. After identifying the nature of the noise, a denoising scheme should be selected to suppress those noises and artifacts. In literature, hybrid techniques are used to improve the overall performance of the ECG detection algorithms. Hybrid techniques combine two techniques to achieve better denoising at the expense of increased computation complexity and processing delay.

The presence of noises and artifacts in the ECG signal produces errors in QRS and R peak detection. Hence denoising step is a very crucial part of CVD detection. The literature survey showed that many proposed algorithms achieved appropriate denoising results with few ECG records. No single denoising scheme is validated using all records from all the standard datasets. Among the various denoising techniques, the filtering technique is quite effective when the noise occurs in a known frequency range and does not overlap with the frequency range of the ECG signal. When the noise spectrum and an ECG signal overlap, the transform techniques such as DFT and DCT have shown good denoising performance without distorting the signal. Line fitting techniques such as S-G filtering may appear a powerful tool when the frequency range of noise is unpredictable and widespread. S-G filtering can smooth the signal without destroying the properties of an ECG signal. Other transform techniques, such as STFT

and wavelet, have also been used for denoising, but they are not suitable for ECG signals of longer duration.

Decomposition techniques like EMD, EEMD, VMD, and Fourier decomposition methods help suppress specific noises such as baseline wander, PLI, and EMG noise. These techniques can remove some of the noises and artifacts present in the ECG signal. The performance of these algorithms is evaluated using a few ECG records. Most denoising techniques have successfully overcome the BW and PLI noise, but removing other noises is still challenging. In several studies, beat averaging is used to remove noise, but its usefulness and effect on the specificity and sensitivity of detection algorithms require further studies.

Detection of the QRS complex or R peak depends on the quality of the ECG signal. In the presence of artifacts and noises, the detection accuracy may decrease, and the wrong identification of CVD is possible. Hence, before detection, denoising is essential. Various methods are available in the literature for detecting QRS complexes and R peak detection. Almost all these techniques use a preprocessing or denoising step before detection to improve detection accuracy. Recent studies reported excellent detection accuracies by excluding noisy records from the standard dataset. The detection accuracies of some of the proposed ECG detectors are very high when applied to a limited dataset and under specific conditions, and the algorithms are not validated over all the datasets. Further, when implemented in a realtime system, most of these algorithms suffer from low detection accuracies.

Although different researchers have proposed various QRS denoising and detection techniques, many are not tested against all standard databases, hence a fair comparison to evaluate their performance. Some proposed algorithms in the literature achieved high sensitivity and accuracy by excluding noisy records from the database. Therefore, these algorithms may not be helpful for clinical purposes. Most detection techniques have used different pre-processing and detection methods, which results in complexity and time consumption. To the best of our knowledge, no technique is proposed in the literature that can be used for denoising and detection and provides good performance results. Although wavelet transform is used for denoising and detection, the performance is not very good. Also, selecting a mother wavelet in a wavelet transform is difficult. The practical implementation of the proposed algorithms is a big challenge in ECG signal analysis. Recent studies show that the lossless data compression of the ECG signal is also essential, along with denoising and detection. The lossless compression capability is necessary because it minimizes storage, transmission, and computational resources. In the literature, very few algorithms have compression capability. Our studies reveal that the evaluation parameters like accuracy and sensitivity represent the

overall performance of the algorithms. However, the portion of the algorithm accountable for improving the evaluation parameters is not provided. The assessment of the algorithms based on features is very important as it would help in the secondary analysis and explaining the cause of abnormalities in a heart. In the literature, the outcomes of the proposed algorithms are not compared with the output of an ECG recorder used by medical professionals. This comparison helps to validate the proposed algorithms and demonstrate the efficacy of the proposed algorithm over methods currently in practice.

3.7. SUMMARY

CVD poses a severe health risk worldwide. CVDs can be accurately predicted by analyzing ECG signals. This chapter discusses the problems associated with the techniques to analyze the ECG signal. The primary step in ECG signal analysis is the removal of various noises present in the ECG signal. Denoising is the most critical step in ECG signal processing because the denoising step directly influences the outcome of the detection process. Many researchers suggest various techniques for denoising by minimizing or removing the effect of noises. The techniques used for denoising are based on time, frequency, time-frequency, and sparsity domain. Some hybrid techniques, arrived at by combining two approaches, also remove noise from an ECG signal. Each method has its benefits and drawbacks, which are discussed in this chapter.

The CVD can be detected by identifying the morphological features of a denoised ECG signal. In the literature, R peak and QRS complex are used to detect the characteristics of an ECG signal. Before detection, almost all algorithms use denoising or noise removal techniques. Various techniques proposed in the literature have achieved commendable ECG peak detection accuracies on the standard databases. Here detection techniques and their performance parameters are summarized in this chapter. This literature survey is summarized and published in [24].

CHAPTER 4

DENOISING OF ECG SIGNAL FOR DETECTION OF CARDIOVASCULAR DISEASE

Cardiovascular diseases (CVDs) are emerging as a severe threat to humanity as they cause higher mortality rates and untimely deaths. The scariness of CVD is forcing researchers to concentrate on CVD and cardiac health. Early diagnosis and monitoring of cardiac health can minimize the severity of CVD. Recent technologies in the medical field have changed the traditional way of analyzing cardiac health and made the resources approachable, affordable, and easily understandable. In practice, electrocardiogram (ECG) is a widely accepted non-invasive clinical tool to analyze cardiac health. ECG, a graphical representation of the electrical activity of heart tissues, represents cardiac health status. An ECG signal consists of a P wave, QRS complex, and T wave originating due to depolarization and repolarization of atria and ventricles. An ECG signal and its constituent waves for one cardiac cycle are shown in Fig. 4.1.

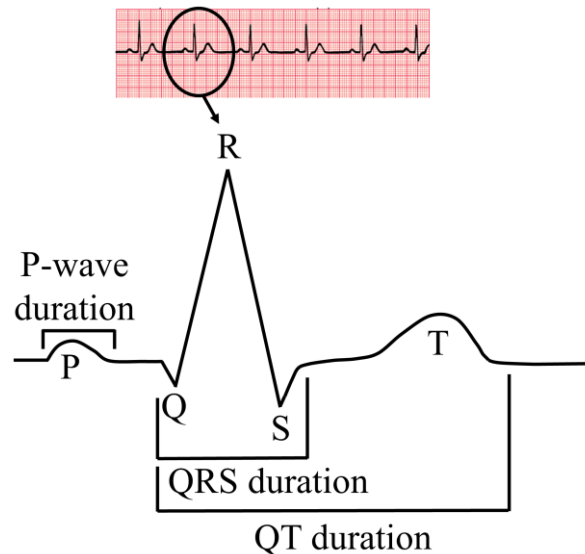


Fig. 4.1: Simplified representation of an ECG signal

While recording an ECG signal, various noises such as power line interference (PLI), baseline wander (BW), motion artifact (MA), electrode contact noise, and instrumentation noise contaminate the signal. The presence of these noises severely affects the outcome of the analysis; hence denoising these signals is essential. This chapter proposes an algorithm based on the Fourier decomposition method (FDM) to denoise the ECG signal.

4.1. ECG SIGNAL DENOISING METHODS

In the previous decades, various research groups focused on the automatic detection of CVDs

by detecting QRS complexes, a prominent feature of an ECG signal. Automatic detection of CVD increases the probability of timely diagnostics, lowers the probability of human error, and reduces the cost and time of ECG signal analysis. The block diagram of an automatic ECG analysis system is shown in Fig. 4.2. An automatic ECG analysis system comprises denoising, signal transformation, feature extraction, and fiducial point detection steps. The denoising or preprocessing step removes or minimizes the noises present in the ECG signal. The denoised ECG signal is applied to the signal transformation unit. The signal transformation performs non-linear operations like squaring to convert bipolar ECG signals into unipolar ECG signals. The feature extraction unit is used to extract various morphological features like the slope of the QRS complex, duration of the QRS complex, and statistical features to complete ECG signal analysis. Finally, with the help of these extracted features, fiducial points such as R peak, QRS complex, and P wave are detected.

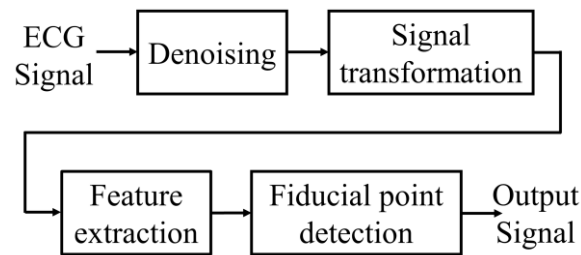


Fig. 4.2: Block diagram of an automatic ECG signal analysis system

Various noises in the ECG signal affect the ECG signal analysis. Various methods such as time domain filtering, frequency domain filtering, digital filtering, recursive filtering, adaptive filtering, wavelet transform (WT), empirical mode decomposition (EMD), ensemble empirical mode decomposition (EEMD), variational mode decomposition (VMD), and deep learning-based methods are used to denoise ECG signals. The filtering method to denoise ECG signals is simple and popular but greatly influences the ECG signal characteristics. Adaptive filters are suitable for removing noises outside the frequency band of the ECG signal. However, its performance degrades in the case of in-band noise [183]. Time-frequency domain methods remove these shortcomings of the filtering methods. WT is a popular time-frequency domain approach to analyzing nonlinear and nonstationary signals. WT provides noise cancelation by decomposing the ECG signal into the time-frequency domain. In the wavelet-based denoising, three approaches, namely wavelet modulus maxima denoising, thresholding denoising, and related denoising (denoising based on dependencies between wavelet coefficient), are used to extricate regular wavelet coefficient from the noise [59]. Thresholding is a widely used denoising technique in methods based on wavelets. In 1995, Donoho suggested soft and hard

thresholding techniques for wavelet coefficient denoising [184]. Although hard and soft thresholding provides satisfactory performance, they exhibit some limitations. Hard thresholding leads to oscillations and discontinuities and may be sensitive to small changes in an ECG signal [56]. In soft thresholding, the amplitude is distorted in the reconstructed ECG signal. The efficacy of the WT-based method is dependent on the selection of mother wavelets. It is challenging to select an optimal wavelet to provide all desirable results. These drawbacks of wavelet transform are removed by other techniques like EMD, EEMD, and complete ensemble empirical mode decomposition (CEEMD) [185].

EMD is an eminent and extensively used method for analyzing nonlinear and nonstationary signals. EMD decomposes the noisy signal into a set of IMFs, which are finite and bandlimited. These IMFs are directly derived from the signal. EMD has limitations like mode mixing, aliasing, end effect artifacts, and detrend uncertainty. Moreover, EMD lacks mathematical explanation, which makes decomposition results challenging to interpret. The mode mixing problem of EMD is resolved using EEMD [75]. EEMD, a noise-assisted EMD, uses white noise to reduce the mode mixing problem of EMD. Although EEMD has numerous advantages over EMD, the number of ensemble trails and amplitude of added noise are two crucial factors that affect the performance of the EEMD. Limitations such as lack of mathematical description, recursive shift, and inability to withstand noise in the EMD decomposition method are addressed by a decomposition technique known as VMD [186]. VMD decomposes the signal into several modes having some specific sparsity properties. VMD has shown a better performance than EMD in terms of noise and sampling error [187]. However, a major limitation of VMD is selecting the number of modes (k) in advance. Large k values may yield mode mixing, whereas small values may result in duplicate modes [187].

Deep learning-based ECG signal denoising techniques are gaining more attention. The efficiency of deep learning-based methods depends on the size of the data. However, the availability of large-size data is not always possible. In the automatic ECG signal analysis system, a noisy ECG signal can mislead the diagnostic. In the presence of noises, a normal ECG signal may be detected as an abnormal ECG signal, or the ECG signal belonging to an unhealthy heart may be predicted as a healthy heart. Hence, a denoised ECG signal is essential in a computer-assisted ECG analysis system. This chapter proposes an ECG denoising method based on the FDM. FDM is based on the Fourier method and is an attractive tool for analyzing nonlinear and nonstationary signals [188]. The nonlinear and nonstationary nature of ECG signals makes FDM a suitable choice for ECG signal denoising. Unlike wavelet transform, FDM is free from mode mixing and has a proper mathematical formulation. FDM decomposes

signals into bandlimited Fourier intrinsic band functions (FIBFs). The FIBFs correspond to bands that are intrinsic to signals. FDM also provides the time-frequency-energy representation of an ECG signal to reveal the characteristics of the ECG signal. This method not only denoises the ECG signal but also provides spectral information that can be used for further analysis.

4.2. MATHEMATICAL DESCRIPTION OF FOURIER DECOMPOSITION METHOD

FDM is a Fourier-based adaptive signal decomposition technique. FDM decomposes the nonlinear and nonstationary signal into complete, orthogonal, and local FIBFs. The FIBFs are adaptive, energy-preserving, and complete. Let $s(t)$ be an arbitrary signal defined in the interval $[p, q]$ that satisfies Dirichlet conditions. The FIBFs of $s(t)$ are defined as a set of functions $\{x_i(t) : x_i(t) \in [p, q], 1 < i < N\}$ that satisfy the following criterion:

(i) $s(t) = \sum_{i=1}^M x_i(t) + d_0$, here d_0 represents average value of $s(t)$.

(ii) $\int_p^q x_i(t) dt = 0, \forall i$ FIBFs have zero mean value.

(iii) FIBFs obey the orthogonality condition, for $i \neq l$.

(iv) Analytical representation of FIBFs is possible that is $x_i(t) + j\hat{x}_i(t) = v_i(t)e^{j\varphi_i(t)}$ with amplitude $v_i(t) \geq 0$, and instantaneous frequency $\omega_i(t) = \frac{d\varphi_i(t)}{dt} \geq 0, \forall t. \hat{x}_i(t)$ is equivalent to

the Hilbert transform of FIBF $x_i(t)$.

Thus, FIBF is a summation of the *zero* mean sinusoidal function of consecutive frequency bands. The amplitude and frequency in each FIBF are time functions; hence FIBFs represent amplitude and frequency-modulated signals. In FIBFs, the instantaneous frequencies provide the time-frequency-energy distribution of the signal. This representation has the advantage of explaining the imbedded structures of a signal. FIBFs of a signal are the consequence of the Fourier method-based zero-phase filters. FDM also provides two different views through the time-frequency energy distribution of a signal (high to low frequency and low to high frequency). The superior capability of FDM to handle the nonlinear and nonstationary signal makes this method a powerful tool for ECG signal denoising. FDM is classified into two types: continuous time Fourier decomposition method and discrete Fourier decomposition method.

4.2.1 Continuous Time Fourier Decomposition Method

Continuous-time FDM decomposes a continuous-time signal into a set of FIBFs. Let $s(t)$ be a

real-valued signal defined in a time interval $t' \leq t \leq t'+T$. The periodic extension of this signal can be constructed as,

$$s_T(t) = \sum_{k=-\infty}^{\infty} s(t-kT) \text{ such that } s(t) = s_T(t) \times r(t) \text{ where } \begin{cases} r(t) = 1, \text{ for } t' \leq t \leq t'+T \\ 0 \text{ Otherwise} \end{cases} \quad (4.1)$$

The Fourier series expansion of $s_T(t)$ is given by Eq. (4.2).

$$s_T(t) = a_0 + \sum_{n=1}^{\infty} [a_n \cos(n\omega_0 t) + b_n \sin(n\omega_0 t)] \quad (4.2)$$

Here $a_0 = \frac{1}{T} \int_{t'}^{t'+T} s_T(t) dt$, $a_n = \frac{2}{T} \int_{t'}^{t'+T} s_T(t) \cos n\omega_0 t dt$, $b_n = \frac{2}{T} \int_{t'}^{t'+T} s_T(t) \sin n\omega_0 t dt$, and

$$\omega_0 = \frac{2\pi}{T} \text{ rad/s.}$$

Using complex exponential representation, Eq. (4.2) can be written as:

$$s_T(t) = a_0 + \frac{1}{2} \sum_{n=1}^{\infty} [c_n \exp(jn\omega_0 t) + c_n^* \exp(-jn\omega_0 t)] \quad (4.3)$$

Here, $c_n = (a_n - jb_n)$ and $c_n^* = (a_n + jb_n)$, From Eq. (4.3),

$$s_T(t) = a_0 + \text{Re}\{w_T(t)\} \quad (4.4)$$

$\text{Re}\{w_T(t)\}$ represents the real part of $w_T(t)$. The analytic function $w_T(t)$ is defined as:

$$w_T(t) = \sum_{n=1}^{\infty} c_n \exp(jn\omega_0 t) \quad (4.5)$$

To find a set of analytic FIBFs, we can write $w_T(t)$ as:

$$w_T(t) = \sum_{i=1}^M v_i(t) \exp(j\varphi_i(t)) \quad (4.6)$$

Here, to obtain analytic FIBFs, in a forward search manner (from low to high-frequency scan),

$$v_1(t) \exp(j\varphi_1(t)) = \sum_{n=1}^{N_1} c_n \exp(jn\omega_0 t) \quad (4.7)$$

$$\text{and, } v_2(t) \exp(j\varphi_2(t)) = \sum_{n=N_1+1}^{N_2} c_n \exp(jn\omega_0 t) \quad (4.8)$$

$$\text{and, } v_M(t) \exp(j\varphi_M(t)) = \sum_{n=N_{M-1}+1}^{\infty} c_n \exp(jn\omega_0 t) \quad (4.9)$$

or in general,

$$v_i(t) \exp(j\varphi_i(t)) = \sum_{n=N_{i-1}+1}^{N_i} c_n \exp(jn\omega_0 t), \text{ for } i = 1, 2, 3, \dots, M. \quad (4.10)$$

Here, $N_0 = 0$ and $N_M = \infty$.

In Eq. (4.10) the real parts of analytic FIBFs represent the FIBFs. In low-to-high frequency checks, a minimum number of analytic FIBFs is obtained by starting i with $(N_{i-1}+1)$ and adding

more terms to get the maximum value of N_i such that $(N_{i-1} + 1) \leq N_i \leq \infty$, $v_i(t) \geq 0$,

$$\omega_i(t) = \frac{d\varphi(t)}{dt} \geq 0 \forall \text{ all } t.$$

Here, $v_i(t)$ and $\omega_i(t)$ are the instantaneous amplitude and instantaneous frequency of i^{th} FIBF, respectively.

Similarly, to obtain analytic FIBFs in reverse search direction (from high-to-low frequency check), the lower and upper limits of Eq. (4.10) are $n = N_i$ to $(N_{i-1}-1)$. In this case, the value of N_0 and N_M are ∞ and 1, respectively. The value of i starts with $(N_{i-1}-1)$ and decreases to a minimum value of N_i such that $1 \leq N_i \leq (N_{i-1}-1)$.

Equation (4.6) has a form of generalized Fourier series expansion, and this representation is local, complete, adaptive, and orthogonal. Thus in Eq. (4.6), the presence of instantaneous amplitude and instantaneous frequency makes the representation efficient by expanding the signal into a finite number of analytic FIBFs. The real part of these analytic FIBFs are FIBFs in which the amplitude and frequency are functions of time.

4.2.2 Discrete Fourier Decomposition Method

Discrete FDM is used for discrete-time signals. Let $s[n]$ represent a discrete signal with length N . $s[n]$ can be written as

$$s[n] = \sum_{k=0}^{N-1} S[k] \exp\left(\frac{j2\pi kn}{N}\right) \quad (4.11)$$

Here,

$$S[k] = \left(\frac{1}{N}\right) \sum_{n=0}^{N-1} s[n] \exp\left(\frac{-j2\pi kn}{N}\right) \quad (4.12)$$

If N is an even number $S[0]$ and $S[N/2]$ are real, and Eq. (4.11) is given by

$$s[n] = s[0] + \sum_{k=1}^{\frac{N}{2}-1} S[k] \exp\left(\frac{j2\pi kn}{N}\right) + S\left[\frac{N}{2}\right] \exp(j\pi n) + \sum_{k=\frac{N}{2}+1}^{N-1} S[k] \exp\left(\frac{j2\pi kn}{N}\right) \quad (4.13)$$

For real $s[n]$,

$$w_1[n] = \sum_{k=1}^{\frac{N}{2}-1} S[k] \exp\left(\frac{j2\pi kn}{N}\right) \quad (4.14)$$

is the complex conjugate of $w_2[n] = \sum_{k=\frac{N}{2}+1}^{N-1} S[k] \exp\left(\frac{j2\pi kn}{N}\right)$ (4.15)

Equation (4.13) can be written as,

$$s[n] = S[k] + 2 \operatorname{Re}\{w_1[n]\} + S\left[\frac{N}{2}\right] (-1)^n \quad (4.16)$$

$Re\{w_1[n]\}$ is the real part of $w_1[n]$. Now, the analytic signal $w_1[n]$ can be written as,

$$\sum_{k=1}^{\frac{N-1}{2}} S[k] \exp\left(\frac{j2\pi kn}{N}\right) = \sum_{i=1}^M v_i[n] \exp(j\varphi_i[n]) \quad (4.17)$$

In left-to-right frequency search (forward search) of FIBFs,

$$v_1[n] \exp(j\varphi_1[n]) = \sum_{k=1}^{N_1} S[k] \exp\left(\frac{j2\pi kn}{N}\right) \quad (4.18)$$

and

$$v_2[n] \exp(j\varphi_2[n]) = \sum_{k=N_1+1}^{N_2} S[k] \exp\left(\frac{j2\pi kn}{N}\right) \quad (4.19)$$

and

$$v_M[n] \exp(j\varphi_M[n]) = \sum_{k=N_{M-1}+1}^{\frac{N-1}{2}} S[k] \exp(j2\pi kn/N) \quad (4.20)$$

or in general,

$$v_i[n] \exp(j\varphi_i[n]) = \sum_{k=N_{i-1}+1}^{N_i} S[k] \exp\left(\frac{j2\pi kn}{N}\right) \quad (4.21)$$

Here, the value of N_0 and N_M are 0 and $(N/2-1)$, respectively.

In the left-to-right frequency search $\left(\frac{N}{2}-1\right)$, for each i , the minimum number of FIBFs is obtained by finding a maximum value of N_i such that $N_{i-1}+1 \leq N_i \leq (N/2-1)$, and the phase $\varphi_i[n]$ is a monotonically increasing function.

Similarly, in a high-to-low frequency search for FIBFs, the lower and upper limits in Eq. (4.21) range from $k = N_i$ to $N_{i-1}-1$. In this case, the values of N_0 and N_M are $\frac{N}{2}$ and 1, respectively. For each i , the minimum value of N_i is selected such that $1 \leq N_i \leq (N_{i-1}-1)$ and phase $\varphi_i[n]$ is a monotonically increasing function.

Thus, FDM can provide two interpretations: a low-to-high frequency search or a high-to-low frequency search of a signal. Both interpretations may be the same or provide different signal features depending on the signal.

4.3. ECG SIGNAL DENOISING USING THE FOURIER DECOMPOSITION METHOD

Various noises in an ECG signal can mislead the cardiac diagnosis. An efficient denoising method reduces the effect of noises, improves the detection accuracy of ECG characteristics, and aids cardiac diagnosis. Although numerous denoising techniques like filtering, frequency-domain analysis, and time-frequency domain analysis are found in the literature, the optimal

selection of the technique is critical. With its superior capability of handling nonstationary and nonlinear signals, FDM can potentially analyze nonstationary biological signals. FDM decomposes a signal into intrinsic bands to reveal the inherent contents, which helps identify the noise and unwanted components in a signal. The time-frequency-energy (TFE) representation of a signal provided by FDM helps remove noise from the signals. Hence, FDM is selected to analyze and denoise ECG signals. Various noises such as PLI, BW, MA, muscle contraction, and EMG contaminate the ECG signal and severely affect the final diagnosis. Hence, the removal of these noises is essential. In this section, a method employing the virtues of FDM is presented to denoise the ECG signal. The block diagram of the methodology is shown in Fig. 4.3.

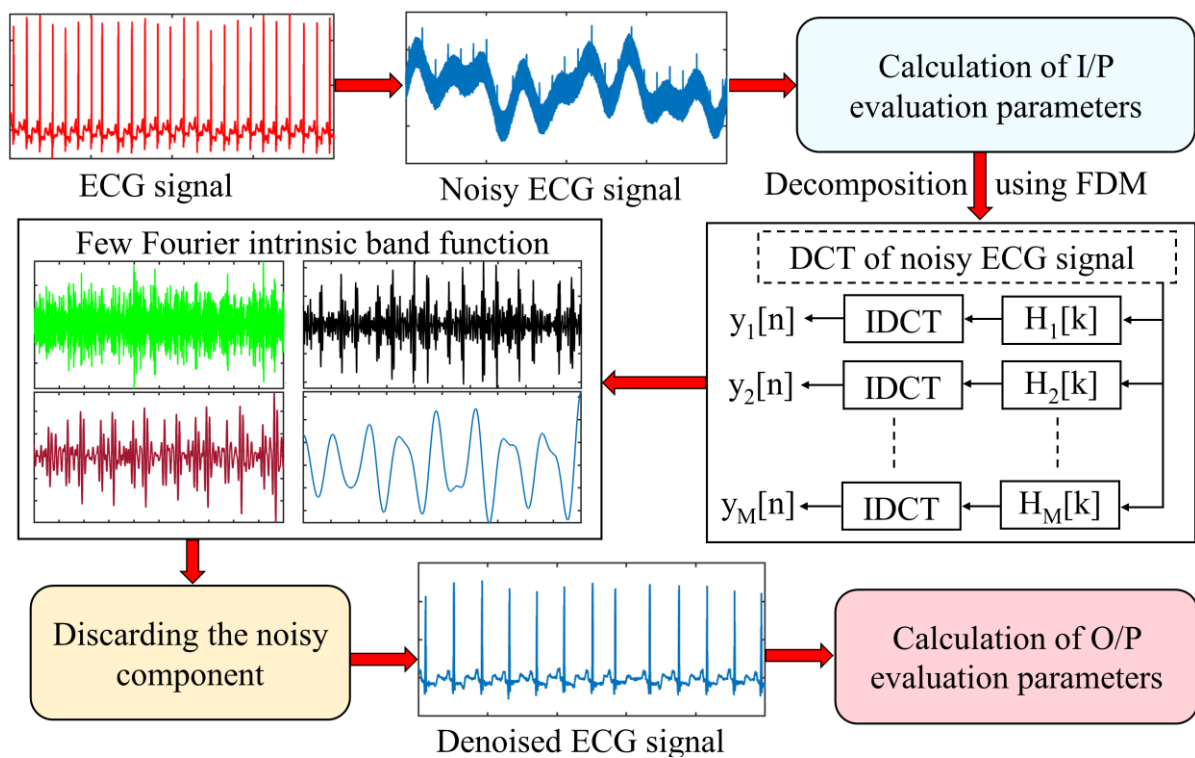


Fig. 4.3: Flow chart of the FDM-based denoising method

The FDM method chooses a clean ECG signal from the standard database, and various noises are added. Adding these noises to the clean ECG signal is necessary to study the effect of various noises and their eventual removal from the ECG signal. Later noisy ECG signals are used to study the method. Different types of noise, like white Gaussian noise, PLI, BW, MA, muscle contraction, and EMG, are added to the clean ECG signal. These noises are added at different values of the input *SNR* to observe the efficacy of the methodology. After adding these noises, the resultant noisy ECG signal is decomposed using FDM. FDM decomposes the input signal $y[n]$ into a set of FIBFs. These FIBFs are orthogonal or linearly independent and

nonorthogonal but energy preserving (LINOEP). The decomposed signal $y[n]$ is expressed using Eq. (4.22) [188].

$$y[n] = e_0 + \sum_{i=1}^M x_i[n] = e_0 + \sum_{i=1}^M e_i[n] \quad (4.22)$$

Here, e_0 is the average value of the given signal, and $x_i[n]$ and $e_i[n]$ represent the i^{th} orthogonal and LINOEP FIBFs, respectively. Fig. 4.4 illustrates the FDM approach using DCT and discrete DFT-based zero-phase filter bank with $H_i(k) \in \mathbb{R} \geq 0 \forall i, k$. The decomposition of the signal $y[n]$ yields a set of M orthogonal FIBFs $\{y_1[n], y_2[n], \dots, y_M[n]\}$. The i^{th} band frequency response in DFT-based FDM can be obtained by selecting $H_i(k) = 1$ for the desired frequency bands; otherwise, zero. The filters in the filter bank are represented by Eq. (4.23).

$$H_i(k) = \begin{cases} 1, & \forall (K_{i-1} + 1) \leq k \leq K_i \text{ and } (N - K_i) \leq k \leq (N - K_{i-1} - 1) \\ 0, & \text{otherwise} \end{cases} \quad (4.23)$$

Here, $i = \{1, 2, \dots, M\}$, $K_0 = 0$ and $K_M = \frac{N}{2}$ when N is even or $K_M = \frac{(N-1)}{2}$ if N is odd.

The i^{th} FIBF $y_i[n]$ can be obtained by inverse DFT (IDFT) using Eq. (4.24).

$$y_i[n] = \sum_{k=0}^{N-1} \left[H_i(k) \times Y(k) e^{\left(\frac{j2\pi kn}{N}\right)} \right] \quad (4.24)$$

Here, $Y(k)$ represents the DFT of the signal $y[n]$, and $H_i(k)$ is the response of the i^{th} ZPF. Similarly, in the case of DCT-based FDM, the response of the i^{th} filter $H_i(k)$ can be described by Eq. (4.25).

$$H_i(k) = \begin{cases} 1, & (k_{m-1} + 1) \leq k \leq k_m \\ 0, & \text{otherwise} \end{cases} \quad (4.25)$$

Here, $K_0 = 0$ and $K_M = N$. For the i^{th} FIBF $y_i[n]$, the type 2 inverse DCT is used as given in Eq. (4.26).

$$y_i[n] = \sqrt{\frac{2}{N}} \sum_{k=0}^{N-1} \sigma_k H_i(k) Y_{c2}[k] \cos\left(\frac{\pi k (2n+1)}{2N}\right) \quad (4.26)$$

$Y_{c2}[k]$ is the DCT of signal $y[n]$, $\sigma_k = 1$ for $k \neq 0$ and when $k = 0$, $\sigma_k = \frac{1}{\sqrt{2}}$.

FDM decomposes the signal $y[n]$ into M number of FIBFs. Some FIBFs correspond to various noises, and the rest of the FIBFs represent various ECG signal bands. M number of FIBFs, require one DCT and $(M-2)$ IDCT operations. The FFT algorithm is used to implement the entire operation, which minimizes the computational complexity. In this FDM-based

technique, the DCT of the noisy signal $y[n]$ is computed. Then with the help of a zero-phase filter bank, the signal is decomposed into M FIBFs. These FIBFs correspond to various components present in an ECG signal. The FIBFs that correspond to noise components are discarded. The remaining FIBFs represent the band of clean ECG signals.

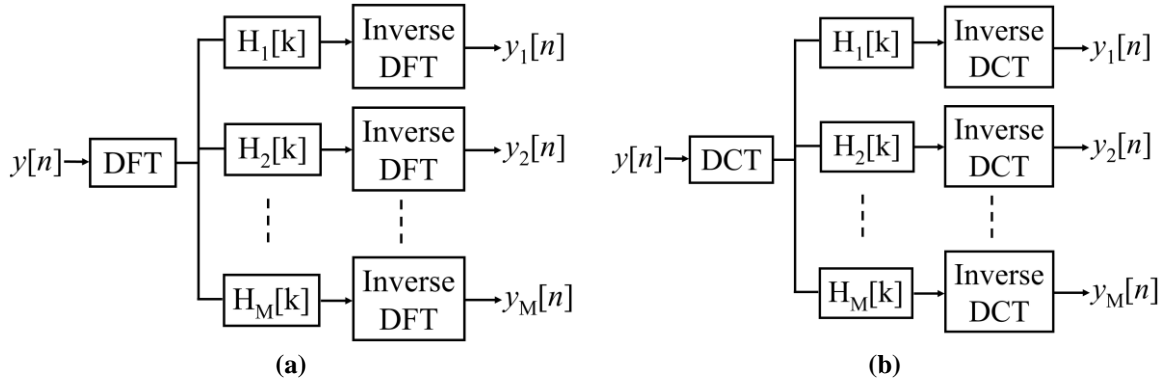


Fig. 4.4: Block diagram of (a) FDM based on DFT (b) FDM based on DCT

4.4. SIMULATIONS AND PERFORMANCE EVALUATION OF THE FDM-BASED DENOISING METHOD

The proposed method is implemented using MATLAB® and evaluated on realtime ECG signal and online available MIT-BIH arrhythmia database and noise stress test database. The sampling frequency of ECG signals in the MIT-BIH arrhythmia and noise stress test databases is 360 Hz. All the *forty-eight* ECG signals with a *ten*-second duration are used to validate the proposed FDM-based denoising method. The efficacy of the proposed FDM-based denoising method is measured in terms of output signal-to-noise ratio (SNR_{out}) and output percentage root mean square difference (PRD_{out}) given by (3.3) and (3.6).

An ECG signal is recorded using the iworx® IX-TA-220 recorder to evaluate the efficacy of the proposed method on realtime ECG signals. The performance of the proposed FDM-based denoising method is evaluated on publicly available ECG databases. Sampling frequency and other parameters of the realtime ECG signal are selected as the same as the MIT-BIH arrhythmia database. A realtime ECG signal is recorded by considering different kinds of

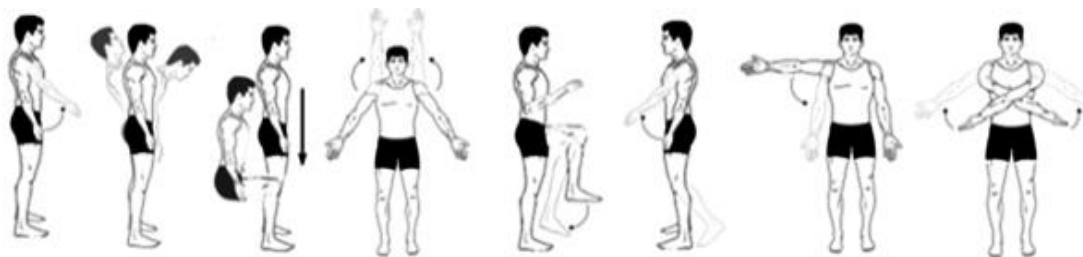


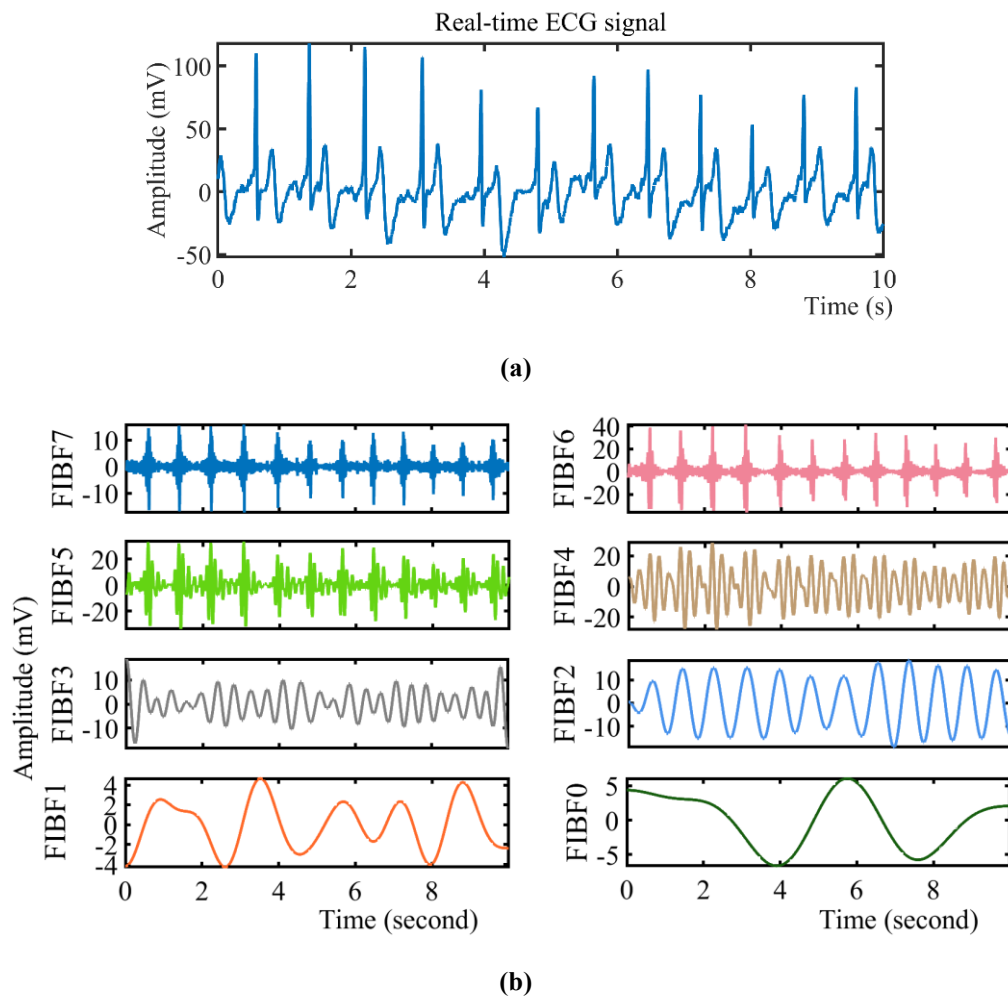
Fig. 4.5: A pictorial representation of body movements during daily activities, used for recording the realtime ECG signal

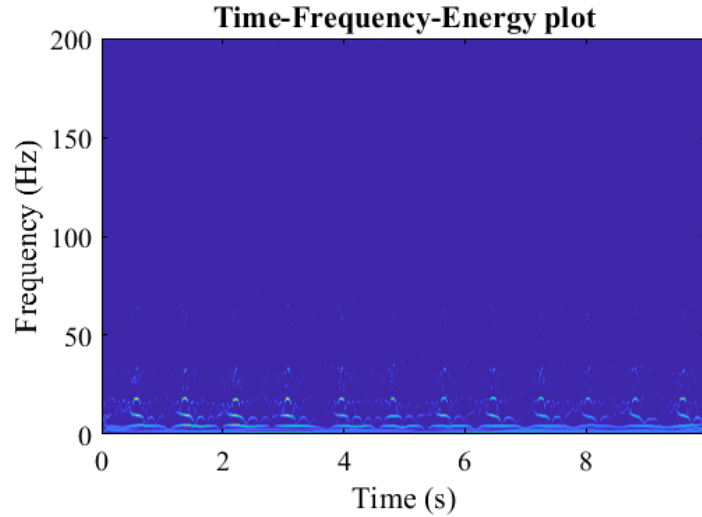
movements that a person might perform during daily activities. A pictorial representation of these body movements is shown in Fig. 4.5. Such movements of a person create various noises while recording an ECG signal.

The *eight* FIBFs and TFE representations of realtime ECG signals are shown in Fig. 4.6 to assess the performance of the proposed FDM-based denoising method on ECG signal measured in realtime. Fig. 4.6 (a) shows the recorded real-time ECG signal. The FIBFs and TFE distribution of the realtime ECG signal are shown in Fig. 4.6 (b) and Fig. 4.6 (c), respectively. Fig. 4.6 (d) gives the denoised real-time ECG signal. Detailed results obtained from the proposed method for other noises are discussed below. This work is published in [189].

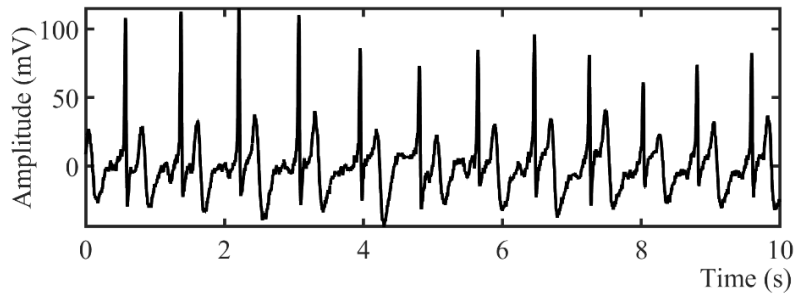
4.4.1 Simulation Results with Power Line Interference

To analyze the effect of PLI, the most common noise, PLI of 60 Hz, is added to a clean ECG signal to obtain a noisy ECG signal. These noise samples are added to clean ECG signals at *five* levels of SNR_{in} , -10 dB, -5 dB, 0 dB, 5 dB, and 10 dB, respectively. The performance of the proposed FDM-based denoising method is evaluated in terms of the output signal-to-noise ratio (SNR_{out}) and percentage root mean square difference (PRD_{out}). The computed SNR_{out} and





(c)



(d)

Fig. 4.6: (a) Realtime ECG signal (b) FIBFs obtained by the proposed FDM-based denoising method (c) TFE plot of realtime ECG signal (d) denoised realtime ECG signal

PRD_{out} values for MIT-BIH arrhythmia records are listed in Table 4.1 and Table 4.2.

It is evident from Table 4.1 that the proposed FDM-based denoising method rejects PLI noise to achieve SNR_{out} at all levels of SNR_{in} . The proposed FDM-based denoising method with PLI provides an SNR_{out} ranging from 34 dB to 41 dB at different values of input SNR for ECG signals from the MIT-BIH arrhythmia database. In removing the PLI, obtained PRD_{out} values at different values of SNR_{in} are presented in Table 4.2. Our method attains lower PRD_{out} values at different values of SNR_{in} .

The performance of the proposed FDM-based denoising method and other existing methods for removing PLI from ECG signals in terms of SNR_{out} and PRD_{out} are compared in Table 4.3 and Table 4.4, respectively. The proposed FDM-based denoising method provides the highest SNR_{out} compared with EMD-WT (empirical mode decomposition-wavelet transform) method [190] and EVD (eigenvalue decomposition) method [80]. For ECG signal 105, the proposed method provides a SNR_{out} of 39.22 dB, whereas a SNR_{out} of 22.4 dB and 6.4 dB is reported in

[190] and [80]. Similarly, for ECG signal 118, the proposed FDM-based denoising method

Table 4.1: SNR_{out} after removing 60 Hz PLI from MIT-BIH arrhythmia database ECG signals at different SNR_{in}

| ECG signal | SNR_{out} at different values of SNR_{in} | | | |
|------------|---|-------|------|------|
| | -10 dB | -5 dB | 0 dB | 5 dB |
| 100 | 37.9 | 38.1 | 38.1 | 38.1 |
| 101 | 39.5 | 39.6 | 39.7 | 39.7 |
| 102 | 36.4 | 36.6 | 36.6 | 36.8 |
| 103 | 39.3 | 39.4 | 39.4 | 39.5 |
| 104 | 38.8 | 38.9 | 38.9 | 38.9 |
| 105 | 39.2 | 39.3 | 39.4 | 39.4 |
| 106 | 38.0 | 38.2 | 38.3 | 38.5 |
| 107 | 39.2 | 39.4 | 39.5 | 39.5 |
| 108 | 37.2 | 37.5 | 37.8 | 37.9 |
| 109 | 36.3 | 36.3 | 36.4 | 36.4 |
| 111 | 36.3 | 36.8 | 36.9 | 36.9 |
| 112 | 40.0 | 40.1 | 40.2 | 40.2 |
| 113 | 35.1 | 35.2 | 35.6 | 35.7 |
| 115 | 34.9 | 35.0 | 35.1 | 35.1 |
| 116 | 34.9 | 35.0 | 35.1 | 35.1 |
| 117 | 39.9 | 39.9 | 40.0 | 40.1 |
| 118 | 37.3 | 37.4 | 37.5 | 37.5 |
| 119 | 38.3 | 38.5 | 38.7 | 38.8 |
| 121 | 36.4 | 36.5 | 36.7 | 36.8 |
| 122 | 38.9 | 38.9 | 39.2 | 39.3 |
| 123 | 35.7 | 35.8 | 35.9 | 35.9 |
| 124 | 39.1 | 39.2 | 39.4 | 39.6 |
| 200 | 39.4 | 39.6 | 39.9 | 39.9 |
| 201 | 38.1 | 38.4 | 38.7 | 38.8 |
| 202 | 35.8 | 35.8 | 36.2 | 36.5 |
| 205 | 39.5 | 39.6 | 39.6 | 39.6 |
| 209 | 39.3 | 39.4 | 39.7 | 39.7 |
| 210 | 37.5 | 37.5 | 37.6 | 37.6 |
| 212 | 39.2 | 39.3 | 39.7 | 39.8 |
| 213 | 38.4 | 38.5 | 38.6 | 38.6 |
| 214 | 37.5 | 37.5 | 37.6 | 37.8 |
| 219 | 36.2 | 36.3 | 36.5 | 36.6 |
| 220 | 40.1 | 40.1 | 40.3 | 40.3 |
| 221 | 35.7 | 35.8 | 35.9 | 35.9 |
| 231 | 38.5 | 38.6 | 38.6 | 38.7 |
| 233 | 38.2 | 38.3 | 38.5 | 38.6 |
| 234 | 37.8 | 37.9 | 38.0 | 38.0 |

Table 4.2: PRD_{out} from the proposed FDM-based denoising method with 60 HZ PLI corrupted ECG signals from MIT-BIH arrhythmia database

| ECG signal | PRD_{out} at different SNR_{in} | | | |
|------------|-------------------------------------|-------|-------|-------|
| | -10 dB | -5 dB | 0 dB | 5 dB |
| 100 | 0.712 | 0.742 | 0.760 | 0.760 |
| 101 | 0.355 | 0.378 | 0.400 | 0.400 |
| 102 | 0.471 | 0.482 | 0.490 | 0.490 |
| 103 | 0.35 | 0.382 | 0.400 | 0.400 |
| 104 | 0.483 | 0.507 | 0.520 | 0.520 |
| 105 | 0.305 | 0.341 | 0.350 | 0.360 |
| 106 | 0.517 | 0.52 | 0.530 | 0.530 |
| 107 | 0.431 | 0.439 | 0.450 | 0.450 |
| 108 | 0.613 | 0.62 | 0.640 | 0.650 |
| 109 | 0.741 | 0.769 | 0.780 | 0.780 |
| 111 | 0.45 | 0.467 | 0.477 | 0.480 |
| 112 | 0.544 | 0.57 | 0.580 | 0.590 |
| 113 | 0.536 | 0.546 | 0.567 | 0.580 |
| 115 | 0.325 | 0.336 | 0.350 | 0.370 |
| 116 | 0.165 | 0.189 | 0.200 | 0.210 |
| 117 | 0.429 | 0.455 | 0.470 | 0.471 |
| 118 | 0.698 | 0.722 | 0.730 | 0.740 |
| 119 | 0.729 | 0.740 | 0.750 | 0.770 |
| 121 | 0.571 | 0.579 | 0.580 | 0.600 |
| 122 | 0.740 | 0.740 | 0.770 | 0.770 |
| 123 | 0.468 | 0.470 | 0.480 | 0.500 |
| 124 | 0.630 | 0.650 | 0.650 | 0.680 |
| 200 | 0.271 | 0.291 | 0.301 | 0.331 |
| 201 | 0.211 | 0.231 | 0.239 | 0.248 |
| 202 | 0.586 | 0.592 | 0.613 | 0.632 |
| 205 | 0.286 | 0.308 | 0.320 | 0.320 |
| 209 | 0.310 | 0.317 | 0.330 | 0.340 |
| 210 | 0.171 | 0.179 | 0.190 | 0.190 |
| 212 | 0.412 | 0.440 | 0.460 | 0.490 |
| 213 | 0.448 | 0.480 | 0.500 | 0.500 |
| 214 | 0.432 | 0.441 | 0.460 | 0.476 |
| 219 | 0.659 | 0.680 | 0.694 | 0.697 |
| 220 | 0.311 | 0.358 | 0.380 | 0.389 |
| 221 | 0.288 | 0.300 | 0.310 | 0.320 |
| 231 | 0.634 | 0.668 | 0.680 | 0.690 |
| 233 | 0.713 | 0.730 | 0.741 | 0.768 |
| 234 | 0.503 | 0.534 | 0.540 | 0.540 |

Table 4.3: Comparison of the proposed FDM-based denoising method to EVD and EMD-WT-based denoising methods using SNR_{out} for ECG signals corrupted with PLI

| ECG signal | SNR_{in} | Proposed FDM-based denoising method | EMD-WT method [190] | EVD method [80] |
|------------|---------------|-------------------------------------|---------------------|-----------------|
| | | SNR_{out} | | |
| 100 | -10 dB | 37.9 | 12.5 | 19.0 |
| | -5 dB | 38.1 | 14.4 | 27.5 |
| | 0 dB | 38.1 | 14.5 | 28.1 |
| | 5 dB | 38.1 | 13.3 | 28.1 |
| 101 | -10 dB | 39.5 | 14.7 | 14.2 |
| | -5 dB | 39.7 | 15.9 | 27.7 |
| | 0 dB | 39.7 | 17.2 | 27.7 |
| | 5 dB | 39.7 | 16.2 | 29.1 |
| 103 | -10 dB | 39.3 | 15.6 | 8.3 |
| | -5 dB | 39.4 | 19.5 | 32.3 |
| | 0 dB | 39.4 | 20.1 | 33.0 |
| | 5 dB | 39.5 | 19.8 | 33.0 |
| 105 | -10 dB | 39.2 | 22.4 | 6.4 |
| | -5 dB | 39.3 | 23.8 | 14.0 |
| | 0 dB | 39.4 | 24.4 | 31.9 |
| | 5 dB | 39.4 | 25.4 | 32.6 |
| 109 | -10 dB | 36.3 | 24.1 | 6.9 |
| | -5 dB | 36.3 | 26.3 | 17.9 |
| | 0 dB | 36.4 | 27.3 | 35.3 |
| | 5 dB | 36.4 | 28.1 | 35.3 |
| 112 | -10 dB | 40.0 | 19.7 | 6.8 |
| | -5 dB | 40.1 | 20.7 | 40.2 |
| | 0 dB | 40.2 | 23.2 | 41.8 |
| | 5 dB | 40.2 | 23.6 | 41.8 |
| 118 | -10 dB | 37.3 | 16.6 | 14.3 |
| | -5 dB | 37.5 | 16.8 | 15.9 |
| | 0 dB | 37.5 | 18.6 | 45.4 |
| | 5 dB | 37.5 | 20.6 | 45.5 |

performs better as compared to EMD-WT and EVD methods at low SNR_{in} (-10 dB and -5 dB) but at 0 and 10 dB SNR_{in} the outcome of the proposed FDM-based denoising method is comparable to the EVD method. For most of the ECG signals compared in Table 4.3, the proposed FDM-based denoising method provides the highest SNR_{out} at low SNR_{in} (-10 dB and -5 dB). This work is published in [189].

Table 4.4 compares the computed PRD_{out} to the existing EMD-WT method [190], and EVD [80] for the PLI corrupted ECG signals from the MIT-BIH arrhythmia database. Results show that the proposed FDM-based denoising method provides the lowest PRD_{out} compared to [80] and [190].

Table 4.4: Comparison of the proposed FDM-based denoising method to EVD and EMD-WT-based denoising methods using PRD_{out} for ECG signals corrupted with PLI

| ECG signal | SNR_{in} | Proposed FDM-based denoising method | EMD-WT [190] | EVD [80] |
|------------|------------|-------------------------------------|--------------|----------|
| | | PRD_{out} | | |
| 213 | -10 dB | 0.448 | 2.666 | 3.037 |
| | -5 dB | 0.480 | 2.700 | 3.089 |
| | 0 dB | 0.500 | 2.728 | 3.424 |
| | 5 dB | 0.500 | 2.739 | 3.449 |
| 221 | -10 dB | 0.288 | 1.139 | 2.313 |
| | -5 dB | 0.300 | 1.169 | 2.364 |
| | 0 dB | 0.310 | 1.194 | 2.399 |
| | 5 dB | 0.320 | 1.204 | 2.427 |
| 231 | -10 dB | 0.634 | 2.819 | 3.017 |
| | -5 dB | 0.668 | 2.852 | 3.059 |
| | 0 dB | 0.680 | 2.876 | 3.091 |
| | 5 dB | 0.690 | 2.891 | 3.138 |
| 234 | -10 dB | 0.503 | 3.389 | 2.823 |
| | -5 dB | 0.534 | 3.416 | 2.868 |
| | 0 dB | 0.540 | 3.447 | 2.899 |
| | 5 dB | 0.540 | 3.466 | 2.931 |

4.4.2 Simulation Results with White Gaussian Noise

The performance of the proposed FDM-based denoising method is evaluated with white Gaussian noise. The results obtained to suppress white Gaussian noise are shown in Table 4.5. Simulation results show that the proposed FDM-based method produces high SNR_{out} values at different SNR_{in} levels. The SNR_{out} increases with the increasing SNR_{in} . At lower SNR_{in} , the proposed FDM-based denoising method produces a high SNR_{out} . The performance of the proposed FDM-based denoising method for white Gaussian noise in terms of PRD_{out} is presented in Table 4.6 for various ECG signals of the MIT-BIH arrhythmia database.

In Table 4.6, the PRD values are computed for different values of input SNR (-10 dB, -5 dB, 0 dB, 5 dB, and 10 dB). As demonstrated in Table 4.6, the obtained values of PRD for white Gaussian noise are low. The performance of the proposed FDM-based denoising method for white Gaussian noise corrupted ECG signals is compared to two other methods: NLM (nonlocal means method) [67] and modified EMD method [191]. The comparison is made in terms of PRD_{out} at an SNR_{in} of 10 dB and shown in Fig. 4.7. The FDM-based proposed method provides the lowest PRD values compared to [67] and [191].

Table 4.5: Computed SNR_{out} , after removal of white Gaussian noise, at different SNR_{in}

| ECG signal | SNR_{out} at different values of SNR_{in} | | | | |
|------------|---|-------|------|------|-------|
| | -10 dB | -5 dB | 0 dB | 5 dB | 10 dB |
| 100 | 42.2 | 42.3 | 42.4 | 42.4 | 42.4 |
| 101 | 43.4 | 43.5 | 43.6 | 43.6 | 43.6 |
| 102 | 43.4 | 43.6 | 43.7 | 43.8 | 43.8 |
| 103 | 43.9 | 43.0 | 43.1 | 43.1 | 43.1 |
| 104 | 44.0 | 44.1 | 44.2 | 44.2 | 44.2 |
| 105 | 48.1 | 48.2 | 48.2 | 48.2 | 48.2 |
| 106 | 46.6 | 46.7 | 46.7 | 46.8 | 46.9 |
| 107 | 46.0 | 46.1 | 46.2 | 46.4 | 46.4 |
| 108 | 43.3 | 43.3 | 43.4 | 43.6 | 43.7 |
| 109 | 42.5 | 42.6 | 42.7 | 42.7 | 42.7 |
| 111 | 47.2 | 47.2 | 47.3 | 47.4 | 47.6 |
| 112 | 49.6 | 49.7 | 49.8 | 49.8 | 49.9 |
| 113 | 46.3 | 46.4 | 46.5 | 46.7 | 46.7 |
| 115 | 47.8 | 47.9 | 47.9 | 48.0 | 48.0 |
| 116 | 41.4 | 41.4 | 41.5 | 41.6 | 41.6 |
| 117 | 47.1 | 47.2 | 47.2 | 47.3 | 47.3 |
| 118 | 46.9 | 46.1 | 46.2 | 46.2 | 46.2 |
| 119 | 47.6 | 47.7 | 47.8 | 47.8 | 47.9 |
| 121 | 48.2 | 48.3 | 48.3 | 48.5 | 48.9 |
| 122 | 46.5 | 46.6 | 46.7 | 46.8 | 46.9 |
| 123 | 45.6 | 45.3 | 45.4 | 45.5 | 45.5 |
| 124 | 47.4 | 47.4 | 47.5 | 47.6 | 47.8 |
| 205 | 47.9 | 48.0 | 48.1 | 48.1 | 48.1 |
| 209 | 43.3 | 43.4 | 43.5 | 43.5 | 43.5 |
| 210 | 45.7 | 45.8 | 45.8 | 45.9 | 45.9 |
| 212 | 43.0 | 43.1 | 43.2 | 43.4 | 43.5 |
| 213 | 43.4 | 43.5 | 43.6 | 43.7 | 43.7 |
| 221 | 40.5 | 40.6 | 40.7 | 40.7 | 40.7 |
| 231 | 45.7 | 45.8 | 45.9 | 45.9 | 45.9 |
| 234 | 44.7 | 44.8 | 44.9 | 44.9 | 44.9 |

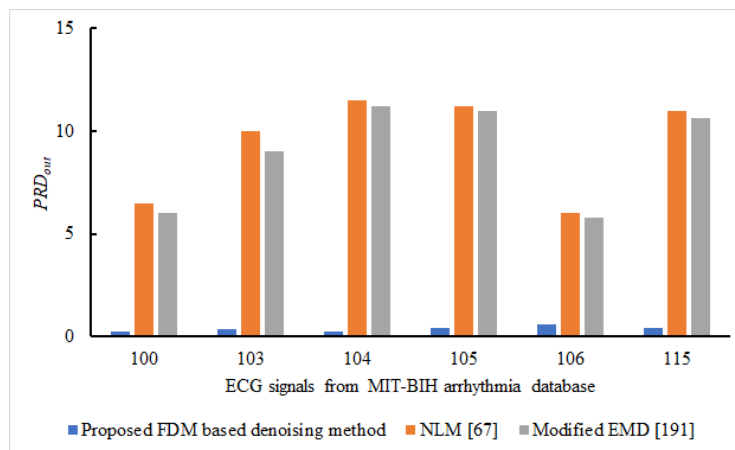


Fig. 4.7: Comparison of PRD_{out} with other existing methods in the case of white Gaussian noise corrupted ECG signals

Table 4.6: Computed PRD_{out} after removing white Gaussian noise at different SNR_{in}

| ECG signal | PRD_{out} at different values of SNR_{in} | | | | |
|------------|---|-------|-------|-------|-------|
| | -10 dB | -5 dB | 0 dB | 5 dB | 10 dB |
| 100 | 0.197 | 0.213 | 0.230 | 0.230 | 0.231 |
| 101 | 0.622 | 0.646 | 0.660 | 0.670 | 0.668 |
| 102 | 0.601 | 0.611 | 0.630 | 0.650 | 0.650 |
| 103 | 0.329 | 0.352 | 0.360 | 0.370 | 0.371 |
| 104 | 0.195 | 0.223 | 0.230 | 0.240 | 0.238 |
| 105 | 0.380 | 0.401 | 0.410 | 0.420 | 0.421 |
| 106 | 0.531 | 0.540 | 0.549 | 0.560 | 0.569 |
| 107 | 0.361 | 0.369 | 0.380 | 0.389 | 0.398 |
| 108 | 0.457 | 0.460 | 0.469 | 0.480 | 0.480 |
| 109 | 0.208 | 0.231 | 0.250 | 0.250 | 0.252 |
| 111 | 0.290 | 0.310 | 0.330 | 0.356 | 0.360 |
| 112 | 0.269 | 0.295 | 0.310 | 0.310 | 0.315 |
| 113 | 0.320 | 0.331 | 0.340 | 0.349 | 0.360 |
| 115 | 0.404 | 0.410 | 0.421 | 0.430 | 0.446 |
| 116 | 0.195 | 0.218 | 0.230 | 0.240 | 0.237 |
| 117 | 0.300 | 0.327 | 0.340 | 0.340 | 0.346 |
| 118 | 0.471 | 0.492 | 0.510 | 0.510 | 0.512 |
| 119 | 0.370 | 0.377 | 0.380 | 0.390 | 0.387 |
| 121 | 0.314 | 0.320 | 0.320 | 0.350 | 0.359 |
| 122 | 0.210 | 0.219 | 0.230 | 0.240 | 0.251 |
| 123 | 0.527 | 0.530 | 0.530 | 0.550 | 0.557 |
| 124 | 0.710 | 0.716 | 0.720 | 0.730 | 0.731 |
| 205 | 0.484 | 0.504 | 0.520 | 0.530 | 0.527 |
| 209 | 0.510 | 0.517 | 0.527 | 0.540 | 0.540 |
| 210 | 0.443 | 0.450 | 0.450 | 0.470 | 0.479 |
| 212 | 0.610 | 0.622 | 0.640 | 0.640 | 0.660 |
| 213 | 0.597 | 0.617 | 0.630 | 0.630 | 0.635 |
| 221 | 0.308 | 0.333 | 0.340 | 0.350 | 0.348 |
| 231 | 0.849 | 0.878 | 0.900 | 0.910 | 0.907 |
| 234 | 0.383 | 0.405 | 0.420 | 0.420 | 0.424 |

4.4.3 Simulation Results with Baseline Wander

Baseline wander is a common low-frequency noise with a high probability of occurrence in an ECG signal. BW is caused due to respiration and movement of the subject. The presence of BW in ECG signals makes the interpretation of ECG signals difficult. The proposed FDM-based denoising method removes the BW from the ECG signals. The values of SNR_{out} of the selected ECG signals at various SNR_{in} for BW are presented in Table 4.7. From Table 4.7, our

method provides better SNR_{out} at the different values of SNR_{in} . For ECG signal-101, the proposed FDM-based denoising method provides a SNR_{out} of 26.17 dB and 26.28 dB at an input SNR of -10 dB and -5 dB, respectively. This work is published in [178].

The efficacy of the proposed FDM-based denoising method for removing BW from the ECG signal is compared with the other existing techniques, including the EVD [80] and the EKF method [192] in Table 4.8.

The proposed FDM-based denoising method provides high SNR_{out} against the compared

Table 4.7: Computed SNR_{out} after removing BW by the proposed FDM-based denoising method at different SNR_{in}

| ECG signal | SNR_{out} at different values of SNR_{in} | | | | |
|------------|---|-------|------|------|-------|
| | -10 dB | -5 dB | 0 dB | 5 dB | 10 dB |
| 100 | 24.5 | 24.6 | 24.7 | 24.7 | 24.7 |
| 101 | 26.2 | 26.3 | 26.3 | 26.4 | 26.4 |
| 102 | 26.5 | 26.5 | 26.7 | 26.8 | 26.9 |
| 103 | 25.8 | 25.9 | 26.0 | 26.0 | 26.1 |
| 104 | 25.2 | 25.3 | 25.4 | 25.5 | 25.6 |
| 105 | 25.8 | 25.9 | 26.0 | 26.0 | 26.0 |
| 106 | 27.1 | 27.2 | 27.3 | 27.5 | 27.5 |
| 107 | 27.7 | 27.8 | 27.9 | 27.9 | 27.9 |
| 108 | 26.3 | 26.4 | 26.4 | 26.5 | 26.6 |
| 109 | 28.0 | 28.2 | 28.2 | 28.3 | 28.3 |
| 111 | 25.5 | 25.6 | 25.8 | 25.9 | 25.9 |
| 112 | 27.9 | 28.0 | 28.1 | 28.2 | 28.2 |
| 113 | 24.7 | 24.8 | 24.9 | 25.0 | 24.9 |
| 115 | 28.5 | 28.6 | 28.7 | 28.8 | 28.8 |
| 116 | 26.5 | 26.7 | 26.7 | 26.8 | 26.8 |
| 117 | 26.1 | 26.3 | 26.4 | 26.4 | 26.4 |
| 118 | 23.7 | 23.9 | 24.0 | 24.1 | 24.1 |
| 119 | 25.0 | 25.1 | 25.2 | 25.4 | 25.5 |
| 121 | 25.9 | 25.9 | 26.1 | 26.2 | 26.3 |
| 122 | 25.7 | 25.8 | 25.9 | 25.9 | 25.9 |
| 123 | 24.3 | 24.4 | 24.4 | 24.6 | 24.7 |
| 124 | 26.3 | 26.4 | 26.5 | 26.5 | 26.6 |
| 205 | 25.7 | 25.8 | 25.9 | 26.1 | 26.1 |
| 209 | 24.4 | 24.5 | 24.7 | 24.7 | 24.8 |
| 210 | 27.2 | 27.3 | 27.4 | 27.4 | 27.4 |
| 212 | 26.8 | 26.9 | 27.0 | 27.1 | 27.1 |
| 213 | 28.0 | 28.1 | 28.2 | 28.3 | 28.4 |
| 221 | 27.2 | 27.2 | 27.3 | 27.3 | 27.5 |
| 231 | 26.3 | 26.4 | 26.4 | 26.7 | 26.8 |

Table 4.8: Comparison SNR_{out} of the proposed FDM-based denoising method with EVD and EKF methods to remove BW

| ECG signal | SNR_{in} | Proposed FDM-based denoising method | EVD method [80] | EKF method [192] |
|------------|------------|-------------------------------------|-----------------|------------------|
| | | SNR_{out} | | |
| 100 | -10 dB | 24.5 | 8.4 | 3.9 |
| | -5 dB | 24.6 | 10.9 | 7.1 |
| | 0 dB | 24.7 | 12.6 | 10.2 |
| | 5 dB | 24.7 | 13.1 | 11.3 |
| 101 | -10 dB | 26.2 | 7.6 | 4.0 |
| | -5 dB | 26.3 | 9.8 | 6.8 |
| | 0 dB | 26.3 | 11.4 | 9.2 |
| | 5 dB | 26.4 | 11.8 | 10.6 |
| 103 | -10 dB | 25.8 | 6.7 | 6.0 |
| | -5 dB | 25.9 | 8.7 | 7.1 |
| | 0 dB | 26.0 | 10.9 | 8.2 |
| | 5 dB | 26.0 | 11.9 | 10.2 |
| 105 | -10 dB | 25.8 | 3.5 | 4.1 |
| | -5 dB | 25.9 | 5.7 | 6.3 |
| | 0 dB | 26.0 | 7.4 | 8.8 |
| | 5 dB | 26.0 | 9.1 | 9.9 |
| 109 | -10 dB | 28.0 | 3.4 | 4.1 |
| | -5 dB | 28.2 | 4.8 | 6.6 |
| | 0 dB | 28.2 | 6.5 | 8.3 |
| | 5 dB | 28.3 | 8.4 | 9.3 |
| 111 | -10 dB | 25.5 | 3.2 | 4.3 |
| | -5 dB | 25.6 | 4.1 | 6.9 |
| | 0 dB | 25.8 | 5.3 | 8.6 |
| | 5 dB | 25.9 | 7.5 | 9.9 |
| 112 | -10 dB | 27.9 | 4.9 | 3.4 |
| | -5 dB | 28.0 | 7.2 | 5.6 |
| | 0 dB | 28.1 | 9.3 | 7.2 |
| | 5 dB | 28.2 | 10.3 | 8.0 |
| 113 | -10 dB | 24.7 | 7.1 | 3.7 |
| | -5 dB | 24.8 | 8.6 | 6.0 |
| | 0 dB | 24.9 | 9.6 | 7.7 |
| | 5 dB | 25.0 | 9.6 | 8.5 |
| 115 | -10 dB | 28.5 | 10.1 | 7.6 |
| | -5 dB | 28.6 | 11.8 | 7.3 |
| | 0 dB | 28.7 | 13.6 | 8.2 |

| ECG signal | SNR_{in} | Proposed FDM-based denoising method | EVD method [80] | EKF method [192] |
|------------|------------|-------------------------------------|-----------------|------------------|
| | | SNR_{out} | | |
| 116 | 5 dB | 28.8 | 13.3 | 10.2 |
| | -10 dB | 26.5 | 4.2 | 4.0 |
| | -5 dB | 26.7 | 6.4 | 6.8 |
| | 0 dB | 26.7 | 8.7 | 9.2 |
| 117 | 5 dB | 26.8 | 10.2 | 10.6 |
| | -10 dB | 26.2 | 6.4 | 3.4 |
| | -5 dB | 26.3 | 7.9 | 5.4 |
| | 0 dB | 26.4 | 8.9 | 6.7 |
| 118 | 5 dB | 26.4 | 8.9 | 7.3 |
| | -10 dB | 23.7 | 3.1 | 3.4 |
| | -5 dB | 23.9 | 5.2 | 6.6 |
| | 0 dB | 24.0 | 7.7 | 9.2 |
| 122 | 5 dB | 24.1 | 9.3 | 10.8 |
| | -10 dB | 25.7 | 3.5 | 3.9 |
| | -5 dB | 25.8 | 5.7 | 6.7 |
| | 0 dB | 25.9 | 8.3 | 9.0 |
| 210 | 5 dB | 25.9 | 10.0 | 10.3 |
| | -10 dB | 27.2 | 4.2 | 4.0 |
| | -5 dB | 27.3 | 6.2 | 6.5 |
| | 0 dB | 27.4 | 8.7 | 8.3 |
| 212 | 5 dB | 27.4 | 9.8 | 9.3 |
| | -10 dB | 26.8 | 4.7 | 4.0 |
| | -5 dB | 26.9 | 7.0 | 6.9 |
| | 0 dB | 27.0 | 9.6 | 9.5 |
| | 5 dB | 27.1 | 10.8 | 10.6 |

methods. For ECG signal 111, the obtained SNR_{out} , at $SNR_{in} = -10$ dB, is better than the EVD [80] and EKF [192] methods by 22.32 dB and 21.22 dB, respectively. For other ECG signals compared in Table 4.8, the proposed FDM-based denoising method provides the best SNR_{out} . This work is published in [189].

In the case of BW, PRD_{out} for the selected ECG signal computed by the proposed FDM-based denoising method is given in Table 4.9. The proposed FDM-based denoising method provides low PRD values at different SNR_{in} . For ECG signal-115, the computed PRD_{out} are 0.121, 0.150, 0.171, 0.180, and 0.188 at -10 dB, -5 dB, 0 dB, 5 dB, and 10 dB SNR_{in} , respectively.

The performance of the proposed FDM-based denoising method is compared to the EVD

method [80] and EMD-WT method [190] in Table 4.10 in terms of PRD_{out} . The comparison is made for ECG signals from the MIT-BIH arrhythmia database at various values of SNR_{in} . From Table 4.10, the proposed FDM-based denoising method provides the lowest PRD_{out} compared to EVD [80] and EMD-WT methods [190]. For ECG signal-210, at -10 dB SNR_{in} , the computed PRD_{out} is 0.128, whereas EVD [80] and EMD-WT methods [190] provide a PRD_{out} of 2.431 and 1.776, respectively. Similarly, at 10 dB SNR_{in} , for ECG signal-210, the computed PRD_{out} 0.203 is least against 2.553 (EVD) and 1.861 (EMD-WT). This work is published in [189].

Table 4.9: Computed PRD_{out} by the proposed FDM-based denoising method when the ECG signals are corrupted with BW noise

| ECG signal | PRD_{out} at different values of SNR_{in} | | | | |
|------------|---|-------|-------|-------|-------|
| | -10 dB | -5 dB | 0 dB | 5 dB | 10 dB |
| 100 | 0.417 | 0.417 | 0.430 | 0.440 | 0.444 |
| 101 | 0.884 | 0.906 | 0.920 | 0.930 | 0.932 |
| 102 | 0.624 | 0.630 | 0.650 | 0.650 | 0.657 |
| 103 | 0.547 | 0.578 | 0.590 | 0.600 | 0.604 |
| 104 | 0.610 | 0.631 | 0.650 | 0.690 | 0.810 |
| 105 | 0.141 | 0.167 | 0.180 | 0.200 | 0.205 |
| 106 | 0.439 | 0.447 | 0.460 | 0.480 | 0.480 |
| 107 | 0.470 | 0.475 | 0.490 | 0.490 | 0.497 |
| 108 | 0.491 | 0.501 | 0.510 | 0.530 | 0.547 |
| 109 | 0.204 | 0.227 | 0.240 | 0.250 | 0.258 |
| 111 | 0.421 | 0.447 | 0.470 | 0.480 | 0.482 |
| 112 | 0.296 | 0.322 | 0.340 | 0.360 | 0.359 |
| 113 | 0.267 | 0.294 | 0.320 | 0.340 | 0.340 |
| 115 | 0.121 | 0.150 | 0.170 | 0.180 | 0.188 |
| 116 | 0.500 | 0.530 | 0.550 | 0.570 | 0.573 |
| 117 | 0.173 | 0.200 | 0.220 | 0.240 | 0.247 |
| 118 | 0.502 | 0.528 | 0.550 | 0.570 | 0.571 |
| 119 | 0.340 | 0.347 | 0.350 | 0.375 | 0.390 |
| 121 | 0.440 | 0.443 | 0.450 | 0.470 | 0.470 |
| 122 | 0.249 | 0.278 | 0.290 | 0.310 | 0.314 |
| 123 | 0.410 | 0.420 | 0.430 | 0.430 | 0.440 |
| 124 | 0.130 | 0.139 | 0.160 | 0.170 | 0.170 |
| 200 | 0.278 | 0.279 | 0.281 | 0.285 | 0.285 |
| 202 | 0.341 | 0.351 | 0.351 | 0.355 | 0.356 |
| 205 | 0.569 | 0.570 | 0.590 | 0.599 | 0.660 |
| 209 | 0.590 | 0.598 | 0.620 | 0.630 | 0.643 |
| 210 | 0.128 | 0.154 | 0.180 | 0.200 | 0.203 |
| 212 | 0.335 | 0.361 | 0.390 | 0.400 | 0.405 |

4.4.4 Simulation Results with Muscle Contraction, Motion Artifacts, And Electromyographic Noise

Noises such as muscle contraction, MA, and EMG distort an ECG signal. Their presence in the ECG signal severely affects the analysis and can produce erroneous results. The performance of the proposed FDM-based denoising method is studied in the presence of muscle contraction, MA, and EMG at different values of SNR_{in} . The computed values of SNR_{out} with muscle contraction, MA, and EMG noise corrupted realtime ECG signal at a different level of SNR_{in} are presented in Table 4.11. Table 4.11 shows that the proposed FDM-based denoising method provides appropriate SNR_{out} when an ECG signal is corrupted with muscle contraction, MA, or EMG noise.

Table 4.10: Comparison of the proposed FDM-based denoising method with EVD and EMD-WT methods in terms of PRD_{out} for ECG signals corrupted with BW

| ECG signal | SNR_{in} | Proposed FDM-based denoising method | EVD method [80] | EMD-WT method [190] |
|------------|------------|-------------------------------------|-----------------|---------------------|
| | | PRD_{out} | | |
| 118 | -10 dB | 0.502 | 2.365 | 3.165 |
| | -5 dB | 0.528 | 2.400 | 3.200 |
| | 0 dB | 0.550 | 2.439 | 3.229 |
| | 5 dB | 0.570 | 2.464 | 3.253 |
| | 10 dB | 0.571 | 2.477 | 3.271 |
| 122 | -10 dB | 0.249 | 2.610 | 3.488 |
| | -5 dB | 0.278 | 2.668 | 3.517 |
| | 0 dB | 0.290 | 2.697 | 3.539 |
| | 5 dB | 0.310 | 2.722 | 3.568 |
| | 10 dB | 0.314 | 2.741 | 3.581 |
| 210 | -10 dB | 0.128 | 2.431 | 1.776 |
| | -5 dB | 0.154 | 2.489 | 1.804 |
| | 0 dB | 0.180 | 2.513 | 1.828 |
| | 5 dB | 0.200 | 2.541 | 1.849 |
| | 10 dB | 0.203 | 2.553 | 1.861 |
| 212 | -10 dB | 0.335 | 3.007 | 2.611 |
| | -5 dB | 0.361 | 3.066 | 2.662 |
| | 0 dB | 0.390 | 3.093 | 2.687 |
| | 5 dB | 0.400 | 3.128 | 2.700 |
| | 10 dB | 0.405 | 3.150 | 2.732 |

From Table 4.11, it is clear that the proposed FDM-based denoising method effectively

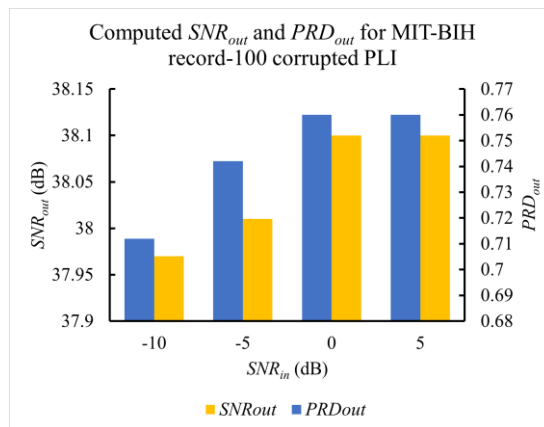
suppresses muscle contraction, MA, and EMG noise presented in realtime ECG signal and provides a SNR_{out} of 27.42 dB, 29.39 dB, and 27.94 dB, respectively.

Table 4.11: Computed SNR_{out} , after removing muscle contraction, motion artifacts, and electromyographic noise from an ECG signal acquired in realtime with different SNR_{in}

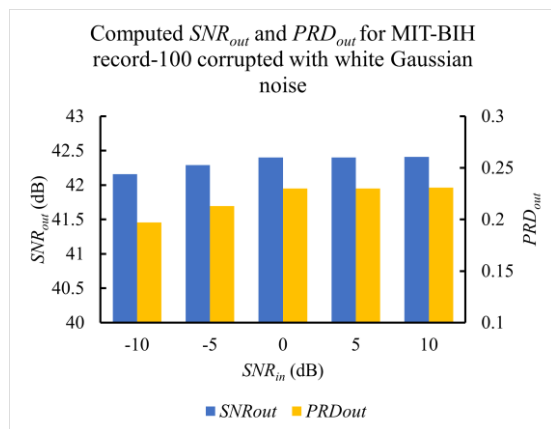
| Noise | SNR_{out} at different SNR_{in} | | | | |
|--------------------|-------------------------------------|-------|------|------|-------|
| | -10 dB | -5 dB | 0 dB | 5 dB | 10 dB |
| Muscle contraction | 27.42 | 27.58 | 27.7 | 27.7 | 27.72 |
| MA | 29.39 | 29.44 | 29.5 | 29.6 | 29.61 |
| EMG | 27.94 | 28.09 | 28.2 | 28.3 | 28.31 |

Table 4.12: Computed PRD_{out} , after removing muscle contraction, motion artifacts, and Electromyographic noise from an ECG signal acquired in realtime with different SNR_{in}

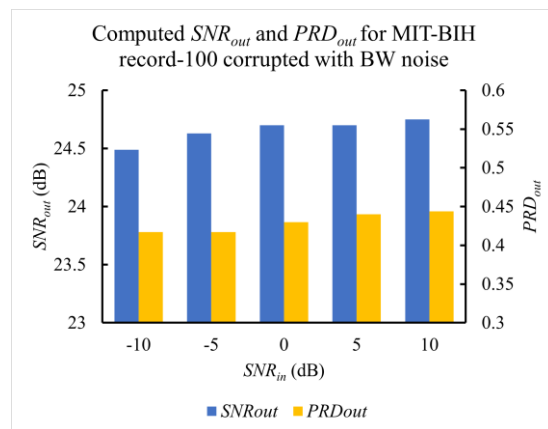
| Noise | PRD_{out} at different values of SNR_{in} | | | | |
|--------------------|---|-------|------|------|-------|
| | -10 dB | -5 dB | 0 dB | 5 dB | 10 dB |
| Muscle contraction | 0.758 | 0.79 | 0.8 | 0.81 | 0.815 |
| MA | 1.003 | 1.03 | 1.05 | 1.06 | 1.066 |
| EMG | 0.736 | 0.75 | 0.77 | 0.79 | 0.788 |



(a)



(b)



(c)

Fig. 4.8: SNR_{out} and PRD_{out} for ECG signal-100 in the presence of (a) PLI, (b) white Gaussian noise, (c) BW

PRD_{out} values obtained from the proposed FDM-based denoising method with muscle contraction, MA, and EMG noise are shown in Table 4.12. From Table 4.12, at -10 dB SNR_{in} , the proposed FDM-based denoising method provides low PRD_{out} of 0.758, 1.003, and 0.736 for muscle contraction, MA, and EMG, respectively.

The efficacy of the proposed FDM-based denoising method for PLI, white Gaussian noise, BW, muscle contraction, MA, and EMG noises are summarized in terms of average SNR_{out} and average PRD_{out} in Fig. 4.9 and Fig. 4.10, respectively. From Fig. 4.9 for white Gaussian noise, the proposed FDM-based method provides the best average SNR_{out} at every input signal-to-noise ratio value. The proposed FDM-based method provides a SNR_{out} greater than 25 dB when an ECG signal acquired in realtime is corrupted by muscle contraction, MA, and EMG. This work is published in [189].

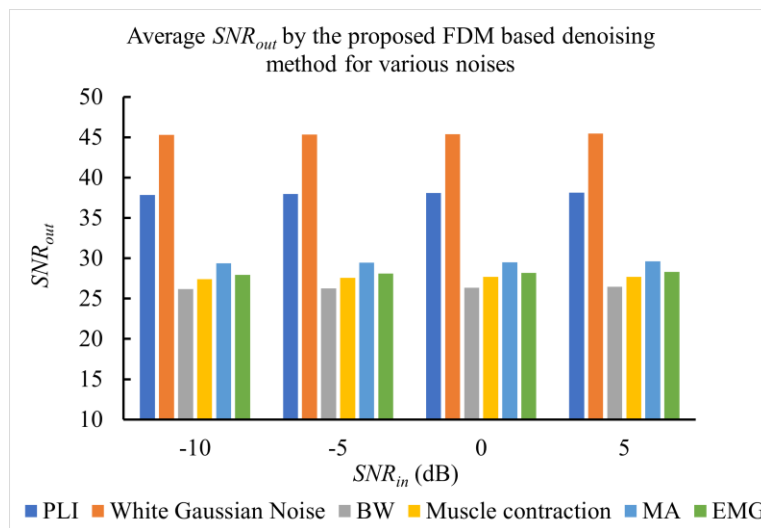


Fig. 4.9: Average SNR_{out} by the proposed FDM-based denoising method at different values of SNR_{in} in the presence of various noise

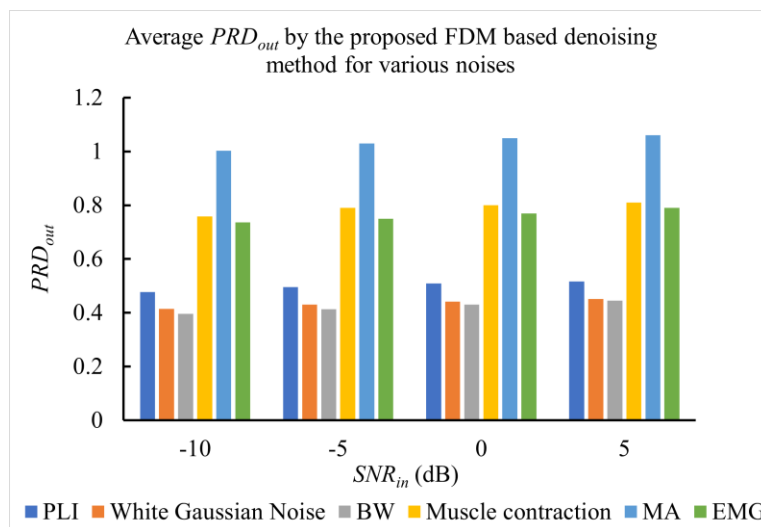


Fig. 4.10: Average PRD_{out} by the proposed FDM-based denoising method at different values of SNR_{in} in the presence of various noises

4.5. SUMMARY

The nonstationary nature and various noises in an ECG signal make the analysis difficult. The noise removal or denoising is an essential step in ECG signal analysis. Different techniques like filtering, adaptive filtering, EMD-WT, and EVD have been proposed to denoise a noise-contaminated ECG signal. Filtering the ECG signal can distort important medical information. These techniques do not achieve accurate noise reduction. Also, the In this chapter, an efficient denoising method using FDM is proposed to remove various noises from an ECG signal. The DCT-based FDM is used to denoise a noisy ECG signal. The proposed FDM-based denoising method improves SNR_{out} and PRD_{out} when the ECG signal is corrupted with PLI, white Gaussian noise, and BW. The proposed FDM-based denoising method removes noises significantly by preserving the clean ECG signal peaks. The simulation results show that the proposed FDM-based denoising method can be used as an effective preprocessing step in ECG signal analysis to detect CVDs. The proposed FDM-based denoising method is based on the DCT; hence its hardware implementation is also feasible. This work is summarized and published in [189].

CHAPTER 5

ECG SIGNAL ANALYSIS USING QRS COMPLEX DETECTION

In clinical practice, electrocardiogram (ECG) is a critical diagnostic tool to detect cardiovascular disease (CVD). An automatic ECG signal analysis system provides information on the cardiac health of a subject by counting and detecting the location of QRS complexes. Detection of QRS complexes provides valuable information to diagnose CVD and other heart abnormalities. This chapter uses a fractional Fourier transform (FrFT) algorithm, a time-frequency domain technique, to efficiently detect QRS complexes in an ECG signal. The FrFT rotates an ECG signal in the time-frequency plane to enhance a weakened QRS complex and improve the detection accuracy of a QRS complex.

5.1. DETECTION OF QRS COMPLEX

CVD is a type of illness that affects both the heart and blood vessels. CVD is a severe health problem for individuals that can lead to mortality. Early detection and treatment intervention can reduce the morbidity and mortality rate due to CVDs. Continuous monitoring and analysis of an ECG signal can better diagnose, control, and prevent CVDs. ECG is a non-invasive and universally adopted method to monitor and examine subjects with CVDs. ECG signal, the reflection of cardiac electrical activity, is a vital clinical diagnostic tool. ECG signal comprises various waves representing different electrical activities performed by heart tissues. These components have characteristic features (amplitude, duration, and shape), which are used to understand the behavior of the heart. Of these three signals, the QRS complex is the most informative and visually prominent segment in an ECG signal. Therefore, most of the automatic ECG signal analysis is based on detecting QRS complexes [193]. In automatic or computer-based ECG signal analysis, the shape and location of the QRS complex are studied to reflect on cardiac health.

Various researchers have proposed many algorithms to detect QRS complexes. Most of these algorithms are based on R peak detection. Detection of the QRS complex is difficult, especially in the case of abnormal ECG signals or noise-corrupted ECG signals. Various noises such as baseline wander (BW), power line interference (PLI), electromyographic (EMG), and motion artifacts (MA) dominate other noises present in an ECG signal. A noise-corrupted ECG signal, if not denoised, can provide wrong information about cardiac health [31].

The QRS complex detection comprises two stages: preprocessing and decision stage. In the

preprocessing or denoising stage, the QRS complexes are enhanced by minimizing the noises in an ECG signal. The occurrence of an R peak in the ECG signal is detected in the decision stage. A denoised ECG signal is used to mark the position of the R peak for QRS complex detection. In the literature, many R peak detection algorithms, such as the hidden Markov model, zero-crossing detection, and min-max difference algorithm [90, 123, 125, 150], are proposed by various authors. The QRS complex detection technique suggested by Pan-Tompkins [34] is prevalent and extensively used. The QRS complex detection in [34] involves linear filtering and nonlinear transformation. However, these algorithms process ECG signals in the time or frequency domain; hence, they cannot follow the time-varying morphology of an ECG signal [146]. Many other QRS complex detection algorithms based on the time-frequency domain are proposed to handle the nonstationary nature of ECG signals. Bajaj and Kumar [146] used fractional Stockwell transform and fractional Stockwell Shannon energy to detect the R peak in an ECG signal. In [121], FFT based R peak detection algorithm is proposed. The QRS complex detection technique based on empirical mode decomposition [194] also decomposes the signal into intrinsic mode functions.

This chapter uses FrFT, a time-frequency domain technique, to analyze an ECG signal. The ability to capture the nonstationary features of a signal makes FrFT an attractive choice for analyzing biomedical signals. The FrFT is a generalized version of FT with a parameter α representing the rotation of a signal in the time-frequency plane. The rotation of the axis does not alter the time and frequency content. Like FT, the FrFT decomposes the signal on an orthonormal chirp basis [195]. This work uses the virtues of FrFT to analyze ECG signals. The FrFT is used to detect the QRS complex by detecting the R-peak.

5.2. MATHEMATICAL DESCRIPTION OF FRACTIONAL FOURIER TRANSFORM

A brief mathematical description of FrFT is presented in this section. The FrFT is broadly classified into continuous FrFT and discrete FrFT, which are discussed here.

5.2.1 Continuous Fractional Fourier Transform

The FrFT generalizes the FT by revealing the mixed time-frequency contents of a signal [196]. In FT, a signal $s(t)$ along the time axis is converted into $S(\omega)$ along the frequency axis, which can be thought of as a rotation by $\pi/2$ radians from time domain representation to frequency domain representation [197]. By generalizing the rotation angle, the FrFT can represent a signal into intermediate domains between the time and frequency domains. Fig. 5.1 shows the α^{th} order FrFT of a signal that corresponds to a rotation by an angle $\Theta = \alpha\pi/2$ radian in the time-

frequency plane.

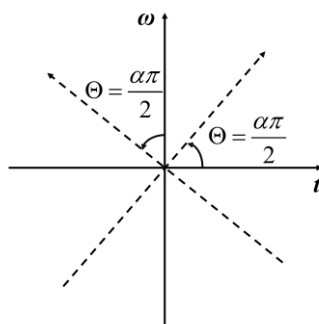


Fig. 5.1: Rotation of axis in FrFT

Mathematically, the FrFT of a signal $s(t)$ is expressed using Eq. (5.1).

$$S_{\Theta}(u) = \int_{-\infty}^{+\infty} s(t)K_{\Theta}(t,u)dt \quad (5.1)$$

Here, $S_{\Theta}(u)$ is α^{th} order FrFT of $s(t)$. $K_{\Theta}(t, u)$ is known as the kernel of FrFT and is defined by Eq. (5.2) [198, 199].

$$K_{\Theta}(t,u) = \begin{cases} \sqrt{\frac{1-j \cot \Theta}{2\pi}} e^{j\left(\frac{t^2+u^2}{2} \cot \Theta - ut \csc \Theta\right)} & \text{if } \Theta \neq n\pi \\ \delta(t-u) & \text{if } \Theta = 2n\pi \\ \delta(t+u) & \text{if } \Theta = (2n+1)\pi \end{cases} \quad (5.2)$$

The FrFT kernel represents a set of orthonormal complex exponential functions whose instantaneous frequency linearly varies with α . These functions are known as chirps. The kernel $K_{\Theta}(t, u)$ satisfies the following properties described in Eq. (5.3) through Eq. (5.6).

$$K_{\Theta}^*(t,u) = K_{-\Theta}(t,u) \quad (5.3)$$

$$\int_{-\infty}^{\infty} K_{\Theta_1}(t,u)K_{\Theta_2}(t,w)du = K_{\Theta_1+\Theta_2}(t,w) \quad (5.4)$$

$$\int_{-\infty}^{\infty} K_{\Theta}(u,t).K_{\Theta}^*(t,u')dt = \delta(u-u') \quad (5.5)$$

$$s(t) = \int_{-\infty}^{\infty} K_{\Theta}(u).K_{\Theta}^*(t,u)du \quad (5.6)$$

The numerical calculation of FrFT involves the following steps:

- (i) multiplication by a chirp
- (ii) Computation of Fourier transform with argument scaled by $csc\alpha$
- (iii) an additional multiplication by a chirp

(iv) The last step is multiplication by complex amplitude.

The choice of α , fractional order, offers a degree of freedom, making the FrFT more flexible than the conventional Fourier transform. The FrFT satisfies the linearity and additive properties. For $\alpha = 1$, FrFT is a conventional Fourier transform, and $\alpha = 0$ means no transform. FrFT with an angle $-\Theta$ is the inverse FrFT with an angle Θ and is expressed using Eq. (5.7).

$$s(t) = \int_{-\infty}^{\infty} S_{\Theta}(u)K_{-\Theta}(u,t)du \quad (5.7)$$

5.2.2 Discrete Fractional Fourier Transform

The discrete fractional Fourier transform of a signal $x[n]$ is defined using Eq. (5.8).

$$F_{\alpha}[m,n] = \sum_{k=0, k \neq (N-1+N \bmod 2)}^N \psi_k[m] \exp\left(-j\frac{\pi}{2}k\alpha\right) \psi_k[n] \quad (5.8)$$

Here, $\psi_k[n]$ is the k^{th} order discrete Hermite-Gaussian function, and N is the number of samples of the signal to be transformed. $\exp\left(-j\frac{\pi}{2}k\right)$ is the α^{th} power of the eigenvalue $\lambda_k = \exp\left(-j\frac{\pi}{2}k\right)$ of the FT. The defining difference equation of the Hermite-Gaussian function is given by Eq. (5.9) [200].

$$x[n+1] - 2x[n] + x[n-1] + 2\left(\cos\left(\frac{2\pi}{N}n\right) - 1\right)x[n] = \lambda x[n] \quad (5.9)$$

The coefficients of Eq. (5.9) are periodic with a period N (number of samples). Considering Eq. (5.9) over a single period ($0 \leq n \leq N-1$) and using the periodic property ($x[n+1] = x[n]$), Eq. (5.9) is expressed as in (5.10).

$$\begin{bmatrix} -2 & 1 & 1 & \cdot & \cdot & \cdot & 1 \\ 1 & 2\cos\left(\frac{2\pi}{N}\right) - 4 & \cdot & \cdot & \cdot & \cdot & 0 \\ 1 & \cdot & \cdot & \cdot & \cdot & \cdot & \cdot \\ \cdot & \cdot & \cdot & \cdot & \cdot & \cdot & \cdot \\ 1 & 0 & \cdot & \cdot & 2\cos\left[\left(\frac{2\pi \times (N-1)}{N}\right)\right] - 4 & \cdot & \cdot \end{bmatrix} \begin{bmatrix} x[0] \\ x[1] \\ \cdot \\ \cdot \\ \cdot \\ x[N-1] \end{bmatrix} = \lambda \begin{bmatrix} x[0] \\ x[1] \\ \cdot \\ \cdot \\ \cdot \\ x[N-1] \end{bmatrix} \quad (5.10)$$

or,

$$[S][x(n)] = \lambda[x(n)] \quad (5.11)$$

The left-most matrix in Eq. (5.10) is denoted as the \mathbf{S} matrix. The matrix \mathbf{S} and DFT matrix of the signal commute. The common eigenvector set of the \mathbf{S} and DFT matrix follows the property of uniqueness and orthogonality. This unique and orthogonal eigenvector set represents the discrete Hermite-Gaussian function $\psi_k[n]$. DFT matrix has all its eigenvectors which are either

even or odd. Therefore, the common eigenvector of the DFT and \mathbf{S} matrices must consist of both even and odd vectors. A matrix \mathbf{P} searches the common eigenvector with even and odd spaces. The matrix \mathbf{P} decomposes $x[n]$ into even and odd components. The eigenvector of \mathbf{S} is even/odd extension of eigenvector of \mathbf{PSP}^{-1} . The similarity transform \mathbf{PSP}^{-1} has the form given by Eq.(5.12).

$$PSP^{-1} = PSP = \begin{bmatrix} E & 0 \\ 0 & O \end{bmatrix} \quad (5.12)$$

The set of common eigenvectors of the DFT and \mathbf{S} matrix can be obtained from the \mathbf{E} and \mathbf{O} matrix eigenvectors. The even eigenvector of \mathbf{S} can be found as $P[ev_k^T : 0 \dots\dots\dots 0]^T$, where ev_k is the eigenvector of \mathbf{E} with k zero crossings ($0 \leq k \leq [N/2]$). Similarly, $P[0 \dots\dots\dots 0 : od_k^T]^T$ represents the odd eigenvector of \mathbf{S} . Here, od_k is the eigenvector of \mathbf{O} with $(2k + 1)$ zero-crossings. Finally, $\psi_k[n]$, the k^{th} order Hermite-Gaussian function can be obtained by finding the eigenvector of \mathbf{S} with k zero crossings.

5.3. FRACTIONAL FOURIER TRANSFORM-BASED ALGORITHM TO DETECT QRS COMPLEX

This work detects QRS complexes by identifying the R peak in the ECG signal. The R peak is detected with the help of a BPF and discrete FrFT. The flow chart of the proposed FrFT-based algorithm is shown in Fig. 5.2. A standard ECG signal $x_r[n]$ is taken as the input signal. While recording the ECG signal, some noises like PLI, MA, BW, and EMG get added to the ECG signal. In the proposed FrFT-based method, the noisy ECG signal $x_e[n]$ is obtained by adding two frequently occurring noises, the MA signal $x_m[n]$ and PLI signal $x_p[n]$, to the input ECG signal $x_r[n]$ as given in Eq. (5.13).

$$x_e[n] = x_r[n] + x_p[n] + x_m[n] \quad (5.13)$$

In the presence of noises, extracting accurate information on the P wave, QRS complex, and T wave from the ECG signal is challenging. Therefore, removing noises from the ECG signal is essential for accurately detecting the R peak. A BPF used in [34] with a frequency range of 5-15 Hz is used to improve the signal-to-noise ratio of the noisy ECG signal. The transfer function of an M^{th} order BPF is given in Eq. (5.14).

$$H_b(z) = \frac{\sum_{j=0}^M a_j z^{-j}}{\sum_{j=0}^M b_j z^{-j}} \quad (5.14)$$

Here, $j = 0, 1, 2, \dots, M$, and M is the order of the BPF. In the proposed method, a_j and b_j are the filter coefficients, and $M = 3$ provides low computation complexity.

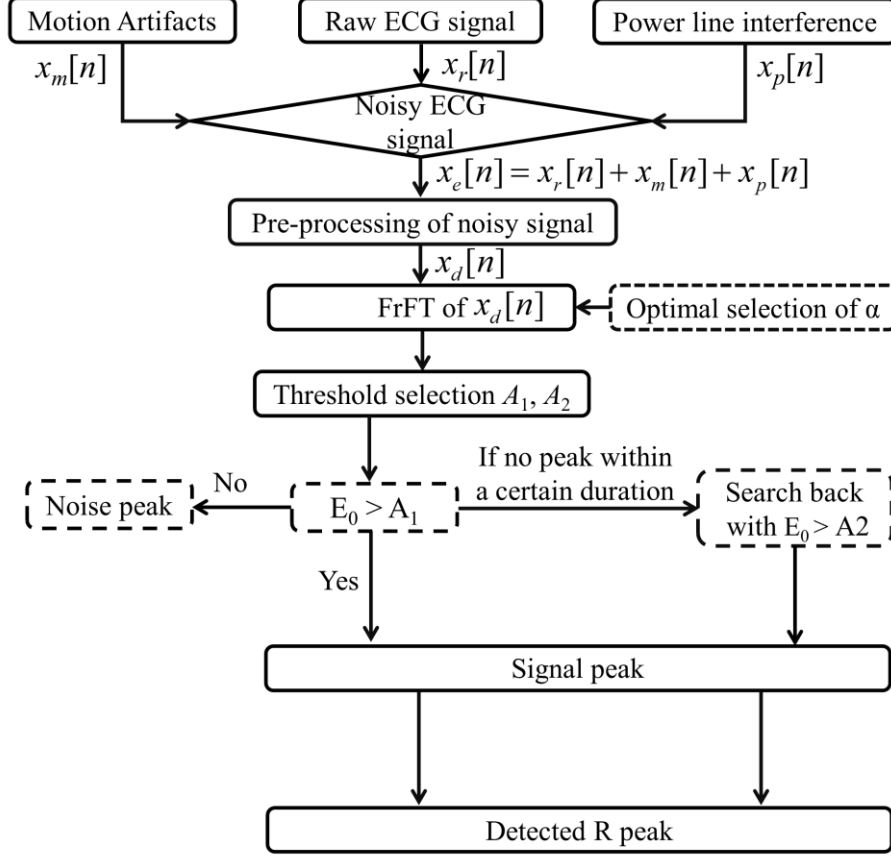


Fig. 5.2. Flow chart of the proposed FrFT-based peak detection method

BPF improves the signal-to-noise ratio by minimizing noise and providing a preprocessed signal $x_d[n]$. The preprocessed signal $x_d[n]$ is given by Eq. (5.15).

$$x_d[n] = x_e[n] * h_b[n] \quad (5.15)$$

Here, $*$ represents the convolution operation, and $h_b[n]$ is the impulse response of the BPF. After denoising, the rotation property of FrFT is used to detect the R peak. The discrete FrFT of the denoised signal is given by Eq. (5.16).

$$F_\alpha[m, n] = \sum_{k=0, k \neq (N-1+N \bmod 2)}^N \psi_k[m] \exp\left(-j \frac{\pi}{2} k \alpha\right) \psi_k[n] \quad (5.16)$$

Here, N represents the number of samples. $\Psi_k[n]$ is the k^{th} discrete Hermite-Gaussian function. The Hermite-Gaussians functions are the eigenvectors of the DFT. Further, the rotated signal is applied to the thresholding operation to detect the R peak. Two adaptive threshold levels A_1 and A_2 , are used to detect the R peak.

$$A_1 = N_p + 0.25(E_p - N_p) \quad (5.17)$$

$$A_2 = 0.5A_1 \quad (5.18)$$

Here, N_p is the estimated noise peak, and E_p is the estimated signal peak. The higher threshold

A_1 is used to analyze the signal out of these two thresholds. When the signal peak E_0 is less than A_1 , no R peak is noticed within a specific time duration. Then a search back method with a lower threshold A_2 is used. The two-level threshold detection minimizes the probability of missed R peak.

The main steps of the proposed algorithm for R peak detection are as follows:

Step 1: Preprocessing

ECG signals are corrupted with various types of noises. PLI and MA are the most common noises in the ECG signal. The presence of noises in an ECG signal creates ambiguity regarding cardiac health. Therefore, removing these noises is a vital step before further processing. The proposed algorithm generates a noisy ECG signal $x_e[n]$, consisting of PLI and MA. The preprocessing is performed with a BPF with cut-off frequencies 5-15Hz. BPF makes the algorithms fast, simple, and physically implementable in an embedded system.

Step 2: FrFT of a denoised ECG signal

The FrFT rotates the signal by an angle $\Theta = \alpha\pi/2$ in the joint time-frequency plane and is used for R peak detection. The preprocessed ECG signal $x_d[n]$ is applied to discrete FrFT. The **S** and **P** matrices are computed to obtain the discrete FrFT of the signal.

Step 3: Selection of threshold

Most of the QRS complex detection algorithms are based on R peak detection. This algorithm selects the threshold based on the adaptive thresholding defined in Eq. (5.17) and Eq. (5.18).

Step 4: Search-back algorithm

The search-back algorithm allows the re-evaluation of the previously rejected QRS peak when a sufficient time is passed without detecting an R peak. Therefore, a new lower threshold, 0.5 times the older threshold, is set to detect the missed R peak.

Step 5: Detection of R-peak

Finally, locating an R peak indicates the presence of the QRS complex.

5.4. PERFORMANCE EVALUATION AND RESULTS

The proposed work is implemented in MATLAB R2020b. The system uses an Intel® Core™ i3-4030U CPU @ 1.90GHz processor with 12 GB RAM. The operating system is Microsoft® Windows 10. The performance of the proposed FrFT-based method is validated using the MIT-BIH arrhythmia database and MIT-BIH noise stress test database, available at PhysioNet [55]. The performance of the proposed FrFT-based QRS complex detection method is evaluated using sensitivity (Se) (3.7), positive predictivity (+P) (3.9), detection error rate (Er) (3.12), F-score (Fs) (3.14), and QRS detection rate (QDR) (3.13).

5.4.1 Qualitative Analysis of the FrFT-based QRS Complex Detection Method

The qualitative analysis of the proposed FrFT-based QRS complex detection method is represented in Fig. 5.3. Fig. 5.3 illustrates the qualitative assessment of the proposed method for detecting QRS complexes using FrFT. Initially, a noisy input signal is created by introducing PLI and MA to standard MIT-BIH arrhythmia ECG signals. The raw ECG signal from the MIT-BIH dataset (record-207) is depicted in Fig. 5.3(a). The addition of PLI and MA generates a noise-corrupted ECG signal, as shown in Fig. 5.3(b). To mitigate the noise, a BPF with a passband of 5-15 Hz is employed. The selection of this frequency range in ECG signal analysis, along with the filter's efficiency in faster processing, makes BPF an advantageous preprocessing step. Subsequently, the preprocessed signal undergoes Discrete FrFT, transforming it into a time-frequency plane. Fig. 5.3(c) displays the Discrete FrFT version of the preprocessed signal. Finally, an adaptive thresholding scheme is employed to identify the QRS complexes. Fig. 5.3(d) showcases the detected QRS complexes for the selected MIT-BIH ECG signal (record-207), with arrows indicating their locations. The detected QRS complexes for MIT-BIH record-118 and record-223 are illustrated in Fig. 5.3(e) and Fig. 5.3(f), respectively.

5.4.2 Quantitative Analysis of the FrFT-Based QRS Complex Detection Method

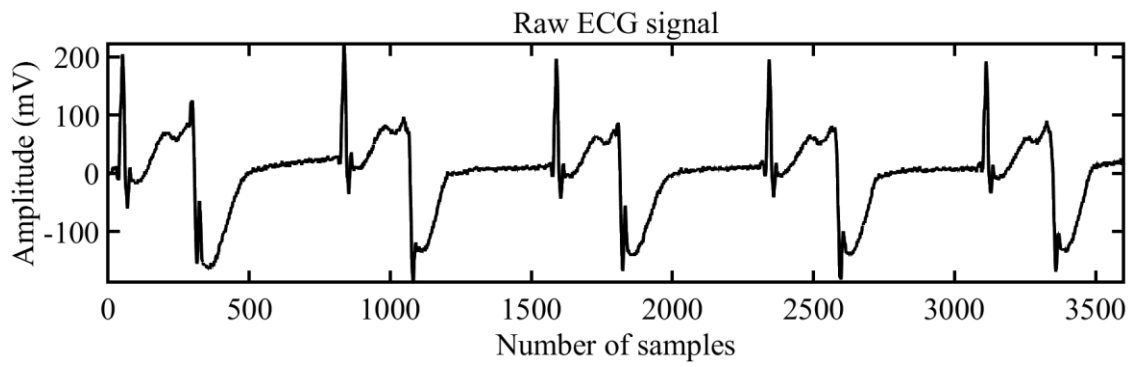
In the proposed FrFT-based QRS complex detection method, the value of α plays a vital role in detecting the QRS complex. The effect α on the detection of the QRS complex is illustrated in Fig. 5.4. The variation in the number of detected QRS complexes with different values of α for ECG signal-222 from the MIT-BIH database is demonstrated in Fig. 5.4.

From Fig. 5.4, the value of α directly influences the efficacy of the proposed method. For $\alpha = 0.5$, the proposed FrFT-based QRS complex detection method appropriately detects the QRS complexes.

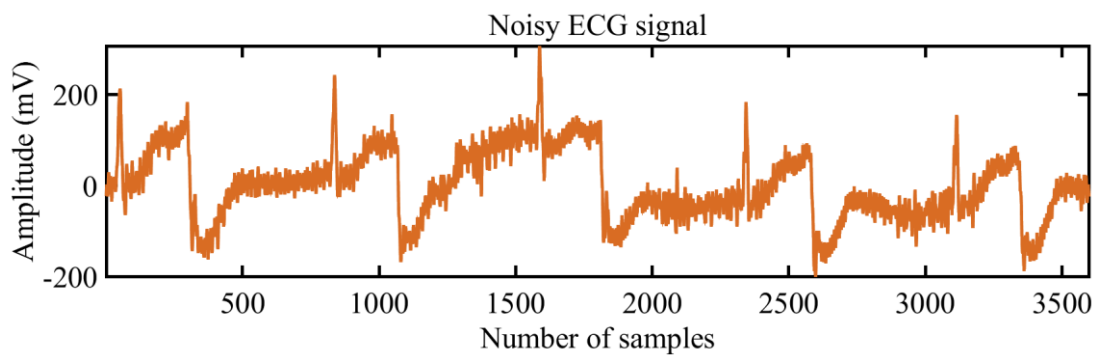
For experimental purposes, a *ten*-second ECG signal is selected. The detection results of ECG signal-222 from the MIT-BIH database for different values of α are tabulated in Table 5.1. From Table 5.1, when the value of α lies about the middle of the time and frequency axis, meaning $\alpha = 0.5$. The proposed method provides the best results.

To evaluate the performance of the proposed FrFT-based QRS complex detection method value of $\alpha = 0.5$ is selected in this work. ECG signals from the MIT- BIH arrhythmia database validate the proposed method. The simulation results for these ECG signals from the MIT-BIH arrhythmia database are tabulated in Table 5.2. The proposed method provides a sensitivity of 99.83% with a detection error rate of 0.01%. The F-score obtained by the proposed FrFT-based

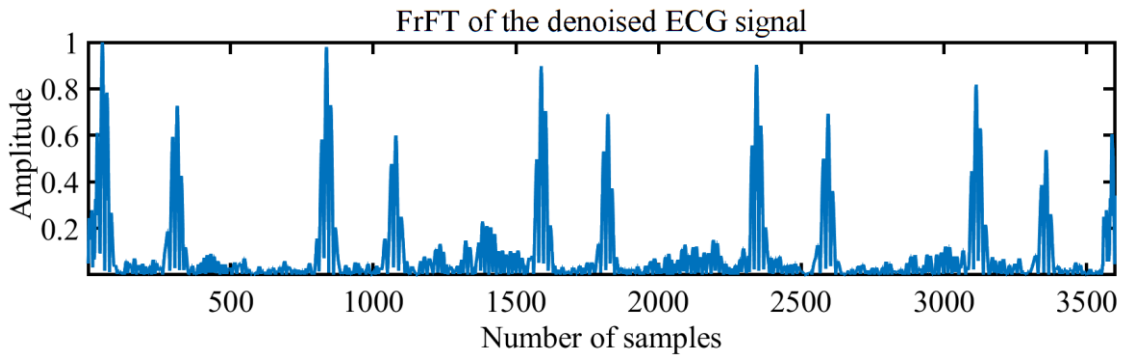
QRS complex detection method is 0.9952. The detection error rate provided by the proposed



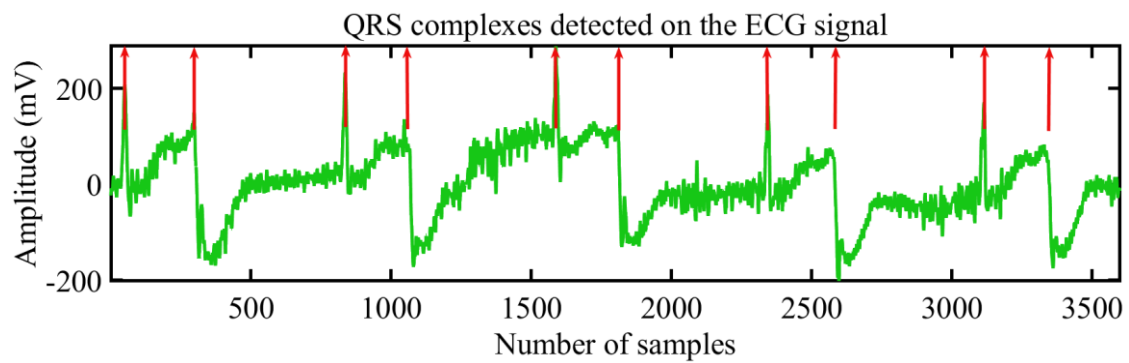
(a)



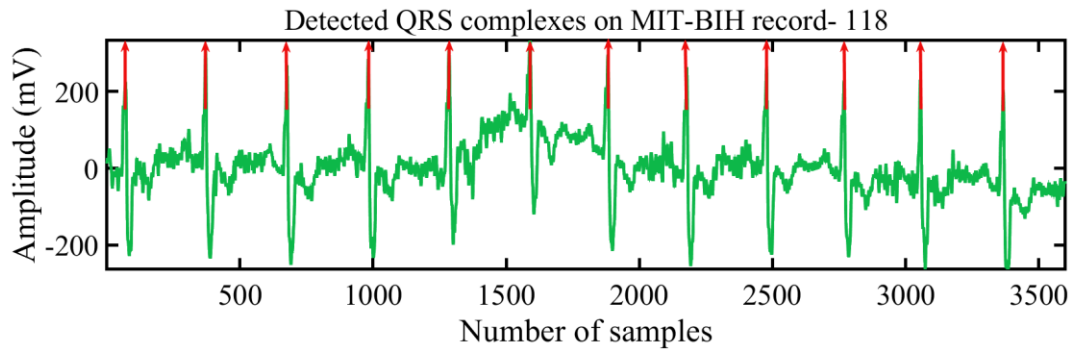
(b)



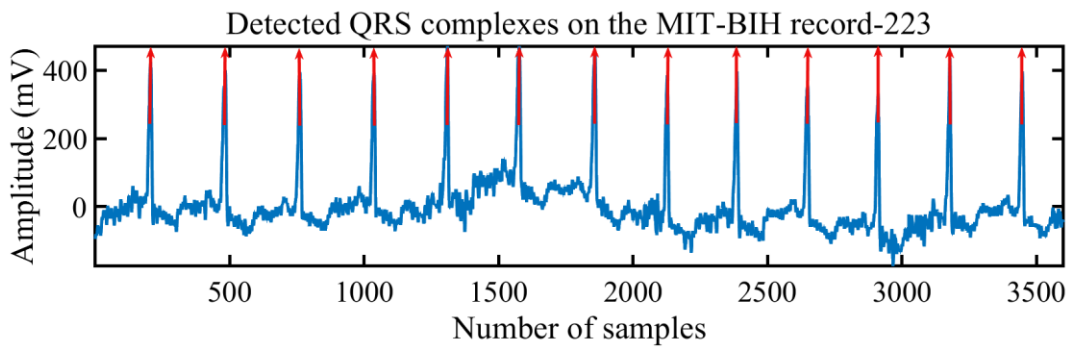
(c)



(d)



(e)



(f)

Fig. 5.3: (a) The raw ECG signal (MIT-BIH record-207) (b) noisy ECG signal (c) fractional Fourier transformed ECG signal (d) detected QRS complexes (represented by an arrow) on the record-207 (e) detected QRS complexes on the record-118 (f) detected QRS complexes

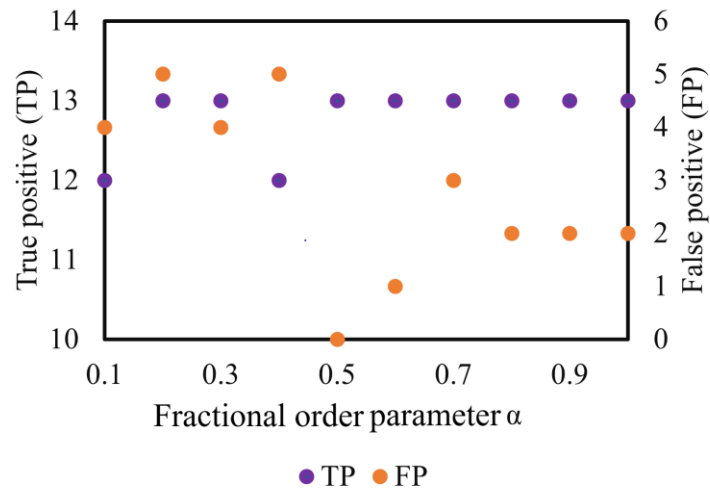


Fig. 5.4: Variation of TP and FP with α for record-222, record-222 contains 13 TP peaks

FrFT-based QRS complex detection method is the lowest as compared to other existing techniques such as filtering [34], a digital differentiator-based technique [120], particle swarm optimization [124], the max-min difference [125], MaMeMi filter [129], a forward prediction-based technique [142], fractional Stockwell transform and Shannon energy [146], multiscale

mathematical morphology [201], quadratic filter [202], and optimized knowledge-based method [203]. ECG signals 104, 113, 116, 205, and 208 have a detection error rate of less than 0.3%, while the rest of the records have a 0% detection error rate. *Forty-two* records are correctly detected, providing 100% sensitivity, 100% positive predictivity, and 0% detection error rate. The proposed FrFT-based QRS complex detection method is compared with the existing methods in Table 5.3.

Table 5.1: Effect of α on the detection of QRS complexes in ECG signal-222 from MIT-BIH arrhythmia database

| α | TP | FP | Sample number of FP | FN | Sample number of FN |
|------------|----|----|------------------------------|----|---------------------|
| 0.1 | 12 | 4 | 1383, 2887, 3094, 3475 | 1 | 3520 |
| 0.2 | 13 | 5 | 1523, 1731, 2020, 2206, 2602 | 0 | - |
| 0.3 | 13 | 4 | 1383, 2206, 2409, 3094 | 0 | - |
| 0.4 | 12 | 5 | 1438, 2206, 2891, 3007, 3475 | 1 | 2939 |
| 0.5 | 13 | 0 | - | 0 | - |
| 0.6 | 13 | 1 | 3475 | 0 | - |
| 0.7 | 13 | 3 | 1383, 2284, 3475 | 0 | - |
| 0.8 | 13 | 2 | 1383, 2284 | 0 | - |
| 0.9 | 13 | 2 | 1383 2284 | 0 | - |
| 1.0 | 13 | 2 | 1383, 2284 | 0 | - |

Table 5.2: The performance evaluation parameters for the FrFT-based QRS detection algorithm evaluated on the MIT-BIH database

| ECG signal | Se | +P | Er | Fs | QDR |
|------------|------|------|------|--------|-------|
| 100 | 100 | 100 | 0 | 1 | 100 |
| 101 | 100 | 100 | 0 | 1 | 100 |
| 102 | 100 | 100 | 0 | 1 | 100 |
| 103 | 100 | 100 | 0 | 1 | 100 |
| 104 | 92.3 | 92.3 | 0.23 | 0.923 | 92.3 |
| 105 | 100 | 100 | 0 | 1 | 100 |
| 106 | 100 | 100 | 0 | 1 | 100 |
| 107 | 100 | 100 | 0 | 1 | 100 |
| 109 | 100 | 100 | 0 | 1 | 100 |
| 111 | 100 | 100 | 0 | 1 | 100 |
| 112 | 100 | 100 | 0 | 1 | 100 |
| 113 | 100 | 90.9 | 0.1 | 0.9523 | 90.9 |
| 114 | 100 | 100 | 0 | 1 | 100 |
| 115 | 100 | 100 | 0 | 1 | 100 |
| 116 | 100 | 92.8 | 0.07 | 0.9627 | 92.8 |
| 117 | 100 | 100 | 0 | 1 | 100 |
| 118 | 100 | 100 | 0 | 1 | 100 |
| 119 | 100 | 100 | 0 | 1 | 100 |

| ECG signal | <i>Se</i> | +P | <i>Er</i> | <i>Fs</i> | <i>QDR</i> |
|-------------------|------------------|-----------|------------------|------------------|-------------------|
| 121 | 100 | 100 | 0 | 1 | 100 |
| 122 | 100 | 100 | 0 | 1 | 100 |
| 123 | 100 | 100 | 0 | 1 | 100 |
| 124 | 100 | 100 | 0 | 1 | 100 |
| 200 | 100 | 100 | 0 | 1 | 100 |
| 201 | 100 | 100 | 0 | 1 | 100 |
| 202 | 100 | 100 | 0 | 1 | 100 |
| 203 | 100 | 100 | 0 | 1 | 100 |
| 205 | 100 | 93.7 | 0.06 | 0.9675 | 93.7 |
| 207 | 100 | 100 | 0 | 1 | 100 |
| 208 | 100 | 94.1 | 0.06 | 0.9696 | 94.1 |
| 209 | 100 | 100 | 0 | 1 | 100 |
| 210 | 100 | 100 | 0 | 1 | 100 |
| 212 | 100 | 100 | 0 | 1 | 100 |
| 213 | 100 | 100 | 0 | 1 | 100 |
| 214 | 100 | 100 | 0 | 1 | 100 |
| 215 | 100 | 100 | 0 | 1 | 100 |
| 217 | 100 | 100 | 0 | 1 | 100 |
| 219 | 100 | 100 | 0 | 1 | 100 |
| 220 | 100 | 100 | 0 | 1 | 100 |
| 221 | 100 | 100 | 0 | 1 | 100 |
| 222 | 100 | 100 | 0 | 1 | 100 |
| 223 | 100 | 100 | 0 | 1 | 100 |
| 228 | 100 | 100 | 0 | 1 | 100 |
| 230 | 100 | 100 | 0 | 1 | 100 |
| 231 | 100 | 100 | 0 | 1 | 100 |
| 232 | 100 | 100 | 0 | 1 | 100 |
| 233 | 100 | 100 | 0 | 1 | 100 |
| 234 | 100 | 100 | 0 | 1 | 100 |

Sensitivity, positive predictivity, and detection error rate compare the work with other existing methods. The proposed FrFT-based QRS complex detection method outperforms in terms of sensitivity and detection error rate against particle swarm optimization [124], the max-min difference [125], a forward prediction-based technique [142], and multiscale mathematical morphology [201] techniques. Nearly all the true peaks in the ECG records are accurately detected. The proposed FrFT-based QRS complex detection method correctly detects 99.83% of the total beats. The proposed FrFT-based QRS complex detection method provides a positive predictivity of 99.22% with MIT-BIH records. From Table 5.2, it is evident that the proposed

FrFT-based QRS complex detection method approximately detects all the QRS complexes. The rotation property of the FrFT helps detect QRS complexes by enhancing those R peaks whose amplitude is attenuated due to noises.

Table 5.3: Performance comparison of the proposed FrFT-based QRS complex detection method with other existing methods using the MIT-BIH arrhythmia database

| Algorithms | <i>Se</i> | <i>+P</i> | <i>Er</i> |
|---|------------------|------------------|------------------|
| Pan et al. [34] | 99.76 | 99.56 | 0.68 |
| Nayak et al. [120] | 99.92 | 99.92 | 0.15 |
| Jain et al. [124] | 99.75 | 99.83 | 0.41 |
| Pandit et al. [125] | 99.65 | 99.66 | 0.69 |
| Castells et al. [129] | 99.41 | 99.63 | 0.88 |
| Deepu et al. [142] | 99.64 | 99.81 | 0.54 |
| Bajaj and Kumar [146] | 99.99 | 99.97 | 0.03 |
| Zhang and Lian [201] | 99.81 | 99.8 | 0.38 |
| Phukpattaranont [202] | 99.82 | 99.81 | 0.38 |
| Elgendi [203] | 99.78 | 99.87 | NR |
| Proposed FrFT-based QRS complex detection method (without noise) | 99.83 | 99.48 | 0.008 |
| Proposed FrFT-based QRS complex detection method (with noise) | 99.83 | 99.03 | 0.01 |

NR*-Not Reported

5.5. SUMMARY

FT is an attractive choice to analyze stationary signals but has limitations while analyzing nonstationary signals. FrFT, a generalized version of FT, a time-frequency domain technique, helps analyze signals with varying temporal morphology. The higher flexibility of FrFT compared to FT makes it a suitable choice for analyzing biomedical signals. In this chapter, the QRS complex detection in ECG signal is performed with the help of FrFT. The FrFT aids in detecting QRS complexes by rotating the signal in the time-frequency plane. The combination of BPF and FrFT allows its hardware implementation using embedded systems. The proposed FrFT-based QRS complex detection method results show that the algorithm appropriately detects QRS complexes in the presence of MA and PLI noise. The value of the fractional-order parameter of an FrFT plays a crucial role in detecting QRS complexes. $\alpha = 0.5$ is the optimum value because the rotation of the signal lies in the middle of the time and frequency plane and balances the emphasis on low and high frequencies in the ECG signal. The qualitative results show that the proposed method can detect the QRS complexes from a noisy ECG signal.

CHAPTER 6

CLASSIFICATION OF CARDIAC ARRHYTHMIA

Cardiac arrhythmia, characterized by irregular heartbeats, results in a critical health condition if not diagnosed and treated early. A cardiac arrhythmia occurs when the electrical impulses in the heart that coordinate the heartbeats are improper or irregular. Such faulty signaling results heart to beat too slow (bradycardia), fast (tachycardia), or irregularly. Cardiac arrhythmia includes atrial fibrillation, atrial flutter, ventricular fibrillation, supraventricular tachycardia, and ventricular tachycardia. Atrial fibrillation and ventricular fibrillation are the two most common cardiac arrhythmia. These cardiac arrhythmias cause heart strokes and other heart complications leading to an increased risk of heart failure and cardiovascular disease (CVD). Early and accurate cardiac arrhythmia detection is vital to prevent various heart-related diseases. Electrocardiogram (ECG) is a popular and reliable method to detect cardiac arrhythmia and heart-related diseases. Presently, the medical fraternity demands automated cardiac arrhythmia detectors, which can help lower the burden of medical practitioners by identifying cardiac abnormalities in their early stages. The automated cardiac arrhythmia detector must be accurate, wearable, and capable of examining real-time ECG signals within a prescribed latency. This chapter proposes a deep learning-based method to effectively classify the ECG signals into three classes: healthy heart, atrial fibrillation, and ventricular fibrillation, and detect two cardiac arrhythmias: atrial fibrillation and ventricular fibrillation using a time-frequency spectrogram of ECG signals.

6.1. CLASSIFICATION OF ECG SIGNALS

The need for accurate, wearable, and fast-processing cardiac arrhythmia detectors compel researchers to develop intelligent, self-learning, and prognostic cardiac arrhythmia detectors that can assist medical practitioners by detecting cardiac abnormalities early and accurately. Recent advancements in computational intelligence and machine learning have shown the potential to develop such cardiac arrhythmia detectors. Machine learning has emerged as a vital tool for classifying and diagnosing cardiac arrhythmia in the past few years. Machine learning-based methods can save time, cost, and medical test expenses by detecting cardiac arrhythmia early and accurately [204]. In the literature, various approaches are proposed to classify ECG signals. In machine learning, various features computed from the available data are used to make decisions. Support vector machine (SVM), naïve Bayes, random forest tree, and k-nearest neighbor (KNN) are a few classifiers that have shown promising results in detecting cardiac arrhythmia. Although machine learning provides promising results in detecting cardiac

arrhythmia, extraction and selection of features are tricky.

Deep learning, a sub-set of machine learning, is one of the most effective methods to analyze and interpret data in many scientific fields, including healthcare. Deep learning emulates how humans acquire certain knowledge types by screening, detecting, and predicting diseases. Deep learning algorithms possess better learning capabilities than traditional machine learning algorithms. Deep learning-based networks extract independent features with less data pre-processing, making them suitable for analyzing high-dimensional data [205]. Deep learning classifiers based on recurrent neural network (RNN), dense neural network (DNN), long short-term memory (LSTM), and convolutional neural network (CNN) are used to detect arrhythmias. In this chapter, a system based on deep CNN is proposed to classify the ECG signals of a human subject into three cardiac conditions: healthy heart, atrial fibrillation, and ventricular fibrillation. The proposed superlet transform (SLT) based classification method identifies the R peaks to classify the ECG signals without extra noise removal steps, which lowers the hardware complexity. This work uses the SLT technique to transform one-dimensional input ECG signals into a time-frequency spectrogram. The 2D images obtained from SLT are used to input deep CNN. Three pre-trained classifiers: AlexNet, GoogLeNet, and DenseNet-201, classify the ECG signals into healthy heart, atrial fibrillation, and ventricular fibrillation classes.

6.2. MATHEMATICAL DESCRIPTION OF SUPERLET TRANSFORM

SLT can overcome the resolution problems of STFT and CWT by combining frequency resolution with temporal resolution. Unlike STFT and CWT, SLT provides a new spectral estimation that reveals the transient oscillation events of signals [206]. The SLT can provide a time-frequency spectrogram with high resolution in time and frequency localization compared to STFT and CWT. This property makes SLT suitable for analyzing transient oscillation events in signals like ECG and electroencephalogram.

Superlet (SL) employs multiple wavelets to produce a better TF resolution and is less leaky than a single wavelet. Wavelets with fewer cycles provide a good temporal resolution with a degraded frequency resolution. On the other hand, wavelets with many cycles provide a low temporal resolution at a better frequency resolution. SLT combines good temporal and appropriate frequency resolutions to provide a super-resolution. SLT improves the frequency resolution using wavelets with many cycles and ample time spread parameters in the higher-frequency range while maintaining the temporal resolution at low frequencies. In TF analysis, the Morlet wavelet is popular. The equation (6.1) defines the mother wavelet of the Morlet

wavelet.

$$\Phi(t) = \left(e^{ift} - e^{-\frac{1}{2}f^2 t^2} \right) e^{-\frac{1}{2}t^2} \quad (6.1)$$

In SL, the mother wavelet is a modified Morlet wavelet defined by Eq. (6.2).

$$\psi_{f,p}(t) = \frac{1}{B_p \sqrt{2\pi}} e^{-\frac{t^2}{2B_p^2}} e^{j2\pi ft} \quad (6.2)$$

The displacement parameter or time spread parameter (in second) B_p is given by Eq. (6.3). f is the central frequency, and p is the number of base cycles.

$$B_p = \frac{p}{D \times f} \quad (6.3)$$

The parameter B_p controls the time variance of the wavelet. B_p has an inverse relationship with the frequency, implying that a small B_p corresponds to a broader frequency response. The value of B_p is selected so that the wave covers p cycles within D standard deviations of a Gaussian envelope. D and p are design parameters. Normalization of the wavelet is an essential factor because it directly influences the ability of the time-frequency spectrogram to express various properties of data. The virtue of normalization is the detection of those events which are self-similar across the scale. In normalization, the events with equal peak amplitude and shape are compressed to give a similar intensity representation. In this study, the wavelet is normalized to the unit integral of the modulus to analyze an ECG signal. For a mother wavelet, the number of cycles p is fixed and selected so that the wavelet is admissible (to remove its mean).

SL is a group of finite wavelets with the same central frequency extending over multiple bandwidths.

$$SL_{f,m} = \left\{ \psi_{f,m} \mid p = p_1, p_2, p_3, \dots, p_m \right\} \quad (6.4)$$

Here, m represents the order of SL. p_1, p_2, \dots, p_m indicate the number of cycles in the individual wavelet in the set. The order of SL is the number of wavelets in the set. In SL, the number of cycles in a wavelet is decided using additive ($p_i = p_1 + i - 1$) or multiplicative. This study determines the number of cycles in a wavelet using the multiplicative relation defined in Eq. (6.5).

$$p_i = i \times p \quad (6.5)$$

Here, $i=1, 2, 3 \dots m$. An SL of order one has one wavelet with p_1 cycles. Similarly, SL of order n has n wavelet $\{p_1, p_2, p_3, \dots, p_n\}$ with $p_2 = 2p_1, p_3 = 3p_1, \dots$, and $p_n = np_1$. SL combines multiple wavelets to detect localized time-frequency packets. In the higher-frequency band, SL

decreases the redundancy of representation.

The SL of a signal $s(t)$ responds $R[SL_{f,m}]$ is the geometrical mean of the responses of individual wavelets as given in Eq. (6.6):

$$R[SL_{f,m}] = \sqrt[m]{\prod_{i=1}^m R[\psi_{f,p_i}]} = \sqrt[m]{\prod_{i=1}^m \left| \sqrt{2} \frac{1}{a} \int_{-\infty}^{\infty} s(\tau) \psi_{f,p_i} \left(\frac{\tau-t}{a} \right) d\tau \right|} \quad (6.6)$$

Here $R[\psi_{f,p_i}]$ is the response to the signal $s(t)$ provided by i^{th} wavelet in the set and defined in Eq. (6.7).

$$R[\psi_{f,p_i}] = s(t) * \psi_{f,p_i}(t) = \frac{1}{a} \int_{-\infty}^{\infty} s(\tau) \psi_{f,p_i} \left(\frac{\tau-t}{a} \right) d\tau \quad (6.7)$$

The i^{th} order wavelet $\psi_{p_i}(t)$ in an SL is given by Eq. (6.8).

$$\psi_{p_i}(t) = \frac{Df}{p \cdot i \cdot \sqrt{2\pi}} e^{-\frac{1}{2} \left[\frac{Dft}{p \cdot i} \right]^2} e^{j2\pi ft} \quad (6.8)$$

The SL estimates the oscillation packets present in the signal at central frequency f . The SLT is like a CWT. In CWT, one uses wavelets, while in SLT, SLs are used. The SLT is suitable for the narrowband, and adaptive SLT (ASLT) is preferred in a wide frequency range. In an ASLT, a low order is used for lower frequencies, increasing with frequency for higher frequencies. As the central frequency increases, then the order of SL is automatically adjusted. This ability of ASLT compensates for the increase in wavelet bandwidth with an increase in frequency. To provide an enhanced time-frequency representation in ASLT, the increase in order as a function of frequency is given by Eq. (6.9).

$$ASL_f = SL_{f,m} \Big|_m = a(f) \quad (6.9)$$

Here, $a(f)$ is a uniformly increasing function of central frequency with integer values given by Eq. (6.10).

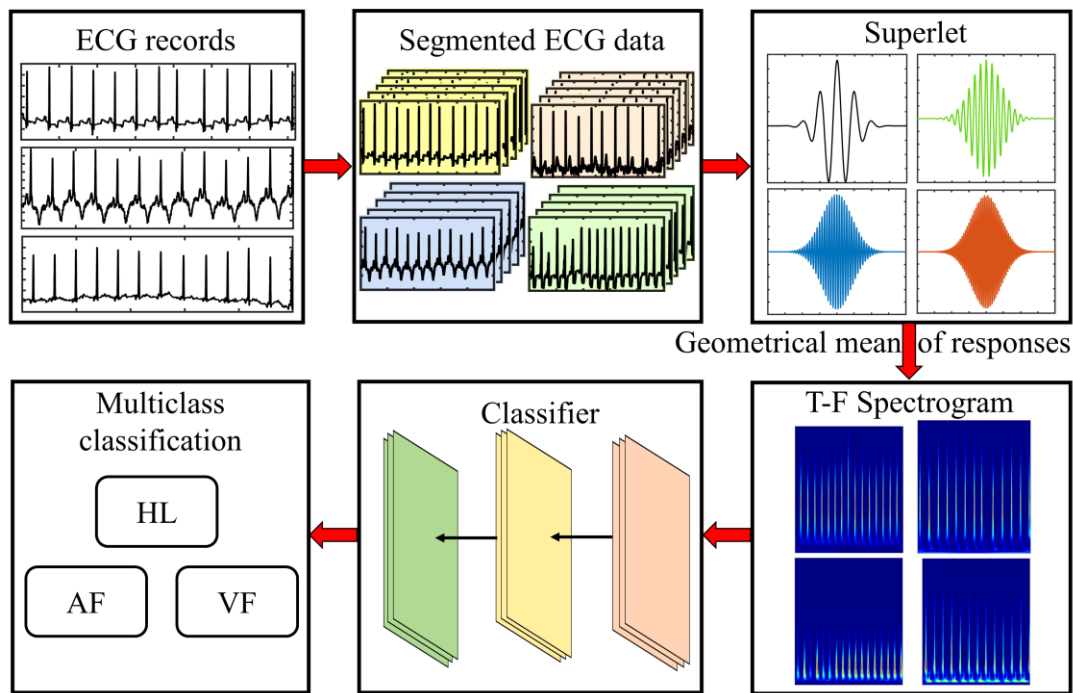
$$a(f) = m_{\min} + (m_{\max} - m_{\min}) \times \left[\frac{f - f_{\min}}{f_{\max} - f} \right] \quad (6.10)$$

Here, m_{\max} and m_{\min} are the orders of those SLs that correspond to the largest and smallest central frequencies, f_{\max} and f_{\min} , respectively.

6.3. CLASSIFICATION OF ARRHYTHMIAS USING SUPERLET TRANSFORM AND DEEP CONVOLUTIONAL NETWORKS

The superior image-classifying ability of deep CNNs makes them an attractive choice in the

medical field. This chapter uses a combination of SLT and deep CNN to detect two popular CVDs: atrial fibrillation and ventricular fibrillation. The block diagram of the proposed method is shown in Fig. 6.1. Different databases are selected to increase the number of ECG signals in each class, namely healthy heart, atrial fibrillation, and ventricular fibrillation. AF termination challenge database provides the ECG signals that reflect the episode of atrial fibrillation. CU ventricular tachyarrhythmia database and MIT-BIH malignant ventricular database provide ECG signals reflecting the episodes of ventricular fibrillation. The Fantasia and MIT-BIH arrhythmia databases provide ECG signals with a healthy heart condition. All the ECG signals in this work are taken across lead-II. In the proposed SLT-based classification method, the ECG signals from different databases are first segmented into segments of *ten*-second duration. This segmentation process increases the number of ECG signals for a healthy heart, atrial fibrillation, and ventricular fibrillation.



HL: Healthy heart, **AF:** atrial fibrillation, **VF:** ventricular fibrillation

Fig. 6.1: Block diagram of the proposed SLT-based method

The next step applies SLT to the segmented *ten*-second ECG signals. Each wavelet in SL provides a time-frequency spectrogram of the *ten*-second ECG signal. When all the responses of the wavelets in SL are combined geometrically, it provides a sharper and less redundant time-frequency spectrogram to the ECG signal. Thus, SLT converts the 1-D ECG signal into a 2-D image. 2310 2-D images are obtained using SLT belonging to healthy heart, atrial fibrillation, and ventricular fibrillation. Each class has 700 images, of which 105 are used to

validate the classifier. Apart from training and validation images, a set of 210 images (70 from each class) is used to test the classifier. The resultant 2-D images time-frequency spectrogram are used to classify the ECG signals into healthy heart, atrial fibrillation, and ventricular fibrillation. AlexNet, GoogLeNet, and DenseNet-201 are the *three* pre-trained convolutional neural networks used in this work. The last layers in the *three* networks are replaced with new layers to classify the ECG signals into *three* classes.

AlexNet was developed by Alex Krizhevsky, Ilya Sutskever, and Geoff Hinton in 2012 [207]. AlexNet was designed to categorize 1.2 million high-resolution images into 1000 classes in the ImageNet LSVRC-2010 contest. The input to the AlexNet is an image, and the output is the class of the object. The schematic of AlexNet architecture is shown in Fig. 6.2. AlexNet consists of a convolution layer, rectified linear unit layer, pooling layer, and fully connected layers. Specifically, AlexNet has *five* convolutional layers along with *three* fully connected layers. Using a rectified linear unit in AlexNet makes learning speedy and easy.

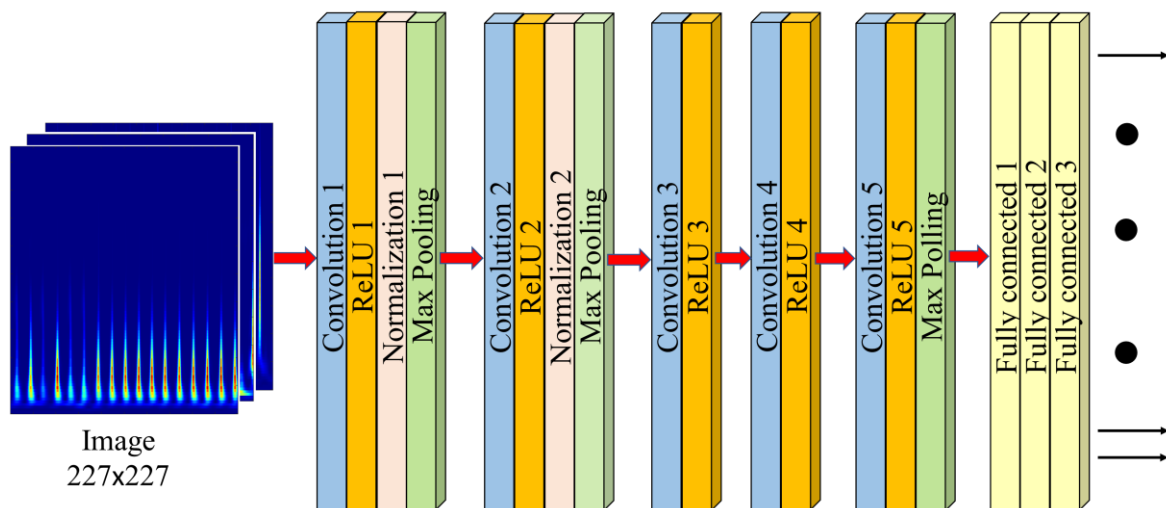


Fig. 6.2: The architecture of AlexNet

The pooling layer in the network aggregates the information in neighboring groups in the same kernel. In AlexNet, an image with a resolution of $227 \times 227 \times 3$ is applied to the first convolutional layer with 96 (11×11) kernels with a stride of *four*. The input is passed through the normalization layer, pooling layers, and the first convolutional layer. The output of the first convolutional layer is fed as an input to the second convolutional layer. The second convolutional layer has 256 kernels with a size of $5 \times 5 \times 48$. The third convolutional layer with 384 kernels of size $3 \times 3 \times 256$ connects the second and fourth convolutional layers. The output of the third convolutional layer is fed as an input to the fourth convolutional layer with 384 kernels of size $3 \times 3 \times 192$. The fifth convolutional layer with 256 kernels of size $3 \times 3 \times 192$ accepts its input from the output of the fourth convolutional layer. All *three* fully connected layers of the AlexNet

with 4096 neurons each perform the same operation. They perform a weighted sum operation with an added bias term. The third fully connected layer produces an output that, on passing through the softmax activation function, provides the prediction of the network.

The second pre-trained CNN used in this work is GoogLeNet. It is twenty-two layers deep pre-trained CNN. GoogLeNet, based on the inception architecture, is different from AlexNet. The GoogLeNet was designed so that the network could run on limited computational resources [208]. GoogLeNet uses techniques such as global average pooling and 1×1 convolution to create a deeper architecture. In inception architecture, 1×1 convolution is used to reduce the biases and weights of the networks [208]. At the end of GoogLeNet architecture, the global average pooling method takes a size 7×7 feature map and averages it to 1×1 . The schematic architecture of GoogLeNet is shown in Fig. 6.3. In the GoogLeNet architecture, two auxiliary classifiers are attached to the output of the inception module. These auxiliary classifiers are used during training. They contribute weighted loss (weighted by 0.3) to the total loss of the network. But during inference time, auxiliary classifiers are discarded. The structure of auxiliary classifiers consists of the following layers:

- 1) An average pooling layer with a filter size of 5×5 and a stride of 3.
- 2) A 1×1 convolution layer with 128 filters is used to reduce dimension and rectify linear activation.
- 3) A fully connected layer having 1024 outputs and rectified linear activation

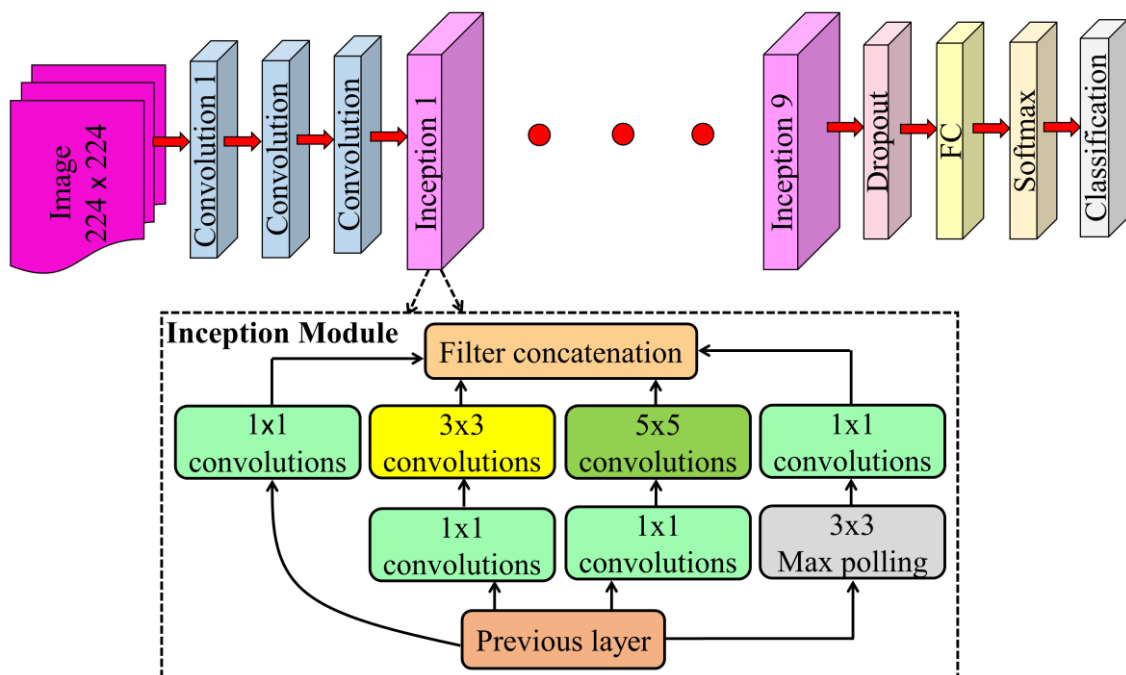


Fig. 6.3: GoogLeNet architecture

- 4) A dropout layer with a dropout ratio of 70%.
- 5) A *softmax* layer as a classifier that predicts the same 1000 classes as the primary classifier GoogLeNet accepts an image of size 224×224 .

DenseNet is the third pre-trained CNN that is used in this work. In DenseNet, all the layers are directly connected in a forward feed fashion [206]. The direct connection between layers ensures maximum information flow. Each layer obtains its input from the feature maps of all the preceding layers. The feature map of a layer act as an input for all successive layers. A DenseNet with P layers has $P(P+1)/2$ connections, whereas traditional convolutional networks only have P connections. In DenseNet, the dense connection reduces the problems like gradient vanishing and exploding and facilitates feature reuse.

DenseNet combines the property of identity mapping, deep supervision, and diversified depth. The improved flow of information and gradient makes DenseNet easy to train. In the proposed method, DenseNet-201, a version of DenseNet, is used to classify ECG records. The number "201" indicates the depth of the network. The pre-trained DenseNet-201 has been trained to classify images into 1000 classes. The schematic of DenseNet architecture is shown in Fig. 6.4.

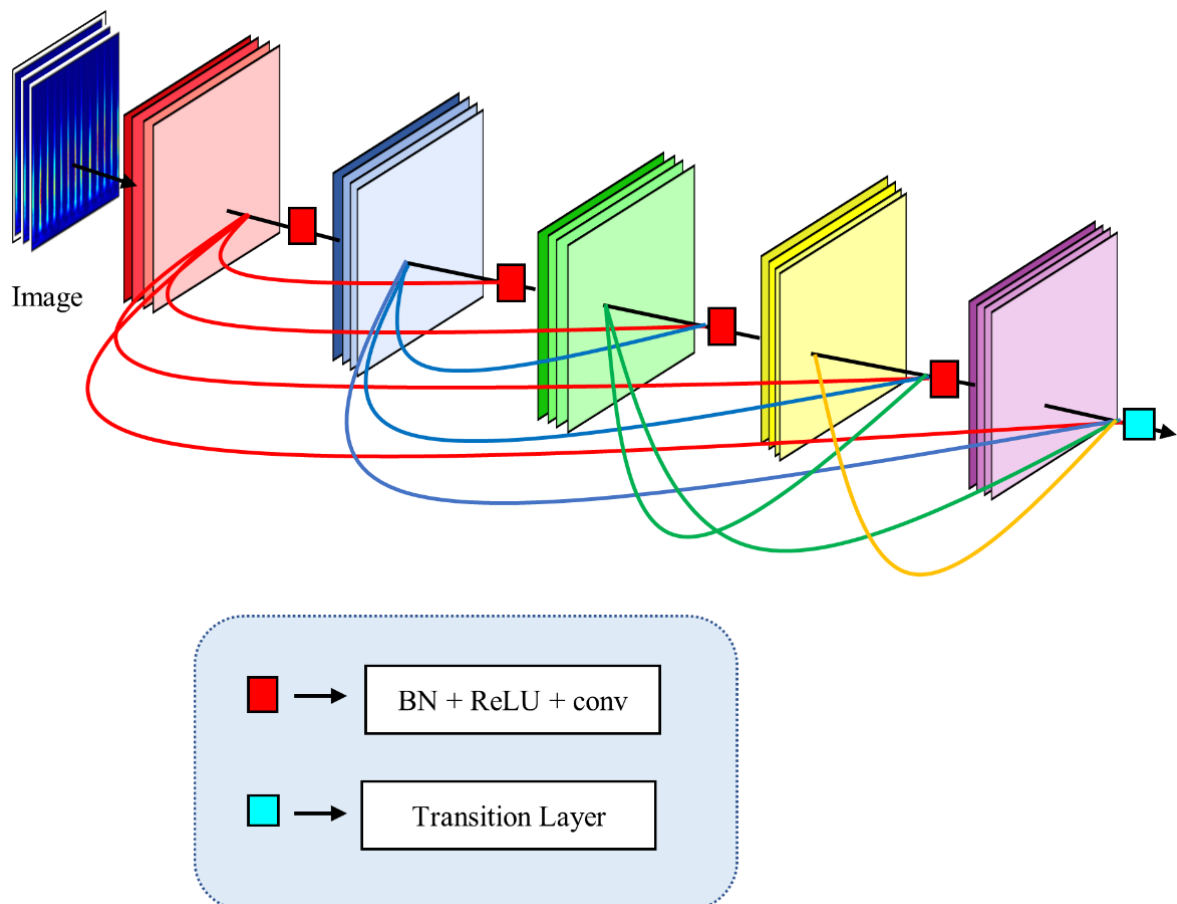


Fig. 6.4: Architecture of DenseNet-201

6.4. SIMULATIONS AND PERFORMANCE EVALUATION OF THE SLT-BASED CLASSIFICATION TECHNIQUE

The simulations are performed on a computer with AMD Ryzen 5 4500U CPU @ 2.38 GHz, 8 GB of RAM, and a 64-bit Windows 10 operating system.

The proposed SLT-based classification method is tested using five standard ECG databases: MIT-BIH arrhythmia database [169], AF termination challenge database [170], CU ventricular tachyarrhythmia database [174], MIT-BIH malignant ventricular database [207], and Fantasia database [178]. The performance metrics used to validate the proposed method includes accuracy (A_c) (3.10), sensitivity (S_e) (3.7), specificity (S_p) (3.8), precision ($prec$) (3.9), and F-score (F_s) (3.14).

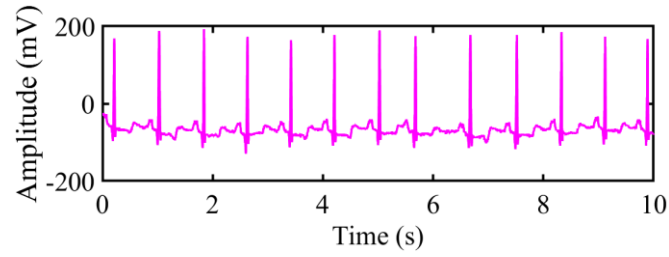
6.4.1 Time-Frequency Representation of ECG signals Using SLT

The SLs have excellent capability to reveal high-frequency bursts in a single trial. The SL functions like a band-pass filter with narrow bandwidths and concentrates the frequency resolution with increasing order. The wavelet normalization in SL suppresses the redundancy of time-frequency representation. Normalizing wavelets in SL facilitates instantaneous power detection at a scale-independent frequency [208]. Due to this normalization, high-frequency oscillations (QRS complex) can be detected in the ECG signals. An ECG signal (record-100) from MIT-BIH arrhythmia, its SLT, and detected QRS complex peaks are shown in Fig. 6.5 (a), Fig. 6.5 (b), and Fig. 6.5 (c) respectively. The duration of the ECG signal (record-100) is *ten* seconds.

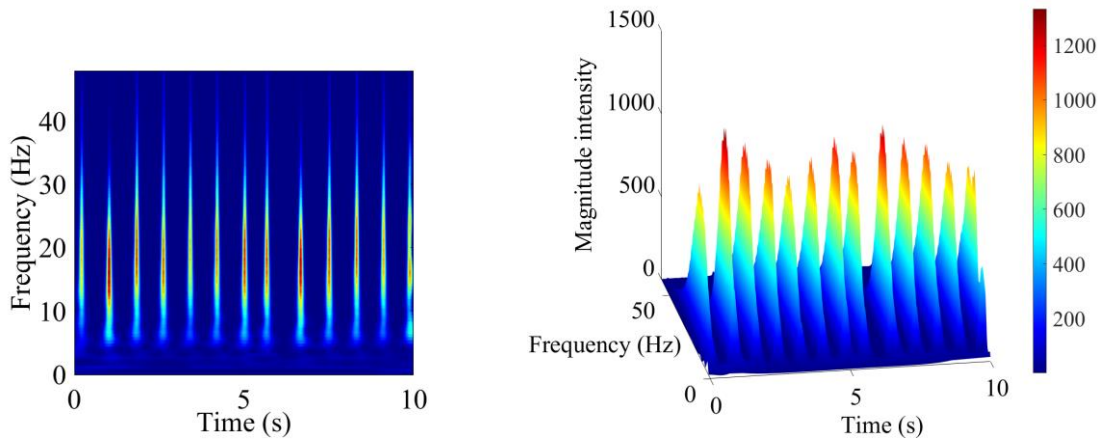
For MIT-BIH ECG signal (record-209), its time-frequency spectrogram and detected QRS complex peaks are shown in Fig. 6.6 (a), Fig. 6.6 (b), and Fig. 6.6 (c), respectively. Similarly, for ECG signal-record cu13, taken from CU ventricular tachyarrhythmia database, the time-frequency spectrogram and a few detected QRS complexes are demonstrated in Fig. 6.7 (a), Fig. 6.7 (b), and Fig. 6.7 (c), respectively.

The effect of standard deviation (D) on the detection parameter for ECG signal-100 from the MIT-BIH arrhythmia database is shown in Table 6.1. For $D = 0.33$, all thirteen QRS complex peaks of ECG signal-100 are detected. For $D = 1.2$, the SLT precisely identified the timestamp of eight QRS complex peaks, and five QRS complex peaks were detected at different locations from their annotated locations.

Fig. 6.8 shows the QRS complex peak detection variation with design parameters p and f . The number of correctly detected QRS complex peaks in the ten-second ECG signal-100 differs for different base cycles and central frequencies. Table 6.2 summarizes the QRS complex peaks



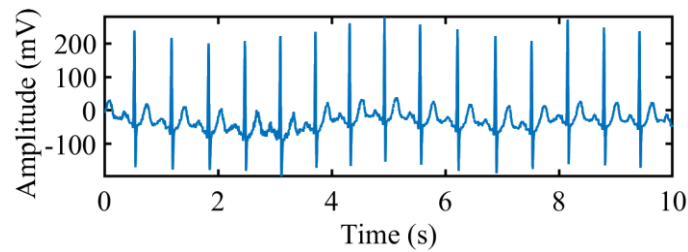
(a)



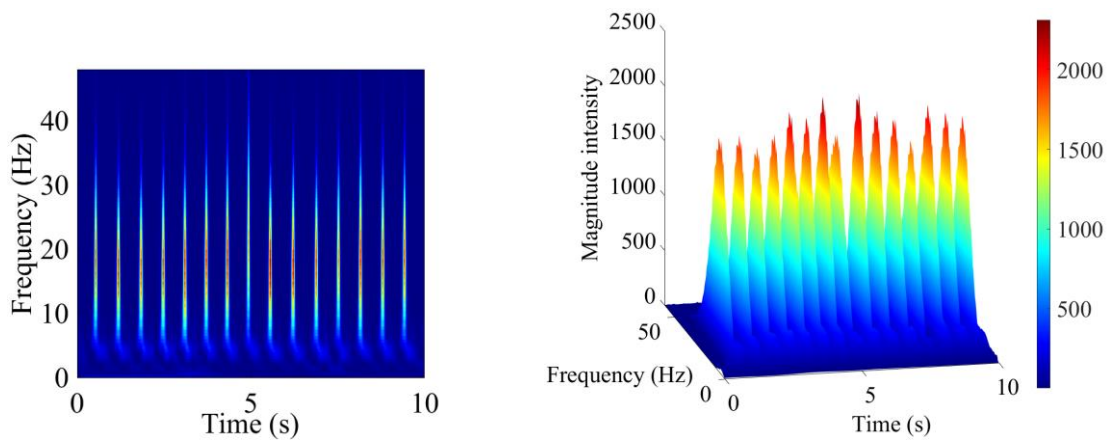
(b)

(c)

Fig. 6.5: (a) The ECG signal-100 from MIT-BIH arrhythmia database (b) Time-frequency power spectrum of ECG signal-100 (c) detected QRS complex peaks in ECG signal-100



(a)



(b)

(c)

Fig. 6.6: (a) The ECG signal-209 from MIT-BIH arrhythmia database (b) Time-frequency power spectrum of ECG signal -209 (c) detected QRS complex peaks in ECG signal -209

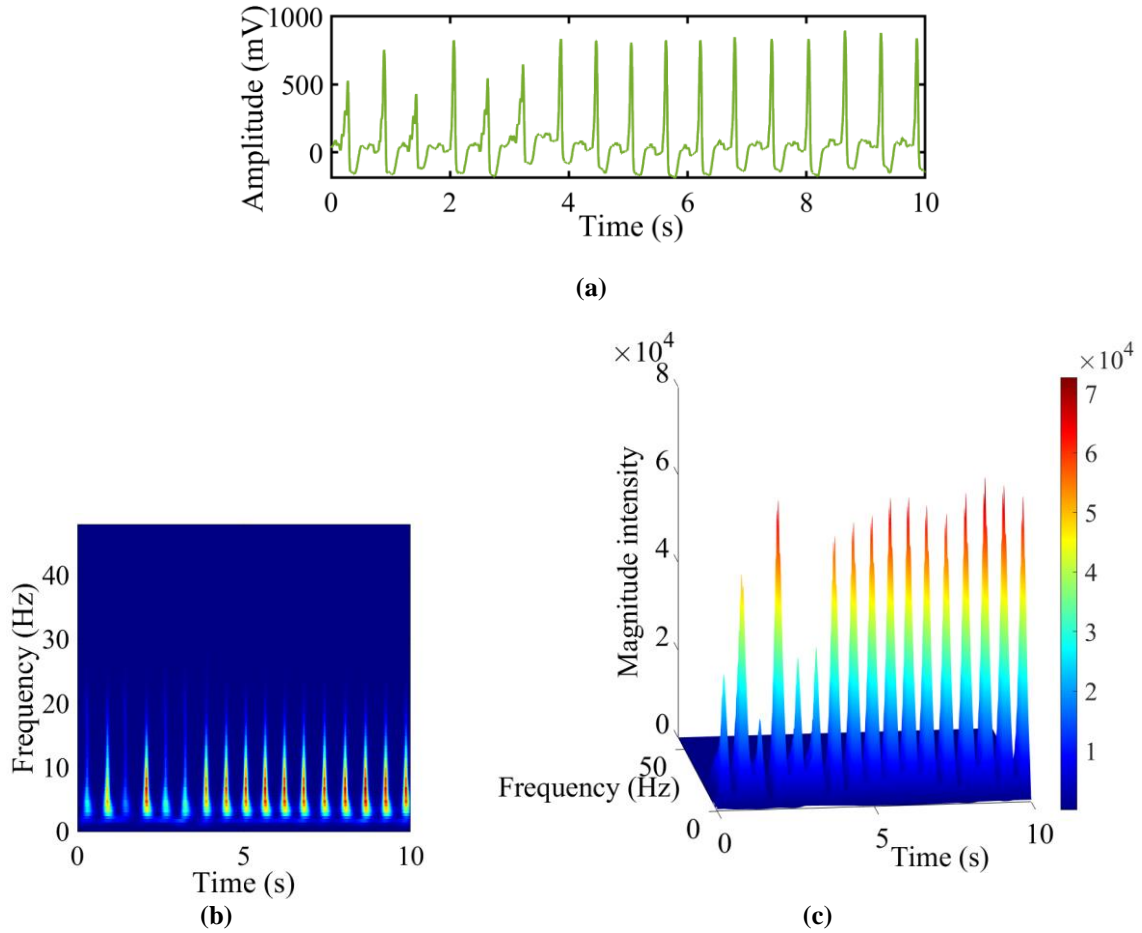


Fig. 6.7: (a) ECG signal-cu13 from CU ventricular tachyarrhythmia database (b) Time-frequency power spectrum of ECG signal -cu13 (c) detected QRS complex peaks in ECG signal-cu13

detected as the base cycle and central frequency are varied at a constant $D = 0.33$. With $p = 3$ and $f = 1$ Hz, all the peaks of ECG signal-100 are detected precisely.

Table 6.1: Variation of locations of QRS complex peaks with standard deviation (D) for ECG signal-100 from MIT-BIH arrhythmia database

| Standard deviation (D) | Time spread parameter (Bp) (second) | No. of QRS complex peaks detected at the annotated location | No. of QRS complex peaks detected at a different location from their annotated location |
|------------------------|---|---|---|
| 1.2 | 2.5 | 8 | 5 |
| 0.5 | 3 | 10 | 3 |
| 0.33 | 4.5 | 13 | 0 |
| 0.27 | 5.5 | 12 | 1 |
| 0.2 | 7.5 | 12 | 1 |

SLT has superior noise handling capability as compared to STFT and CWT, which is demonstrated in Fig. 6.9. The time-frequency spectrogram of a noisy ECG record is computed using STFT, CWT, and SLT, and the resulting spectrograms are shown in Fig. 6.9 (a) to Fig. 6.9 (d), respectively. Fig. 6.9 shows that the spectrogram obtained from SLT is least affected

by the noise. This work is published in [209].

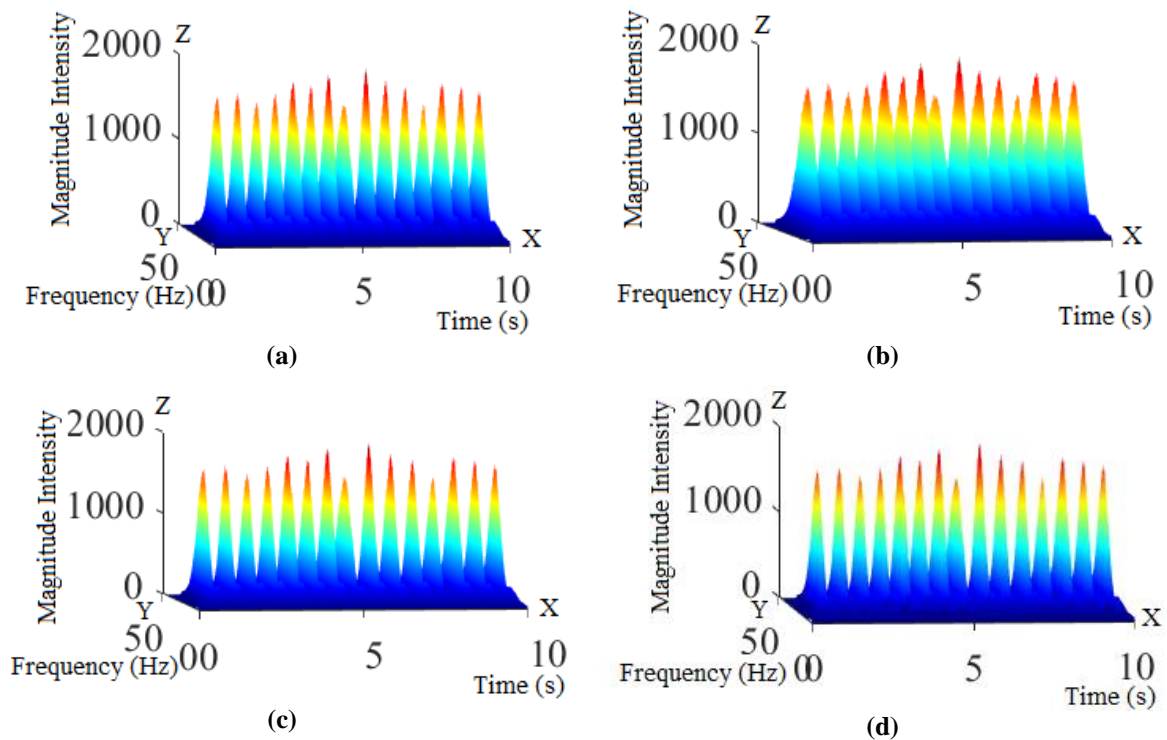


Fig. 6.8: Variation of detection parameter with base cycle and central frequency for ECG signal-100 from MIT-BIH arrhythmia database (a) $p=3$, $f=1$ Hz (b) $p=6$, $f=2$ Hz (c) $p=9$, $f=3$ Hz (d) $p=12$, $f=4$ Hz

The time-frequency spectrogram of STFT and CWT is contaminated with noise in the ECG signal. The superior denoising capability of SLT denoises the noisy ECG signal, thus showing better denoising capabilities without requiring extra filters. Hence, the SLT reduces the hardware complexity. The SLT provides a sharp and high-resolution spectrogram even in the presence of noises.

Table 6.2: Variation of locations of QRS complex peaks with base cycle and central frequency for ECG signal-100 from MIT-BIH arrhythmia database

| Number of base cycles (p) | Central frequency (f) (Hz) | No. of QRS complex peaks detected at the correct location | No. of QRS complex peaks detected at a different location |
|-------------------------------|--------------------------------|---|---|
| 3 | 1 | 13 | 0 |
| 6 | 2 | 8 | 5 |
| 9 | 3 | 11 | 2 |
| 12 | 4 | 8 | 5 |

In the proposed SLT-based classification method, the time-frequency spectrogram of ECG records computed using SLT is used as an image to classify ECG records. With the help of SL, a database of 2100 images (700 images for each class) is prepared. For classification, deep learning methods are used. The deep learning method extracts features from the images and efficiently recognizes the class of the image. AlexNet, GoogLeNet, and DenseNet-201 are used

to classify ECG records. The classifiers are trained with 85% of the data and validated using

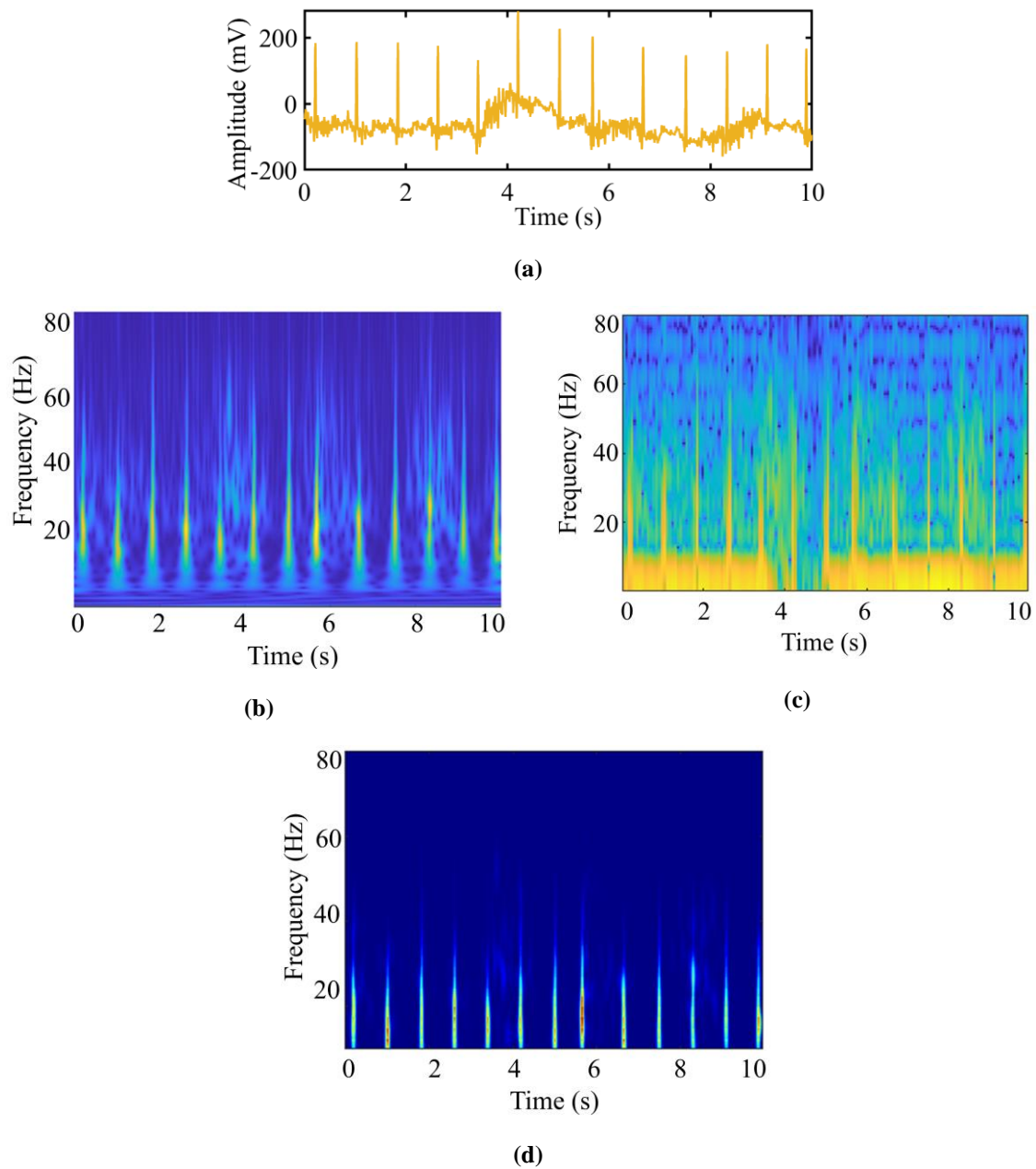


Fig. 6.9: (a) Noisy ECG record and its time-frequency representation provided by (b) STFT (c) CWT (d) SLT the remaining 15% of the data in the database. A separate set of data with 210 images (with 70 images belonging to each class) is used for testing the performance of classifiers.

6.4.2 Classification of Images With Deep Convolutional Neural Networks

The obtained images from SLT are used as inputs to three pre-trained classifiers, namely AlexNet, GoogLeNet, and DenseNet-201. The usage of pre-trained networks offers several advantages, such as a reduction in training time, better generalization, avoidance of overfitting, and better initialization. The simulated results from all *three* pre-trained networks are given below.

6.4.2.1 Simulation results with AlexNet

In AlexNet, the last three layers are changed, while the rest are unchanged. The parameters of AlexNet need a little adoption according to new images. This work uses the root mean square propagation optimizer to train the transferred AlexNet. In this work, as the layers of pre-trained AlexNet are replaced to work on a different database, the name transferred AlexNet. The learn rate is 10^{-5} , with a batch size of *thirty-two*. The classifier provides an overall validation accuracy of 92.7% and a testing accuracy of 92.9%. The confusion matrix of AlexNet for validation and test database are shown in Fig. 6.10 (a) and Fig. 6.10 (b), respectively.

| | | Confusion Matrix | | | |
|--------------|----|------------------|----------------|---------------|---------------|
| Output Class | AF | 100 31.7% | 5 1.6% | 3 1.0% | 92.6% 7.4% |
| | HL | 2 0.6% | 92 29.2% | 2 0.6% | 95.8% 4.2% |
| | VF | 3 1.0% | 8 2.5% | 100 31.7% | 90.1% 9.9% |
| | | 95.2% 4.8% | 87.6% 12.4% | 95.2% 4.8% | 92.7% 7.3% |
| | | AF | HL | VF | |
| | | Target Class | | | (a) |

| | | Confusion Matrix | | | |
|--------------|----|------------------|---------------|----------------|----------------|
| Output Class | AF | 66 31.4% | 2 1.0% | 3 1.4% | 93.0% 7.0% |
| | HL | 3 1.4% | 67 31.9% | 5 2.4% | 89.3% 10.7% |
| | VF | 1 0.5% | 1 0.5% | 62 29.5% | 96.9% 3.1% |
| | | 94.3% 5.7% | 95.7% 4.3% | 88.6% 11.4% | 92.9% 7.1% |
| | | AF | HL | VF | |
| | | Target Class | | | (b) |

Fig. 6.10: (a) Confusion matrix of validation database (b) Confusion matrix of test database by AlexNet

From the confusion matrix of the test database, *sixty-six* images are correctly classified as atrial fibrillation, corresponding to 31.4% of all 210 images. *Two* images of a healthy heart are incorrectly classified as atrial fibrillation. Similarly, three images belonging to ventricular fibrillation are incorrectly classified as atrial fibrillation—the proposed method correctly classified *sixty-seven* and *sixty-two* images for a healthy heart and ventricular fibrillation class. The performance measures are calculated from the confusion matrix in Table 6.3 to obtain more insights from the AlexNet-based model. In confusion matrices, HL, AF, and VF represent a healthy heart, atrial fibrillation, and ventricular fibrillation. The performance metrics such as accuracy (Ac), sensitivity (Se), specificity (Sp), precision ($prec$), and F-score (Fs) are evaluated on the test database and listed in Table 6.3.

Table 6.3: Detection summary (on test dataset) for each class using SLT and transferred AlexNet

| Class | Ac (%) | Se (%) | Sp (%) | $prec$ (%) | Fs (%) |
|-------|----------|----------|----------|------------|----------|
| AF | 95.7 | 94.2 | 96.4 | 92.9 | 93.5 |
| HL | 94.7 | 95.7 | 94.2 | 89.3 | 92.3 |
| VF | 95.2 | 88.5 | 98.5 | 96.8 | 92.5 |

For atrial fibrillation, the accuracy (Ac), sensitivity (Se), specificity (Sp), precision ($prec$), and F-score (Fs) are 95.7%, 94.2%, 96.4%, 92.9%, and 93.5%, respectively. For a healthy heart, these performance metrics are 94.7%, 95.7%, 94.2%, 89.3%, and 92.3%, respectively. Similarly, these performance metrics for ventricular fibrillation are 95.2%, 88.5%, 98.5%, 96.8%, and 92.5%, respectively. This work is published in [209].

6.4.2.2 Simulation results with GoogLeNet

In GoogLeNet, the images are resized to 224×224 . The learn rate is 10^{-5} , with a batch size of *thirty-two*. The GoogLeNet provides an overall accuracy of 91.4% on the validation database, and the overall accuracy is 93.8% on the test database. The confusion matrices obtained from GoogLeNet on the validation and test databases are shown in Fig. 6.11 (a) and Fig. 6.11 (b), respectively.

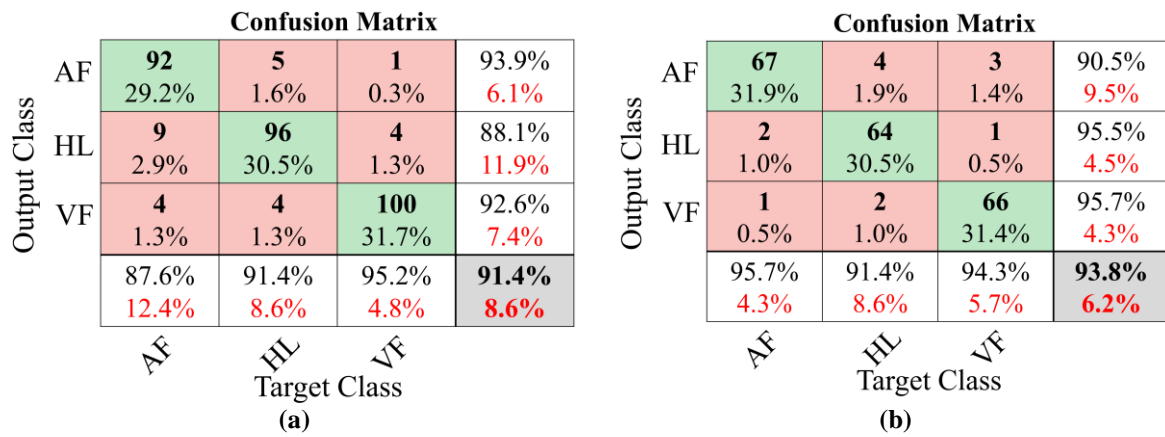


Fig. 6.11: (a) Confusion matrix of validation database (b) Confusion matrix of test database by transferred GoogLeNet

Table 6.4: Detection summary (on test dataset) for each class using SLT and transferred GoogLeNet

| Class | Ac (%) | Se (%) | Sp (%) | $prec$ (%) | Fs (%) |
|-------|----------|----------|----------|------------|----------|
| AF | 95.2 | 95.7 | 95.0 | 90.5 | 93.0 |
| HL | 95.7 | 91.4 | 97.8 | 95.5 | 93.4 |
| VF | 96.6 | 94.2 | 97.8 | 95.6 | 94.8 |

From the confusion matrix shown in Fig. 6.11 (b), *sixty-seven* images are correctly classified as atrial fibrillation. *Sixty-four* images are correctly classified as a healthy heart. Similarly, *sixty-six* images are correctly classified as ventricular fibrillation. *Four* healthy heart images are incorrectly classified as atrial fibrillation, corresponding to 1.9% of 210 test images. The performance metrics for each class on the test database are listed in Table 6.4. For atrial fibrillation, the accuracy (Ac), sensitivity (Se), specificity (Sp), precision ($prec$), and F-score

(F_s) are 95.2%, 95.7%, 95.0%, 90.5%, and 93.0%, respectively. These performance metrics for the healthy heart class are 95.7%, 91.4%, 97.8%, 95.5%, and 93.4%, respectively. This work is published in [209].

6.4.2.3 Simulation results with DenseNet-201

For DenseNet-201, the learn rate and batch sizes are 10^{-5} and *thirty-two*, respectively. The root mean square propagation optimizer is used to train the transferred DenseNet-201. The confusion matrix for the validation and test database are shown in Fig. 6.12 (a) and Fig. 6.12 (b), respectively. 96.2% of images are correctly classified, whereas 3.8% are wrongly classified. The classifier correctly detects seventy images of atrial fibrillation. *Sixty-seven* images of a healthy heart are correctly classified.

Similarly, *sixty-five* images of ventricular fibrillation are correctly classified by the proposed method. *Two* healthy heart images are incorrectly identified as atrial fibrillation. Similarly, *one* healthy heart image is misclassified as ventricular fibrillation. Also, *five* ($1+4$) ventricular fibrillation images are incorrectly classified as healthy heart (*one*) and atrial fibrillation (*four*), respectively. This work is published in [209].

| | | Confusion Matrix | | | |
|--------------|----|------------------|----------------|---------------|----------------|
| Output Class | AF | 98 31.1% | 5 1.6% | 0 0.0% | 95.1% 4.9% |
| | HL | 4 1.3% | 91 28.9% | 1 0.3% | 94.8% 5.2% |
| | VF | 3 1.0% | 9 2.9% | 104 33.0% | 89.7% 10.3% |
| | | 93.3% 6.7% | 86.7% 13.3% | 99.0% 1.0% | 93.0% 7.0% |
| | | AF | HL | VF | |
| | | Target Class | | | |
| | | (a) | | | |

| | | Confusion Matrix | | | |
|--------------|----|------------------|---------------|---------------|---------------|
| Output Class | AF | 70 33.3% | 2 1.0% | 4 1.9% | 92.1% 7.9% |
| | HL | 0 0.0% | 67 31.9% | 1 0.5% | 98.5% 1.5% |
| | VF | 0 0.0% | 1 0.5% | 65 31.0% | 98.5% 1.5% |
| | | 100.0% 0.0% | 95.7% 4.3% | 92.9% 7.1% | 96.2% 3.8% |
| | | AF | HL | VF | |
| | | Target Class | | | |
| | | (b) | | | |

Fig. 6.12: (a) Confusion matrix of validation database (b) Confusion matrix of test database by transferred DenseNet-201

The performance measures in terms of accuracy (Ac), sensitivity (Se), specificity (Sp), precision ($prec$), and F-score (F_s) are tabulated in Table 6.5. The above results show that the DenseNet-201 performs better than other methods and provides an overall accuracy of 96.2%. DenseNet-201 provides the best accuracy for each class compared to AlexNet and GoogLeNet. The AlexNet has shown the lowest performance, with an overall accuracy of 92.9% on the test database. The performance of GoogLeNet and AlexNet is comparable, with an overall test accuracy of 93.8% (SLT + GoogLeNet).

In the proposed SLT-based classification method, the performance of AlexNet, GoogLeNet, and DenseNet-201 is compared in terms of true positive (TP), true negative (TN), false positive

(*FP*), and false negative (*FN*) for each class in Table 6.6. These parameters, true positive (*TP*), true negative (*TN*), false positive (*FP*), and false negative (*FN*) are computed using the obtained confusion matrixes on the test database and tabulated in Table 6.6. This work is published in [206].

Table 6.5: Detection summary of the test dataset for each class using SLT and transferred DenseNet-201

| Class | <i>Ac</i> (%) | <i>Se</i> (%) | <i>Sp</i> (%) | <i>prec</i> (%) | <i>Fs</i> (%) |
|-------|---------------|---------------|---------------|-----------------|---------------|
| AF | 97.1 | 100 | 95.7 | 92.1 | 95.8 |
| HL | 98.0 | 95.7 | 99.2 | 98.5 | 97.0 |
| VF | 97.1 | 92.8 | 99.2 | 98.4 | 95.6 |

Table 6.6: Summary of computed true positive (*TP*), true negative (*TN*), false positive (*FP*), and false negative (*FN*) for the SLT-based classification method

| Class | SLT + AlexNet | | | | SLT + GoogLeNet | | | | SLT + DenseNet-201 | | | |
|-------|---------------|-----------|-----------|-----------|-----------------|-----------|-----------|-----------|--------------------|-----------|-----------|-----------|
| | <i>TP</i> | <i>TN</i> | <i>FP</i> | <i>FN</i> | <i>TP</i> | <i>TN</i> | <i>FP</i> | <i>FN</i> | <i>TP</i> | <i>TN</i> | <i>FP</i> | <i>FN</i> |
| AF | 66 | 135 | 5 | 4 | 67 | 133 | 7 | 3 | 70 | 134 | 6 | 0 |
| HL | 67 | 132 | 8 | 3 | 64 | 137 | 3 | 6 | 66 | 137 | 3 | 4 |
| VF | 62 | 138 | 2 | 8 | 66 | 137 | 3 | 4 | 65 | 139 | 1 | 5 |

Although the DenseNet-201 has provided good results, its training time and structure complicity are higher than AlexNet and GoogLeNet. The efficiency of the models used in this study is compared in Table 6.7. Table 6.7 compares the models developed using a combination of SLT and transferred networks based on the number of layers, training time, and testing time. The training time and testing time of AlexNet are the lowest, while for DenseNet-201, it is the highest.

Table 6.7: Performance comparison of different models on the combination of SLT and transferred network

| Model | Number of layers | Training Time (hour) | Testing Time (second) | Accuracy (%) |
|--------------|------------------|----------------------|-----------------------|--------------|
| AlexNet | 25 | 0.6 | 3.8 | 92.9 |
| GoogLeNet | 144 | 2.6 | 8.1 | 93.8 |
| DenseNet-201 | 708 | 13.4 | 10.4 | 96.2 |

Table 6.8 compares the proposed SLT+ DenseNet-201 method with other existing methods for detecting atrial fibrillation. The proposed SLT+ DenseNet-201 method outperforms the

compared methods. The proposed SLT+ DenseNet-201 method provides the best result by correctly detecting all the images of atrial fibrillation without any noise removal or preprocessing steps. The proposed SLT+ DenseNet-201 method shows a sensitivity of 100% for atrial fibrillation, which means it would not miss any subject suffering from atrial fibrillation. The proposed SLT + DenseNet-201 method provides the best F-score for atrial fibrillation.

Table 6.8: Performance comparison of various methods for atrial fibrillation detection

| Reference | Method | <i>Se</i> (%) | <i>Sp</i> (%) | prec (%) | <i>Fs</i> (%) |
|---|-----------------------------|---------------|---------------|-------------|---------------|
| Mathunjwa et al. (2021) [208] | Recurrent plot + CNN | 86.79 | NR | 73.61 | 79.65 |
| Lai et al. (2020) [210] | Patch-based lead + CNN | 93.1 | 93.4 | NR | NR |
| Ross-Howe and Tizhoosh (2019) [211] | Spectrogram+ DenseNet + SVM | 88.38 ± 0.02 | 95.14 ± 0.01 | NR | NR |
| Fan et al. (2018) [212] | MS-CNN | 92.41 | 97.70 | 85.43 | 88.78 |
| Proposed SLT-based classification method [209] | SLT + AlexNet | 94.2 | 96.4 | 92.9 | 93.5 |
| Proposed SLT-based classification method [209] | SLT + GoogLeNet | 95.7 | 95.0 | 90.5 | 93.0 |
| Proposed SLT-based classification method [209] | SLT + DenseNet-201 | 100 | 95.7 | 92.1 | 95.8 |

Table 6.9: Performance comparison of various methods for ventricular fibrillation detection

| Reference | Method | <i>Ac</i> (%) | <i>Se</i> (%) | <i>Sp</i> (%) | <i>Fs</i> (%) |
|---|---|---------------|---------------|---------------|---------------|
| Lee et al. (2013) [213] | Morphological features + SVM | NA | 95.12 | 96.67 | NA |
| Tripathy et al. (2018) [214] | DTFT + LS-SVM | 89.81 | 86.38 | 93.97 | NA |
| Mohanty et al. (2018) [215] | TF and statistical features + cubic SVM | 92.23 | 79.43 | 81.44 | NA |
| Proposed SLT-based classification method [209] | SLT + AlexNet | 95.2 | 88.5 | 98.5 | 92.5 |
| Proposed SLT-based classification method [209] | SLT + GoogLeNet | 96.6 | 94.2 | 97.8 | 94.8 |
| Proposed SLT-based classification method [209] | SLT + DenseNet-201 | 97.1 | 92.8 | 99.2 | 95.6 |

The performance of the proposed SLT+ DenseNet-201 method for ventricular fibrillation is compared in Table 6.9. From Table 6.9, the proposed SLT+ DenseNet-201 method outperforms other compared methods by providing the highest accuracy and specificity of 97.1% and 99.2%, respectively. Table 6.10 compares the proposed method with other arrhythmia detection methods. The proposed method is also evaluated with STFT and CWT. To compare the efficacy of the proposed method (SLT + DenseNet-201) with STFT and CWT, the images are prepared in the same manner as for SLT. The proposed method with STFT provides an overall accuracy (on the test database) of 81.4%, 83.8%, and 91.0% for AlexNet, GoogLeNet, and DenseNet-201, respectively. Similarly, with the CWT, the results on the test database are 92.4%, 92.2%, and 94.8% for AlexNet, GoogLeNet, and DenseNet-201, respectively. The results show that the proposed SLT-based classification method outperforms STFT and CWT-based classification methods. The results show that the proposed SLT+ DenseNet-201 method with SLT outperforms STFT and CWT. This work is published in [209].

Table 6.10: Performance comparison of the proposed method with other existing methods

| Reference | Method | Number of classes | Ac (%) |
|--|---------------------------------------|-------------------|-------------|
| Llamedo and Martinez (2012) [216] | LDC + EMCA | 3 | 95.42 |
| Essa and Xie (2021) [217] | Median filter + CNN-LSTM + RRHOS-LSTM | 4 | 95.81 |
| Baygin et al., (2021) [218] | HIT + SVM | 7 | 92.95 |
| Proposed STFT-based classification method [209] | STFT + AlexNet | 3 | 81.4 |
| Proposed CWT-based classification method [209] | CWT + AlexNet | 3 | 92.4 |
| Proposed SLT-based classification method [209] | SLT + AlexNet | 3 | 92.9 |
| Proposed STFT-based classification method [209] | STFT + GoogLeNet | 3 | 83.8 |
| Proposed CWT-based classification method [209] | CWT + GoogLeNet | 3 | 92.2 |
| Proposed SLT-based classification method [209] | SLT + GoogLeNet | 3 | 93.8 |
| Proposed STFT-based classification method [209] | STFT + DenseNet-201 | 3 | 91.0 |
| Proposed CWT-based classification method [209] | CWT + DenseNet-201 | 3 | 94.8 |
| Proposed SLT-based classification method [209] | SLT + DenseNet-201 | 3 | 96.2 |

**LDC*: Linear discriminant classifier, *EMCA*: Expectation-maximization clustering algorithm, *RRHOS*: RR intervals and higher-order statistics, *HIT*: Homeomorphically irreducible tree

6.5. SUMMARY

This chapter proposes a SLT + DenseNet-201 method to classify healthy heart, atrial fibrillation, and ventricular fibrillation from ECG records. In the proposed SLT+ DenseNet-201 method, the combination of SL and deep neural network architectures successfully detect cardiac arrhythmia. Results show that the SL can correctly detect cardiac arrhythmias. In the study, SL converts one-dimensional ECG records into two-dimensional RGB images by providing the time-frequency spectrogram. The results show that the DenseNet-201 successfully detected all the images under the atrial fibrillation categories. In other cases, the performance of DenseNet is reasonable compared to AlexNet and GoogLeNet. In the proposed method, denoising of ECG signals is not required, which reduces the computational requirements. With more training data, the proposed method may be implemented for clinical practice and by classifying more types of arrhythmias. This work is summarized and published in [209].

CHAPTER 7

SECURITY AND COMPRESSION OF ECG SIGNAL

In previous years, the advancement of the internet and communication networks created many avenues for information exchange. The internet is a ubiquitous information exchange infrastructure and has become a part of life. Communication between people and exchanging information and data has become more accessible and convenient with the internet. But the transmission of information and data over the internet is not secure. While using the internet, preventing data from unauthorized access is a primary concern. Technological advancement and the growth of the internet show new avenues in the secure and efficient transmission of biomedical information. Biomedical signals like electrocardiogram (ECG) and electroencephalogram (EEG) provide vital information on health conditions and have become popular in biometric identity and security applications. The exchange of biomedical information with medical practitioners to seek remote medical assistance demands secure and efficient transmission. Hence, modern healthcare systems demand a secure and reliable transmission of these signals.

At present, the demand for secure and reliable transmission of ECG signals is ever-increasing. Watermarking is a possible solution to protect and secure ECG signals. Also, in modern health care systems, sometimes it is required to continuously observe the ECG signal of a subject over extended periods of duration, which generates a large volume of data. This data must be transmitted remotely to a hospital or a medical practitioner. This demands a large storage capacity and channel bandwidth to store and transmit generated ECG data. Thus, ECG signal compression is vital for efficiently transmitting and storing ECG data in large volumes. In this chapter, a method is proposed that integrates watermarking and compression of an ECG signal of a subject.

7.1. WATERMARKING OF ECG SIGNAL

Secure and efficient transmission of biomedical signals containing sensitive and vital health information of a subject over the network is challenging. As an ECG signal contains the vital cardiac information of a subject, watermarking is an attractive choice to secure the cardiac information. ECG watermarking can provide secure transmission of an ECG signal and restore it to its original state. While watermarking an ECG signal, the ECG signal is the cover signal, and subject details are watermarked. Two approaches, frequency and spatial domains, are used to embed a watermark in the ECG signal. The frequency is modified in the frequency domain, whereas the intensities of pixels are modified in the spatial domain. Fig. 7.1 shows the block

diagram of an architecture to watermark ECG signals.

Embedding watermarking data to mask an ECG signal degrades the quality of the information in an ECG signal, thus affecting the diagnosis. Deterioration of the ECG signal may result in the loss of critical health information, which is the primary disadvantage of ECG signal watermarking [219]. The QRS complex, R peak, P, and T waves provide critical diagnostic information in an ECG signal. Hence, ECG watermarking should minimally affect the signal to preserve the information for accurate diagnosis and still provide sufficient security.

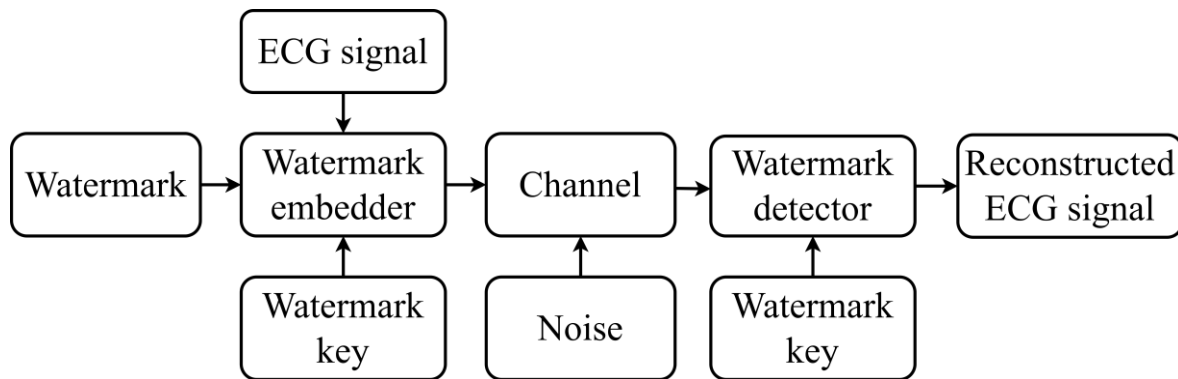


Fig. 7.1: Block diagram of the ECG watermarking system

Apart from security, watermarking adds additional information to the signal. The virtues of watermarking technique that make it valuable to apply to ECG signal transmission are (i) watermarking is imperceptible, (ii) embedded watermarks are inseparable from the embedded work, (iii) watermarked signals undergo the same transformation as the signal [220]. The desirable properties of a watermarking system are listed below:

Effectiveness is defined as the probability of detecting messages just after embedding. Ideally, 100% effectiveness is desired.

Fidelity represents the similarity between the watermarked and the original signal.

Data payload is the number of bits encoded within a signal or within a unit of time by a watermark encoder. Data payload encodes within a signal or within a unit of time.

The false-positive rate is the number of signals identified as watermark embedded, but they have no embedded watermark. The watermarking system should possess a low false-positive rate.

Robustness represents the ability to detect watermarks after signal processing. A robust watermark system should withstand rotation, scaling, cropping, compression, additive Gaussian noise, and many more operations.

Security implies the ability of the watermark to protect the information against hostile attacks. Any process that spoils the purpose of watermarking is known as a hostile attack. The types of

attacks are categorized as unauthorized embedding, unauthorized detection, and unauthorized removal. Unauthorized embedding and removal are classified as active attacks as they modify the cover signal. Unauthorized detection is a passive attack because it does not modify the cover signal. A secret watermark is required and must be undetectable by unauthorized users. As the volume of medical images in healthcare continues to grow, the security of these images becomes a paramount concern. In the healthcare domain, watermarking emerges as a potential solution to safeguard and prevent unauthorized modifications to medical images. In telemedicine, watermarking is widely employed to verify the authenticity and integrity of medical images. Moreover, in the context of telemedicine, watermarking plays a crucial role in ensuring the secure transmission of medical information and images [221]. Within healthcare applications, watermarking techniques prove suitable for protecting electronic subject records against unauthorized access [222].

In literature, various groups of researchers have proposed many algorithms for ECG watermarking. Sanivarapu et al. [223] proposed a wavelet-based ECG watermarking approach to hide the subject information in the ECG signal as a QR image. In this work, a 1D-ECG signal is converted into a 2D-ECG image. The resultant 2D-ECG image is decomposed using DWT. The QR image and the detail coefficients of the wavelet are decomposed using QR decomposition. In the next step, the watermarking data is embedded into a 2D-ECG image.

The embedded subject information is easily extractable without distortion. Jero et al. [224] proposed a curvelet-based ECG signal watermarking. In [224], the 2D-ECG image is obtained from a 1D-ECG signal. Jero et al. [224] use curvelet transform, adaptive selection of watermark position, and a new threshold selection algorithm to obtain a high-quality watermarked signal. Kaur et al. [225] proposed a simple embed watermarking technique using a low-frequency chirp signal. This method allows complete removal of the embedded watermark at the receiver due to blind recovery.

Jero et al. [226] used the discrete wavelet transform (DWT) and singular value decomposition (SVD) to watermark an ECG signal. DWT decomposes the ECG signal, and SVD embeds the secret data in the decomposed signal. Results show that the proposed method in [226] achieved a very low signal degradation. The available methods in the literature use a 2D-ECG image to watermark an ECG signal. Banerjee and Singh [227] propose a new technique of steganography to hide subject information in which the encryption is performed within the TP segment of the ECG signal. In [228], Advanced Encryption Standard (AES), a public-key encryption is utilized to encrypt the ECG signal. Mathivanan et al. [228] devised a method for encrypting ECG signals, involving the transformation of ECG samples into binary equivalents

for decimal values. Subsequently, these binary strings are associated with corresponding strings known as Quick Response codes, which are further remapped to alternative decimal values. The resultant decimal values are then employed in lieu of the original ones. In [229], chaos-based cryptography using the Badola map is proposed to secure ECG signals in telemedicine.

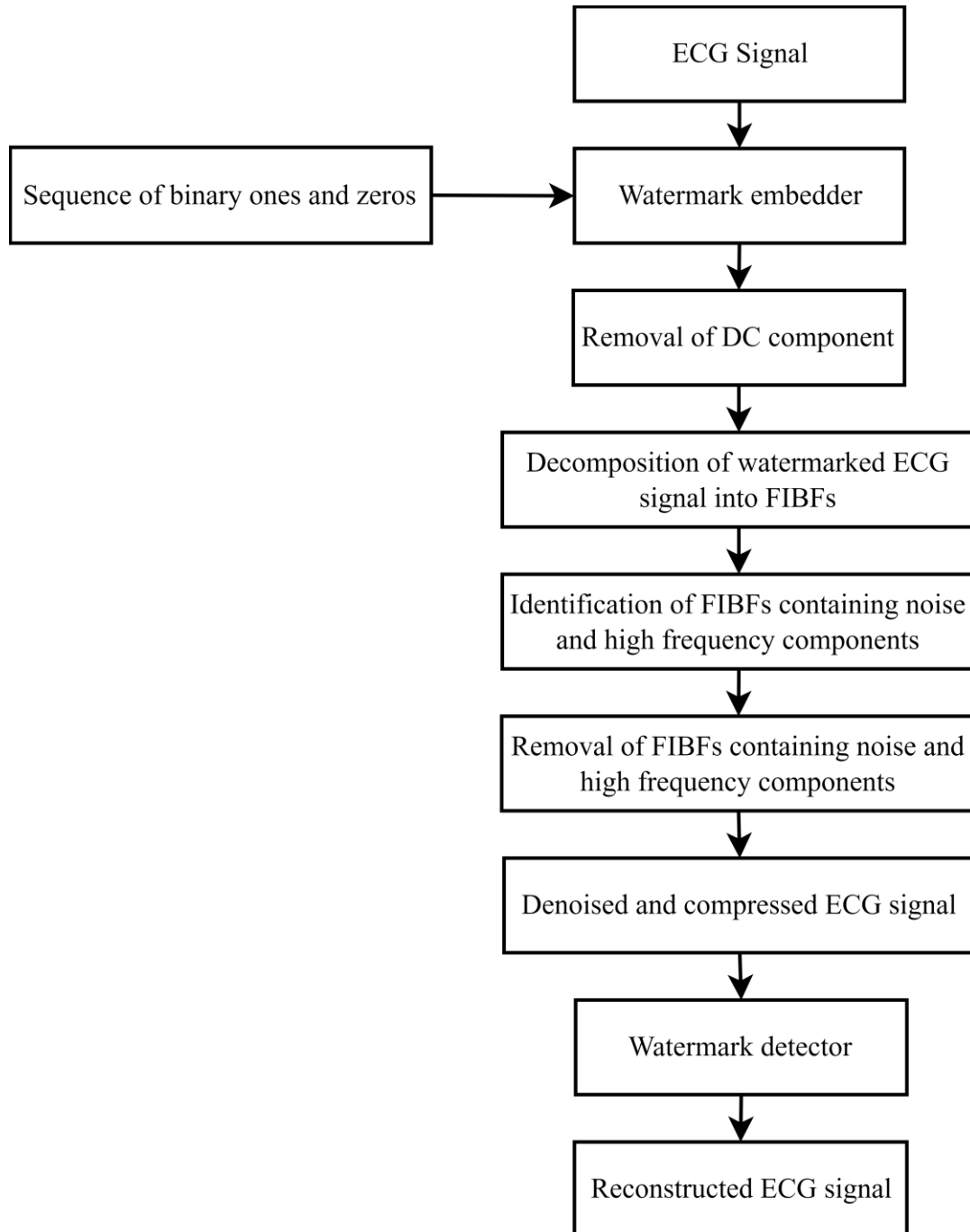


Fig. 7.2: Process flow diagram of the FDM based method

In this chapter, to protect the ECG signal, a 1D-ECG watermarking technique using FDM is proposed. The proposed watermarking scheme keeps the watermarked signal quality at a

satisfying level without damaging the characteristics of the ECG signal. This ability of the watermarking process makes it difficult to notice or perceive the embedded information in the watermarked signal. Fig. 7.2 shows the process flow diagram of the proposed watermarking method using FDM [230]. The watermarks in the proposed method are embedded in the ECG signal. A sequence of binary ones and zeros are added at even and odd-numbered samples of the ECG signal to produce a watermarked ECG signal. This watermarking does not alter the shape of the ECG signal. Hence the diagnosability is not influenced by watermarking. The watermarked ECG signal is further processed with the FDM. The FDM technique using DFT based zero-phase filter bank is shown in Fig. 7.3. The FDM decomposes the watermarked ECG signal $w[n]$ into a set of orthogonal FIBFs $w_i[n]$ with desirable frequency bands as described by Eq. (7.1).

$$w[n] = d_0 + \sum_{i=1}^M w_i[n] \quad (7.1)$$

Here d_0 is the mean value of watermarked ECG signal $w[n]$, and $w_i[n]$ represents M orthogonal FIBFs with $i = 1, 2, 3, \dots, M$. The frequency response of the i^{th} filter in a zero-phase filter bank is defined using Eq. (7.2)

$$H_i[k] = \begin{cases} 1, & k_{i-1} + 1 \leq k \leq k_i, (N - k_i) \leq k \leq (N - k_{i-1} - 1) \\ 0, & \text{otherwise} \end{cases} \quad (7.2)$$

Here N represents the length of the signal, $k_0 = 0$, and $k_M = N/2$. $w_i[n]$ are found by taking inverse DFT as defined by Eq. (7.3)

$$w_i[n] = \sum_{k=0}^{N-1} \left[H_i[k] W[k] \exp\left(\frac{j2\pi kn}{N}\right) \right] \quad (7.3)$$

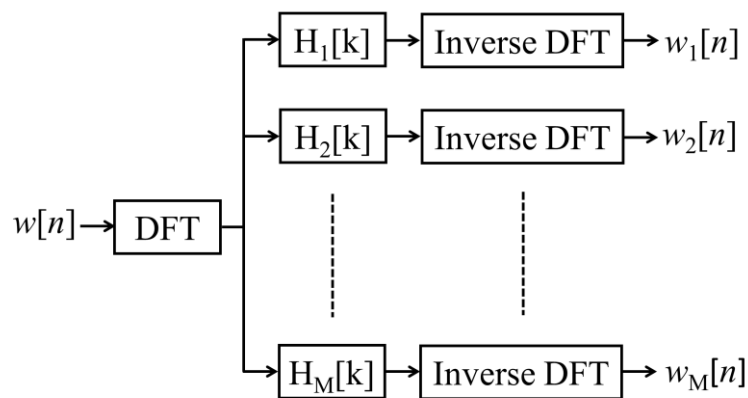


Fig. 7.3: A schematic representation of DFT based FDM

In this method, FDM decomposes the watermarked ECG signal into three FIBFs. The second

FIBF corresponding to the high-frequency components of the signal is discarded. The combination of the remaining two FIBFs provides the watermarked reconstructed ECG signal. The FDM removes noises and artifacts present in the ECG signal. The FDM improves the output signal-to-noise ratio (SNR_{out}) and provides data compression by removing the redundant information present in the original signal. In the last step, the reconstructed original ECG signal is obtained from the compressed ECG signal by removing the watermarked sequence embedded in the original ECG signal.

7.2. SIMULATIONS AND PERFORMANCE EVALUATION OF THE FDM-BASED WATERMARKING METHOD

The proposed FDM-based watermarking method is implemented in MATLAB® R2020. All the parameters described above are evaluated on a computer with the following configuration: Intel® Core i3-4030U CPU @ 1.90 GHz, 1.90 GHz, and 12 GB RAM. ECG signals from the MIT-BIH arrhythmia database are used to validate the efficacy of the proposed FDM-based method. The performance of this method is evaluated using the output signal-to-noise ratio (SNR_{out}) (3.3) and output percentage root mean square difference (PRD_{out}) (3.6).

The SNR_{out} is a measure of the quality of the output signal. A large value of SNR_{out} reflects the better quality of the output signal. PRD quantifies the quality of the reconstructed signal by computing the difference between the original and reconstructed signal. A lower value of PRD indicates the efficacy of the method in signal reconstruction.

Table 7.1 shows the PRD_{out} value obtained at different input signal-to-noise ratio (SNR_{in}) values for ECG signals of the MIT-BIH arrhythmia database. The PRD_{out} is computed for an SNR_{in} of -10 dB, -5 dB, 0 dB, 5 dB, and 10 dB, respectively. From Table 7.1, the proposed method provides low PRD_{out} values at different SNR_{in} . For record 104, the value of PRD_{out} is 0.338% and 0.187% at -10 dB and 10 dB SNR_{in} , respectively. Record 116 has PRD_{out} values of 0.375% and 0.294% at 0 dB and 5 dB, respectively. Record 209 has PRD_{out} values of 0.537% and 0.515% at 0 dB and 5 dB, respectively. This work is published in [230].

Similarly, the SNR_{out} for various ECG signals at different SNR_{in} is tabulated in Table 7.2. The proposed FDM-based watermarking method improved the appropriate signal-to-noise ratio for various ECG signals at different SNR_{in} . For record 221, SNR_{out} is 19.1 dB and 30.8 dB at -5 dB and 10 dB SNR_{in} . Record 112 has a 13.5 dB output signal-to-noise ratio at -10 dB SNR_{in} . Record 117 has a 19.4 dB output signal-to-noise ratio at -5 dB SNR_{in} . This work is published in [230]. Table 7.3 shows the obtained SNR_{out} values for different types of noise-contaminated realtime ECG signals. The proposed method provides good SNR_{out} at different values of SNR_{in} . For ECG

signal corrupted with muscle contraction noise the proposed method provides an SNR_{out} of 28.7 dB and 31 dB at 5 dB and 10 dB SNR_{in} , respectively. This work is published in [230].

Table 7.1: PRD_{out} of various MIT-BIH ECG signals as a function of SNR values

| ECG Record | PRD_{out} (%) at different SNR_{in} | | | | |
|------------|---|-------|-------|-------|-------|
| | -10 dB | -5 dB | 0 dB | 5 dB | 10 dB |
| 100 | 0.531 | 0.507 | 0.431 | 0.328 | 0.3 |
| 101 | 0.668 | 0.618 | 0.457 | 0.349 | 0.311 |
| 102 | 0.616 | 0.598 | 0.511 | 0.43 | 0.36 |
| 103 | 0.471 | 0.448 | 0.369 | 0.279 | 0.254 |
| 104 | 0.338 | 0.311 | 0.237 | 0.21 | 0.187 |
| 105 | 0.421 | 0.405 | 0.371 | 0.298 | 0.258 |
| 107 | 0.529 | 0.511 | 0.511 | 0.501 | 0.501 |
| 109 | 0.452 | 0.419 | 0.372 | 0.301 | 0.271 |
| 111 | 0.381 | 0.36 | 0.313 | 0.248 | 0.24 |
| 112 | 0.515 | 0.498 | 0.364 | 0.286 | 0.257 |
| 113 | 0.385 | 0.372 | 0.365 | 0.324 | 0.301 |
| 114 | 0.522 | 0.514 | 0.471 | 0.397 | 0.298 |
| 116 | 0.437 | 0.413 | 0.375 | 0.294 | 0.264 |
| 117 | 0.446 | 0.42 | 0.373 | 0.319 | 0.292 |
| 118 | 0.512 | 0.503 | 0.468 | 0.403 | 0.384 |
| 200 | 0.891 | 0.88 | 0.813 | 0.781 | 0.717 |
| 201 | 0.64 | 0.615 | 0.507 | 0.411 | 0.305 |
| 202 | 0.673 | 0.624 | 0.552 | 0.431 | 0.413 |
| 203 | 0.772 | 0.765 | 0.716 | 0.691 | 0.668 |
| 205 | 0.627 | 0.612 | 0.563 | 0.521 | 0.5 |
| 207 | 0.524 | 0.510 | 0.498 | 0.414 | 0.4 |
| 208 | 0.751 | 0.748 | 0.732 | 0.7 | 0.682 |
| 209 | 0.574 | 0.564 | 0.537 | 0.515 | 0.504 |
| 210 | 0.433 | 0.425 | 0.41 | 0.396 | 0.38 |
| 212 | 0.561 | 0.55 | 0.532 | 0.509 | 0.468 |
| 213 | 0.635 | 0.613 | 0.584 | 0.536 | 0.504 |
| 214 | 0.715 | 0.707 | 0.692 | 0.658 | 0.658 |
| 215 | 0.497 | 0.488 | 0.488 | 0.434 | 0.411 |
| 217 | 0.590 | 0.581 | 0.569 | 0.561 | 0.554 |
| 220 | 0.671 | 0.644 | 0.623 | 0.620 | 0.614 |
| 221 | 0.548 | 0.536 | 0.445 | 0.401 | 0.37 |
| 222 | 0.662 | 0.652 | 0.638 | 0.535 | 0.517 |
| 228 | 0.44 | 0.431 | 0.410 | 0.391 | 0.369 |
| 231 | 0.689 | 0.614 | 0.541 | 0.5 | 0.468 |
| 232 | 0.708 | 0.69 | 0.601 | 0.586 | 0.516 |
| 233 | 0.715 | 0.702 | 0.684 | 0.614 | 0.599 |
| 234 | 0.624 | 0.592 | 0.423 | 0.386 | 0.342 |

Table 7.2: Output SNR obtained at different values of SNR_{in}

| ECG Record | SNR_{out} (dB) at different SNR_{in} | | | | |
|------------|--|-------|------|------|-------|
| | -10 dB | -5 dB | 0 dB | 5 dB | 10 dB |
| 100 | 13.15 | 18.2 | 23.3 | 27.5 | 30.4 |
| 101 | 10.7 | 18.3 | 24.5 | 27.1 | 29.8 |
| 102 | 10.9 | 15.6 | 22.8 | 26.8 | 30 |
| 103 | 12.8 | 17.9 | 23.1 | 27.9 | 30.8 |
| 104 | 11.6 | 19 | 23.9 | 27.6 | 29.9 |
| 105 | 10.6 | 18.7 | 24.2 | 27.4 | 30.4 |
| 106 | 12.2 | 16.8 | 21.3 | 25.2 | 29.7 |
| 107 | 11.8 | 12.1 | 19.9 | 24.6 | 28.6 |
| 108 | 11.4 | 17.8 | 22.6 | 26.1 | 29.2 |
| 109 | 12.2 | 18.3 | 23.7 | 27.5 | 30.7 |
| 111 | 12.8 | 18 | 24 | 28.2 | 31.1 |
| 112 | 13.5 | 19.2 | 24.1 | 27.7 | 29.9 |
| 113 | 13.1 | 16.4 | 21.7 | 25.7 | 28.9 |
| 114 | 12.7 | 17.6 | 23.3 | 28.6 | 31 |
| 115 | 14.3 | 18.4 | 24.6 | 28.2 | 30 |
| 106 | 12.2 | 16.8 | 21.3 | 25.2 | 29.7 |
| 107 | 11.8 | 12.1 | 19.9 | 24.6 | 28.6 |
| 108 | 11.4 | 17.8 | 22.6 | 26.1 | 29.2 |
| 109 | 12.2 | 18.3 | 23.7 | 27.5 | 30.7 |
| 111 | 12.8 | 18 | 24 | 28.2 | 31.1 |
| 112 | 13.5 | 19.2 | 24.1 | 27.7 | 29.9 |
| 113 | 13.1 | 16.4 | 21.7 | 25.7 | 28.9 |
| 114 | 12.7 | 17.6 | 23.3 | 28.6 | 31 |
| 115 | 14.3 | 18.4 | 24.6 | 28.2 | 30 |
| 116 | 13.1 | 18.8 | 23.6 | 28.1 | 30.5 |
| 117 | 9.6 | 19.4 | 23.1 | 26.9 | 30.6 |
| 118 | 12.9 | 17.8 | 23.9 | 27.8 | 30.9 |
| 119 | 12.4 | 16 | 21.5 | 26.1 | 29.8 |
| 121 | 13.4 | 17.6 | 22.4 | 27.3 | 29.3 |
| 122 | 12.7 | 16.5 | 21 | 24.8 | 28.8 |
| 123 | 10.4 | 15.6 | 20.5 | 25.8 | 30.1 |
| 124 | 11.1 | 15.3 | 19.8 | 24.7 | 29.4 |
| 200 | 13.3 | 19.5 | 24.7 | 28.3 | 31.2 |
| 201 | 11.7 | 17.6 | 23.4 | 25.3 | 28 |
| 202 | 12.9 | 17.2 | 22.1 | 27.2 | 30.2 |
| 203 | 13.6 | 17.8 | 23 | 26.7 | 29.9 |
| 205 | 10.4 | 18.7 | 24.3 | 28 | 30.4 |
| 207 | 12 | 18.1 | 22.5 | 27.5 | 31.2 |
| 208 | 12.5 | 16.9 | 22.7 | 26.2 | 31.3 |
| 213 | 11.8 | 18.5 | 23.8 | 27.7 | 29.8 |
| 214 | 14.1 | 17.4 | 22.6 | 24.1 | 28.9 |
| 215 | 13.8 | 15.6 | 21.4 | 23.8 | 30.6 |
| 217 | 15.1 | 18.6 | 23.2 | 28.4 | 31.6 |
| 220 | 13.9 | 17.8 | 22.1 | 27 | 31.6 |
| 221 | 9.7 | 19.1 | 23.4 | 27.2 | 30.8 |

| ECG Record | SNR_{out} (dB) at different SNR_{in} | | | | |
|------------|--|-------|------|------|-------|
| | -10 dB | -5 dB | 0 dB | 5 dB | 10 dB |
| 222 | 14.3 | 18.4 | 24.5 | 28.1 | 31.2 |
| 231 | 10.9 | 18.8 | 23.7 | 28.1 | 30.7 |
| 232 | 13 | 19.5 | 24 | 29.2 | 31.9 |
| 233 | 14.4 | 18.9 | 23.5 | 26.9 | 30.1 |
| 234 | 12 | 19.3 | 22.9 | 27.9 | 30.4 |

Table 7.3: Output SNR obtained at different values of SNR_{in} in the presence of various noises

| ECG Record | SNR_{out} (dB) | | | | |
|---|------------------|-------|------|------|-------|
| | -10 dB | -5 dB | 0 dB | 5 dB | 10 dB |
| ECG signal corrupted with muscle contraction | 11.7 | 18.9 | 23.3 | 28.7 | 31 |
| ECG signal corrupted with motion artifact | 10.4 | 17.9 | 24.2 | 26.8 | 30.4 |
| ECG signal corrupted with Electromyographic noise | 12 | 16.4 | 22.3 | 27.6 | 30.8 |

7.3. COMPRESSION OF ECG SIGNALS USING THE FOURIER DECOMPOSITION METHOD

With advancements in communication and digital storage technology, ECG signal compression is getting more attention from researchers. ECG signal compression techniques are classified into three categories: (i) time-domain techniques, (ii) frequency (transform) domain techniques, and (iii) hybrid techniques [231]. Time-domain techniques are based on direct data compression and parameter extraction, while frequency-domain techniques are transformation-based. Compression techniques, such as differential pulse code modulation (DPCM), reduce signal redundancy by considering the correlation between inter-sample. Although DPCM-based compression techniques are simple and easy to implement, they suffer from a low compression rate. Data compression by entropy coding is based on assigning the variable-length codewords to the signal according to the frequency of occurrence. Huffman and Shannon Fano coding methods are commonly used for assigning variable-length codewords to the signals. The frequently occurring signals are assigned a shorter codeword length, while less occurring signals have longer codeword lengths. However, in variable-length coding, decoding errors may occur due to transmission errors.

In the field of telemedicine, tediagnosis and telesurgery where a large amount of medical data is transmitted over a network, signal integrity is an important issue. Any alteration in medical images can significantly mislead the diagnosis and treatment. However, to efficiently transmit and store a large amount of medical data compression is required. A compression technique

may introduce loss of information, compromising the diagnostic value of medical data. In clinical applications where such diagnostic values are crucial for accurate diagnosis the trade-off between signal integrity and compression efficiency becomes vital. While selecting the compression algorithm the medical practitioner must assess the impact of compression on signal fidelity. A high compression ratio may affect the essential diagnostic values and morphological features of biomedical signals degrading the signal integrity. So, in healthcare applications, it is important to make an equilibrium between compression efficiency and signal integrity [232].

In the transform compression technique, the input signal is preprocessed by a linear orthogonal transform. The transformed output is appropriately encoded with fewer data needed to characterize the input signal. Many orthogonal transforms, such as Karhunen-Loeve transform [233], Fourier transform [234], and discrete cosine transform [235], are used to compress the ECG signal. New techniques based on discrete wavelet transform (DWT) [236] and neural networks [237] are also used to compress an ECG signal. The use of DWT provides a better localization of different morphological features of the ECG signal. In neural network-based compression, the data is compressed by extracting the features of the ECG signal through self-learning. Although the neural network-based approach has strong adaptability, anti-interference, and parallel processing, optimizing hidden layers is difficult. In this chapter, the ECG signal compression is achieved by the FDM. FDM being free from mode mixing, end effect artifacts, and detrend uncertainty, preserves the valuable information embedded in the ECG signal.

7.4. SIMULATIONS AND PERFORMANCE EVALUATION OF THE FDM-BASED COMPRESSION METHOD

The proposed FDM-based approach safeguards the ECG signal and compresses it to minimize the storage and transmission bandwidth requirement. The performance of the proposed method is evaluated using compression ratio (CR) and computational time (CT). The CR is the measure of relative reduction in the data size.

$$CR = \frac{(\text{Data size of ECG signal before compression})}{(\text{Data size of ECG signal after compression})} \quad (7.4)$$

ECG signals from the MIT-BIH arrhythmia database are taken to validate the proposed FDM-based method. The FFT is used to compute the DFT of the signal, and the computational complexity of the proposed FDM-based method is equal to $(N \log_2 N)$. Hence the proposed FDM-based method has the advantage of low computation complexity.

Fig. 7.4 shows the simulation results obtained from the proposed FDM-based method. Record number 109 from the MIT-BIH arrhythmia database, selected as an ECG input, is shown in Fig. 7.4 (a). The watermarked ECG signal and the reconstructed ECG signal are shown in Fig. 7.4 (b) and Fig. 7.4 (c), respectively. Fig. 7.4 (d) depicts the reconstructed ECG signal as a replica of the input ECG signal. This work is published in [230].

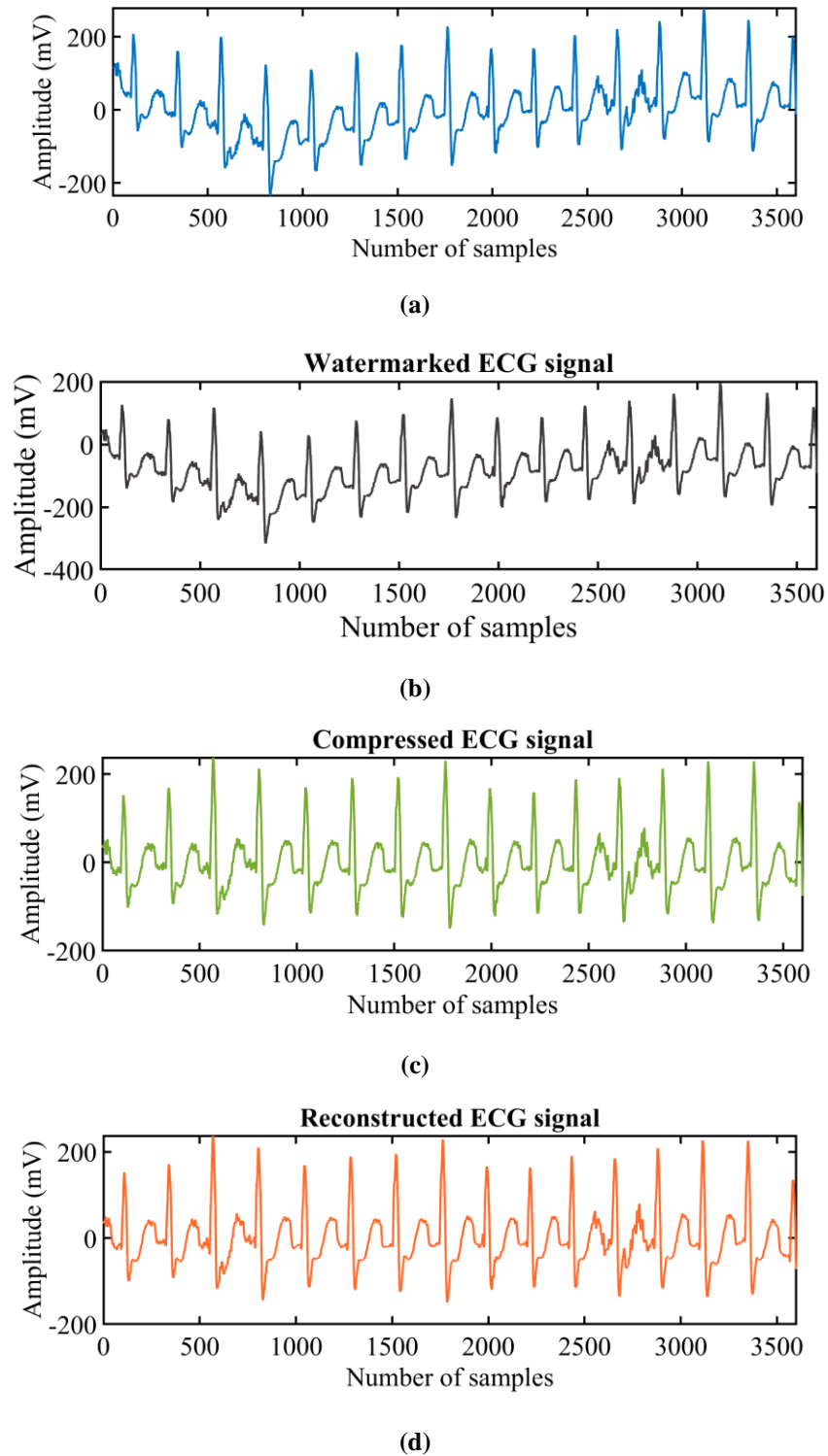


Fig. 7.4: (a) Input ECG signal (MIT-BIH-109) (b) ECG signal with watermark (c) compressed ECG signal (d) reconstructed output ECG signal

It is clear from Fig. 7.4 (c) that the proposed FDM-based method provides lossless compression. The compression ratio is used to measure the compression ability of the proposed FDM-based method. The CR for various ECG records is shown in Table 7.4. This work is published in [230].

The proposed FDM-based method provides an excellent compression ratio. For ECG signal-101 from the MIT-BIH arrhythmia database, the compression ratio is 35.2, while 33.6 is the compression ratio for ECG signal-118. The computation time is an indicative measurement of the complexity of the proposed method. Table 7.4 depicts the computation time for the ECG record. For ECG signal-205, the computation time is 12.935 seconds, while ECG signal record-221 has a computation time of 12.033 seconds. This work is published in [230].

Table 7.4: Compression ratio and computation time for ECG records

| ECG signal | CR | CT (second) | ECG signal | (CR) | CT (second) |
|------------|------|-------------|------------|------|-------------|
| 100 | 34.1 | 13.271 | 200 | 33.8 | 13.841 |
| 101 | 35.2 | 13.660 | 201 | 29.7 | 12.612 |
| 102 | 33.1 | 13.133 | 202 | 31.9 | 13.7 |
| 103 | 30.8 | 13.044 | 203 | 33.4 | 13.218 |
| 104 | 33.7 | 13.480 | 205 | 34.0 | 12.935 |
| 105 | 33.7 | 13.560 | 207 | 29.0 | 13.751 |
| 106 | 32.4 | 13.213 | 208 | 27.3 | 12.258 |
| 107 | 31.4 | 13.718 | 209 | 31.0 | 13.018 |
| 108 | 30.1 | 13.014 | 210 | 33.0 | 13.892 |
| 109 | 32.8 | 13.465 | 213 | 31.5 | 12.342 |
| 111 | 29.7 | 12.816 | 214 | 29.6 | 13.152 |
| 112 | 31.4 | 13.727 | 215 | 30.4 | 13.481 |
| 113 | 32.4 | 12.575 | 217 | 27.8 | 13.155 |
| 114 | 28.8 | 13.156 | 219 | 31.8 | 12.86 |
| 115 | 27.5 | 12.982 | 221 | 31.0 | 12.033 |
| 116 | 30.9 | 13.384 | 228 | 29.4 | 13.161 |
| 117 | 32.0 | 13.308 | 230 | 33.4 | 12.014 |
| 118 | 33.6 | 13.499 | 231 | 32.7 | 12.167 |
| 119 | 28.1 | 12.517 | 233 | 29.6 | 13.476 |
| 122 | 30.7 | 13.113 | 234 | 31.8 | 12.166 |

7.5. COMPARISON WITH EXISTING WORKS

Furthermore, a comparison of the *PRD* and *CR* of the proposed method with other techniques is presented in Table 7.5. Table 7.5 shows that the proposed FDM-based method provides a high compression ratio and low *PRD* values. For ECG signal-100, Fathi et al.[238] achieved a *CR* of 31.42 with a *PRD* of 3.21%, while Pandey et al.[239] obtained a *CR* of 31.42 with a

PRD of 1%. The proposed FDM-based method provides a *CR* of 34.1 with a *PRD* of only 0.3%. Similarly, for ECG signal-101, the proposed FDM-based method provides a *CR* of 35.2 with a *PRD* of 0.311%. In comparison, the methods in [238] and [239] provide *CR* of 28.47 (*PRD*-3.41%) and 19.21 (*PRD*-1.19%), respectively. The proposed FDM-based method provides a compression ratio of 30.8 to 35.2, while the *PRD* value ranges from 0.254% to 0.311%. The other existing method proposed by Fathi et al. [238] provides a compression ratio ranging from 26.56 to 31.42 with a *PRD* value ranging from 3.07% to 5.34%. The method suggested by Pandey et al. [239] offers a compression ratio ranging from 15.6 to 22.08, while the *PRD* value ranges from 1% to 1.19%.

Table 7.5: Comparing the results of the proposed FDM-based method and some existing methods

| ECG signal | Fathi et al. [216] | | Pandey et al. [217] | | Proposed FDM-based method [209] | |
|------------|--------------------|----------------|---------------------|----------------|---------------------------------|----------------|
| | <i>CR</i> | <i>PRD</i> (%) | <i>CR</i> | <i>PRD</i> (%) | <i>CR</i> | <i>PRD</i> (%) |
| 100 | 31.42 | 3.21 | 16.87 | 1 | 34.1 | 0.3 |
| 101 | 28.47 | 3.41 | 19.21 | 1.19 | 35.2 | 0.311 |
| 103 | 26.56 | 5.34 | 15.6 | 1.01 | 30.8 | 0.254 |
| 117 | 29.34 | 3.07 | 22.08 | 1.01 | 32 | 0.292 |

The above results show the efficacy of the proposed FDM-based method. The high *CR* shows the high compression ability and a lower value of *PRD* reflects the lossless nature of the proposed FDM-based method.

7.6. SUMMARY

This chapter uses an FDM-based technique to analyze ECG watermarking and compression. The proposed method can secure the transmission of ECG signals and reduce the transmission bandwidth while preserving the shape of the ECG signal waveform. The simulation results show that the proposed watermarking scheme does not alter the ECG signal characteristics. The proposed method effectively removes the noise components and improves the quality of the reconstructed ECG signal. The proposed FDM-based method provides a low percentage *PRD*, high *SNR_{out}*, and high compression ratio compared to existing techniques. Hence, the proposed watermarking and compression technique using FDM provides an efficient, reliable, and secure way to transfer the ECG signals by minimizing the losses in the original ECG signal. The proposed FDM-based technique with denoising and compression ability secures the ECG signals with less hardware complexity. So, the proposed FDM-based method may be implemented in portable devices to transmit denoised and compressed ECG signals to remote medical practitioners. This work is summarized and published in [230].

CHAPTER 8

CONCLUSIONS AND FUTURE WORK

Globally, cardiovascular disease (CVD) detection is a primary concern due to its high mortality and morbidity rate. Electrocardiogram (ECG) is a popular tool to detect CVD and other heart abnormalities. However, ECG signals suffer from various noises that mislead the diagnosis. Removal of these noises is essential for the detection of CVD. This report uses a method based on the FDM to denoise the ECG signals taken from the MIT-BIH arrhythmia database. The performance of the proposed denoising method is also validated with real time ECG signal. The proposed method provides relevant results with noises such as PLI, BW, white Gaussian noise, MA, Muscle contraction, and EMG at different signal-to-noise ratio values. The obtained low *PRD* values also reflect the efficacy of the proposed FDM-based denoising method.

In ECG signals, characteristics such as R peak and QRS complex are used to evaluate the heart's functioning and detect CVDs. An algorithm utilizing FrFT is used to detect the QRS complex peaks. The proposed algorithm is evaluated in the presence and absence of PLI and MA both. A BPF is used to reduce the noise level in the ECG signals. Using the proposed FrFT-based algorithm, an overall sensitivity, positive predictivity, and error of 99.83%, 99.48%, and 0.008, respectively, is obtained without PLI and MA. In the presence of PLI and MA, the proposed FrFT-based method gives an overall sensitivity, positive predictivity, and error of 99.83%, 99.03%, and 0.01, respectively.

Further, the classification of arrhythmias using ECG signals is considered in this report. This work does detect two popular arrhythmias, namely, atrial fibrillation and ventricular fibrillation. A combination of SLT and deep CNN is used to classify ECG signals into three classes: healthy heart, atrial fibrillation, and ventricular fibrillation. Results show that SLT, with superior denoising capability, can detect the QRS complex peak by providing a high-resolution TF spectrogram. SLT converts the one-dimensional ECG signals into 2D images, which are utilized for classification by deep CNN. Three deep CNNs AlexNet, GoogLeNet, and DenseNet-201, are used to classify the ECG signals. The proposed method with DenseNet-201 gives the best results with a classification accuracy of 96.2%. The proposed SLT+DenseNet-201 method does not require any extra denoising step, reducing the circuit complexity.

Secure and efficient transmission of ECG signal is also essential as ECG signal contains not only cardiac information but also personal information. Watermarking emerges as an efficient

tool to secure ECG signals. Watermarking can protect ECG signals without altering the morphological features. However, a long-duration ECG signal is required to detect cardiac abnormalities effectively, and efficient transmission of this signal is highly needed. In this work, ECG signal security and compression are achieved using FDM. In the proposed FDM-based method, the ECG signal is watermarked first, and then this watermarked signal is compressed using FDM. Also, the obtained results show the efficacy of the proposed method to remove the noises and improve the reconstructed ECG signal quality. Compared to existing techniques, the low PRD , high SNR_{out} , and high compression ratio prove that the proposed watermarking and compression technique using FDM is an efficient, reliable, and secure way to transfer the ECG signals.

The proposed techniques can be utilized for other biomedical signals in the future. Also, the number of classes to cover many CVDs can be extended. In the future, through the application of rigorous cross-validation techniques, the model may achieve generalization across diverse subject datasets. Also, detailed exploration and optimization of neural network hyperparameters may improve performance and efficiency. In the proposed work, a single FDM-based technique is employed to achieve denoising, compression, and security of the ECG signal. This technique utilises FFT reducing computational complexity and expediting the process. Consequently, the proposed FDM-based technique is suitable for implementation in real-world applications. The hardware realization of the proposed methodology is considered a further extension of this work. In the future, we plan to collaborate with hospitals to implement our SLT-based algorithm, aiming to obtain additional ECG records for optimizing the proposed algorithm. Through this collaboration, we intend to validate the results of our SLT-based algorithm with medical practitioners. Following optimization with an increased number of ECG records, we aim to develop an efficient system for CVD detection.

Publications From The Thesis

JOURNAL PAPER

- [1] Tripathi, Prashant Mani, Ashish Kumar, Rama Komaragiri, and Manjeet Kumar. "A Review on Computational Methods for Denoising and Detecting ECG Signals to Detect Cardiovascular Diseases." *Archives of Computational Methods in Engineering* (2021): 1-40. DOI: 10.1007/s11831-021-09642-2. Impact Factor: **8.171**.
- [2] Tripathi, Prashant Mani, Ashish Kumar, Rama Komaragiri, and Manjeet Kumar. "A novel approach for real-time ECG signal denoising using Fourier decomposition method." *Research on Biomedical Engineering*, DOI: 10.1007/s42600-022-00237-9. Impact Factor: **1.80**.
- [3] Tripathi, Prashant Mani, A. Kumar, M. Kumar, and R. Komaragiri, "Multilevel Classification and Detection of Cardiac Arrhythmias With High-Resolution Superlet Transform and Deep Convolution Neural Network," *IEEE Transactions on Instrumentation and Measurement*, vol. 71, pp. 1-13, 2022, Art no. 4006113, DOI: 10.1109/TIM.2022.3186355. Impact Factor: **5.332**.
- [4] Tripathi, Prashant Mani, Ashish Kumar, Rama Komaragiri, and Manjeet Kumar. "Watermarking of ECG signals compressed using Fourier decomposition method." *Multimedia Tools and Applications* (2022): 1-15. DOI:10.1007/s11042-021-11492-w. Impact Factor: **2.577**.
- [5] Tripathi, Prashant Mani, Ashish Kumar, Rama Komaragiri, and Manjeet Kumar. "QRS complex detection using a fast Fourier transform." communicated in *Biomedical Engineering Letters*.
- [6] Tripathi, Prashant Mani, Ashish Kumar, Rama Komaragiri, and Manjeet Kumar. "Multi-label Arrhythmia Classification of ECG Signal Using Deep Learning Techniques: Performance Evaluation of Deep Convolution Neural Network," *communicated in Journal of Biomedical Informatics*.

CONFERENCE PAPER

- [1] Tripathi, Prashant Mani, Ashish Kumar, Manjeet Kumar, and Rama S. Komaragiri. "Hardware Requirements of Different Wavelet Filter Bank Architectures for ECG Signal Denoising." In 2022 IEEE Conference on Interdisciplinary Approaches in Technology and Management for Social Innovation (IATMSI), pp. 1-5. IEEE, 2022.

REFERENCES

- [1] [Online]. Available: <https://world-heart-federation.org/resource/world-heart-vision-2030-driving-policy-change/> (CHANGE, DRIVING POLICY. “WORLD HEART VISION 2030.”) (last accessed on 10/06/2023).
- [2] [Online]. Available: [https://www.who.int/en/newsroom/factsheets/detail/cardio-vascular-diseases-\(CVD\)](https://www.who.int/en/newsroom/factsheets/detail/cardio-vascular-diseases-(CVD)). (last accessed on 06/02/2023).
- [3] Roth, Gregory A., George A. Mensah, Catherine O. Johnson, Giovanni Addolorato, Enrico Ammirati, Larry M. Baddour, Noël C. Barengo et al. “Global burden of cardiovascular diseases and risk factors, 1990–2019: update from the GBD 2019 study.” *Journal of the American College of Cardiology* 76, no. 25 (2020): 2982-3021.
- [4] Zhao, Dong. "Epidemiological features of cardiovascular disease in Asia." *JACC: Asia* 1, no. 1 (2021): 1-13.
- [5] [Online]. Available: <https://www.escardio.org/Research/ESC-Atlas-of-cardiology>. (last accessed on 06/02/2024).
- [6] Siontis, Konstantinos C., Peter A. Noseworthy, Zachi I. Attia, and Paul A. Friedman. "Artificial intelligence-enhanced electrocardiography in cardiovascular disease management." *Nature Reviews Cardiology* 18, no. 7 (2021): 465-478.
- [7] Reddy, K. Srinath, Bela Shah, Cherian Varghese, and Anbumani Ramadoss. “Responding to the threat of chronic diseases in India.” *The Lancet* 366, no. 9498 (2005): 1744-1749.
- [8] Prabhakaran, Dorairaj, Panniyammakal Jeemon, Meenakshi Sharma, Gregory A. Roth, Catherine Johnson, Sivadasanpillai Harikrishnan, Rajeev Gupta et al. “The changing patterns of cardiovascular diseases and their risk factors in the states of India: the Global Burden of Disease Study 1990–2016.” *The Lancet Global Health* 6, no. 12 (2018): e1339-e1351.
- [9] Indian Council of Medical Research, Public Health Foundation of India, Institute for Health Metrics and Evaluation. GBD India compares data visualization. <http://vizhub.healthdata.org/gbdcompare/> India. (last accessed on 06/02/2024).
- [10] Biel, Lena, Ola Pettersson, Lennart Philipson, and Peter Wide. “ECG analysis: a new approach in human identification.” *IEEE Transactions on Instrumentation and Measurement* 50, no. 3 (2001): 808-812.
- [11] Barrett, Kim E., Scott Boitano, Susan M. Barman, and Heddwen L. Brooks. “Ganong’s review of medical physiology twenty.” (2010).

- [12] [Online]. Available: <https://litfl.com/p-wave-ecg-library/>(last accessed on 06/02/2024).
- [13] [Online]. Available: <https://www.heartfoundation.org.nz/your-heart/heart-tests> (last accessed on 06/02/2024).
- [14] Petersen, Steffen E., Paul M. Matthews, Fabian Bamberg, David A. Bluemke, Jane M. Francis, Matthias G. Friedrich, Paul Leeson et al. "Imaging in population science: cardiovascular magnetic resonance in 100,000 participants of UK Biobank-rationale, challenges and approaches." *Journal of Cardiovascular Magnetic Resonance* 15, no. 1 (2013): 1-10.
- [15] Lüderitz, Berndt, and Antoni Bayés de Luna. "The history of electrocardiography." *Journal of electrocardiology* 50, no. 5 (2017): 539-539.
- [16] McNamara, Nicholas, Abdalla Ibrahim, Zahir Satti, Munir Ibrahim, and Thomas J. Kiernan. "Acute pericarditis: a review of current diagnostic and management guidelines." *Future Cardiology* 15, no. 02 (2019): 119-126.
- [17] Bonelli, Paolo, Irene Giannini, Maria Vittoria Matassini, and Alessio Menditto. "Drug Effects on ECGs." *New Concepts in ECG Interpretation* (2019): 137-146.
- [18] Lezo, J. S., J. A. Sobrino, J. Codina, I. Maté, and A. Epeldegui. "Vectocardiography in tetralogy of Fallot before." *Chest* 68, no. 4 (1975).
- [19] Goldberger, Ary L., "Goldberger's clinical electrocardiography." ECG basics: waves, intervals, and segments 2 (2013): 8-14.
- [20] Goldstein, Steven A., Itzhak Kronzon, Bijoy Khandheria, and Victor Mor-Avi, eds. ASE's comprehensive echocardiography. *Elsevier Health Sciences*, 2015.
- [21] Kern, Morton J., Paul Sorajja, and Michael J. Lim. Cardiac catheterization handbook. *Elsevier Health Sciences*, 2015.
- [22] Stirrup, James, Michelle Williams, Russell Bull, and Ed Nicol, eds. Cardiovascular computed tomography. *Oxford University Press*, 2019.
- [23] Manning, Warren J., and Dudley J. Pennell. Cardiovascular Magnetic Resonance E-Book. *Elsevier Health Sciences*, 2010.
- [24] Tripathi, Prashant Mani, Ashish Kumar, Rama Komaragiri, and Manjeet Kumar. "A Review on Computational Methods for Denoising and Detecting ECG Signals to Detect Cardiovascular Diseases." *Archives of Computational Methods in Engineering* (2021): 1-40.
- [25] Luz, Eduardo José da S., William Robson Schwartz, Guillermo Cámara-Chávez, and David Menotti. "ECG-based heartbeat classification for arrhythmia detection: A survey." *Computer Methods and Programs in Biomedicine* 127 (2016): 144-164.

- [26] Goldberger, Ary Louis, and Emanuel Gold-berger. "Clinical electrocardiography, a simplified approach." *Critical Care Medicine* 9, no. 12 (1981): 891-892.
- [27] LeCun, Yann, Yoshua Bengio, and Geoffrey Hinton. "Deep learning." *Nature* 521, no. 7553 (2015): 436-444.
- [28] Jafari, Mahboobeh, Afshin Shoeibi, Marjane Khodatars, Navid Ghassemi, Parisa Moridian, Niloufar Delfan, Roohallah Alizadehsani et al. "Automated Diagnosis of Cardiovascular Diseases from Cardiac Magnetic Resonance Imaging Using Deep Learning Models: A Review." *arXiv preprint arXiv:2210.14909* (2022).
- [29] Friesen, Gary M., Thomas C. Jannett, Manal Afify Jadallah, Stanford L. Yates, Stephen R. Quint, and H. Troy Nagle. "A comparison of the noise sensitivity of nine QRS detection algorithms." *IEEE Transactions on Biomedical Engineering* 37, no. 1 (1990): 85-98.
- [30] Satija, Udit, Barathram Ramkumar, and M. Sabarimalai Manikandan. "A review of signal processing techniques for electrocardiogram signal quality assessment." *IEEE Reviews in Biomedical Engineering* 11 (2018): 36-52.
- [31] Clifford, Gari D., Francisco Azuaje, and Patrick Mcsharry. "ECG statistics, noise, artifacts, and missing data." *Advanced Methods and Tools for ECG Data Analysis* 6 (2006): 18.
- [32] Li, Zhou, Xiaolei Li, Zhijun Zhu, Shan Zeng, Yanyan Wang, Yongjian Wang, and Aimin Li. "Signal analysis of electrocardiogram and statistical evaluation of myocardial enzyme in the diagnosis and treatment of patients with pneumonia." *IEEE Access* 7 (2019): 113751-113759.
- [33] Bailón, Raquel, Leif Sornmo, and Pablo Laguna. "A robust method for ECG-based estimation of the respiratory frequency during stress testing." *IEEE Transactions on Biomedical Engineering* 53, no. 7 (2006): 1273-1285.
- [34] Pan, Jiapu, and Willis J. Tompkins. "A real-time QRS detection algorithm." *IEEE Transactions on Biomedical Engineering* 3 (1985): 230-236.
- [35] Kligfield, Paul, Leonard S. Gettes, James J. Bailey, Rory Childers, Barbara J. Deal, E. William Hancock, Gerard Van Herpen, et al. "Recommendations for the standardization and interpretation of the electrocardiogram: part I: the electrocardiogram and its technology a scientific statement from the American Heart Association Electrocardiography and Arrhythmias Committee, Council on Clinical Cardiology; the American College of Cardiology Foundation; and the Heart Rhythm Society endorsed by the International Society for Computerized

- Electrocardiology.” *Journal of the American college of cardiology* 49, no. 10 (2007): 1109-1127.
- [36] Luo, Shen, and Paul Johnston. “A review of electrocardiogram filtering.” *Journal of Electrocardiology* 43, no. 6 (2010): 486-496.
- [37] [Online]. Available: [https://www.analog.com/media/en/training-seminars/design-handbooks/Basic-Linear-Design/Chapter8 .pdf](https://www.analog.com/media/en/training-seminars/design-handbooks/Basic-Linear-Design/Chapter8.pdf). (last accessed on 06/02/2024).
- [38] Kumar, Ashish, Rama Komaragiri, and Manjeet Kumar. “Design of efficient fractional operator for ECG signal detection in implantable cardiac pacemaker systems.” *International Journal of Circuit Theory and Applications* 47, no. 9 (2019): 1459-1476.
- [39] Acharya, U. Rajendra, Shankar M. Krishnan, Jos AE Spaan, and Jasjit S. Suri, eds. *Advances in Cardiac Signal Processing*. Berlin, Germany:: springer, 2007.
- [40] Jagtap, Sonal K., and M. D. Uplane., “Digital filter approach for ECG in signal processing.” In *Proceedings of international conference on advances in computing*, pp. 1075-1082. Springer India, 2012.
- [41] Wang, Kening, Shengqian Ma, Jing Feng, Weizhao Zhang, Manhong Fan, and Dan Zhao. “Design of ECG signal acquisition system based on DSP.” *Procedia Engineering* 29 (2012): 3763-3767.
- [42] Lee, Yujin, and Dosik Hwang. “Periodicity-based nonlocal-means denoising method for electrocardiography in low SNR non-white noisy conditions.” *Biomedical Signal Processing and Control* 39 (2018): 284-293.
- [43] Christov, Ivaylo, Tatyana Neycheva, Ramun Schmid, Todor Stoyanov, and Roger Abächerli. “Pseudo-real-time low-pass filter in ECG, self-adjustable to the frequency spectra of the waves.” *Medical & Biological Engineering & Computing* 55, no. 9 (2017): 1579-1588.
- [44] C. Watford, *Understanding ECG Filtering, EMS 12-Lead, EMS-Topics*, 2014.
- [45] Thakor, Nitish V., and Y-S. Zhu. “Applications of adaptive filtering to ECG analysis: noise cancellation and arrhythmia detection.” *IEEE Transactions on Biomedical Engineering* 38, no. 8 (1991): 785-794.
- [46] Wang, Xiao, You Zhou, Minglei Shu, Yinglong Wang, and Anming Dong. “ECG baseline wander correction and denoising based on sparsity.” *IEEE Access* 7 (2019): 31573-31585.
- [47] Wang, Jianhong, Yongqiang Ye, Xiang Pan, and Xudong Gao. “Parallel-type fractional zero-phase filtering for ECG signal denoising.” *Biomedical Signal Processing and*

Control 18 (2015): 36-41.

- [48] Cuomo, Salvatore, Giuseppe De Pietro, Raffaele Farina, Ardelio Galletti, and Giovanna Sannino. "A revised scheme for real time ecg signal denoising based on recursive filtering." *Biomedical Signal Processing and Control* 27 (2016): 134-144.
- [49] Mourad, Nasser. "ECG denoising algorithm based on group sparsity and singular spectrum analysis." *Biomedical Signal Processing and Control* 50 (2019): 62-71.
- [50] Cuomo, Salvatore, Giuseppe De Pietro, Raffaele Farina, Ardelio Galletti, and Giovanna Sannino. "A novel O (n) numerical scheme for ECG signal denoising." *Procedia Computer Science* 51 (2015): 775-784.
- [51] Panigrahy, D., and P. K. Sahu. "Extended Kalman smoother with differential evolution technique for denoising of ECG signal." *Australasian Physical & Engineering Sciences in Medicine* 39, no. 3 (2016): 783-795.
- [52] Jenkal, Wissam, Rachid Latif, Ahmed Toumanari, Azzedine Dliou, Oussama El B'charri, and Fadel MR Maoulainine. "An efficient algorithm of ECG signal denoising using the adaptive dual threshold filter and the discrete wavelet transform." *Biocybernetics and Biomedical Engineering* 36, no. 3 (2016): 499-508.
- [53] Singh, Pratik, Gayadhar Pradhan, and S. Shahnawazuddin. "Denoising of ECG signal by non-local estimation of approximation coefficients in DWT." *Biocybernetics and Biomedical Engineering* 37, no. 3 (2017): 599-610.
- [54] Lin, H-Y., S-Y. Liang, Y-L. Ho, Y-H. Lin, and H-P. Ma. "Discrete-wavelet-transform-based noise removal and feature extraction for ECG signals." *IRBM* 35, no. 6 (2014): 351-361.
- [55] Wang, Fang, and Zhong Ji. "Application of the dual-tree complex wavelet transform in biomedical signal denoising." *Bio-medical Materials and Engineering* 24, no. 1 (2014): 109-115.
- [56] El B'charri, Oussama, Rachid Latif, Khalifa Elmansouri, Abdenbi Abenaou, and Wissam Jenkal. "ECG signal performance de-noising assessment based on threshold tuning of dual-tree wavelet transform." *Biomedical Engineering Online* 16, no. 1 (2017): 26.
- [57] Zhang, Sheng, Jie Gao, Jie Yang, and Shun Yu. "A Mallat based wavelet ECG denoising algorithm." In *Applied mechanics and materials*, vol. 263, pp. 2267-2270. Trans Tech Publications Ltd, 2013.
- [58] Peng, Ziran, and Guojun Wang. "Study on optimal selection of wavelet vanishing moments for ECG denoising." *Scientific Reports* 7, no. 1 (2017): 1-11.

- [59] Han, Guoqiang, and Zhijun Xu. "Electrocardiogram signal denoising based on a new improved wavelet thresholding." *Review of Scientific Instruments* 87, no. 8 (2016): 084303.
- [60] Hong, H. E., and T. A. N. Yonghong. "A novel adaptive wavelet thresholding with identical correlation shrinkage function for ECG noise removal." *Chinese Journal of Electronics* 27, no. 3 (2018): 507-513.
- [61] Kumar, Ashish, Rama Komaragiri, and Manjeet Kumar. "Heart rate monitoring and therapeutic devices: a wavelet transform based approach for the modeling and classification of congestive heart failure." *ISA Transactions* 79 (2018): 239-250.
- [62] Kumar, Ashish, Rama Komaragiri, and Manjeet Kumar. "Design of wavelet transform based electrocardiogram monitoring system." *ISA Transactions* 80 (2018): 381-398.
- [63] Smital, Lukáš, Martin Vitek, Jiří Kozumplík, and Ivo Provazník. "Adaptive wavelet wiener filtering of ECG signals." *IEEE Transactions on Biomedical Engineering* 60, no. 2 (2012): 437-445.
- [64] Hao, Huan, Huali Wang, Naveed ur Rehman, Liang Chen, and Hui Tian. "An improved multivariate wavelet denoising method using subspace projection." *IEICE Transactions on Fundamentals of Electronics, Communications and Computer Sciences* 100, no.3(2017):769-775.
- [65] Kumar, Ashish, Rama Komaragiri, and Manjeet Kumar. "Time–frequency localization using three-tap biorthogonal wavelet filter bank for electrocardiogram compressions." *Biomedical Engineering Letters* 9, no. 3 (2019): 407-411.
- [66] Yadav, Santosh Kumar, Rohit Sinha, and Prabin Kumar Bora. "Electrocardiogram signal denoising using non-local wavelet transform domain filtering." *IET Signal Processing* 9, no. 1 (2015): 88-96.
- [67] Tracey, Brian H., and Eric L. Miller. "Nonlocal means denoising of ECG signals." *IEEE Transactions on Biomedical Engineering* 59, no. 9 (2012): 2383-2386.
- [68] Qian, Chunqiang, Honghong Su, and Helong Yu. "Local means denoising of ECG signal." *Biomedical Signal Processing and Control* 53 (2019): 101571.
- [69] Anapagamini, S. A., and R. Rajavel. "Hardware implementation of ECG denoising system using TMS320C6713 DSP processor." *International Journal of Biomedical Engineering and Technology* 21, no. 1 (2016): 95-108.
- [70] Jain, Shweta, Varun Bajaj, and Anil Kumar. "Riemann Liouville fractional integral based empirical mode decomposition for ECG denoising." *IEEE Journal of Biomedical and Health Informatics* 22, no. 4 (2017): 1133-1139.

- [71] Kumar, Shailesh, Damodar Panigrahy, and P. K. Sahu. "Denoising of Electrocardiogram (ECG) signal by using empirical mode decomposition (EMD) with non-local mean (NLM) technique." *Biocybernetics and Biomedical Engineering* 38, no. 2 (2018): 297-312.
- [72] Rakshit, Manas, and Susmita Das. "An efficient ECG denoising methodology using empirical mode decomposition and adaptive switching mean filter." *Biomedical Signal Processing and Control* 40 (2018): 140-148.
- [73] Kabir, Md Ashfanoo, and Celia Shahnaz. "Denoising of ECG signals based on noise reduction algorithms in EMD and wavelet domains." *Biomedical Signal Processing and Control* 7, no. 5 (2012): 481-489.
- [74] Singh, Pratik, Syed Shahnawazuddin, and Gayadhar Pradhan. "An efficient ECG denoising technique based on non-local means estimation and modified empirical mode decomposition." *Circuits, Systems, and Signal Processing* 37, no. 10 (2018): 4527-4547.
- [75] Jain, Shweta, Varun Bajaj, and Anil Kumar. "Effective de-noising of ECG by optimised adaptive thresholding on noisy modes." *IET Science, Measurement & Technology* 12, no. 5 (2018): 640-644.
- [76] Wang, Mengjiao, Zequan Zhou, Zhijun Li, and Yicheng Zeng. "An adaptive denoising algorithm for chaotic signals based on improved empirical mode decomposition." *Circuits, Systems, and Signal Processing* 38, no. 6 (2019): 2471-2488.
- [77] Das, M. K., and S. Ari. "Analysis of ECG signal denoising method based on S-transform." *IRBM* 34, no. 6 (2013): 362-370.
- [78] Singhal, Amit, Pushpendra Singh, Binish Fatimah, and Ram Bilas Pachori. "An efficient removal of power-line interference and baseline wander from ECG signals by employing Fourier decomposition technique." *Biomedical Signal Processing and Control* 57 (2020): 101741.
- [79] Tan, Chunyu, Liming Zhang, and Hau-tieng Wu. "A novel Blaschke unwinding adaptive-Fourier-decomposition-based signal compression algorithm with application on ECG signals." *IEEE Journal of Biomedical and Health Informatics* 23, no. 2 (2018): 672-682.
- [80] Sharma, Rishi Raj, and Ram Bilas Pachori. "Baseline wander and power line interference removal from ECG signals using eigenvalue decomposition." *Biomedical Signal Processing and Control* 45 (2018): 33-49.
- [81] Kumar, Ashish, Harshit Tomar, Virender Kumar Mehla, Rama Komaragiri, and

- Manjeet Kumar. "Stationary wavelet transform based ECG signal denoising method." *ISA Transactions* 114 (2021): 251-262.
- [82] Prashar, Navdeep, Meenakshi Sood, and Shruti Jain. "Design and implementation of a robust noise removal system in ECG signals using dual-tree complex wavelet transform." *Biomedical Signal Processing and Control* 63, (2021): 102212.
- [83] Edmonson, William, Juan Carlos Palacios, Chang An Lai, and Haniph Latchman. "A global optimization method for continuous-time adaptive recursive filters." *IEEE Signal Processing Letters* 6, no. 8 (1999): 199-201.
- [84] [Online]. Available: <https://cs.stanford.edu/people/eroberts/courses/soco/projects/data-compression/lossy/jpeg/dct.htm>. (last accessed on 10/06/2023).
- [85] Shaik, Basheeruddin Shah, G. V. S. S. K. R. Naganjaneyulu, T. Chandrasheker, and A. V. Narasimhadhan. "A method for QRS delineation based on STFT using adaptive threshold." *Procedia Computer Science* 54 (2015): 646-653.
- [86] Singh, Brij N., and Arvind K. Tiwari. "Optimal selection of wavelet basis function applied to ECG signal denoising." *Digital Signal Processing* 16, no. 3 (2006): 275-287.
- [87] Sabherwal, Pooja, Monika Agrawal, and Latika Singh. "Automatic detection of the R peaks in single-lead ECG signal." *Circuits, Systems, and Signal Processing* 36, no. 11 (2017): 4637-4652.
- [88] Sahoo, Santanu, Prativa Biswal, Tejaswini Das, and Sukanta Sabut. "De-noising of ECG signal and QRS detection using Hilbert transform and adaptive thresholding." *Procedia Technology* 25 (2016): 68-75.
- [89] Banerjee, S., R. Gupta, and M. Mitra. "Delineation of ECG characteristic features using multiresolution wavelet analysis method." *Measurement* 45, no. 3 (2012): 474-487.
- [90] Rakshit, Manas, and Susmita Das. "An efficient wavelet-based automated R-peaks detection method using Hilbert transform." *Biocybernetics and Biomedical Engineering* 37, no. 3 (2017): 566-577.
- [91] Park, Jeong-Seon, Sang-Woong Lee, and Unsang Park. "R peak detection method using wavelet transform and modified shannon energy envelope." *Journal of Healthcare Engineering* 2017 (2017).
- [92] Li, Cuiwei, Chongxun Zheng, and Changfeng Tai. "Detection of ECG characteristic points using wavelet transforms." *IEEE Transactions on Biomedical Engineering* 42, no. 1 (1995): 21-28.
- [93] Li, Peng, Xu Zhang, Ming Liu, Xiaohui Hu, Bo Pang, Zhaolin Yao, Hanjun Jiang, and Hongda Chen. "A 410-nW efficient QRS processor for mobile ECG monitoring in 0.18-

- μm CMOS.” *IEEE Transactions on Biomedical Circuits and Systems* 11, no. 6 (2017): 1356-1365.
- [94] Yochum, Maxime, Charlotte Renaud, and Sabir Jacquir. “Automatic detection of P, QRS and T patterns in 12 leads ECG signal based on CWT.” *Biomedical Signal Processing and Control* 25 (2016).
- [95] Sabherwal, Pooja, Latika Singh, and Monika Agrawal. “Aiding the detection of QRS complex in ECG signals by detecting S peaks independently.” *Cardiovascular Engineering and Technology* 9, no. 3 (2018): 469-481.
- [96] Yu, Kaimin, Lei Feng, Yunfei Chen, Minfeng Wu, Yuanfang Zhang, Peibin Zhu, Wen Chen, Qihui Wu, and Jianzhong Hao. "Accurate wavelet thresholding method for ECG signals." *Computers in Biology and Medicine* 169 (2024): 107835.
- [97] Huang NE, Shen Z, Long SR, Wu MC, Shih EH, Zheng Q, Tung CC, Liu HH. “The empirical mode decomposition method and the Hilbert spectrum for non-stationary time series analysis”. *Proc. Roy. Soc. London*, vol. 454A, pp 903–995, 1998.
- [98] Labate, Domenico, Fabio La Foresta, Gianluigi Occhiuto, Francesco Carlo Morabito, Aime Lay-Ekuakille, and Patrizia Vergallo. “Empirical mode decomposition vs. wavelet decomposition for the extraction of respiratory signal from single-channel ECG: A comparison.” *IEEE Sensors Journal* 13, no. 7 (2013): 2666-2674.
- [99] Karagiannis, Alexandros, and Philip Constantinou. “Noise-assisted data processing with empirical mode decomposition in biomedical signals.” *IEEE Transactions on Information Technology in Biomedicine* 15, no. 1 (2010): 11-18.
- [100] Chang, Kang-Ming. “Arrhythmia ECG noise reduction by ensemble empirical mode decomposition.” *Sensors* 10, no. 6 (2010): 6063-6080.
- [101] Wu, Zhaohua, and Norden E. Huang. “Ensemble empirical mode decomposition: a noise-assisted data analysis method.” *Advances in Adaptive Data Analysis* 1, no. 01 (2009): 1-41.
- [102] Rajesh, Kandala NVPS, and Ravindra Dhuli. “Classification of ECG heartbeats using nonlinear decomposition methods and support vector machine.” *Computers in Biology and Medicine* 87 (2017): 271-284.
- [103] Jebaraj, Jenitta, and Rajeswari Arumugam. “Ensemble empirical mode decomposition-based optimised power line interference removal algorithm for electrocardiogram signal.” *IET Signal Processing* 10, no. 6 (2016): 583-591.
- [104] Maji, U., M. Mitra, and S. Pal. “Detection and characterisation of QRS complex in VMD domain.” (2015): 101-5.

- [105] Goovaerts, Griet, Sibasankar Padhy, Bert Vandenberg, Carolina Varon, Rik Willems, and Sabine Van Huffel. "A machine-learning approach for detection and quantification of QRS fragmentation." *IEEE Journal of Biomedical and Health Informatics* 23, no. 5 (2018): 1980-1989.
- [106] Chawla, M. P. S. "PCA and ICA processing methods for removal of artifacts and noise in electrocardiograms: A survey and comparison." *Applied Soft Computing* 11, no. 2 (2011): 2216-2226.
- [107] Hu, Lei, Wenjie Cai, Ziyang Chen, and Mingjie Wang. "A lightweight U-Net model for denoising and noise localization of ECG signals." *Biomedical Signal Processing and Control* 88 (2024): 105504.
- [108] Sharma, Tanushree, and Kamalesh Kumar Sharma. "QRS complex detection in ECG signals using locally adaptive weighted total variation denoising." *Computers in Biology and Medicine* 87 (2017): 187-199.
- [109] Saadi, Dorthe B., George Tanev, Morten Flintrup, Armin Osmanagic, Kenneth Egstrup, Karsten Hoppe, Poul Jennum, Jørgen L. Jeppesen, Helle K. Iversen, and Helge BD Sorensen. "Automatic real-time embedded QRS complex detection for a novel patch-type electrocardiogram recorder." *IEEE Journal of Translational Engineering in Health and Medicine* 3 (2015): 1-12.
- [110] Kim, Jinkwon, and Hangsik Shin. "Simple and robust realtime QRS detection algorithm based on spatiotemporal characteristic of the QRS complex." *PloS one* 11, no. 3 (2016): e0150144.
- [111] Yakut, Önder, and Emine Dođru Bolat. "An improved QRS complex detection method having low computational load." *Biomedical Signal Processing and Control* 42 (2018): 230-241.
- [112] Ferdi, Y., J. P. Herbeuval, A. Charef, and B. Boucheham. "R wave detection using fractional digital differentiation." *ITBM-RBM* 24, no. 5-6 (2003): 273-280.
- [113] Benmalek, M., and A. Charef. "Digital fractional order operators for R-wave detection in electrocardiogram signal." *IET Signal Processing* 3, no. 5 (2009): 381-391.
- [114] Nayak, Chandan, Suman Kumar Saha, Rajib Kar, and Durbadal Mandal. "Automated QRS complex detection using MFO-based DFOD." *IET Signal Processing* 12, no. 9 (2018): 1172-1184.
- [115] Nayak, Chandan, Suman Kumar Saha, Rajib Kar, and Durbadal Mandal. "An efficient QRS complex detection using optimally designed digital differentiator." *Circuits, Systems, and Signal Processing* 38, no. 2 (2019): 716-749.

- [116] Bashar, Syed Khairul, Yeonsik Noh, Allan J. Walkey, David D. McManus, and Ki H. Chon. "VERB: VFCDM-based electrocardiogram reconstruction and beat detection algorithm." *IEEE Access* 7 (2019): 13856-13866.
- [117] Chin, Wen-Long, Cheng-Chieh Chang, Cheng-Lung Tseng, Ying-Zhe Huang, and Tao Jiang. "Bayesian real-time QRS complex detector for healthcare system." *IEEE Internet of Things Journal* 6, no. 3 (2019): 5540-5549.
- [118] Gutiérrez-Rivas, Raquel, Juan Jesús García, William P. Marnane, and Alvaro Hernández. "Novel real-time low-complexity QRS complex detector based on adaptive thresholding." *IEEE Sensors Journal* 15, no. 10 (2015): 6036-6043.
- [119] Nayak, Chandan, Suman Kumar Saha, Rajib Kar, and Durbadal Mandal. "An efficient and robust digital fractional order differentiator-based ECG Pre-processor design for QRS detection." *IEEE Transactions on Biomedical Circuits and Systems* 13, no. 4 (2019): 682-696.
- [120] Nayak, Chandan, Suman Kumar Saha, Rajib Kar, and Durbadal Mandal. "An optimally designed digital differentiator-based pre-processor for R-peak detection in electrocardiogram signal." *Biomedical Signal Processing and Control* 49 (2019): 440-464.
- [121] Kumar, Ashish, Ramana Ranganatham, Rama Komaragiri, and Manjeet Kumar. "Efficient QRS complex detection algorithm based on Fast Fourier Transform." *Biomedical Engineering Letters* 9, no. 1 (2019): 145-151.
- [122] Xie, Qingsong, Shikui Tu, Guoxing Wang, Yong Lian, and Lei Xu. "Feature enrichment based convolutional neural network for heartbeat classification from electrocardiogram." *IEEE Access* 7 (2019): 153751-153760.
- [123] Yazdani, Sasan, and Jean-Marc Vesin. "Extraction of QRS fiducial points from the ECG using adaptive mathematical morphology." *Digital Signal Processing* 56 (2016): 100-109.
- [124] Jain, Shweta, Anil Kumar, and Varun Bajaj. "Technique for QRS complex detection using particle swarm optimisation." *IET Science, Measurement & Technology* 10, no. 6 (2016): 626-636.
- [125] Pandit, Diptangshu, Li Zhang, Chengyu Liu, Samiran Chattopadhyay, Nauman Aslam, and Chee Peng Lim. "A lightweight QRS detector for single lead ECG signals using a max-min difference algorithm." *Computer Methods and Programs in Biomedicine* 144 (2017): 61-75.
- [126] Christov, Ivaylo I. "Real time electrocardiogram QRS detection using combined

- adaptive threshold.” *Biomedical Engineering Online* 3, no. 1 (2004): 28.
- [127] Lee, Miran, Dajeong Park, Suh-Yeon Dong, and Inchan Youn. “A novel R peak detection method for mobile environments.” *IEEE Access* 6 (2018): 51227-51237.
- [128] Sharma, Lakhan Dev, and Ramesh Kumar Sunkaria. “A robust QRS detection using novel pre-processing techniques and kurtosis based enhanced efficiency.” *Measurement* 87 (2016): 194-204.
- [129] Castells-Rufas, David, and Jordi Carrabina. “Simple real-time QRS detector with the MaMeMi filter.” *Biomedical Signal Processing and Control* 21 (2015): 137-145.
- [130] Jain, Shweta, Mitul Kumar Ahirwal, Anil Kumar, Varun Bajaj, and G. K. Singh. “QRS detection using adaptive filters: A comparative study.” *ISA Transactions* 66 (2017): 362-375.
- [131] Elgendi, Mohamed, Amr Mohamed, and Rabab Ward. “Efficient ECG compression and QRS detection for e-health applications.” *Scientific Reports* 7, no. 1 (2017): 1-16.
- [132] Zidelmal, Zahia, Ahmed Amirou, D. Ould-Abdeslam, Ali Moukadem, and Alain Dieterlen. “QRS detection using S-Transform and Shannon energy.” *Computer Methods and Programs in Biomedicine* 116, no. 1 (2014): 1-9.
- [133] Biswal, Birendra. “ECG signal analysis using modified S-transform.” *Healthcare Technology Letters* 4, no. 2 (2017): 68-72.
- [134] Chen, Chieh-Li, and Chun-Te Chuang. “A QRS detection and R point recognition method for wearable single-lead ECG devices.” *Sensors* 17, no. 9 (2017): 1969.
- [135] Merah, M., T. A. Abdelmalik, and B. H. Larbi. “R-peaks detection based on stationary wavelet transform.” *Computer Methods and Programs in Biomedicine* 121, no. 3 (2015): 149-160.
- [136] Berwal, Deepak, Ashish Kumar, and Yogendera Kumar. “Design of high performance QRS complex detector for wearable healthcare devices using biorthogonal spline wavelet transform.” *ISA Transactions* 81 (2018): 222-230.
- [137] Rekik, S., and N. Ellouze. “Enhanced and optimal algorithm for QRS detection.” *IRBM* 38, no. 1 (2017): 56-61.
- [138] Sharma, Ashish, Shivnarayan Patidar, Abhay Upadhyay, and U. Rajendra Acharya. “Accurate tunable-Q wavelet transform based method for QRS complex detection.” *Computers & Electrical Engineering* 75 (2019): 101-111.
- [139] Farashi, Sajjad. “A multiresolution time-dependent entropy method for QRS complex detection.” *Biomedical Signal Processing and Control* 24 (2016): 63-71.
- [140] Ravanshad, Nassim, Hamidreza Rezaee-Dehsorkh, Reza Lotfi, and Yong Lian. “A

- level-crossing based QRS-detection algorithm for wearable ECG sensors.” *IEEE Journal of Biomedical and Health Informatics* 18, no. 1 (2013): 183-192.
- [141] Qin, Qin, Jianqing Li, Yinggao Yue, and Chengyu Liu. “An adaptive and time-efficient ECG R-peak detection algorithm.” *Journal of healthcare engineering* 2017 (2017).
- [142] Deepu, Chacko John, and Yong Lian. “A joint QRS detection and data compression scheme for wearable sensors.” *IEEE Transactions on Biomedical Engineering* 62, no. 1 (2014): 165-175.
- [143] Tang, Xiaochen, Qisong Hu, and Wei Tang. “A real-time QRS detection system with PR/RT interval and ST segment measurements for wearable ECG sensors using parallel delta modulators.” *IEEE Transactions on Biomedical Circuits and Systems* 12, no. 4 (2018): 751-761.
- [144] Hou, Zhongjie, Yonggui Dong, Jinxi Xiang, Xuewu Li, and Bin Yang. “A real-time QRS detection method based on phase portraits and box-scoring calculation.” *IEEE Sensors Journal* 18, no. 9 (2018): 3694-3702.
- [145] Li, Yanjun, Xiaoying Tang, Zhi Xu, and Hong Yan. “A novel approach to phase space reconstruction of single lead ECG for QRS complex detection.” *Biomedical Signal Processing and Control* 39 (2018): 405-415.
- [146] Bajaj, Aditi, and Sanjay Kumar. “QRS complex detection using fractional Stockwell transform and fractional Stockwell Shannon energy.” *Biomedical Signal Processing and Control* 54 (2019): 101628.
- [147] Hossain, Md Billal, Syed Khairul Bashar, Allan J. Walkey, David D. McManus, and Ki H. Chon. “An accurate QRS complex and P-wave detection in ECG signals using complete ensemble empirical mode decomposition with adaptive noise approach.” *IEEE access* 7 (2019): 128869-128880.
- [148] Gupta, V., M. Mittal, and V. Mittal. “R-peak detection using chaos analysis in standard and real time ECG databases.” *IRBM* 40, no. 6 (2019): 341-354.
- [149] Jia, Menghan, Feiteng Li, Jiaquan Wu, Zhijian Chen, and Yu Pu. “Robust QRS detection using high-resolution wavelet packet decomposition and time-attention convolutional neural network.” *IEEE Access* 8, (2020): 16979-16988.
- [150] Chen, Hanjie, and Koushik Maharatna. “An Automatic R and T Peak Detection Method Based on the Combination of Hierarchical Clustering and Discrete Wavelet Transform.” *IEEE journal of Biomedical and Health Informatics* 24, no. 10 (2020): 2825-2832.
- [151] Modak, Sudipta, Luay Yassin Taha, and Esam Abdel-Raheem. “A Novel Method of

- QRS Detection Using Time and Amplitude Thresholds With Statistical False Peak Elimination.” *IEEE Access* 9 (2021): 46079-46092.
- [152] Fotoohinasab, Atiyeh, Toby Hocking, and Fatemeh Afghah. “A greedy graph search algorithm based on changepoint analysis for automatic QRS complex detection.” *Computers in Biology and Medicine* 130, (2021): 104208.
- [153] Morshedlou, Farnaz, Nassim Ravanshad, and Hamidreza Rezaee-Dehsorkh. “An ultra-low power analog QRS-detection circuit for ambulatory ECG monitoring.” *AEU-International Journal of Electronics and Communications* 129, (2021): 153551.
- [154] Kumar, Ashish, Ramana Ranganatham, Samayveer Singh, Rama Komaragiri, and Manjeet Kumar. “A robust digital ECG signal watermarking and compression using biorthogonal wavelet transform.” *Research on Biomedical Engineering* 37, no. 1 (2021): 79-85.
- [155] Kumar, Ashish, Rama Komaragiri, and Manjeet Kumar. “From pacemaker to wearable: techniques for ECG detection systems.” *Journal of Medical Systems* 42, no. 2 (2018): 1-17.
- [156] Kumar, Ashish, Manjeet Kumar, and Rama Komaragiri. “Design of a biorthogonal wavelet transform based R-peak detection and data compression scheme for implantable cardiac pacemaker systems.” *Journal of Medical Systems* 42, no. 6 (2018): 1-12.
- [157] Kumar, Ashish, Virender Kumar Mehla, Harshit Tomar, Manjeet Kumar, and Rama Komaragiri. “Classification of Normal and Abnormal ECG signals using Support Vector Machine and Fourier Decomposition Method.” In *2020 IEEE International Symposium on Smart Electronic Systems (iSES)(Formerly iNiS)*, pp. 161-166. IEEE, 2020.
- [158] Coast, Douglas A., Richard M. Stern, Gerald G. Cano, and Stanley A. Briller. “An approach to cardiac arrhythmia analysis using hidden Markov models.” *IEEE Transactions on Biomedical Engineering* 37, no. 9 (1990): 826-836.
- [159] Kohler, B-U., Carsten Hennig, and Reinhold Orglmeister. “The principles of software QRS detection.” *IEEE Engineering in Medicine and Biology Magazine* 21, no. 1 (2002): 42-57.
- [160] Silipo, Rosaria, and Carlo Marchesi. “Artificial neural networks for automatic ECG analysis.” *IEEE Transactions on Signal Processing* 46, no. 5 (1998): 1417-1425.
- [161] Kohler, B. U., Carsten Hennig, and Reinhold Orglmeister. “QRS detection using zero crossing counts.” *Applied Genomics and Proteomics* 2, no. 2 (2003): 138-145.

- [162] Cao, Hua, and Laurent Peyrodie. "Variational Mode Decomposition-Based Simultaneous R Peak Detection and Noise Suppression for Automatic ECG Analysis." *IEEE Sensors Journal* 23, no. 8 (2023): 8703-8713.
- [163] Peng, Xiangdong, Huaqiang Zhu, Xiao Zhou, Congcheng Pan, and Zejun Ke. "ECG Signals Segmentation Using Deep Spatiotemporal Feature Fusion U-Net for QRS Complexes and R-Peak Detection." *IEEE Transactions on Instrumentation and Measurement* 72 (2023): 1-12.
- [164] De Giovanni, Elisabetta, Tomas Teijeiro, Grégoire P. Millet, and David Atienza. "Adaptive R-Peak Detection on Wearable ECG Sensors for High-Intensity Exercise." *IEEE Transactions on Biomedical Engineering* 70, no. 3 (2022): 941-953.
- [165] Ajdaraga, Era, and Marjan Gusev. "Analysis of sampling frequency and resolution in ECG signals." In *2017 25th Telecommunication Forum (TELFOR)*, pp. 1-4. IEEE, 2017.
- [166] Bailey, James J., Alan S. Berson, Arthur Garson Jr, Leo G. Horan, Peter W. Macfarlane, David W. Mortara, and Christoph Zywiets. "Recommendations for standardization and specifications in automated electrocardiography: bandwidth and digital signal processing. A report for health professionals by an ad hoc writing group of the Committee on Electrocardiography and Cardiac Electrophysiology of the Council on Clinical Cardiology, American Heart Association." *Circulation* 81, no. 2 (1990): 730-739.
- [167] Malik, M. "Task force of the European society of cardiology and the North American society of pacing and electrophysiology. Heart rate variability. Standards of measurement, physiological interpretation, and clinical use." *Eur Heart J.* 17 (1996): 354-381.
- [168] A.L. Goldberger, L.A.N. Amaral, L. Glass, J.M. Hausdorff, P.C. Ivanov, R.G. Mark, J.E. Mietus, G.B. Moody, C.K. Peng, H.E. Stanley, PhysioBank, PhysioToolkit, and PhysioNet – components of a new research resource for complex physiologic signals, *Circulation* 101 E215–E220, 2000.
- [169] Moody, George B., and Roger G. Mark. "The impact of the MIT-BIH arrhythmia database." *IEEE Engineering in Medicine and Biology Magazine* 20, no. 3 (2001): 45-50.
- [170] Moody, George. "A new method for detecting atrial fibrillation using RR intervals." *Computers in cardiology* (1983): 227-230.
- [171] Moody, George B., W. Muldrow, and Roger G. Mark. "A noise stress test for

- arrhythmia detectors.” *Computers in Cardiology* 11, no. 3 (1984): 381-384.
- [172] Albrecht, Paul. “ST segment characterization for long term automated ECG analysis.” PhD diss., Massachusetts Institute of Technology, Department of Electrical Engineering and Computer Science, 1983.
- [173] American Heart Association. “AHA database.” URL <http://www.americanheart.org> (1989). (last accessed on 10/06/2023).
- [174] Nolle, F. M., F. K. Badura, J. M. Catlett, R. W. Bowser, and M. H. Sketch. “CREI-GARD, a new concept in computerized arrhythmia monitoring systems.” *Computers in Cardiology* 13 (1986): 515-518.
- [175] Baim, Donald S., Wilson S. Colucci, E. Scott Monrad, Harton S. Smith, Richard F. Wright, Alyce Lanoue, Diane F. Gauthier, Bernard J. Ransil, William Grossman, and Eugene Braunwald. “Survival of patients with severe congestive heart failure treated with oral milrinone.” *Journal of the American College of Cardiology* 7, no. 3 (1986): 661-670.
- [176] Taddei, A., G. Distanto, M. Emdin, P. Pisani, G. B. Moody, C. Zeelenberg, and C. Marchesi. “The European ST-T database: standard for evaluating systems for the analysis of ST-T changes in ambulatory electrocardiography.” *European Heart Journal* 13, no. 9 (1992): 1164-1172.
- [177] Laguna, Pablo, Roger G. Mark, A. Goldberg, and George B. Moody. “A database for evaluation of algorithms for measurement of QT and other waveform intervals in the ECG.” in *Computers in Cardiology 1997*, pp. 673-676. IEEE, 1997.
- [178] Iyengar, Nikhil, C. K. Peng, Raymond Morin, Ary L. Goldberger, and Lewis A. Lipsitz. “Age-related alterations in the fractal scaling of cardiac interbeat interval dynamics.” *American journal of physiology-regulatory, integrative and comparative physiology* 271, no. 4 (1996): R1078-R1084.
- [179] Bousseljot, R., D. Kreiseler, and A. Schnabel. “Nutzung der EKG-Signaldatenbank CARDIODAT der PTB über das Internet.” *Biomedizinische Technik/Biomedical engineering* 40, no. s1 (1995): 317-318.
- [180] Behar, Joachim A., Laurent Bonnemains, Vyacheslav Shulgin, Julien Oster, Oleksii Ostras, and Igor Lakhno. “Noninvasive fetal electrocardiography for the detection of fetal arrhythmias.” *Prenatal Diagnosis* 39, no. 3 (2019): 178-187.
- [181] Penzel, Thomas, George B. Moody, Roger G. Mark, Ary L. Goldberger, and J. Hermann Peter. “The apnea-ECG database.” in *Computers in Cardiology 2000. Vol. 27 (Cat. 00CH37163)*, pp. 255-258. IEEE, 2000.

- [182] Andreotti, Fernando, Joachim Behar, Sebastian Zauneder, Julien Oster, and Gari D. Clifford. "An open-source framework for stress-testing non-invasive fetal ECG extraction algorithms." *Physiological Measurement* 37, no. 5 (2016): 627.
- [183] Bing, Pingping, Wei Liu, and Zhihua Zhang. "DeepCEDNet: An Efficient Deep Convolutional Encoder-Decoder Networks for ECG Signal Enhancement." *IEEE Access* 9 (2021): 56699-56708.
- [184] Donoho D. L., "De-noising by soft-thresholding," *IEEE Transactions on Information Theory* 41, no. 3 (1995): 613-627.
- [185] Torres, María E., Marcelo A. Colominas, Gastón Schlotthauer, and Patrick Flandrin. "A complete ensemble empirical mode decomposition with adaptive noise." In *2011 IEEE international conference on acoustics, Speech and Signal Processing (ICASSP)*, pp. 4144-4147. IEEE, 2011.
- [186] Dragomiretskiy, Konstantin, and Dominique Zosso. "Variational mode decomposition." *IEEE Transactions on Signal Processing* 62, no. 3 (2013): 531-544.
- [187] Nazari, Mojtaba, and Sayed Mahmoud Sakhaei. "Successive variational mode decomposition." *Signal Processing* 174 (2020): 107610.
- [188] Singh, Pushpendra, Shiv Dutt Joshi, Rakesh Kumar Patney, and Kaushik Saha. "The Fourier decomposition method for nonlinear and nonstationary time series analysis." *Proceedings of the Royal Society A: Mathematical, Physical and Engineering Sciences* 473, no. 2199 (2017): 20160871.
- [189] Tripathi, Prashant Mani, Ashish Kumar, Rama Komaragiri, and Manjeet Kumar., "A novel approach for real-time ECG signal denoising using Fourier decomposition method." *Research on Biomedical Engineering* 38, no. 4 (2022): 1037-1049.
- [190] Agrawal, Sakshi, and Anubha Gupta. "Fractal and EMD based removal of baseline wander and powerline interference from ECG signals." *Computers in Biology and Medicine* 43, no. 11 (2013): 1889-1899.
- [191] Singh, Pratik, Syed Shahnawazuddin, and Gayadhar Pradhan., "Significance of modified empirical mode decomposition for ECG denoising." In *2017 39th Annual International Conference of the IEEE Engineering in Medicine and Biology Society (EMBC)*, pp. 2956-2959. IEEE, 2017.
- [192] Sameni, Reza, Mohammad Bagher Shamsollahi, Christian Jutten, and Massoud Babaie-Zade. "Filtering noisy ECG signals using the extended Kalman filter based on a modified dynamic ECG model." In *Computers in Cardiology, 2005*, pp. 1017-1020. IEEE, 2005.

- [193] Burguera, Antoni. “Fast QRS detection and ECG compression based on signal structural analysis.” *IEEE Journal of Biomedical and Health Informatics* 23, no. 1 (2018): 123-131.
- [194] Li, Hongqiang, Xiaofei Wang, Lei Chen, and Enbang Li., “Denoising and R-peak detection of electrocardiogram signal based on EMD and improved approximate envelope.” *Circuits, Systems, and Signal Processing* 33, no. 4 (2014): 1261-1276.
- [195] Ozaktas, Haldun M., Orhan Arikan, M. Alper Kutay, and Gozde Bozdağt., “Digital computation of the fractional Fourier transform.” *IEEE Transactions on Signal Processing* 44, no. 9 (1996): 2141-2150.
- [196] Serhani, Mohamed Adel, Hadeel T El Kassabi, Heba Ismail, and Alramzana Nujum Navaz., “ECG monitoring systems: Review, architecture, processes, and key challenges.” *Sensors* 20, no. 6 (2020): 1796.
- [197] Yang, Cary. “Applications of the fractional Fourier transform.” http://www.cs.cmu.edu/~lblum/flac/Presentations/Yang_final_draft.pdf (last accessed on 10/06/2023).
- [198] Almeida, Luis B. “The fractional Fourier transform and time-frequency representations.” *IEEE Transactions on signal processing* 42, no. 11 (1994): 3084-3091.
- [199] Gupta, V., and M. Mittal. “A comparison of ECG signal pre-processing using FrFT, FrWT and IPCA for improved analysis.” *IRBM* 40, no. 3 (2019): 145-156.
- [200] S. N. Elaydi, *An Introduction to Difference Equations*. New York: Springer, 1996
- [201] Zhang, Fei, and Yong Lian., “QRS detection based on multiscale mathematical morphology for wearable ECG devices in body area networks.” *IEEE Transactions on Biomedical Circuits and Systems* 3, no. 4 (2009): 220-228.
- [202] Phukpattaranont, Pornchai. “QRS detection algorithm based on the quadratic filter.” *Expert Systems with Applications* 42, no. 11 (2015): 4867-4877.
- [203] Elgendi, Mohamed. “Fast QRS detection with an optimized knowledge-based method: Evaluation on 11 standard ECG databases.” *PLoS one* 8, no. 9 (2013): e73557.
- [204] Canlas Jr., R.D.: *Data Mining in Healthcare: Current Applications and Issues* (2009)
- [205] Sun, Jin-Yu, Hui Shen, Qiang Qu, Wei Sun, and Xiang-Qing Kong. “The application of deep learning in electrocardiogram: Where we came from and where we should go?.” *International Journal of Cardiology* 337 (2021): 71-78.
- [206] Moca, Vasile V., Harald Bârzan, Adriana Nagy-Dăbâcan, and Raul C. Mureşan. “Time-frequency super-resolution with superlets.” *Nature communications* 12, no. 1 (2021):

1-18.

- [207] Krizhevsky, Alex, Ilya Sutskever, and Geoffrey E. Hinton. "Imagenet classification with deep convolutional neural networks." *Advances in Neural Information Processing Systems* 25 (2012): 1097-1105.
- [208] Szegedy, Christian, Wei Liu, Yangqing Jia, Pierre Sermanet, Scott Reed, Dragomir Anguelov, Dumitru Erhan, Vincent Vanhoucke, and Andrew Rabinovich. "Going deeper with convolutions." In *Proceedings of the IEEE conference on computer vision and pattern recognition*, (2015), 1-9.
- [206] Huang, Gao, Zhuang Liu, Laurens Van Der Maaten, and Kilian Q. Weinberger. "Densely connected convolutional networks" In *Proceedings of the IEEE conference on computer vision and pattern recognition*, (2017), 4700-4708.
- [207] Greenwald, S. D. "The MIT-BIH Malignant Ventricular Arrhythmia Database." *Physionet. Org* (1992).
- [208] Mathunjwa, Bhekumuzi M., Yin-Tsong Lin, Chien-Hung Lin, Maysam F. Abbod, and Jiann-Shing Shieh. "ECG arrhythmia classification by using a recurrence plot and convolutional neural network." *Biomedical Signal Processing and Control* 64 (2021): 102262.
- [209] Tripathi, Prashant Mani, A. Kumar, M. Kumar, and R. Komaragiri, "Multilevel Classification and Detection of Cardiac Arrhythmias With High-Resolution Superlet Transform and Deep Convolution Neural Network." *IEEE Transactions on Instrumentation and Measurement*, vol. 71, pp. 1-13, 2022, Art no. 4006113,
- [210] Lai, Dakun, Yuxiang Bu, Ye Su, Xinshu Zhang, and Chang-Sheng Ma. "Non-standardized patch-based ECG lead together with deep learning based algorithm for automatic screening of atrial fibrillation." *IEEE Journal of Biomedical and Health Informatics* 24, no. 6 (2020): 1569-1578.
- [211] Ross-Howe, Sara, and Hamid R. Tizhoosh. "Atrial fibrillation detection using deep features and convolutional networks." In *2019 IEEE EMBS International Conference on Biomedical & Health Informatics (BHI)*, pp. 1-4. IEEE, 2019.
- [212] Fan, Xiaomao, Qihang Yao, Yunpeng Cai, Fen Miao, Fangmin Sun, and Ye Li. "Multiscaled fusion of deep convolutional neural networks for screening atrial fibrillation from single lead short ECG recordings." *IEEE Journal of Biomedical and Health Informatics* 22, no. 6 (2018): 1744-1753.
- [213] Lee, Seung Hwan, Hyun-Chul Ko, and Young-Ro Yoon. "Classification of ventricular arrhythmia using a support vector machine based on morphological features." In *2013*

35th Annual International Conference of the IEEE Engineering in Medicine and Biology Society (EMBC), pp. 5785-5788. IEEE, 2013.

- [214] Tripathy, Rajesh K., Alejandro Zamora-Mendez, José A. De la O Serna, Mario R. Arrieta Paternina, Juan G. Arrieta, and Ganesh R. Naik. "Detection of life threatening ventricular arrhythmia using digital Taylor Fourier transform." *Frontiers in Physiology* 9 (2018): 722.
- [215] Mohanty, Monalisa, Santanu Sahoo, Pradyut Biswal, and Sukanta Sabut. "Efficient classification of ventricular arrhythmias using feature selection and C4. 5 classifier." *Biomedical Signal Processing and Control* 44 (2018): 200-208.
- [216] Llamedo, Mariano, and Juan Pablo Martínez. "An automatic patient-adapted ECG heartbeat classifier allowing expert assistance." *IEEE Transactions on Biomedical Engineering* 59, no. 8 (2012): 2312-2320.
- [217] Essa, Ehab, and Xianghua Xie. "An ensemble of deep learning-based multi-model for ECG heartbeats arrhythmia classification." *IEEE Access* 9 (2021): 103452-103464.
- [218] Baygin, Mehmet, Turker Tuncer, Sengul Dogan, Ru-San Tan, and U. Rajendra Acharya. "Automated arrhythmia detection with homeomorphically irreducible tree technique using more than 10,000 individual subject ECG records." *Information Sciences* 575 (2021): 323-337.
- [219] Sanivarapu, Prasanth Vaidya, Kandala NVPS Rajesh, NV Rajasekhar Reddy, and N. Chandra Sekhar Reddy. "Patient data hiding into ECG signal using watermarking in transform domain." *Physical and Engineering Sciences in Medicine* 43, no. 1 (2020): 213-226.
- [220] Cox, Ingemar, Matthew Miller, Jeffrey Bloom, Jessica Fridrich, and Ton Kalker. *Digital Watermarking and Steganography*. Morgan kaufmann, 2007.
- [221] Liu, Xiyao, Jieting Lou, Hui Fang, Yan Chen, Pingbo Ouyang, Yifan Wang, Beiji Zou, and Lei Wang. "A novel robust reversible watermarking scheme for protecting authenticity and integrity of medical images." *Ieee Access* 7 (2019): 76580-76598.
- [222] Peng, Haipeng, Bo Yang, Lixiang Li, and Yixian Yang. "Secure and traceable image transmission scheme based on semitensor product compressed sensing in telemedicine system." *IEEE Internet of Things Journal* 7, no. 3 (2019): 2432-2451.
- [223] Sanivarapu, Prasanth Vaidya, Kandala NVPS Rajesh, NV Rajasekhar Reddy, and N. Chandra Sekhar Reddy. "Patient data hiding into ECG signal using watermarking in transform domain." *Physical and Engineering Sciences in Medicine* 43, no. 1 (2020): 213-226.

- [224] Jero, S. Edward, Palaniappan Ramu, and S. Ramakrishnan. "ECG steganography using curvelet transform." *Biomedical Signal Processing and Control* 22 (2015): 161-169.
- [225] Kaur, Suneet, Riya Singhal, Omar Farooq, and Bhavneet Singh Ahuja. "Digital watermarking of ECG data for secure wireless communication." In *2010 International Conference on Recent Trends in Information, Telecommunication and Computing*, pp. 140-144. IEEE, 2010.
- [226] Jero, S. Edward, Palaniappan Ramu, and S. Ramakrishnan. "Discrete wavelet transform and singular value decomposition-based ECG steganography for secured patient information transmission." *Journal of medical systems* 38, no. 10 (2014): 1-11.
- [227] Banerjee, Soumyendu, and Girish Kumar Singh. "A new approach of ECG steganography and prediction using deep learning." *Biomedical Signal Processing and Control* 64 (2021): 102151.
- [228] Mathivanan, P., A. Balaji Ganesh, and R. Venkatesan. "QR code-based ECG signal encryption/decryption algorithm." *Cryptologia* 43, no. 3 (2019): 233-253.
- [229] Murillo-Escobar, D., C. Cruz-Hernández, R. M. López-Gutiérrez, and M. A. Murillo-Escobar. "Chaotic encryption of real-time ECG signal in embedded system for secure telemedicine." *Integration* 89 (2023): 261-270.
- [230] Tripathi, Prashant Mani, Ashish Kumar, Rama Komaragiri, and Manjeet Kumar. "Watermarking of ECG signals compressed using Fourier decomposition method." *Multimedia Tools and Applications* (2022): 1-15.
- [231] Manikandan, M. Sabarimalai, and Samarendra Dandapat. "Wavelet-based electrocardiogram signal compression methods and their performances: A prospective review." *Biomedical Signal Processing and Control* 14 (2014): 73-107.
- [232] Baby, Mina K., Aswathy Madhu, and R. P. Aneesh. "Biomedical image integrity check for telemedicine applications by hash embedding & wavelet compression." In *2017 International Conference on Networks & Advances in Computational Technologies (NetACT)*, pp. 178-185. IEEE, 2017.
- [233] Olmos, Salvador, Mar Millán, Jose Garcia, and Pablo Laguna. "ECG data compression with the Karhunen-Loeve transform." In *Computers in Cardiology 1996*, pp. 253-256. IEEE, 1996.
- [234] Al-Nashash, H. A. M. "A dynamic Fourier series for the compression of ECG using FFT and adaptive coefficient estimation." *Medical Engineering & Physics* 17, no. 3 (1995): 197-203.
- [235] Batista, Leonardo Vidal, Elmar Uwe Kurt Melcher, and Luis Carlos Carvalho.

- “Compression of ECG signals by optimized quantization of discrete cosine transform coefficients.” *Medical engineering & physics* 23, no. 2 (2001): 127-134.
- [236] El B'charri, Oussama, Rachid Latif, Wissam Jenkal, and Abdenbi Abenaou. “The ECG signal compression using an efficient algorithm based on the DWT.” *International Journal of Advanced Computer Science and Applications* 1, no. 7 (2016): 181-187.
- [237] Zhang, Bo, Jiasheng Zhao, Xiao Chen, and Jianhuang Wu. “ECG data compression using a neural network model based on multi-objective optimization.” *PloS one* 12, no. 10 (2017): e0182500.
- [238] Fathi, Abdolhossein, and Fatemeh Faraji-Kheirabadi. “ECG compression method based on adaptive quantization of main wavelet packet subbands.” *Signal, Image and Video Processing* 10, no. 8 (2016): 1433-1440.
- [239] Pandey, Anukul, Butta Singh, Barjinder Singh Saini, and Neetu Sood. “A joint application of optimal threshold based discrete cosine transform and ASCII encoding for ECG data compression with its inherent encryption.” *Australasian physical & engineering sciences in medicine* 39, no. 4 (2016): 833-855.